

Future Development of Thermal Spray Coatings

Types, Designs,
Manufacture and Applications

Edited by Nuria Espallargas

Future Development of Thermal Spray Coatings

Related titles

Nanocoatings and ultra-thin films: Technologies and applications
(ISBN 978-1-84569-812-6)

Thermal barrier coatings
(ISBN 978-1-84569-658-0)

Advances in marine antifouling coatings and technologies
(ISBN 978-1-84569-386-2)

The cold spray materials deposition process: Fundamentals and applications
(ISBN 978-1-84569-181-3)

**Woodhead Publishing Series in Metals and
Surface Engineering: Number 65**

Future Development of Thermal Spray Coatings

**Types, Designs, Manufacture
and Applications**

Edited by

Nuria Espallargas



ELSEVIER

AMSTERDAM • BOSTON • CAMBRIDGE • HEIDELBERG
LONDON • NEW YORK • OXFORD • PARIS • SAN DIEGO
SAN FRANCISCO • SINGAPORE • SYDNEY • TOKYO

Woodhead Publishing is an imprint of Elsevier

WP

WOODHEAD
PUBLISHING



Woodhead Publishing Limited is an imprint of Elsevier
80 High Street, Sawston, Cambridge, CB22 3HJ, UK
225 Wyman Street, Waltham, MA 02451, USA
Langford Lane, Kidlington, OX5 1GB, UK

Copyright © 2015 Elsevier Ltd. All rights reserved.

No part of this publication may be reproduced or transmitted in any form or by any means, electronic or mechanical, including photocopying, recording, or any information storage and retrieval system, without permission in writing from the publisher. Details on how to seek permission, further information about the Publisher's permissions policies and our arrangements with organizations such as the Copyright Clearance Center and the Copyright Licensing Agency, can be found at our website: www.elsevier.com/permissions.

This book and the individual contributions contained in it are protected under copyright by the Publisher (other than as may be noted herein).

Notices

Knowledge and best practice in this field are constantly changing. As new research and experience broaden our understanding, changes in research methods, professional practices, or medical treatment may become necessary.

Practitioners and researchers must always rely on their own experience and knowledge in evaluating and using any information, methods, compounds, or experiments described herein. In using such information or methods they should be mindful of their own safety and the safety of others, including parties for whom they have a professional responsibility.

To the fullest extent of the law, neither the Publisher nor the authors, contributors, or editors, assume any liability for any injury and/or damage to persons or property as a matter of products liability, negligence or otherwise, or from any use or operation of any methods, products, instructions, or ideas contained in the material herein.

ISBN: 978-0-85709-769-9 (print)

ISBN: 978-0-85709-774-3 (online)

British Library Cataloguing in Publication Data

A catalogue record for this book is available from the British Library

Library of Congress Cataloging-in-Publication Data

A catalog record for this book is available from the Library of Congress

Library of Congress Control Number: 2015942337

For Information on all Woodhead Publishing publications
visit our website at <http://store.elsevier.com/>



Working together
to grow libraries in
developing countries

www.elsevier.com • www.bookaid.org

Contents

List of contributors	ix
Woodhead Publishing Series in Metals and Surface Engineering	xi
1 Introduction to thermal spray coatings	1
<i>N. Espallargas</i>	
1.1 Introduction and historical overview of thermal spray	1
1.2 Current coatings and equipment	3
1.3 Current market of thermal spray	10
1.4 Future trends and applications	10
References	13
Part One Thermal spray coatings: New types and properties	15
2 Current status and future directions of thermal spray coatings and techniques	17
<i>P. Fauchais</i>	
2.1 Introduction	17
2.2 Spray torches	19
2.3 Measurements and testing	28
2.4 Models	33
2.5 Coating applications and developments	38
2.6 Future trends and applications	39
2.7 Conclusions	41
References	41
3 Feedstock suspensions and solutions	51
<i>R. Moreno, E. Bannier</i>	
3.1 Introduction	51
3.2 Stability and rheology of suspensions	53
3.3 Requirements for thermal spray suspension and solution feedstocks	65
3.4 Suspensions feedstock for thermal spray: types and preparation	71
3.5 Solution precursor feedstock for thermal spray: types and preparation	73
3.6 Conclusions and further developments of suspension and solution precursor feedstock for thermal spray	75
Acknowledgments	76
References	77

4	Status and future trends in suspension spray techniques	81
	<i>A. Killinger</i>	
4.1	Introduction: Suspension spraying	82
4.2	The suspension spray process	84
4.3	Equipment for suspension spraying	93
4.4	Applications	99
4.5	Summary and conclusion	116
	References	117
5	Application of solution precursor spray techniques to obtain ceramic films and coatings	123
	<i>L. Pawłowski</i>	
5.1	Introduction	124
5.2	Solution spray techniques	125
5.3	Preparation of solutions	128
5.4	Phenomena occurring at spraying	128
5.5	Microstructure of films and coatings synthesized by solution spray techniques	133
5.6	Properties of films and coatings	134
5.7	Possible applications of the coatings	138
	References	138
6	Future trends in cold spray techniques	143
	<i>R. Huang, H. Fukanuma</i>	
6.1	Introduction	143
6.2	Cold spray technique	144
6.3	Types of coatings and materials	151
6.4	Applications	158
6.5	Conclusions	160
	References	161
7	Current status and future prospects of warm spray technology	163
	<i>S. Kuroda, J. Kawakita, M. Watanabe, K.H. Kim, R. Molak, H. Katanoda</i>	
7.1	Introduction	163
7.2	Historical review of process development based on HVOF	164
7.3	Process characteristics of WS	170
7.4	Microstructure and mechanical properties of WS metallic coatings	176
7.5	WC–Co cermet coatings	188
7.6	Recent development of high-pressure warm spray (HP-WS)	198
7.7	Conclusion	202
	Acknowledgments	202
	References	203

8	Functionalized thermal spray coatings	207
	<i>S. Armada, R. Schmid, H. Johnsen, N. Espallargas</i>	
8.1	Introduction and background	207
8.2	Capsules technology	209
8.3	Functionalizing thermal spray coatings	214
8.4	Low-friction functionalized thermal spray coatings	218
8.5	Conclusions	226
	References	226
Part Two	New applications of thermal spray coatings	229
9	Thermal spray coatings in environmental barrier coatings	231
	<i>N.M. Melendez, A.G. McDonald</i>	
9.1	Introduction	231
9.2	Types of coatings, materials, and application areas	232
9.3	Thermal spraying fabrication techniques	236
9.4	Future trends	238
	References	239
10	Thermal spray coatings in renewable energy applications	241
	<i>S. Wijewardane</i>	
10.1	Introduction	241
10.2	Biomass incineration boilers	242
10.3	Geothermal piping systems	244
10.4	Offshore wind turbine towers	246
10.5	Hydroturbines	248
10.6	Photocatalytic hydrogen production	249
10.7	Thermoelectric power generation	251
10.8	Thin films for photovoltaic power generation	252
10.9	TPV power generation	253
10.10	Conclusion	254
	References	255
11	Manufacturing engineering in thermal spraying by advanced robot systems and process kinematics	259
	<i>R. Gadow, M. Floristán</i>	
11.1	Introduction	259
11.2	Influence of the process kinematics on the coating properties	260
11.3	Offline programming of robots for thermal spraying applications	265
11.4	Process kinematics optimization	271
11.5	Coupled numerical simulation and offline trajectory generation	274
11.6	Summary and conclusions	276
	References	277
Index		281

This page intentionally left blank

List of contributors

S. Armada SINTEF Materials and Chemistry, Trondheim, Norway

E. Bannier Instituto de Tecnología Cerámica (ITC), Asociación de Investigación de las Industrias Cerámicas (AICE), Castellón, Spain

N. Espallargas Norwegian University of Science and Technology, Trondheim, Norway

P. Fauchais University of Limoges, Limoges, France

M. Floristán Universitaet Stuttgart, Stuttgart, Germany

H. Fukanuma Plasma Giken Co. Ltd., Saitama, Japan

R. Gadow Universitaet Stuttgart, Stuttgart, Germany

R. Huang Plasma Giken Co. Ltd., Saitama, Japan

H. Johnsen SINTEF Materials and Chemistry, Trondheim, Norway

H. Katanoda National Institute for Material Science, Tsukuba, Japan; Kagoshima University, Kagoshima, Japan

J. Kawakita National Institute for Material Science, Tsukuba, Japan; Kagoshima University, Kagoshima, Japan

A. Killinger Universität Stuttgart, Stuttgart, Germany

K.H. Kim National Institute for Material Science, Tsukuba, Japan; Kagoshima University, Kagoshima, Japan

S. Kuroda National Institute for Material Science, Tsukuba, Japan; Kagoshima University, Kagoshima, Japan

A.G. McDonald University of Alberta, Edmonton, AB, Canada

R. Molak National Institute for Material Science, Tsukuba, Japan; Kagoshima University, Kagoshima, Japan

R. Moreno Instituto de Cerámica y Vidrio (ICV), Madrid, Spain

N.M. Melendez University of Alberta, Edmonton, AB, Canada

L. Pawłowski University of Limoges, Limoges, France

R. Schmid SINTEF Materials and Chemistry, Trondheim, Norway

M. Watanabe National Institute for Material Science, Tsukuba, Japan; Kagoshima University, Kagoshima, Japan

S. Wijewardane University of South Florida, Tampa, FL, USA

Woodhead Publishing Series in Metals and Surface Engineering

- 1 **Nickel and chromium plating**
J. K. Dennis and T. E. Such
- 2 **Microbiologically influenced corrosion handbook**
S. Borenstein
- 3 **Surface engineering casebook**
Edited by J. S. Burnell-Gray and P. K. Datta
- 4 **Duplex stainless steels**
Edited by R. Gunn
- 5 **Engineering coatings**
S. Grainger and J. Blunt
- 6 **Developments in marine corrosion**
Edited by J. P. Blitz and C. B. Little
- 7 **Fundamental and applied aspects of chemically modified surfaces**
J. P. Blitz and C. B. Little
- 8 **Paint and surface coatings**
Edited by R. Lambourne and T. A. Strivens
- 9 **Surfacing: Core research from TWI**
TWI
- 10 **Recommended values of thermophysical properties for selected commercial alloys**
K. C. Mills
- 11 **Corrosion of austenitic stainless steels**
Edited by H. S. Katal and B. Raj
- 12 **Fundamentals of metallurgy**
Edited by S. Seetharaman
- 13 **Energy absorption of structures and materials**
G. Lu and T. X. Yu
- 14 **The Hatfield memorial lectures: Developments in iron and steel processing**
Edited by P. R. Beely
- 15 **Laser shock peening**
K. Ding and L. Ye
- 16 **Structural shear joints**
G. T. Hahn, C. A. Rubin and K. A. Iyer
- 17 **Direct strip casting of metals and alloys**
M. Ferry
- 18 **Surface coatings for protection against wear**
Edited by B. G. Mellor
- 19 **Handbook of gold exploration and evaluation**
E. MacDonald
- 20 **The cold spray materials deposition process**
Edited by V. K. Champagne
- 21 **The SGTE casebook: Thermodynamics at work: Second Edition**
Edited by K. Hack

- 22 **Belt conveying of minerals**
E. D. Yardley and L. R. Stace
- 23 **Techniques for corrosion monitoring**
Edited by L. Yang
- 24 **Creep-resistant steels**
Edited by F. Abe
- 25 **Developments in high temperature corrosion and protection of materials**
Edited by W. Gao
- 26 **Mineral wool: Production and properties**
B. Sirok and B. Blagojevic
- 27 **High-performance organic coatings**
Edited by A. S. Khana
- 28 **Hydrometallurgy: Principles and applications**
T. Havlik
- 29 **Corrosion control in the aerospace industry**
Edited by S. Benavides
- 30 **Multiaxial notch fatigue**
L. Susmel
- 31 **Titanium alloys**
W. Sha and S. Malinox
- 32 **Advances in marine antifouling coatings and technologies**
Edited by C. Hellio and D. M. Yebra
- 33 **Maraging steels**
W. Sha and W. Gao
- 34 **Surface engineering of light alloys**
Edited by H. Dong
- 35 **Sintering of advanced materials**
Edited by Z. Z. Fang
- 36 **Managing wastes from aluminium smelter plants**
B. Mazumber and B. K. Mishra
- 37 **Fundamentals of aluminium metallurgy**
Edited by R. Lumley
- 38 **Electroless copper and nickel-phosphorus plating**
W. Sha and X. Wu
- 39 **Thermal barrier coatings**
Edited by H. Xu and H. Guo
- 40 **Nanostructured metals and alloys**
Edited by S. H. Wang
- 41 **Corrosion of magnesium alloys**
Edited by G. L. Song
- 42 **Shape memory and superelastic alloys**
Edited by Y. Yamauchi and I. Ohkata
- 43 **Superplasticity and grain boundaries in ultrafine-grained materials**
A. L. Zhilyaev and A. I Pshenichnyuk
- 44 **Superplastic forming of advanced metallic materials**
Edited by G. Gulliano
- 45 **Nanocoatings and ultra-thin films**
Edited by A. S. H. Makhlof and I. Tiginyanu
- 46 **Stress corrosion cracking**
Edited by V. S. Raja and T. Shoji
- 47 **Tribocorrosion of passive metals and coatings**
Edited by D. Landolt and S. Mischler
- 48 **Metalworking fluids (MWFs) for cutting and grinding**
Edited by V. P. Astakhov and S. Joksch

-
- 49 **Corrosion protection and control using nanomaterials**
Edited by V. S. Saji and R. Cook
- 50 **Laser surface modification of alloys for corrosion and erosion resistance**
Edited by C. T. Kowk
- 51 **Gaseous hydrogen embrittlement of materials in energy technologies Volume 1: The problem, its characterisation and effects on particular alloy classes**
Edited by R. P. Gangloff and B. P. Somerday
- 52 **Gaseous hydrogen embrittlement of materials in energy technologies Volume 2: Mechanisms, modelling and future developments**
Edited by R. P. Gangloff and B. P. Somerday
- 53 **Advances in wrought magnesium alloys**
Edited by C. Bettles
- 54 **Handbook of metal injection molding**
Edited by D. Heaney
- 55 **Microstructure evolution in metal forming processes**
Edited by J. Lin and D. Balint
- 56 **Phase transformations in steels Volume 1: Fundamentals and diffusion-controlled transformations**
Edited by E. Pereloma and D. V. Edmonds
- 57 **Phase transformations in steels Volume 2: Diffusionless transformations, high strength steels, modelling and advanced analytical techniques**
Edited by E. Pereloma and D. V. Edmonds
- 58 **Corrosion prevention of magnesium alloys**
Edited by G. L. Song
- 59 **Fundamentals of magnesium alloy metallurgy**
Edited by M. Pekguleryuz, K. Kainer and A. Kaya
- 60 **Advances in powder metallurgy**
Edited by I. Chang
- 61 **Rare earth-based corrosion inhibitors**
Edited by M. Forsyth and B. Hinton
- 62 **Thermochemical surface engineering of steels**
Edited by E. J. Mittemeijer and M. A. J. Somers
- 63 **Underground pipeline corrosion: Detection, analysis and prevention**
Edited by M. Orazem
- 64 **Handbook of smart coatings for materials protection**
Edited by A. S. H. Makhlof
- 65 **Future Development of Thermal Spray Coatings: Types, Designs, Manufacture and Applications**
Edited by Nuria Espallargas

This page intentionally left blank

Introduction to thermal spray coatings

1

N. Espallargas

1.1 Introduction and historical overview of thermal spray

Thermal spray is a technology that involves a group of techniques and coating processes that improve the performance of a component by adding functionality to surfaces. Thermal spray techniques aim at increasing the lifetime of materials compared to their structural mechanisms of breakdown or to provide them with a specific property (e.g. optical and electrical). Thermal spray is a very versatile technology that can be used in many types of applications and virtually almost on any component. This is why it has grown to become a large worldwide market of several billion dollars since the first produced coatings in the early years of the twentieth century. Its versatility makes this technology suitable for use against wear, corrosion and aggressive and high-temperature environments and for repair and restoration of components.

In the late-nineteenth century and early-twentieth century, Dr. Max Ulrich Schoop (Zurich, Switzerland) and collaborators worked on the development of a series of equipment able to melt and propel metals in the form of powder towards surfaces to produce a coating. In the beginning of this invention, only metals with low melting point were used (i.e. tin and lead) and the process was called *metallizing* (Hermanek, 2014; Davis and Davis & Associates, 2005). Some years and patents later, Dr. Schoop and collaborators produced the first thermal spray device for spraying metal wires. This system was based on the melting of a metal wire in a flame generated by the combustion of fuel with oxygen. The melted metal was afterwards atomized by a compressed gas that propelled the metal droplets onto a substrate to build up a coating. This technique is known nowadays as *flame spray*, and it has been the basis for the development of more advanced techniques such as the high-velocity oxygen fuel (HVOF) in the late 1970s and establishes the big family of the combustion thermal spray techniques (Figure 1.1). In view of the need for new types of metals for corrosion protection, Dr. Schoop's group introduced the *electric arc* as an improvement in the metallizing technique. The electric arc allowed spraying metals with higher melting points (i.e. steel, zinc and stainless steel), being the basis for the development of the second big family of thermal spray techniques based on the use of electrical energy (Figure 1.1). The third and latest family of thermal spray techniques started in the 1980s, and it is based on solid-state spraying; this is propelling the feedstock material onto the substrate for producing coatings in the absence of combustion or electrical energy. This latest family is known as cold spraying and the mechanisms of coating

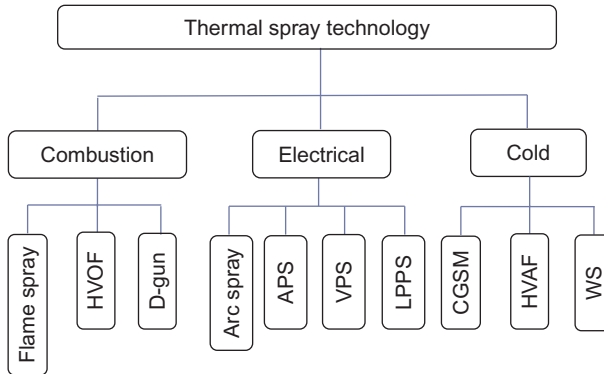


Figure 1.1 Family tree of the thermal spray technology, where the acronyms stand for HVOF (high-velocity oxygen fuel), D-gun (detonation gun), APS (atmospheric plasma spray), VPS (vacuum plasma spray), LPPS (low-pressure plasma spray), CGSM (cold gas spraying method), HVAF (high-velocity air fuel) and WS (warm spray).

build-up are still not fully understood. The more classical combustion techniques have been adapted around the concept of cold spraying, and low-temperature combustion techniques (e.g. warm spray and high-velocity air fuel) have appeared in recent years. However, only the cold gas spraying method can be considered a solid-state spraying technique (i.e. not melting the feedstock material) since the others involve the use of a combusted gas. The goal of the cold spraying techniques is mainly to produce metal coatings without altering the microstructure of the feedstock material and thus keeping a low degree of oxidation and the original structure and properties of the feedstock material. [Figure 1.1](#) summarizes the thermal spray techniques in a family tree.

After the initial periods of thermal spray in the first half of the twentieth century with the development of many patents around the metallizing method by either combustion or electric (arc) techniques, the greatest advance in thermal spray happened after the Second World War with the needs and advances of the space and aircraft age. In this period, techniques able to generate flames with higher temperatures for producing coatings of high melting point materials (ceramics and refractory metals) were necessary. It is in this period when thermal spray technology found its largest development in terms of both equipment and materials (feedstock/consumables). Thermal spray techniques such as the ceramic rod flame spray, the *detonation gun* (D-gun), and the *plasma spray* emerged after the 1940s–1950s with the need for producing robust and durable coatings to protect components used at high temperatures in engines. These developments were possible in a great extent due to the progress in the feedstock materials, which were available in the form of both powder and wire.

The equipment and materials sales and industrial sectors where thermal spraying is used have increased exponentially after the 1950s in parallel with the development of the techniques, processes and research around thermal spray. In addition, diagnostic tools (e.g. observation of individual particles in-flight), optimization of spraying

processes, modelling, nanotechnologies and environmental considerations have contributed with a significant growth to the thermal spray technology.

Nowadays, the main application sectors for thermal spray include aerospace, industrial gas turbine, automotive, biomedical, oil and gas, marine, processing, textile, paper and metal processing industries, among others. This is due to the ability of thermal spray to produce coatings for wear prevention, dimensional restoration and repair, thermal insulation, corrosion and oxidation resistance, lubricity, biocompatibility, etc. The new developments, in terms of both feedstock materials and thermal spray processes, are broadening even more the possibilities of using thermal spraying in new applications and enter into new markets.

1.2 Current coatings and equipment

There are a large number of processes able to apply coatings as there are also a large number of coating materials available in the market. The differences among all coating properties and processes rely on the thickness, substrate temperature achieved during coating and coating material. These three parameters are the ones driving the decision gate for coaters and users for their applications. [Figure 1.2](#) shows a comparison of the different coating processes available in the market with respect to their coating thickness and the temperature of the substrate achieved during coating. Thermal spray covers a large range of coating thicknesses and substrate temperatures, which makes this technology very versatile.

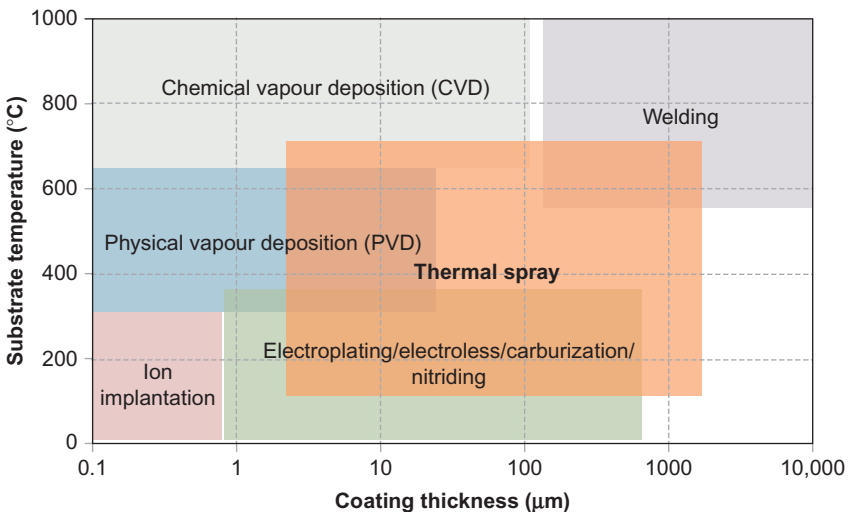


Figure 1.2 Comparison of the different coating processes in the market. Adapted from [Davis and Davis & Associates \(2005\)](#).

The large versatility of thermal spray is achieved thanks to the wide range of thermal spray techniques and equipment available in the market and the developments throughout all history of thermal spray. In addition, the different thermal spray techniques are able to spray also a large variety of materials suitable for many applications.

In this section, a summary of the main thermal spray techniques and their characteristics and materials will be presented. However, the reader is referred to [Davis and Davis & Associates \(2005\)](#) and [Pawlowski \(2008\)](#) for further information on this subject.

1.2.1 Coating build-up and materials

Thermal spray coating build-up process consists of finely dividing materials in a molten or semimolten condition and propelling them onto a substrate. The material that will form a coating is called feedstock, which enters the gun or the flame/jet for being heated to a plastic state (i.e. molten or semimolten) and then accelerated by compressed gas. The heated and accelerated particles strike the surface of a substrate, flatten and form thin splats that adhere to the substrate surface. The splats will eventually cool down and build up splat by splat a lamellar-structured coating as schematically illustrated in [Figure 1.3](#).

The coating build up will give as a result an inhomogeneous microstructure because the feedstock material is typically a powder with a distribution of particle sizes that might have different phases with different chemical compositions. In the same way, if the feedstock material is a wire, the particles formed at the tip of the wire

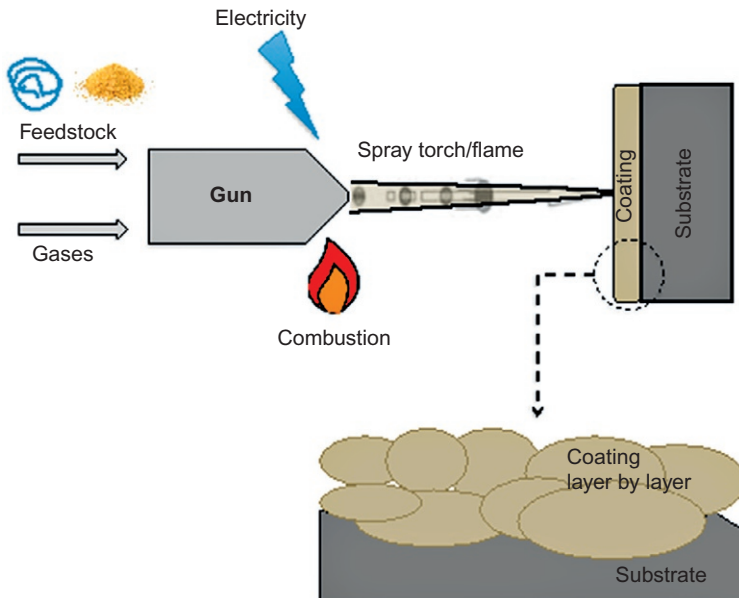


Figure 1.3 Schematic illustration of the thermal spray coating process.

will have different sizes. This leads to different particle temperatures and velocities when arriving at the substrate and therefore different physical states, that is, molten, semimolten or solid. The final microstructure will therefore contain voids (porosity) due to the bad anchoring of particles with different sizes or due to gas entrapment, splats of different sizes, splats with different phase microstructures, new phases (i.e. oxides) and cracks due to stress accumulation. In addition, the lamellar structure of thermal spray coatings will result in anisotropic properties due to the directionality of the coating microstructure.

Typical coating materials are basically any that do not decompose at high temperature (near the melting point). Virtually all types of materials, polymer, metals and ceramics (and their combinations), can be thermally sprayed by selecting the right thermal spray technique and spraying parameters. Until now, there has always been a limitation for ceramics lacking of melting point (e.g. silicon carbide and silicon nitride) due to their ability to sublime/decompose during atmospheric spraying. This limitation has recently been overcome with the development of a new technology for protecting ceramic powder for thermal spray. This technology allows spraying ceramics with no melting point by protecting each individual ceramic particle with a nanolayer of material acting as barrier against heat (Espallargas and Mubarok, 2014).

Table 1.1 shows the most typical materials used in thermal spray and some of their applicability. Choosing proper materials for specific applications is not an easy task and it requires expertise in the application and materials knowledge. Not only are the chemical, mechanical and physical properties of the materials the main factors influencing the coating performance, but also the feedstock characteristics will play a role. Therefore, in many cases, the know-how will control the coating properties and microstructures.

1.2.2 Thermal spray techniques

There are many different types of thermal spray techniques and processes and a more thorough review can be found in Davis and Davis & Associates (2005) and Pawlowski (2008). In this chapter, a short description of the most commonly used techniques in the market will be given. Table 1.2 summarizes the main thermal spray techniques with some specific process characteristics and illustrates the variety of thermal spray techniques and the different coating characteristics that can be achieved with them.

1.2.2.1 Flame spray

Flame spraying is one of the simplest methods for thermal spray nowadays. It is a cheap and easy technique to operate that can use powder, rod and wire feedstock. It was the first thermal spray process developed and it is still in use since 1910s, but with a modern design. The feedstock material is melted in an oxygen-fuel flame, where the fuel can be acetylene, propane and hydrogen, and then, it is accelerated towards the substrate material. The feedstock injection can be axial or radial depending on the type of torch.

Table 1.1 Typical thermal spray materials and their applicability

Coating material	Application							
	Corrosion	Oxidation	Wear	Sliding	Bond coat	Repair	Thermal barrier	Max working T ($^{\circ}\text{C}$)
Al	✓							400
Zn	✓							250
Ni					✓			500
Mo			✓	✓				320
Al-Mg	✓							200
Stainless steel	✓		✓					~500
Co-Al ₂ O ₃ or Cr ₂ O ₃		✓	✓					~1000
CoMoSi (Tribaloy)			✓	✓				~1000
NiAl, NiCr					✓	✓		950
Ni-graphite				✓				950
MCrAlY (M = Fe, Co, Ni)	✓	✓						~1000
Brass			✓	✓				<200
TiB ₂ , ZrB ₂			✓					
TiC, Cr ₃ C ₂ , NbC, TaC, WC			✓					400-500
WC-TiC			✓					800
TaC-NbC			✓					800
Cr ₃ C ₂ -NiCr	✓		✓	✓				800
WC-Co			✓	✓				500
Al ₂ O ₃ , TiO ₂ , ZrO ₂			✓				✓	>1000
AlO ₃ -TiO ₂ , Al ₂ O ₃ -MgO			✓				✓	>1000
Cr ₂ O ₃ -TiO ₂ , Cr ₂ O ₃			✓				✓	>1000
ZrO ₂ -MgO, ZrO ₂ -CaO, ZrO ₂ -SiO ₂			✓				✓	>1000

Table 1.2 Thermal spray techniques comparison

	Flame spray	Arc spray	Detonation gun	HVOF	APS	Cold spray
Flame/jet						
Temperature (°C)	3500	>6000	>4000	2500–3000	10,000–15,000	0–700 (preheated)
Velocity (m/s)	80–100	50–100	>2500	500–2000	300–1000	300–1200
Gas/fuel type	O ₂ /acetylene, propane, hydrogen	Air, nitrogen, argon	O ₂ /acetylene, hydrogen, propane, butane	O ₂ /natural gas, ethylene, propylene, propane, kerosene (liquid), hydrogen	Argon, helium, hydrogen, nitrogen and mixtures of them	Nitrogen, helium, air
Power input (kW)	20	5–10	–	150–300	40–200	–
Feedstock						
Max temperature in-flight (°C)	2500	>3800	–	3300	>3800	250
In-flight velocity (m/s)	50–100	50–150	750–1000	200–1000	50–100	500
Coating						
Porosity (%)	10–15 0 (for self-fluxing)	10–20	<2	<2	5–10	<5
Thickness (µm)	100–2500	100–2000	100–400	50–2000	100–1500	250–600

The main process parameters are spraying distance in the range of 120–250 mm, spraying in open atmosphere and substrate temperatures achieving a maximum of 250 °C (and up to 1000 °C for the self-fluxing coatings due to the post-spraying treatment).

1.2.2.2 Detonation gun

This thermal spray technique appeared with the need of producing dense and well-bonded coatings. The technique resembles the flame spray because it is based on a combustion process; however, the combustion is confined in a long barrel (450–1350 mm) where the feedstock (powder) is ignited together with the combusting gases. The combustion occurs in a detonation fashion, that is, it is intermittent. Classical D-guns can achieve 1–15 detonations per second, but more recently, new detonation systems can achieve up to 100 detonations per second (Fagoaga et al., 1999). These new systems can produce flames working at very high speeds able to create gas-tight coatings.

The main process parameters are spraying distance in the range of 100–300 mm, spraying in open atmosphere and powder feedstock sizes in the range of 5–60 µm.

1.2.2.3 High-velocity oxygen fuel

This technique was developed by Union Carbide (now Praxair) in the mid-1950s, the same company that developed the first generation of D-guns. However, it was in the late 1970s and early 1980s when it had the greatest success with the Jet Kote system. It is similar to the detonation system in the sense that the combustion is confined in a pressurized chamber, and then, the particles are accelerated in a barrel towards the substrate. However, HVOF operates in a continuous combustion fashion, and therefore, the technique is more efficient. This technique has become a standard for spraying cermet (ceramic–metallic such as WC–Co) materials. This technique uses powder feedstock that can be injected axially or radially depending on the type of gun. The gases are injected in the combustion chamber under pressure (0.3–4 MPa). The combusted gas is then accelerated in the barrel leading to supersonic flame velocities. The feedstock is introduced in the barrel by a carrier gas (nitrogen or argon) resulting in a high velocity of the sprayed particles.

The main process parameters are spraying distance in the range of 150–300 mm, spraying in open atmosphere and powder feedstock sizes typically in the range of 5–45 µm.

1.2.2.4 Arc Spray

The wire arc spraying technology was originally invented and patented by Dr. Schoop in the 1910s, and it gained most interest after the 1960s. The process uses a direct-current electric arc that is ignited between two consumable electrode wires that are continuously fed. The electric arc formed between the wire tips melts the feedstock wires while a high-velocity air jet atomizes and propels the molten metal towards the substrate

forming the coating. The high-velocity airflow ranges from 0.8 to 1.8 m³/min, and the thermal efficiency of the electric arc spray process is considerably higher than that of any other thermal spray process.

The main process parameters are spraying distance in the range of 50–170 mm, spraying in open atmosphere, controlled atmosphere and vacuum electrically conductive materials (e.g. Zn, Al, Mo and NiCr alloys) or cored wires containing ceramic phases such as tungsten carbide (WC). The coating porosity can be improved by performing post-spraying treatments.

1.2.2.5 Plasma spray

Plasma spraying consists of spraying a feedstock material by using an ionized gas or gas mixture. Electric fields are used to ionize the gases and produce thermal plasmas or plasma arcs that will be used for propelling the feedstock material towards the substrate surface. In the plasma spray gun, the plasma torch is generated by an anode (copper or graphite) and a cathode (thoriated tungsten). The electric arc discharge generated between the anode and the cathode ionizes the gas (or gas mixture) that expands in the atmosphere forming a jet. The feedstock material (powder) is injected into the jet, accelerated and propelled towards the substrate.

The main process parameters are spraying distance in the range of 60–130 mm, spraying in open atmosphere (APS), controlled atmosphere (LPPS) or vacuum (VPS) and powder feedstock sizes in the range of 20–90 μm. The temperature of the substrate should be kept low (100–200 °C) when spraying ceramic materials to avoid residual stresses in the coating. Post-treatment of the coating can be applied for improving the coating density by annealing or laser treatment.

1.2.2.6 Cold spray

Developed at the end of 1980s, this thermal spray technique aims at producing coatings by using high kinetic energy and not melting the particles during the spraying process. This is with the use of jets that are not the result of the combustion or ionization of a gas. The gas or gas mixture used for cold spraying is compressed up to 3.5 MPa and heated up to 700 °C. This heated gas is then introduced in a convergent–divergent nozzle (Laval type) where it expands to reach supersonic velocities. The feedstock powder material is introduced in the nozzle and the particles are accelerated well below their melting point towards the substrate. The gas temperature and powder feed rate are optimized to obtain the best coating microstructure. The gas composition, temperature and pressure are the controlling parameters of the coating characteristics and vary with the feedstock material type.

The main process parameters are spraying distance in the range of 10–50 mm, spraying in open atmosphere and powder feedstock sizes in the range of 5–20 μm. The criteria for feedstock powder material are that the powders should deform plastically and/or have a low melting point.

1.3 Current market of thermal spray

As mentioned earlier, there are many applications and markets for thermal spray, but the most recognized ones and where the economical volume is larger are the aerospace, the industrial gas turbine and automobile industries. According to a recent review published in 2013 (Dorfman and Sharma, 2013), these industries cover 75% of the total market for thermal spray, which is estimated in approximately \$6.5 billion with 77% of the revenue in coatings and services, 19% in materials and 4% in equipment. Most of this market (two-thirds) is located in Europe, Middle East and North America; however, the highest growth rate has been for Asia (Fukumoto, 2008) and South America as expected from their economical growth. Sixty percent of the thermal spray market belongs to the turbine industry, and therefore, it is expected that this industry will drive the development in the thermal spray technology in the next years.

However, other industrial segments and markets such as the oil and gas, paper, metal processing and biomedical industries can benefit or will require new advancements in thermal spray. For example, cold spray or the suspension/solution spraying techniques have attracted interest in these markets.

Some selected applications in the current markets of aerospace, industrial gas turbine and automobile industries are given in the handbook of thermal spray technology (Davis and Davis & Associates, 2005). An interesting feature among the selected applications is that the general trend is the large use of the classical techniques such as flame spraying and plasma spraying. In aerospace and industrial gas turbine industries, plasma spraying is used for many components since spraying ceramics is the most typical procedure. However, metals and cermets are also widely used materials in many aircraft and turbine components. Common coatings among these three market segments for thermal spray are thermal barrier coatings, abrasives and seals and wear-resistant surfaces.

A summary of the typical thermal spray coatings used in different market segments is shown in Table 1.3.

1.4 Future trends and applications

The aerospace industry has been the most versatile taking the lead on using the latest developments in thermal spray such as the controlled atmosphere plasma spray techniques (low-pressure plasma spray (LPPS) and vacuum plasma spray (VPS)) and HVOF. The automotive industry and other markets such as the biomedical and the maritime industries are in the need for new materials and developments as their business is still developing fast due to the need for reducing fuel consumption. In that sense, the choice of coatings providing less wear and friction, corrosion and oxidation; enhancing hardness; and increasing the operating temperatures is essential for achieving that goal. The current coating materials and techniques are able to achieve these goals, but improvements are still necessary in order to give new values to the coatings

Table 1.3 Summary of coatings for different applications

	Aerospace	Automobile	Industrial gas turbines	Maritime
Thermal barrier coatings				
ZrO ₂ -Y ₂ O ₃ (YSZ) ZrO ₂ - ²⁵ CeO ₂ -Y ₂ O ₃ CeO ₂ -YSZ CaTiO ₃	Turbine components	Piston crowns, cylinder heads, valves, exhaust ports, manifolds, turbochargers, backing plates of brakes	Combustor liner, transition rings, splash plate and fuel injector	
MCrAlY (M = Co, Ni)	Bond coat	Bond coat	Bond coat	
Seals/abradables				
Ni-graphite MCrAlY (M = Co, Ni) Polyesters NiAl-polyesters Al, bronze, babbitt AlSi with polyester, polyimide or BN	Rotating vane assemblies of aircraft turbines		Compressor case Compressor case Compressor case	
Oxidation and corrosion resistance				
MCrAlY (M = Co, Ni) Hastelloy (NiCrMo) Triballoys (Co-Cr-Si-Mo) Al Zn, Zn-Al	Engine components	Exhaust systems	Compressor section carrying moisture and chlorides and parts of the turbine in contact with fuels	Nonsacrificial thermal spray coatings Cathodic protection

Continued

Table 1.3 Continued

	Aerospace	Automobile	Industrial gas turbines	Maritime
Wear resistance and repair				
WC-Co, WC-CoCr and WC-Ni	Hydraulic systems, rebuilding/ repair of worn or corroded components	Prevention of galling in cylinder liners	Rotating shafts	Erosion-corrosion of water turbines
Ni-Al, CuNiIn				
Cr ₃ C ₂ -NiCr	Bond coats, antifretting and clearance control		High-temperature parts of the turbine section	
Triballoys (Co-Cr-Si-Mo)	Seals at high temperature		Compressor	
NiCr, NiCrMo, NiMoAl, alloy 625 and 718		Rebuilding of crankshaft	Build-up and repair	
Mo		Drop erosion in pistons Galling in cylinder liners		

such as environmental compatibility, high fuel efficiency, lower costs, lower weight, reduced maintenance and extended durability.

The growth of new thermal spray techniques, coatings and materials will certainly open the possibility for new markets where thermal spray has still a short business segment. For example, the aerospace, renewable/alternative energy, semiconductor, metal production and marine industries are potential growing areas since these are indeed growing markets in new developing and highly industrialized countries. The increase in the economic value of thermal spray will rely in the growth of knowledge, materials and processes. Therefore, advances in thermal spray are still possible and necessary.

The technology has also a big potential to go beyond its current limits of applications and markets since there are many industries outside the traditional thermal spray market that are aware of its benefits but do not take the risk to move into it. This limitation can only be overcome with advances in both industry and research. Expansion

of thermal spray takes place nowadays thanks to the developments in materials and equipment, diagnostic tools and understanding of the processes.

As mentioned in [Section 1.2.1](#), there is a room for new developments in feedstock production since new feedstock will mean broader market opportunities. In addition, progresses in new thermal spray processes will open the opportunity for new coatings and therefore new applications. Therefore, this book will focus on the latest findings, new trends and future of thermal spray coatings and processes in order to widen the technology to new potential applications.

References

- Davis, J.R., Davis & Associates, (Eds.), 2005. Handbook of Thermal Spray Technology. ASM International, Materials Park, OH.
- Dorfman, M.R., Sharma, A., 2013. Challenges and strategies for growth of thermal spray markets: the six-pillar plan. *J. Therm. Spray Technol.* 22 (5), 559–563.
- Espallargas, N., Mubarok, F., 2014. Thermal spraying of ceramic materials. WO2014068082 A2.
- Fagoaga, I., Barykin, G., De Juan, J., Soroa, T., Vaquero, C., Coatings, A., Inasmet, F., 1999. The high frequency pulse detonation (HFPD) spray process. In: *Thermal Spray 1999: United Thermal Spray Conference (DVS-ASM)*, pp. 282–287.
- Fukamoto, M., 2008. The current status of thermal spraying in Asia. *J. Therm. Spray Technol.* 17 (1), 5–13.
- Hermanek, F.J., 2014. What is Thermal Spray? For the International Thermal Spray Association (ITSA). Online: www.thermalspray.org.
- Pawlowski, L., 2008. *The Science and Engineering of Thermal Spray Coatings*. John Wiley & Sons Ltd., Chichester, England.

This page intentionally left blank

Part One

Thermal spray coatings: New types and properties

This page intentionally left blank

Current status and future directions of thermal spray coatings and techniques

2

P. Fauchais

2.1 Introduction

To be competitive in the market, it is important to be able to produce surfaces that are resistant to wear, corrosion, and aging and retain their electrical, optical, and thermal properties over a long period. It is also interesting to have technologies that help to simplify the product ranges and maintenance requirements. Surface treatments and coating technologies play a prominent role in this respect (Cartier, 2003). Coating technologies allow the deposition of materials with properties quite different from that of the surfaces of the part material. They involve dry and wet processes that can be divided into two groups according to the thickness of the coating. The coatings with thicknesses below a few micrometers are called thin coatings, while those with thicknesses over a few tens of micrometers and below a few millimeters are called thick coatings. Thin coating technologies (Dobkin and Zuraw, 2003; Pawlowski, 2003; Glocker and Shah, 2002; Mahan, 2000; Erkens et al., 2011; Frey and Khan, 2013; Gladish and Smurov, 2011), based on the condensation of gaseous or vapor phase, comprise chemical vapor deposition (CVD), physical vapor deposition (PVD), and pulsed laser deposition (PLD). The production of metal coatings by PVD and CVD processes appeared at the end of the nineteenth century while the production of thick metal coatings appeared at the beginning of the twentieth century with flame and wire-arc spraying. Plasma spraying appeared about 40 years later. However, thermal spraying started to be used in the industry only after 1960:

- (a) Almost up to the 1980s, the development of thermal spray processing (Davis, 2004; Tucker, 2013), including flame, plasma, detonation gun (D-gun), high-velocity oxygen fuel (HVOF), and wire-arc spraying, was carried out in an empirical manner. The way to proceed consisted of (i) varying the operating spray parameters for a powder with particles of given morphology and size distribution and (ii) characterizing the properties of the resulting coating and evaluating its performance in specific use conditions. The procedure was repeated until certain standards were obtained and the parameter setting was padlocked (Friis and Persson, 2003). This approach made it possible to develop efficient coatings and achieve repeatable and rather reliable products. It allowed the monitoring of macroscopic spray parameters, control of feedstock (particle morphology and size distribution), and booth-to-booth consistency.

- (b) At the end of the 1980s and in the 1990s, two new approaches were considered:
- The development of commercially available computerized spray systems. They allowed to continuously follow in real time the main macroscopic parameters of the process in the spray booth such as the arc voltage, powder carrier gas mass flow rate for a given injector at a given position, torch cooling water temperature and flow rate, and water leakage detection. Computers in control panel also helped in monitoring spray system aging. For example, the erosion of plasma torch electrodes, resulting in arc voltage decrease for a given arc current, was automatically corrected by increasing the hydrogen flow rate to raise the voltage back to that obtained with a noneroded anode nozzle.
 - At the same time, there is development in the laboratories of experiments and techniques to measure:
 - the hot gas flow temperature and velocity fields,
 - the particle trajectory distributions within the hot gas jets and effect of the powder carrier gas flow rate on these trajectories (the importance of controlling in-flight the parameters of hot particle, instead of the macroscopic spray parameters, was then demonstrated),
 - the particle velocity and temperature distributions at impact,
 - the substrate and coating temperature evolution during the spray process.

In parallel, numerical models were developed and the comparison of predictions with measurements helped to validate the model assumptions. With such measurements and models, the trial-and-error approach was shifted to a more scientific approach, progressively transforming the thermal spray process from an art to a science (Moreau et al., 2005).

At last, during this period, many efforts were also focused on the standardization of the techniques used for coating property characterization and control of coating performance in service conditions.

- (c) At the end of the 1990s, sensors, less sophisticated but more simple and robust and able to work in the harsh environment of spray booths, were developed on the basis of the techniques developed first in laboratories (Li et al., 2003; Fauchais and Vardelle, 2010). Extensive research on relationships between in-flight particle parameters and coating properties (Fauchais and Vardelle, 2010; Legoux et al., 2002; Planche et al., 2003; Sampath et al., 2009) led then to a drastic enhancement in process understanding and improvement of coating reproducibility and reliability (Sampath et al., 2009). However, the linkage to coating properties is still some sort of enigma (Sampath et al., 2009).

According to Dorfman and Sharma (2013a) in 2012, thermal spraying sales were in the range of € 4.6 billion, with about 50% for air plasma-sprayed coatings. These sales are less than those of the world market of electroplating, representing about € 10 billion (according to the report by Global Industry Analysts, November 2010).

This chapter deals with the current status of the thermal spray processes and the emerging trends. It will examine the following points:

- The evolution of the various spray torches: flame spray, HVOF, high-velocity air fuel (HVOF), D-guns, direct current (d.c.) and radio-frequency (RF) plasma torches, and finally cold spray guns.
- The history of the measurement techniques of gas temperatures and velocities, particle in-flight parameters, and heat fluxes to substrate.
- The process control evolution: from empirical techniques to the monitoring and/or control of the different thermal spray processes thanks to the development of sensors to measure in-flight particle temperatures and velocities, coating temperature during spraying, and stress formation within coating.

- The development of numerical models.
- The coating microstructure, porosity, and main properties (e.g., mechanical, thermal, and electrical) and main applications.
- The future trends and potential applications of nanostructured coatings and the ways to produce them from agglomerates of nanoparticles, glass-structure coatings, suspension, or solution spraying.
- The advantages and disadvantages of nanostructured coatings.

2.2 Spray torches

Dr. Max Ulrich Schoop in Switzerland created the first flame spray torch in 1909 and, in 1910, also developed the arc spray process (Tucker, 2013; Fauchais et al., 2014), but commercial acceptance of thermal spray techniques started in 1960. Gfeller and Baiker in the United States from Union Carbide (now Praxair Surface Technology) introduced in 1955 the D-gun. Direct current plasma torches appeared in the 1940s but commercial plasma spray torches showed up only at the beginning of the 1960s. The RF plasma torches have been commercially available since 1960. However, they were not industrially used before the 1980s. HVOF spraying was invented by Union Carbide in 1958 (Tucker, 2013) and was industrially developed in the early 1980s with the Jet Kote gun of Browning (Fauchais et al., 2014) who also developed later the HVAF process. The latest development has been the cold spray process, which was developed by a group of scientists from the Institute of Theoretical and Applied Mechanics of the Siberian Branch of the Russian Academy of Sciences in the mid-1980s. The first US patent of this technology was issued in 1994.

2.2.1 Flame spraying

In this spray process, a premixed mixture of acetylene and oxygen, fed to the torch nozzle extremity through a ring of 16–18 orifices, burns outside the torch and around the area where powder particles are axially injected with a carrier gas. Figure 2.1 presents the principle of flame spraying. The flame can be made either oxidizing (fuel lean) or reducing (fuel rich), the latter limiting metal powder oxidation during spraying.

The temperatures and velocities obtained with these flame torches are shown in Figure 2.2 (Fauchais et al., 2014). The powder melting temperature can be as high as 60–70% of the maximum flame temperature. Therefore, flame torches are used

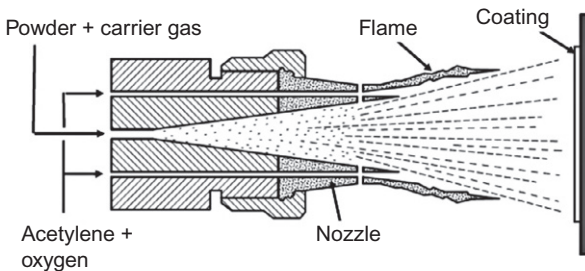


Figure 2.1 Principle of the powder flame spraying process.
Courtesy of Sulzer Metco.

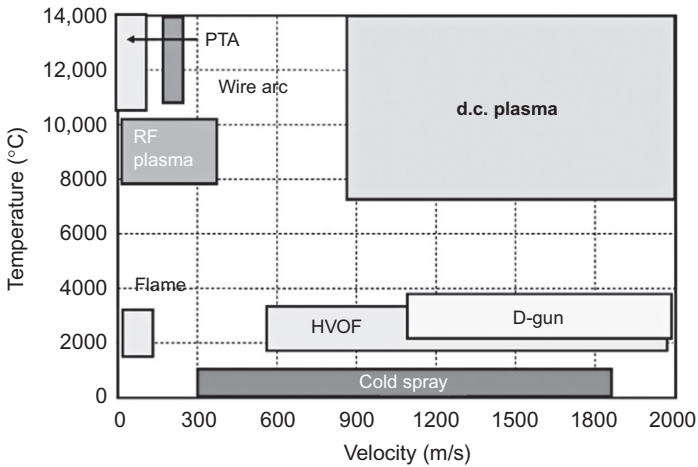


Figure 2.2 Gas temperature versus gas velocity for different thermal spray processes (Fauchais et al., 2014).

to spray metals and self-fluxing alloys with a powder feed rate of 30–50 g/min and deposition efficiency close to 50%. Metal coatings exhibit densities ranging from 85% to 98% but a rather high degree of oxidation (up to 20%). Self-fluxing alloys have functions of self-deoxidization and self-slag formation when remelted after spraying (fusing temperature >1040 °C), and so, the fused coatings are very dense. Flame torches also allow spraying polymer particles when air or nitrogen is blown between the ring-shaped flame and powder (Fauchais et al., 2014).

In the 1960s, wire flame spraying was also developed (Davis, 2004; Tucker, 2013; Fauchais et al., 2014). The metal wire is fed into the flame using air turbines or electrical motors, built into the torch, that push it through the nozzle at a controlled velocity adapted to wire tip melting. The molten tip is then atomized by air or nitrogen with flow rates up to $1 \text{ m}^3/\text{h}$.

Wires of ductile metals with diameters between 1.2 and 4.76 mm are available as coils, spools, or barrels. The process has high deposition rates (10–40 kg/h) and very good thermal efficiency (60–70%). Moreover, substrate heating by the flame is limited. Contrary to powders, the melting temperature of wire material can be up to 90% of flame temperature, allowing the spraying of ceramic materials, such as zirconia, with acetylene–oxygen flame. Based on this principle, Norton's Rokide flame system dedicated to ceramic coatings appeared in the 1960s. As the length of sintered ceramic rods was limited to 608 mm, corresponding to spraying times between 3 and 6 min, ceramic cords were developed later. They consist of a polymer envelop, up to 120 m in length, containing ceramic particles agglomerated with either an organic binder or a mineral one. The decomposition of the former starts at 250 °C while the latter lasts up to 1500 °C. Also, cored wires were developed. They are made up of a ductile envelope containing nonductile particles of either metal or ceramic. In the latter case, they make it possible to spray ceramic–metallic (cermet) coatings.

2.2.2 Wire-arc spraying

If this technique was first developed by Schoop in 1910, it was only commercialized in the 1960s–1970s. This process is “a thermal spray process in which an arc is struck between two consumable electrodes of a coating material, and compressed gas is used to atomize and propel the material to the substrate” (Hermanek, 2001). In this process, the two wire tips (one is the cathode and the other is the anode) are continuously melted and fragmented into droplets by air jets with flow rates from 0.8 to about 3 m³/min, injected with more or less sophisticated nozzles (Davis, 2004; Fauchais et al., 2014; Steffens et al., 1990). Figure 2.3 shows a schematic of a wire-arc spray gun.

Gas velocities are a few hundreds of m/s. As the gas is hardly heated by the arc, the substrate temperature can be maintained below a few tens of °C without cooling. Arc power levels are generally between 2 and 10 kW. As the temperature within the arc is high, a small gas volume can be higher than 20,000 °C and droplet temperatures are generally above the melting temperature. Coatings are rather porous and may contain resolidified particles and oxides (up to 25 wt.%). The process is well suited to high-rate deposition of anticorrosion coatings (zinc, aluminum, and zinc–aluminum corresponding to cathodic protection) on large steel structures with arcs operating up to 400 A in conventional guns and up to 1500 A in specific guns (Sørensen et al., 2009). Cored wires allow the spraying of cermets and metal superalloys (i.e., nickel- and cobalt-based alloys) (Tillmann et al., 2008).

2.2.3 Direct current plasma spraying

Plasma spraying is “a thermal spray process in which a nontransferred arc as a source of heat, ionizes a gas which melts the coating material, in-flight, and propels it to the work piece” (Fauchais et al., 2014; Fauchais, 2004). Plasma is an electrically neutral (same amount of ions and electrons) mixture of molecules, atoms, ions (in fundamental and excited states), electrons, and photons. With the gases used in

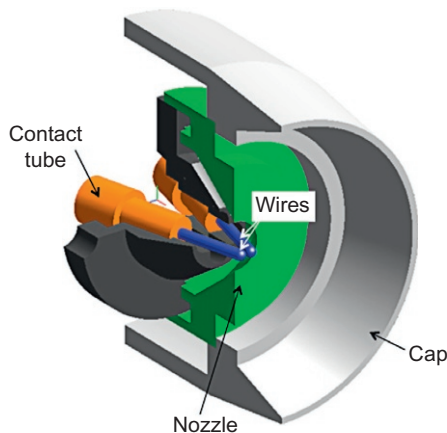


Figure 2.3 Schematic of the wire-arc spray device (Bolot et al., 2008).

plasma spraying, thermal plasma exists as soon as the gas temperature is higher than 7000–8000 °C at atmospheric pressure (Davis, 2004; Tucker, 2013; Fauchais et al., 2014; Fauchais, 2004). The plasma-forming gases Ar, Ar–H₂, Ar–He, Ar–He–H₂, N₂, and N₂–H₂ contain a primary heavy gas (Ar or N₂) for arc stabilization with a reasonable flow rate and also gas and particle acceleration, while the secondary gases (H₂ and He) improve the heat transfer to particles. The high temperatures required to generate the plasma are achieved through a d.c. arc struck between the cathode and the anode nozzles of the torch (Fauchais, 2004). The particles of the coating material, in the tens of μm size range, are injected radially either downstream or slightly upstream of the anode-nozzle exit.

2.2.3.1 Air plasma spraying

One of the first torches commercially available was that of Sulzer Metco (3M torch) in 1970 and then, at the end of the 1970s, that of Plasma Technik (F4 torch), derived from the plasma torch used by SNECMA (Davis, 2004; Tucker, 2013; Fauchais et al., 2014). A schematic of a plasma torch is presented in Figure 2.4. Plasma jet temperatures range between 8000 and 14,000 °C at the nozzle exit (on the jet axis) and gas velocities between 500 and 2600 m/s (subsonic velocities at these temperatures) for anode-nozzle internal diameters (i.d.) between 8 and 6 mm. The corresponding electrical power levels are between 20 and 80 kW.

Plasmas can melt any material, but, as the air surrounding the plasma jet is progressively entrained within the jet, oxygen present as atomic oxygen may react with the melted particles. The powders are generally injected radially in the plasma jet with feeding rates of 3–6 kg/h and deposition efficiency close to 50%. However, the anode arc root continuously moves on the anode wall and the corresponding voltage variation (ΔV) relatively to its mean value (V_m) can be relatively high: $0.5 < \Delta V/V_m < 1.5$ for diatomic plasma-forming gases and $0.5 > \Delta V/V_m$ for monatomic plasma-forming gases. As the power supply maintains a constant current, the power level dissipated in the plasma torch fluctuates accordingly to the arc voltage. For plasma spraying inside tubes or bore holes, the RotaPlasma torch from Sulzer Metco (Barbezat, 2001), with the same design, has the spray nozzle axis perpendicular to the axis of the torch body

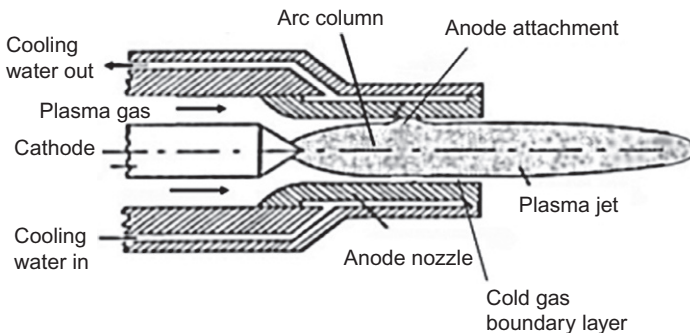


Figure 2.4 Schematic of the plasma spray torch (Fauchais et al., 2014).

and axis of rotation. The gas and cooling-water connections are made through a rotating feedthrough shaft. The torch can be rotated up to 200 rpm and inside diameters ranging between 40 and 500 mm can be coated, over a length of up to 500 mm.

Other torch designs exist such as the following:

- The Triplex Torch of Sulzer Metco. The arc current is divided into three separate arcs with three cathodes and one anode; several electrically insulated segments (“neutrodes”) form the wall of the arc channel and result in high- and low-voltage fluctuations for power level below 80 kW (Barbezat and Landes, 2000; Mauer et al., 2011a).
- The Axial III torch developed by Northwest Mettech (Canada) (Moreau et al., 1995). It consists essentially of three torches arranged such that their axes converge towards an interchangeable water-cooled nozzle, with plasma jets entering water-cooled channels directing the flows into a common nozzle (nozzle extension) with its axis aligned with the central injector and surrounding it. Power levels can reach 150 kW. The major advantages of such a torch are the axial injection of the powder and the common extension nozzle, which delays the mixing with the surrounding air and allows better heating and acceleration of the sprayed particles (Betoule, 1994).
- The water-stabilized plasma torch. It works with a mixture of hydrogen and oxygen resulting from the evaporation of water (Chraska and Hrabovsky, 1992). High arc voltages (260–300 V) and arc powers (80–200 kW) at moderate currents (300–600 A) are obtained, as well as gas temperatures up to 28,000 °C and velocities up to 7000 m/s (Betoule, 1994).
- The PlazJet torch. It has a button-type cathode and a very long anode nozzle, the plasma-forming gas being injected at high flow rates with a strong swirl component. The plasma temperatures are in the order of 10,000 °C or below while the gas velocities are very high as well as the deposition rates (e.g., 17 kg/h of Cr₂O₃) (Morishita, 1991).

2.2.3.2 *Controlled atmosphere or soft vacuum plasma spraying*

The oxidation occurring in air plasma spraying is detrimental for metals and alloys with regard to both coating properties and adhesion to the substrate. Muehlberger from Electro Plasma Inc. (now Sulzer Metco) (Muehlberger, 1988; Ambühl and Meyer, 1999) developed in 1974 an industrial controlled atmosphere spraying system. The equipment is contained in a water-cooled, vacuum-tight chamber where the pressure is maintained between 10 and 70 kPa. Plasma jet lengths can reach 50 cm, but the plasma temperature, except close to the anode-nozzle exit, is only a few thousands °C. These systems are called either vacuum plasma spraying (VPS) or low-pressure plasma spraying (LPPS). They achieve an excellent diffusion between coating (mainly superalloys) and substrate materials maintained at high temperatures. The main disadvantages are (i) a capital cost 5–20 times higher than that of APS systems and (ii) the difficulty to melt refractory materials in soft vacuum due to the Knudsen effect that limits the heat transfer to particles. To spray nonoxide ceramic materials that may decompose (e.g., SiC and B₄C), a controlled atmosphere chamber under Ar atmosphere at atmospheric pressure can be used (Freslon, 1995).

In the last decade, Sulzer Metco has developed a new controlled atmosphere plasma spray process, the plasma spray-physical vapor deposition (PS-PVD) (von Niessen and Gindrat, 2010). It uses a plasma torch with a high power (180 kW, 3000 A, gas flow rate up to 200 slpm) working at a pressure as low as 0.1 kPa (1 mbar)

resulting in a plasma jet more than 2 m in length and up to 0.4 m in diameter. This process can be used to produce coatings in the 1–100 μm thickness range with lamellar, columnar, and mixed microstructures, in particular. Coatings exhibiting a columnar microstructure similar to that of electron beam physical vapor deposition (EB-PVD) have been obtained.

2.2.3.3 RF induction plasmas

The energy transferred into the discharge of RF induction plasma is governed by electromagnetic coupling. A high-frequency voltage is applied to a water-cooled copper coil surrounding the discharge vessel, resulting in a high-frequency current flowing in this coil. This alternating current (coil current) generates a predominantly axial high-frequency oscillating magnetic field within the discharge cavity. This oscillating magnetic field generates a ring-shaped electric field perpendicular to the magnetic field lines, which in turn results, after the initial breakdown, in a ring-shaped alternating current flow (induction current), which sustains the plasma through Joule heating. Such torches were extensively studied in Russia in the 1960s–1970s (Dresvin, 1977). The first industrial torches were made by TAFE at the beginning of the 1980s and by TEKNA (Boulos, 1992) at the end of 1980s. The electrical power ranges between 30 and 100 kW with plasma gas flow rates of 50–100 slpm. The bulk plasma temperature is between 8000 and 10,000 $^{\circ}\text{C}$, and the mean exit plasma velocity is below 100 m/s. These torches allow for the internal axial injection of the powder or precursor, into the center of the discharge cavity using a water-cooled powder injection probe. They work at pressures between 30 and 100 kPa, thus requiring a controlled atmosphere spray chamber. Plasma RF torches with power levels up to 400 kW are now used to spheroidize powder particles.

2.2.4 Detonation gun

This process is a “thermal spray process variation in which the controlled explosion of a mixture of fuel gas, oxygen and powdered coating material is utilized to melt and propel the material to the work piece” (Hermanek, 2001). First developed in Russia, it was introduced in the early 1950s by Gfeller and Baiker working for Union Carbide. Oxygen and acetylene are fed in a barrel or tube about 1 m long that is closed at one end (Figure 2.5). The ignition of the mixture of gases by a spark plug takes place at the closed area of the barrel generating a detonation, which is repeated every time a new gas enters in the barrel (Kadyrov and Kadyrov, 1995).

Pressures around 2 MPa are generated when the combusted gases leave the closed area and travel along the barrel. The powder material injected in the middle of the barrel is then accelerated and heated and, in most cases, melted (Davis, 2004; Tucker, 2013; Fauchais et al., 2014). Gas velocities between 1000 and more than 2000 m/s can be reached (Figure 2.2). They depend strongly on the combustible gas mixture composition and also on pressure. The process is discontinuous with a frequency of up to 10 Hz and noise levels (about 145 dB) requiring the spray gun to be confined in acoustical enclosures. A new process called high-frequency pulse

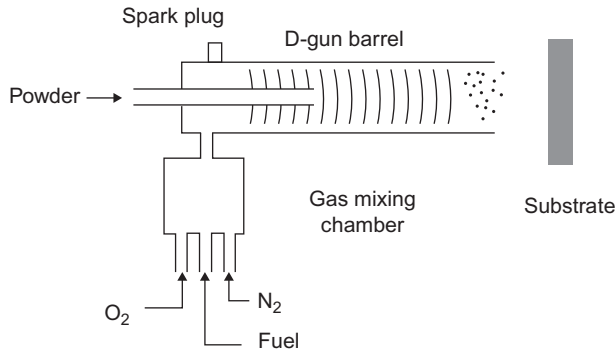


Figure 2.5 Schematic of the detonation gun (Kadyrov and Kadyrov, 1995).

detonation using aerodynamic valves producing discrete batches of explosive gases and powders for each cycle allows spray frequencies over 60 Hz (Belzunce et al., 2002).

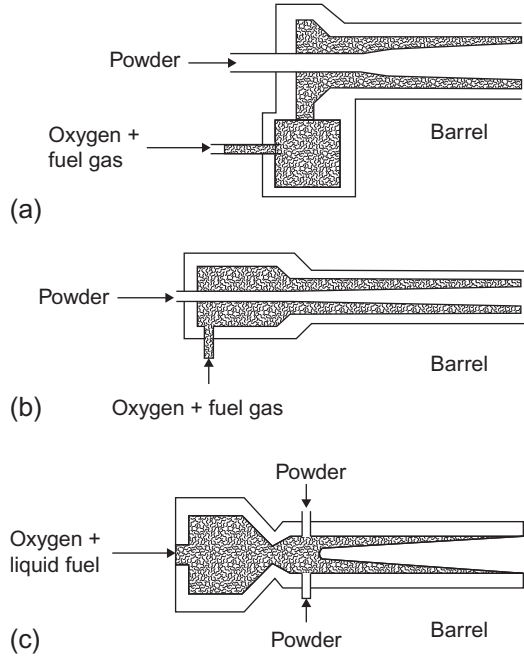
D-guns are mainly used to deposit metals, alloys, and cermets with high density (porosity <1%) and very low oxidation. A recent article of Astakhov (2008) presents the developments of the process. The most important and well-developed applications of the D-gun are the deposition of wear-resistant thermal barrier and electroinsulating and high-temperature oxidation-resistant coatings.

2.2.5 HVOF and HVAF spraying

Union Carbide introduced the HVOF process in 1958, but it was really commercialized in the early 1980s when Browning (1983) introduced the Jet Kote (Deloro Stellite) system working with fuel gas and oxygen. With the “high-velocity oxygen fuel spray process” (Thorpe and Richter, 1992), the combustion is achieved in a pressurized chamber up to 0.8–0.9 MPa, water-cooled or not, followed by a Laval-type barrel up to 30-cm long. The Laval geometry of the barrel generates supersonic velocities of the combusted gases (up to 2000 m/s; see Figure 2.6a) due to the hot gas expansion. The coating feedstock material is introduced axially in the combustion chamber, which requires a pressurized powder feeder. The evolution of the water-cooled HVOF design is the axial flow device shown in Figure 2.6b, where the combustible gases are introduced radially or axially in the combustion chamber, positioned coaxially with the nozzle. This design improves the thermal efficiency of the torch while providing powder axial injection. The last development is presented in Figure 2.6c. The combustion chamber is coaxial with the nozzle, but the powder is injected radially beyond the throat at the beginning of the barrel or in the divergent part of the nozzle. Injecting powders at this point requires powder feeders at lower pressure and, if necessary, multiple-port powder injection for a more uniform loading of the exiting gas stream.

This technique allows for the production of very dense coatings (porosity <0.5%) and with low oxidation in the case of metallic materials. However, for assuring a good

Figure 2.6 Different types of HVOF guns: (a) Jet Kote from Browning; (b) powder axial injection and combustion chamber; and (c) axial chamber with radial powder injection (Fauchais et al., 2014).



performance of the coatings, many metallic and carbide-based cermet materials must avoid or at least drastically reduce oxidation and partial decarburization. This can be achieved by diminishing the gas temperature while increasing its velocity. To that end, Browning developed the HVAF process, which uses air instead of oxygen as combustion gas (Browning, 1992). Air requires at least five times higher flow rates than pure oxygen. For the same fuel-oxygen richness, nitrogen present in air does not participate in the combustion process but must be heated, thus resulting in lower gas temperatures. The gun can be cooled by the airflow, and its efficiency can reach 90%.

Two types of HVOF guns exist depending on the chamber pressure. The low-pressure HVOF gun works at pressures between 0.24 and 0.6 MPa with heat inputs below 600–700 MJ. They use hydrogen, propylene, methane, propane, and heptane as fuel with oxygen or kerosene as fuel with air. The high-pressure HVOF gun is operated in the pressure range 0.62–0.82 MPa and generally uses kerosene either with oxygen or air with heat inputs over 1 GJ. This gun is often termed “hypervelocity gun.” Over the last two decades, according to Gärtner et al. (2006), the development of HVOF systems has been aimed at reducing the temperature of particles and increasing their velocity (Figure 2.7). Higher particle velocities were obtained by using converging–diverging Laval-type barrel designs and higher gas pressures with the presence of noncombustible gases in the combustion chamber. The last developments correspond to power levels up to 300 kW (kerosene 31 slpm, O₂ 965 slpm, and air 500 slpm), the flame being ignited in the combustion chamber with hydrogen pilot flame (88 slpm).

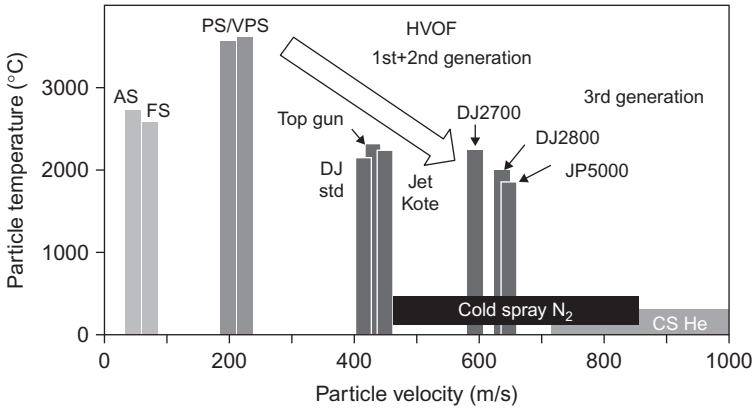


Figure 2.7 Particle temperatures versus particle velocities for different thermal spray processes as measured for high-density materials. The arrow indicates the observed trend of recent developments (AS, powder flame spraying; FS, wire flame spraying; PS, air plasma spraying; VPS, vacuum plasma spraying; CS, cold spray) (Gärtner et al., 2006).

2.2.6 Cold spray

This process is “a kinetic spray process utilizing supersonic jets of a compressed gas to accelerate powder particles, at near-room temperature, to ultra high velocities (up to 1500 m/s). The *non-melted* particles traveling at speeds between 500 and 1500 m/s plastically deform and consolidate on impact with the substrate or underlying layer to create a coating” (Hermanek, 2001). The process is based (Dykhuzen and Smith, 1998; Champagne, 2007; Stoltenhoff et al., 1994) on the gas-dynamic acceleration of particles to supersonic velocities and hence high kinetic energies. As shown in Figure 2.8, it uses (i) convergent–divergent Laval nozzles with upstream pressure between 2 and 2.5 MPa for typical nozzle throat internal diameters in the range of 2–3 mm and (ii) N₂, He, or their mixtures at very high flow rates (up to 5 m³/min). The mass flow rate of the gas must be 10 times that of the entrained powder, typically 6 kg/h, corresponding to 336 m³/h for helium and 52.3 m³/h for nitrogen. Gases introduced are preheated up to 600–700 °C to avoid their liquefaction under expansion

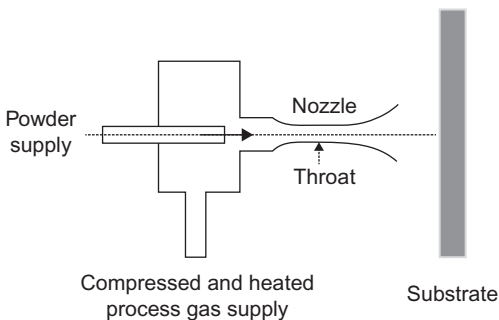


Figure 2.8 Schematic of a cold spray system (Browning, 1992).

and increase their velocity. In the first cold spray systems, the gas-heating device was separated from the gun to which it was connected through a soft pipe that was difficult to thermally insulate for temperatures over 600 °C. In the current systems, the gas heater is fixed on the gun and the gas can reach 1100 °C. As the particles are injected upstream of the nozzle throat, the powder feeder has to be pressurized.

The sprayed particles adhere to the substrate only if their impact velocity is above a critical value that depends on the coating material and varies between 500 and 900 m/s. However, if the impact velocity is much higher than the critical value for the coating material, it can destroy the previously sprayed layers. The spray pattern covers an area of roughly 20–60 mm², and spray rates are about 3–6 kg/h. Deposition efficiencies reach easily 80–90%, and in principle, ductile metals or alloys can be sprayed. However, blends of ductile materials (>50 vol.%) with stronger materials or ceramics can also be used. Now recently, the production of only ceramic coatings (e.g., TiO₂) with specific particle morphology is also tested (Yamada et al., 2010). They are sprayed using a modified version of cold spray called “low-pressure cold spraying” process. In this case, the upstream pressure is below 1 MPa, typically 0.5 MPa with a much lower (about one order of magnitude) gas flow rate of about 0.4 m³/min (Fauchais et al., 2014). Under most of the spraying conditions, the substrate is little heated by the gas exiting the gun (up to 200 °C at the maximum). However, recent systems operate at higher pressure, higher temperature, and higher powder feed rate in order to increase particle velocity and deposition rate, and these conditions result in an increase of the substrate temperature.

2.3 Measurements and testing

Experimental investigations of thermal spray processes started in laboratories in the 1960s and were mainly devoted to characterize plasma jets or flames used for spraying. At the end of the 1970s and in the 1980s, still in laboratories, research works were dedicated to the experimental observation of particles in-flight. The outcome in the 1990s was the development of robust devices, called sensors, that could survive in the harsh atmosphere of spray booths and that were simple enough to avoid the numerous adjustments necessary for laboratory setups. These sensors, coupled to computerized control panels, have helped the beginning of the online control of spray processes. In the 1990s and at the beginning of the new millennium, researchers have also intensively worked on coating buildup. These works have allowed the definition of other important parameters, different from those related to particles in-flight and have improved the online control.

2.3.1 High-energy gas temperatures and velocities of the flame

2.3.1.1 Plasmas

Most temperature measurements are based on the emission spectroscopy of molecules, atoms, and ions. They give the population of the emitting excited level (Fauchais et al., 1989, 1992) and assumptions must be made to deduce a temperature

from this population. The most common assumptions are local thermodynamic equilibrium (LTE) and gas jet axial symmetry. According to the temperature evolution of measured volumetric emission coefficient and detection limits of detectors, temperatures can be measured for a range of about 5000–6000 °C. Thus, below 8000 °C, molecular spectra are used, from 8000 to 14,000 °C atomic lines and over 15,000 °C ion lines. Moreover, radiation collected is the integrated intensity of the light originating along the line of sight (optical path). If the thermal spray jet has a perfect axial symmetry, Abel's inversion is used to determine temperature distributions (Fauchais et al., 1989, 1992). A typical example of results (Roumilhac et al., 1990) is presented in Figure 2.9 showing the effect of the anode-nozzle design on the plasma jet temperature distributions obtained. Another measurement problem is linked to the anodic arc root fluctuations. The arc attachment is continuously fluctuating and brings about a surging and whipping motion of the plasma jet (Duan and Heberlein, 2000, 2002; Coudert et al., 2007; Fauchais et al., 2008a), which is detrimental to the acceleration and heating of the injected particles. However, as the response times of detectors are around milliseconds, fluctuations, typically between 2 and 10 kHz, are integrated and the temperature distribution recorded seems perfectly symmetrical. Temperature distributions or pictures of fluctuating plasmas can be obtained only with fast response time detectors ($<10^{-5}$ s). Nonsymmetrical jets also exist, for example, because of a too strong radial powder carrier gas flow rate or jets issued from Triplex torch (Mauer et al., 2011b). In that case, plasma computer tomography (Landes, 2006) must be used, the emitted radiation under several angles of observation (Mauer et al., 2011b; Landes, 2006) permitting to measure the gas temperature.

Velocity measurements in the plasma jet core are very limited and consist essentially of the measure of the time of flight of the luminous fluctuations of the plasma, which are supposed to propagate at the flow velocity (Coudert et al., 1995; Planche et al., 1998). It should be noted that this method can only be applied at the nozzle exit when using monatomic gases (Ar and He) as plasma-forming gas as the fluctuation level of plasma jet is low.

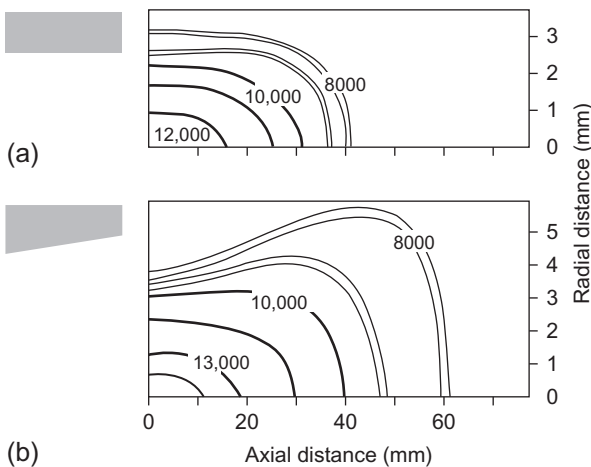


Figure 2.9 Plasma jet isotherms (Ar–H₂ 45–15 slpm, 500 A) for two different nozzle shapes: (a) cylindrical nozzle and (b) slightly divergent nozzle producing longer and broader jet (Roumilhac et al., 1990).

2.3.1.2 *Plasma plumes and combustion flames*

Below 7000–8000 °C, instead of molecular spectra, more sophisticated techniques such as coherent anti-Stokes Raman spectroscopy or Rayleigh scattering can also be used (Eckbreth and Anderson, 1986; Hall and Eckbreth, 1984). These techniques and thermocouples (below 1900 °C) have been used to measure plasma plume and combustion flame temperatures. Enthalpy probes allow determining enthalpy, temperature, velocity, and composition, if they comprise a gas sampling line and a mass spectrometer, of flame or plasma jets. However, the maximum temperatures that enthalpy probes can sustain are below 5000–6000 °C, especially when the gas flow contains hydrogen. Grey et al. (1962) presented this technique in 1962, and since then, it has been developed and used intensively. Now it is possible to perform measurements in compressible jets and probes are available from companies such as TECKNA since 1993, see the review of Blais et al. (2005).

Also, small particles (in the few μm size range) can be injected in flames and plasmas and gas velocity inferred from particle velocities measured by particle image velocimetry (Westerweel, 1993), assuming that the Knudsen effect is negligible and particles are advected with the gas flow. It is generally the case for combustion flames, but not necessarily for plasmas.

2.3.2 *In-flight particle temperatures, velocities, and diameters*

Up to the 1990s, sophisticated measurement devices such as laser Doppler anemometry were used for particle velocity measurement, the phase Doppler shift for velocity and diameter measurement, fast pyrometers (with response time as short as 100 ns) for surface temperature measurement, and CCD cameras for the detection of the hot particle trajectory distribution within first plasma jets and then rapidly for combustion flames. In the 1990s, sensors, able to work in the harsh environment of spray booths, have been developed (Fauchais and Vardelle, 2010). They use the light emitted by hot particles to determine particle temperatures, velocities, diameters, and trajectories. For cold particles, laser beams, illuminating particles, allow measuring their velocities and follow their trajectories. In fact, two types of measurements are performed: local measurements with a small sampling volume, which can be below 1 mm³, for example, measurements with the DPV2000® from Tecnar Co, CN, and ensemble measurements, which do not attempt to distinguish between individual particles within a large volume, for example, SprayView® from Tecnar and SprayWatch® from Oseir, FL. A recent paper of Mauer et al. (2007) compared results obtained with both types of measurements in the same spray conditions. The mean ensemble temperature measurement, achieved with a SprayWatch® focused at the same location as DPV2000, but measuring the whole jet cross section was in good agreement with the mean temperature resulting from the distribution. However, for more precise comparison, distributions obtained with DPV2000 all over the measurement volume of the SprayWatch and weighted by particle frequency should have been determined. Fauchais and Vardelle (2010) obtained similar results. Particle temperature and velocity distributions are by far more informative

than mean values, which obtained more rapidly are however interesting to follow any drift in process operating parameters.

The injection of particles in high-energy jets is a key issue for deposition efficiency and coating properties, especially when the powder is injected radially in plasma jets or HVOF flame sprays (Fauchais and Vardelle, 2010; Vardelle et al., 2001; Kamnis et al., 2008). For any slight change in the torch working conditions, the particle injection velocity, through the carrier gas flow rate, must be adjusted (Vardelle et al., 2001). When the powder is injected axially, the carrier gas flow rate also plays a role on the residence time of particles in the combustion chamber of the HVOF guns (Fauchais et al., 2014).

For all these measurement devices, a prior calibration and regular calibrations after a certain time of use, especially for temperature measurements, are mandatory (Mauer et al., 2011b). Moreover, measured particle temperatures can be biased due to the important difference between overheated small particles and larger poorly heated particles (Fauchais et al., 2014). The measurement of particle diameters is also tricky and the precision is poor (Fauchais et al., 2014), except when using sophisticated methods such as particle shape imaging (Landes, 2006) based on shadow technique.

Overall, these sensors have allowed a much better understanding of the effect of the spray gun working conditions on particle in-flight parameters, especially temperatures and velocities; they have also helped to validate predictions issued from numerical models. In addition, they have allowed drawing what Sampath et al. (Streibl et al., 2006; Vaidya et al., 2008; Sampath et al., 2009; Colmenares-Angulo et al., 2011) called “first-order process maps” that link spray parameters to particle temperatures and velocities. These first-order process maps have been used for process parameterization and feedback control for air plasma spraying and HVOF spraying (Colmenares-Angulo et al., 2011). They are representations of interrelationships between control parameters and measured responses. For example, first-order process maps have been established for three YSZ powder morphologies (Vaidya et al., 2008), linking the plasma torch parameters to the particle state (responses) through a design of experiments approach combined with particle in-flight parameter measurements. Refinements to the representation of the raw particle characteristics were proposed through the use of group parameters (melting index and kinetic energy) from the experimental results.

Correlating the first-order responses with coating properties allows the representation of coating properties in the form of second-order process maps and enables the identification of process windows. It provides a platform that can be used to construct comprehensive process–microstructure–property relationships with implications for coating design, process efficiency, and full-field assessment of manufacturing reliability (Vaidya et al., 2008).

2.3.3 Coating buildup

Measuring the temperature, velocity, or diameter of both particles in-flight and spray jet proved not to be sufficient to determine what will be the coating properties. Coating properties depend on the flattening and solidification of each particle onto the

substrate to form splats, on the splats layering to build up the coating, and on the real contact between splats and substrate or previously deposited layers (Fauchais et al., 2004, 2014; Chandra and Fauchais, 2009). Some studies pointed out the importance of the substrate preheating over a so-called transition temperature T_t . Over T_t , on the one hand, adsorbates and condensates at the substrate surface are desorbed, and, on the other hand, the oxide layer roughness at the surface of metallic substrates might be modified. Upon impact of molten particles, adsorbates and condensates evaporate and generate high gas pressure (over 1000 MPa) lifting the flattening liquid material and resulting in extensively fingered splats (Fauchais et al., 2014). The contact area between splat and substrate is then close to 10–15% of the splat surface, while for splats obtained after preheating the substrate over the transition temperature, disk-shaped splats are obtained with a contact area of 50–60%, resulting in much better thermomechanical coating properties (Fauchais et al., 2014). Preheating the substrate can also modify, at the nanometer scale, the skewness of the oxide layer at the surface of metal substrates and improve the substrate wettability (Fauchais et al., 2014).

The spray pattern is also crucial through the number of passes, scanning step, relative speed between the spray gun and substrate, spray distance, and spray angle (Trifa et al., 2007; Floristán et al., 2012). The spray pattern and the powder feed rate control the evolution of substrate and coating temperature during the spray process and thus the residual stress field in the coating. Therefore, the temperature of substrate and coating under construction are monitored continuously during spraying with infrared (IR) pyrometers or IR tomography in order to control the level of residual stresses in the coating (Fauchais and Vardelle, 2010) that can lead to cracking and mechanical failure in service.

Sensors have also been developed to determine in situ the mechanical properties of the coatings, such as the stress formation or the Young's modulus by recording continuously the curvature of a beam, made of the substrate metal, during the spray process (substrate preheating, coating deposition, and coated part cooling). Of course the beam substrate and forming coating temperatures evolution must also be recorded during the spray process (Fauchais and Vardelle, 2010; Fauchais et al., 2014). Another important parameter also linked to the spray pattern is the evolution of coating thickness during spraying (Fauchais et al., 2014). A novel approach has been recently developed (Nadeau et al., 2006) enabling online, real-time, and noncontact measurement of individual spray pass thickness during deposition. It is based on simple optical triangulation to detect the smooth step profile of a pass over the immediately adjacent uncoated (or previously coated) surface. Substrate temperature and residual stress measurements linked together with in-flight particle parameter measurements and coating properties have permitted to define "a good working area" through factorial design, using in-flight parameters together with coating formation parameters and coating properties. Even artificial neural networks (ANNs) and fuzzy logic (FL) have been implemented (Kanta et al., 2008) to predict spray process parameters to manufacture coatings with the desired structural characteristics. At last, works are devoted to the complex measurement of fully molten particle flattening and cooling, phenomena taking place in a few μs , to better understand coating formation (Dhiman et al., 2007; Goutier et al., 2011).

2.4 Models

In thermal or cold spray processes, the coating performance depends, to a great extent, on the velocity, impact angle, temperature, and size of the particles at impact on the substrate. Therefore, the manufacturing of coatings of good quality or any increase in deposition efficiency requires a broad understanding of the gas jet flow and its interactions with the sprayed particles, in which acceleration and heating depend on their injection force, momentum, and heat exchanges with the gas flow. Another important characteristic for metal particles and nonoxide ceramic ones is their in-flight oxidation, which is strongly linked to the surrounding atmosphere entrainment in the high-temperature jet flow.

In thermal spray engineering, models can help to understand specific phenomena that cannot be easily measured, such as the melting degree, evaporation, or oxidation of particles. They may also help to define a window of operating parameters and particle size distribution to achieve specific particle impact parameters and thus coating microstructure. In addition, models can help to establish relationships between process operating conditions and properties of the particles and spray jet and, thus, suggest the optimal actions to reset the measured properties at the desired level.

However, the development of accurate models requires

- proper data for the thermophysical properties of gases and materials;
- accurate description of the dynamics and thermal behavior of the gas flow, its mixing with the surrounding atmosphere, and its interaction with the part to be covered;
- suitable model for powder injection into the high-energy gas flow;
- appropriate representation of the transport phenomena and heterogeneous chemical reactions that control particle behavior in the flow and at impact.

Finally, before they are applied to the forecasting of the operation of the process under different operating conditions or a new material, models have to be carefully validated by comparing predictions with experimental data established under the same spraying conditions.

Numerous models exist for all spray processes including particle trajectories. For the gas flow, they range from 2-dimensional (2-D) axisymmetric and steady-state flow models to 3-D models either steady or transient. Turbulence must generally be involved in models; the most commonly utilized turbulence models use either a $k-\epsilon$ or a Reynolds stress approach or more recently large-eddy simulation.

Particles and droplets are generally treated as Lagrangian entities, and their trajectories, acceleration, and heating are calculated using the local high-energy gas properties. Steady-state 3-D models have demonstrated the effect of the carrier gas on the temperature and velocity distributions of the high-energy jet and particle trajectories. The predictions showed good agreement with time-averaged experimental measurements. However, for example, for plasma jets exhibiting strong power fluctuations that affect plasma properties, average projections can reproduce only a part of the process. Nevertheless, these models have been used to evaluate operational characteristics of new torch designs and the potential for expanding their range of operating conditions. They have also demonstrated the effect of the particle injection conditions and powder morphology on particle processing.

2.4.1 High-energy gases

The governing equations for the gas jet used in thermal spray processes are the conservation of mass, momentum, and energy with the ideal gas law.

For diffusion combustion, the most detailed flame model is that of Bandyopadhyay and Nylén (Goutier et al., 2011), who considered the eddy dissipation concept where the rates of species of creation/destruction are calculated using the dominant of the two expressions, in which the turbulent kinetic energy (k) and its dissipation rate (ε) participate. As many species must be considered (e.g., 15 for acetylene/oxygen flame) to calculate the Arrhenius reaction rates, a global or overall reaction for combustion is used. When comparing gas velocity and temperature fields predicted by the single-reaction simulations with those predicted by the multireaction model, the authors showed that the gas temperature and velocity fields produced by both models agreed quite closely (Bandyopadhyay and Nylén, 2003).

For HVOF or HVOF in simplified 1-D models, it is assumed that most of the reactions occur in the combustion chamber and the reactions move forward following an equilibrium chemistry model. This assumption is based on the fact that the residence time of the gas in the combustion chamber is much longer than in the subsequent parts (Thorpe and Richter, 1992). The direct solution of these conservation equations for high-Reynolds-number turbulent compressible flow is far beyond the current computation capacity (Li and Christofides, 2005; Srivatsan and Dolatabadi, 2006). However, by applying the Reynolds or Favre averaging, these equations can be simplified in such a way that the small-scale turbulent fluctuations do not have to be directly simulated, and consequently, the computational load can be significantly reduced. Due to the high Reynolds numbers and large pressure gradients in the nozzle, the renormalization group (RNG) k - ε turbulence model is used with the nonequilibrium wall function treatment to enhance the prediction of the wall shear and heat transfer (Li and Christofides, 2005; Srivatsan and Dolatabadi, 2006). In most cases, the 2-D model of gas dynamics is implemented into commercial CFD softwares (e.g., ANSYS Fluent) and is solved by finite-volume method (Li and Christofides, 2005; Srivatsan and Dolatabadi, 2006). For D-gun, either 1-D (Kadyrov and Kadyrov, 1995) or 2-D models (Gavrilenko and Yu, 2007) are used with or without corrections for supersonic velocities.

Numerous models exist for both plasma spray torch operation and plasma spray processes (Chyou and Pfender, 1989; Li and Pfender, 2005). The traditional models assumed axisymmetric and steady-state plasmas, allowing a 2-D treatment of the torch fluid dynamics. The conservation equations are solved numerically together with the relevant Maxwell equations and thermodynamic equations. Typical boundary conditions are an assumed current density profile at the cathode tip and an artificially high electrical conductivity at the anode boundary layer to allow current transfer through the low-temperature layer while keeping the assumption of LTE. Turbulence is generally included in the model but usually for low Reynolds numbers to account for the laminar plasma jet core. Such models have been used to evaluate operational characteristics of new torch designs (Muggli et al., 2007; Molz et al., 2007). More recently, fully 3-D, time-dependent models have been developed for plasma spray torches

(Moreau et al., 2006; Trelles et al., 2009) and the latest couple the electromagnetism equations in the electrodes and electric arc.

For cold spray, the first models considering a 1-D geometry of the Laval nozzle and an isentropic expansion of the flow from the nozzle throat to its exit have helped to define optimal conditions that yield maximum particle acceleration, which corresponds to conditions where a maximum drag force is exerted on the particle (Gärtner et al., 2006). One of the main advantages of 2-D or 3-D compressible models is that they allow the projection of shock waves and their interactions with small particles. 2-D models showed that the exit Mach number of a cold spray nozzle should be fixed according to the coating material and size of the particles to be sprayed, with a particular attention when the particles are light and/or small (Jodoin, 2002). When the supersonic jet impinges on an obstacle positioned perpendicularly to the flow, a deceleration and deviation of the gas flow occurs in front of the obstacle surface. The transition from a high-velocity supersonic flow to a low-velocity subsonic flow occurs in a shock wave that appears at some distance from the substrate surface and affects particle impact velocities, especially that of small particles (Alkhimov et al., 2001). 3-D models, such as that of Samareh and Dolatabadi (2007), showed that the presence of the substrate and its standoff distance and shape have significant effects on the gas flow field near the particle deposition area. This is due to the nature of the supersonic gas flow, which generates compression and expansion waves. The nozzle design also plays a key role in the particle impact velocity distribution (Alkhimov et al., 2001; Li et al., 2007).

2.4.2 Particles in-flight

Comprehensive studies dealing with the different phenomena encountered in the processing of particles in the high-energy gas flows have been published in the 1980s and 1990s by various authors. They mostly concerned plasma flows and considered a single particle (Pfender, 1985, 1989, 1999; Lee et al., 1985). The importance of the radial injection conditions in d.c. plasma jets has been emphasized by many authors (Vardelle et al., 2001; Dussoubs et al., 2001; Zhang et al., 2000). Corresponding studies and developments were published for flame spraying (Bandyopadhyay and Nylén, 2003) and, then, HVOF (Gu et al., 2004; Yang et al., 2002), D-gun (Kadyrov, 1996; Tillmann et al., 2007), and cold spray (Han et al., 2005; Katanoda et al., 2007; Nickel et al., 2007), where the effects of supersonic flows and shock waves must be considered. For suspension and solution precursor spraying, the interactions of the high-energy gas with liquid drops or droplets and formed particles with size ranging from a few hundreds of nanometers to a few tenths of micrometers are now extensively studied. The Knudsen effect is important in plasma jets for the fine particles with which most of the suspensions and solutions are sprayed (Fauchais, 2004; Basu et al., 2006; Shan et al., 2007; Marchand et al., 2008; Meillot et al., 2009; Vincent et al., 2009; Fauchais et al., 2008b) and must be considered in the models.

When a solid particle is injected in a high-energy flow, it is submitted to a drag force and heat transfer. The conventional values of drag and heat transfer coefficients must be corrected to account for various phenomena such as temperature gradients in

the particle boundary layer (Pfender, 1999; Lee et al., 1985); noncontinuum effect (Knudsen effect) (Fauchais et al., 2008b; Lewis and Gauvin, 1973; Chen and Pfender, 1983a,b; Vardelle et al., 1997; Ganser, 1993; Chen and Ping, 1986a); vaporization effect (Vardelle et al., 1996); turbulence effect (Lee et al., 1985); particle shape effect, especially important for cold spray (Fukanuma et al., 2006) where particles do not melt; particle charging, which is no more negligible in VPS (Chen and Ping, 1986b); and thermophoresis effect, particularly for particles below 1 μm (Fauchais et al., 2008b). Also, heat propagation phenomenon within the particles has been considered for particles with low thermal conductivity, especially for particles processed in high thermal conductivity gas flows (e.g., plasma jets) (Fauchais et al., 2008a; Vardelle et al., 1997; Ganser, 1993; Bourdin et al., 1983; Ben-Ettouil et al., 2007, 2008) or in combustion flames (Ivosevic et al., 2006), and vaporization phenomenon (Vardelle et al., 1996; Chen and Pfender, 1982; Yoshida and Akashi, 1977) and the corresponding radiation of vapor (Essoltani et al., 1990, 1994). Chemical reactions between particles and ambient gas have also been considered with reactions due to diffusion (Vardelle et al., 1996) or convection (Neiser et al., 1998) and also reactions related to self-propagating high-temperature synthesis (Borisova and Borisov, 2008). The effects of arc root fluctuations on particle trajectories and treatment in plasma spraying have also been modeled (Meillot and Balmigere, 2008). The injection of a powder with particle size range, and not only a single particle, has also been considered (Samareh and Dolatabadi, 2007; Meillot and Balmigere, 2008), as well as the loading effect due to an increase in the powder feeding rate in RF plasmas (Proulx et al., 1985), in HVOF flame spray (Taylor et al., 2006) (even if with less than 4% of the gas mass flow rate, it can be assumed that the presence of particles will have a negligible effect), and in cold spray (Taylor et al., 2006). Effectively when raising the powder feed rate, the deposition rate and coating thickness increase linearly until a maximum powder mass flow rate is reached. Calculations also show that the impact of too many particles onto the surface of the substrate results in excessive residual stresses causing the coating to peel.

2.4.3 Coating buildup

Effective physical and thermomechanical properties of coatings are strongly dependent on the coating microstructure; they depend on the real contacts between the first splats and substrate, between layered splats, and on pores and cracks, especially for ceramic coatings. Moreover, thermally sprayed coatings present nonperiodic microstructures that make model formulations difficult. A global model taking into account all the phenomena involved in coating buildup does not exist yet. For example, porosity is a key feature of a thermally sprayed coating microstructure. Within ceramic coatings, the porosity network is 3-D and involves pores and intralamellar and interlamellar cracks of various shapes, dimensions, and orientations. The coatings are built up by the layering of millions of particles and their models must be based on a stochastic approach of the formation and piling up of predicted lamellae in the sprayed microstructure. Up to now, only a limited number of splats can be considered to

achieve calculations in a reasonable time. Moreover, the experimental observation of the distribution of pores and cracks is generally limited to 2-D images, while 3-D observation should be necessary (Beauvais et al., 2008) to back up the models. Of course, 3-D structures can be achieved from a series of scanning electron microscopy (SEM) images obtained through the incremental polishing of cross sections. Bobzin et al. (2012) showed that when using 3-D models, the results of the virtual testing and asymptotic homogenization methods match each other more closely compared with the conventional 2-D models. Homogenization methods are based on the assumption that a specific small part of the microstructure can be considered as representative of the entire material. According to the complexity of the structures of sprayed coatings, models are often 2-D and splats are assumed to be disk-shaped, based on the work of Madejski (1976) with or without taking into account curling at the end of the flattening phase. 3-D models are now under development, but the number of splats considered is still limited.

Only a few simplified models trying to relate the coating microstructure to its effective properties have been developed. One of the first was that of Harding et al. (1995), which accounted for particle flattening and solidification and established a set of physically based rules for combining these events to obtain the coating. This model represented reasonably the microstructure of yttria-stabilized zirconia coatings. Ghafouri-Azar et al. (2003) proposed a stochastic 3-D model of a thermal spray coating, predicting coating porosity, thickness, roughness, and the variation of these properties with spray parameters. The model assigned impact properties to molten droplets landing on the substrate by generating random values of particle parameters, assuming that these properties follow normal distributions with user-specified means and standard deviations. Rules were prescribed to calculate splat sizes after droplet impact and their interaction with each other. Porosity was assumed to be solely due to the curl up of the splats as a result of thermal stresses. Bobzin et al. (2009) proposed two different numerical approaches to calculate coating porosity. Sevostianov and Kachanov (2009) focused their study on micromechanics-based models that explicitly expressed the elastic and conductive properties of plasma-sprayed ceramic coatings in terms of relevant microstructural parameters.

Still, the key issue to control the structure of coatings is the understanding of splat formation, which is complex as it depends on both the particle impact parameters (temperature, heat content, velocity, diameter, oxidation stage, and impact angle) and substrate surface parameters (temperature, roughness, material or oxide layer structure and thickness, and the presence or absence of adsorbates and condensates; Fauchais et al., 2004; Chandra and Fauchais, 2009; Dhiman et al., 2007; Armster et al., 2002). All these parameters control the flattening velocity of the liquid particle and its thermal contact with the substrate or previously deposited layer, parameters for which information is still very poor according to the difficulty of measurements (Dhiman et al., 2007).

For cold-sprayed coatings, many studies, including modeling, were devoted to particles in-flight and single ductile particle impacting different substrates, but coating buildup modeling has not yet been studied.

2.5 Coating applications and developments

At its early stages of development, thermal spray technology was mostly used for the repair, rebuilding, retrofitting, and surface protection against corrosion, erosion, and wear (Tucker, 2013; Fauchais et al., 2014). In the 1970s–1980s, thanks to the development of in situ measurements and models in laboratories, a better understanding of the phenomena involved was achieved. In parallel, the wider acceptance of the technology for industrial-scale production has started with applications limited to high added-value components in the aeronautic and nuclear industries. These were mostly driven by the fact that no viable alternative solutions were available, and design engineers and scientists were used to work with rather complex processes. At the end of the 1980s and beginning of 1990s, a wide range of industrial-scale surface modification processes became available. At that period, thermal-sprayed coatings were mainly developed in aircraft, automotive, corrosion protection, original equipment manufacturing, printing and paper, glass, pipes and bottles, and medical and dental industries. They are currently accepted for a large range of applications: tribological and wear-resistant applications including lubrication and low-friction surfaces, corrosion and/or oxidation protection, high-temperature applications, freestanding components, electrical and optical components, electromagnetic shielding, electrical insulation, seals, biomedical applications, superconducting oxides, components with tailored coefficient of thermal expansion to service conditions, magnetic coatings, solid oxide fuel cells, replacement of hard chromium, and ornamental applications. In the 1990s, the techniques developed and/or used in laboratories have been the basis for the development of sensors, less sophisticated but simpler and robust, able to work in the harsh environment of spray booths (Tucker, 2013; Fauchais et al., 2014). In parallel, commercially available computerized systems following continuously in real time the macroscopic parameters of the process in spray booths were developed. With the standardization of techniques for coating characterization and control of coating quality, the development of computerized systems in the process, control panel and sensors, and the coating reproducibility and reliability were drastically improved.

The choice of a specific coating and/or thermal spray process, for a given service condition, depends, however, on the expectation of the user and cost that could be tolerated for the application. This affects, in turn, the selection of the coating material and the spray process. The coating design process is often complicated, by the fact that in practice, components are not always devoted to a single requirement such as resistance to wear or corrosion or electrical insulation or thermal insulation. In most cases, coatings must resist to different combined needs: for example, wear is often found in corrosion environments. The different available spray processes are generally complementary and not competitive, and their overlap in terms of application is not very broad. To select a process, it is important to know the advantages and limitations of each of the thermal spray processes and make the proper decision of the best process for each application.

According to Dorfman and Sharma (2013b), it is estimated that the TS industry is worth approximately \$6.5 billion with the majority of revenue generation in coating services (see Figure 2.10a). In terms of market segmentation, approximately 60% of the total TS market belongs to the turbine industry, 15% belongs to automotive

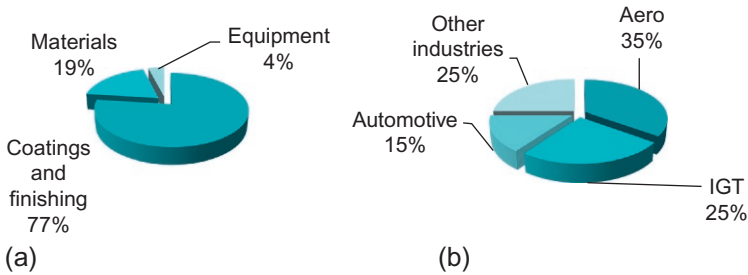


Figure 2.10 (a) Distribution of revenue generation in coating services. (b) Market segmentation in thermal spray industry (Dorfman and Sharma, 2013b).

industry, and the remaining 25% is distributed over a large number of other industries, as shown in Figure 2.10b.

However, a great growth potential exists in the industries where thermal spray is well implanted and also in those where currently the penetration of TS is low. Potential markets comprise the following (TSS, 2014):

- Electronic materials and electronic applications such as sensors, wiring, antennas and RF, energy storage, and energy harvesting. The wide range of materials that can be deposited on different shapes, the absence of the need for postprocessing, the high deposition rates, and the processing at ambient conditions are the advantages of thermal or cold spray.
- The automotive industry to cope with environmental concerns and legislation, the reduction of friction and oil consumption, the improved performances, TBCs, coatings with functional properties, etc.
- Land-based and aeroderivative gas turbines with novel TBC coating architecture and compositions to withstand higher temperatures, longer life and various fuels, a better resistance to calcium–magnesium–aluminosilicate (CMAS), vanadium, water vapor and erosion, higher deposition efficiencies, improved robotic manipulation, overspray recycling, etc.
- Wear- and corrosion-resistant coatings, especially under extreme conditions (temperature, pressure, and environmental), which improvement strongly depends on a better understanding and control of splat formation.
- Development of what is actually done in oil and gas, pulp and paper, metal processing, biomedical, etc.

2.6 Future trends and applications

For about a decade, the interest on manufacturing “thick” finely structured or nanostructured coatings on large surfaces has been increasingly growing. If the vapor deposition routes for producing coatings (CVD, plasma-enhanced CVD (PE-CVD), PVD, EB-PVD, etc.) allow manufacturing nanostructured architectures, film thickness can hardly be higher than a few micrometers, except with the EB-PVD process. Each route, thermal spray and vapor deposition, has different advantages that, if combined, could lead to a new family of coatings. In that sense, Sulzer Metco has developed a new process that combines plasma spray (PS) with physical vapor deposition (PS-PVD) (von Niessen and Gindrat, 2011). This new process involves a high-power

plasma spray torch (180 kW–3000 A, gas flow up to 200 slpm) working at a pressure as low as 1 kPa (10 mbar). Under such low-pressure conditions, the plasma jet reaches more than 2 m in length and up to 0.4 m in diameter. The coatings produced by this process may exhibit microstructures similar to that of EB-PVD coatings (i.e., columnar structures and nearly no porosity) when using a low powder feed rate, adapted spray conditions, and large spray distance (von Niessen and Gindrat, 2011). Therefore, the properties of coatings obtained with PS-PVD are better than those of the PVD and plasma spray processes, and coatings on larger and complex-shaped parts can be obtained.

With conventional plasma spraying, coatings with thickness from 50 μm to a few millimeters are easily achieved but with no real nanostructured architectures after particle melting in the plasma jet. This explains the interest for the different techniques and/or feedstock materials developed this last decade to produce totally or partially nanostructured coatings:

- Spraying iron-based bulk metallic glass compositions (consisting of seven or more alloying elements) with a low critical cooling rate (10^4 K/s) for metallic glass formation (Branagan et al., 2009). After heat treatment at above the crystallization temperature (568 $^\circ\text{C}$, which is less than half the melting temperature), the coatings are devitrified into a multiphase nanocomposite microstructure. Coatings can be produced with plasma, HVOF, and wire arc (with cored wires). Due to the high hardness as compared to conventional metal alloys, the amorphous and nanocomposite coatings can show very good wear and corrosion resistance characteristics. Some coating compositions also present corrosion and wear resistance superior to that of stainless steel used under the same corrosion conditions (Fauchais et al., 2014; Branagan et al., 2009).
- Spraying, by plasma or HVOF, agglomerated nanostructured ceramic particles (Lima and Marple, 2007) with a careful control of the temperature and size distribution of the particles in the thermal spray gas jet to keep part of the particles in a semimolten state. This results in bimodal structures, in which mechanical performance depends on the density of the nano-sized zones. Coatings obtained by this spray route are tougher than the conventional ones (Lima and Marple, 2007; Fauchais et al., 2011).
- Spraying, by cold spray, either nanostructured material with nanosized grains or composite agglomerates made either of micron- and nanoparticles or of only nanoparticles. However, the sprayed particles must be sufficiently ductile (Ajdelsztajn et al., 2006a,b; Wang et al., 2007; Zhang et al., 2008).
- Suspension plasma spraying (SPS) and solution precursor plasma spraying (SPPS) allow achieving finely structured layers with thickness varying from a few micrometers to a few hundreds of micrometers (Fauchais et al., 2011). These techniques, essentially developed for ceramics, seem promising to manufacture dense or porosity-controlled coatings and functionally graded layers. The coatings present very interesting features, especially a much better toughness than conventional coatings due to the finer microstructure. Nevertheless, coatings made from suspensions or solutions injected into hot gases are by far more complex because of the chemistry (choice of solvent, dispersant, precursors, etc.), the liquid fragmentation, and vaporization control of the processes (Fauchais et al., 2011). Actually, diagnostic techniques are not available to measure in-flight droplets below 4–5 μm , which would permit getting a much better understanding of the phenomena involved. New plasma torches should be designed to spray suspensions or solutions. Thus, it could be said that SPS and SPPS are in the same state as conventional spraying was in the 1980s and the beginning

of the 1990s. SPS and SPSS, for the last decade, have been the subject of numerous papers in international reviews and conference proceedings. Indeed, [Killinger et al. \(2011\)](#) pointed out that “to promote industrial implementation, an urgent concern of future research work is to qualify liquid feedstock thermal spray coatings in a more application-oriented way and to communicate the results convincingly. As suspension and solution spray are to be clearly differentiated from classical thermal spray processes, also new industrial standards have to be defined concerning suspension and solution preparation, storage, feeding as well as qualification and handling of raw materials (i.e., ultra-fine powders, solvents, additives, etc.).”

2.7 Conclusions

Since the first industrial developments of plasma and flame spraying in the 1960s, essentially in the aerospace and nuclear industries, thermal spraying has been much developed with new processes such as D-gun and wire arc in the 1970s, HVOF and HVAF in the 1980s, and cold spray at the end of the 1990s. In addition to the development of new thermal spray techniques, the knowledge gained through the coating buildup and properties has allowed for the design of better materials. Indeed, the intensive research on nanostructured coatings and materials performed in the first decade of the millennium began to be used in industry. Although the promising suspensions and solution spraying techniques are still in the state of development, it is only a matter of time and research effort to have a new thermal spray era with new devices and materials devoted to suspension and solution spraying for the industrial applications of the future.

Better understanding of the processes thanks to the development of in situ measurements and numerical models, which allowed shifting from the trial-and-error approach to a more scientific one, has allowed for the standardization of techniques for coating characterization and control of coating quality more targeted toward the service conditions. This was achieved at the end of the 1990s, when the development of simple and robust sensors able to work in the harsh environment of spray booths and also computerized process control systems took place. They have drastically improved process reliability and control. More recently, ANNs and FL have been implemented to control and regulate the processing parameters.

However, as pointed out by [Dorfman and Sharma \(2013b\)](#), “in addition to technological developments, there are other critical factors that need to be addressed to achieve successful market growth. These are (1) young professional recruitment, retention and training, (2) technology outreach, (3) role of professional and trade associations, (4) reduced time to technology transfer, (5) lower the cost of ownership relative to competing technologies, and (6) environment, health and safety.”

References

- Ajdelsztajn, L., Zúñiga, A., Jodoin, B., Lavernia, E.J., 2006a. Cold-spray processing of a nanocrystalline Al–Cu–Mg–Fe–Ni alloy with Sc. *J. Therm. Spray Technol.* 15 (2), 184–190.
- Ajdelsztajn, L., Jodoin, B., Schoenung, J.M., 2006b. Synthesis and mechanical properties of nanocrystalline Ni coatings produced by cold gas dynamic spraying. *Surf. Coat. Technol.* 201, 1166–1172.

- Alkhimov, A.P., Kosarev, V.F., Klinkov, S.V., 2001. The features of cold spray nozzle design. *J. Therm. Spray Technol.* 10 (2), 375–381.
- Ambühl, P., Meyer, P., 1999. Thermal coating technology in controlled atmospheres (Cham-ProTM). In: Lugscheider, E., Kammer, P.A. (Eds.). *Proceedings of the ITSC. DVS, Düsseldorf, Germany*, pp. 291–292.
- Armster, S.Q., Delplanque, J.-P., Rein, M., Lavernia, E.J., 2002. Thermo-fluid mechanisms controlling droplet based materials processes. *Int. Mater. Rev.* 7 (6), 265–301.
- Astakhov, E.A., 2008. Controlling the properties of detonation-sprayed coatings: major aspects. *Powder Metall. Met. Ceram.* 47 (1–2), 70–79.
- Bandyopadhyay, R., Nylén, P., 2003. A computational fluid dynamic analysis of gas and particle flow in flame spraying. *J. Therm. Spray Technol.* 12 (4), 492–503.
- Barbezat, G., 2001. The internal plasma spraying on powerful technology for the aerospace an automotive industries. In: Berndt, C.C., Khor, K.A., Lugscheider, E.F. (Eds.), *In: Proc. International Thermal Spray Conference, Singapore, ASM International, Materials Park, OH*, pp. 135–140.
- Barbezat, G., Landes, K., 2000. Plasma technology TRIPLEX for the deposition of ceramic coatings in the industry. In: Berndt, C.C. (Ed.), *In: Proc. 1st Intern. Thermal Spray Conference, Montreal, Canada, ASM International, Materials Park, OH*, pp. 881–885.
- Basu, S., Jordan, E.H., Cetegen, B.M., 2006. Fluid mechanics and heat transfer of liquid precursor droplets injected into high temperature plasmas. *J. Therm. Spray Technol.* 15 (4), 576–581.
- Beauvais, S., Guipont, V., Jeandin, M., Jeulin, D., Robisson, A., Saenger, R., 2008. Study of the porosity in plasma-sprayed alumina through an innovative three-dimensional simulation of the coating buildup. *Metall. Mater. Trans. A* 39A, 2711–2724.
- Belzunce, F.J., Higuera, V., Poveda, S., Carriles, A., 2002. High temperature oxidation of HFPD thermal-sprayed MCrAlY coatings in simulated gas turbine environments. *J. Therm. Spray Technol.* 11 (4), 461–472.
- Ben-Ettouil, F., Mazhorova, O., Pateyron, B., Ageorges, H., El Ganaoui, M., Fauchais, P., 2007. Fast modelling with “back pressure” model of phase changes along the trajectory of a single particle within a DC plasma jet. *J. Therm. Spray Technol.* 16 (5–6), 744–750.
- Ben-Ettouil, F., Mazhorova, O., Pateyron, B., Ageorges, H., El-Ganaoui, M., Fauchais, P., 2008. Predicting dynamic and thermal histories of agglomerated particles injected within a d.c. plasma jet. *Surf. Coat. Technol.* 202, 4491–4495.
- Betoule, O., 1994. Influence of velocity and temperature distributions of d.c. plasma jets and alumina particles in flight onto coating properties. PhD thesis, University of Limoges, Limoges, France.
- Blais, A., Jodoin, B., Dorier, J.-L., Gindrat, M., Hollenstein, C., 2005. Inclusion of aerodynamic non-equilibrium effects in supersonic plasma jet enthalpy probe measurements. *J. Therm. Spray Technol.* 14 (3), 342–353.
- Bobzin, K., Bagcivan, N., Parkot, D., Kashko, T., Laschet, G., Scheele, J., 2009. Influence of the definition of the representative volume element on effective thermoelastic properties of thermal barrier coatings with random microstructure. *J. Therm. Spray Technol.* 18 (5–6), 988–995.
- Bobzin, K., Kopp, N., Warda, T., Öte, M., 2012. Determination of the effective properties of thermal spray coatings using 2D and 3D models. *J. Therm. Spray Technol.* 21 (6), 1269–1280.
- Bolot, R., Planche, M.-P., Liao, H., Coddet, C., 2008. A three-dimensional model of the wire-arc spray process and its experimental validation. *J. Mater. Process. Technol.* 200, 94–105.
- Borisova, A.L., Borisov, Y.S., 2008. Self-propagating high-temperature synthesis for the deposition of thermal-sprayed coatings. *Powder Metall. Met. Ceram.* 47 (1–2), 80–94.

- Boulos, M.I., 1992. RF induction plasma spraying: state-of-the-art review. *J. Therm. Spray Technol.* 1, 33–40.
- Bourdin, E., Fauchais, P., Boulos, M.I., 1983. Transient heat conduction under plasma conditions. *Int. J. Heat Mass Transf.* 26, 567–582.
- Branagan, D.J., Swank, W.D., Meacham, B.E., 2009. Maximizing the glass fraction in iron-based high velocity oxy-fuel coatings. *Metall. Mater. Trans. A* 40A, 1306–1313.
- Browning, J.A., 1983. Highly concentrated supersonic liquefied material flame spray method and apparatus. US Patent # 4,416,421, November.
- Browning, J.A., 1992. Hypervelocity impact fusion—a technical note. *J. Therm. Spray Technol.* 1 (4), 289–292.
- Cartier, M., 2003. *Handbook of Surface Treatments and Coatings*. ASME Press, NY, USA.
- Champagne, V.K. (Ed.), 2007. *The Cold Spray Materials Deposition Process*. Woodhead Publishing Ltd, Cambridge, England.
- Chandra, S., Fauchais, P., 2009. Formation of solid splats during thermal spray deposition. *J. Therm. Spray Technol.* 18 (2), 148–180.
- Chen, X., Pfender, E., 1982. Heat transfer to a single particle exposed to a thermal plasma. *Plasma Chem. Plasma Process.* 2 (2), 185–212.
- Chen, X., Pfender, E., 1983a. Effect of the Knudsen number on heat transfer to a particle immersed into a thermal plasma. *Plasma Chem. Plasma Process.* 3, 97–113.
- Chen, X., Pfender, E., 1983b. Behavior of small particles in a thermal plasma flow. *Plasma Chem. Plasma Process.* 3, 351–366.
- Chen, X., Ping, H., 1986a. Heat transfer from a rarefied plasma flow to a metallic or non-metallic particle. *Plasma Chem. Plasma Process.* 6 (4), 313–333.
- Chen, X., Ping, H., 1986b. Heat transfer from a rarefied plasma flow to a metallic or nonmetallic particle. *Plasma Chem. Plasma Process.* 6 (4), 313–333.
- Chraska, P., Hrabovsky, M., 1992. An overview of water stabilized plasma guns and their applications. In: Berndt, C.C. (Ed.), In: *Proc. Thermal Spray: International Advances in Coatings Technology*, Orlando, Florida, ASM International, Materials Park, OH, pp. 81–85.
- Chyou, Y.P., Pfender, E., 1989. Modeling of plasma jets with superimposed vortex flow. *Plasma Chem. Plasma Process.* 9 (2), 291–328.
- Colmenares-Angulo, J., Shinoda, K., Wentz, T., Zhang, W., Tan, Y., Sampath, S., 2011. On the response of different particle state sensors to deliberate process variations. *J. Therm. Spray Technol.* 20 (5), 1035–1048.
- Coudert, J.F., Planche, M.P., Fauchais, P., 1995. Velocity measurement of D.C. plasma based on arc root fluctuations. *Plasma Chem. Plasma Process.* 15 (1), 47–70.
- Coudert, J.-F., Rat, V., Rigot, D., 2007. Influence of Helmholtz oscillations on arc voltage fluctuations in a dc plasma spraying torch. *J. Phys. D.: Appl. Phys.* 40, 7357–7366.
- Davis, J.R. (Ed.), 2004. *Handbook of Thermal Spray Technology*. ASM International, Materials Park, OH, USA.
- Dhiman, R., McDonald, A., Chandra, S., 2007. Predicting splat morphology in a thermal spray process. *Surf. Coat. Technol.* 201, 7789–7801.
- Dobkin, D.M., Zuraw, M.K., 2003. *Principles of Chemical Vapor Deposition*. Springer, NY, USA.
- Dorfman, M.R., Sharma, A., 2013a. Challenges and strategies for growth of thermal spray markets: the six-pillar plan. *J. Therm. Spray Technol.* 22 (5), 559–563.
- Dorfman, M., Sharma, A., 2013b. Commentary, challenges and strategies for growth of thermal spray markets: the six-pillar plan. *J. Therm. Spray Technol.*, Commentary 22 (5), 559–563.
- Dresvin, S.V. (Ed.), 1977. *Physics and Technology of Low Temperature Plasmas*. Iowa State University Press, Ames.

- Duan, Z., Heberlein, J., 2000. Anode boundary layer effects in plasma spray torches. In: Berndt, C.C. (Ed.), Proc. 1st International Thermal Spray Conference, Montreal, Quebec. ASM International, Materials Park, OH, USA, pp. 1–7.
- Duan, Z., Heberlein, J., 2002. Arc instabilities in a plasma spray torch. *J. Therm. Spray Technol.* 11 (1), 44–51.
- Dussoubs, B., Vardelle, A., Mariaux, G., Themelis, N.J., Fauchais, P., 2001. Modeling of plasma spraying of two powders. *J. Therm. Spray Technol.* 10 (1), 105–110.
- Dykhuizen, R.C., Smith, M.F., 1998. Gas dynamic principles of cold spray. *J. Therm. Spray Technol.* 7 (2), 205–212.
- Eckbreth, A.C., Anderson, T.J., 1986. Simultaneous rotational coherent anti-Stokes Raman spectroscopy with arbitrary pump-Stokes spectral separation. *Opt. Lett.* 11, 496–498.
- Erkens, G., Vetter, J., Müller, J., auf dem Brinke, T., Fromme, M., Mohnfeld, A., 2011. Plasma-Assisted Surface Coating Processes, Methods, Systems and Applications. Sulzer Metco, Süddeutscher Verlag onpact GmbH, Munich.
- Essoltani, A., Proulx, P., Boulos, M.I., Gleizes, A., 1990. Radiation and self-absorption in argon–iron plasmas at atmospheric pressure. *J. Anal. At. Spectrom.* 5, 543–547.
- Essoltani, A., Proulx, P., Boulos, M.I., Gleizes, A., 1994. Volumetric emission of argon plasmas in the presence of vapors of Fe, Si, and Al. *Plasma Chem. Plasma Process.* 14 (4), 437–450.
- Fauchais, P., 2004. Understanding plasma spraying, an invited review. *J. Phys. D. Appl. Phys.* 37, 2232–2246.
- Fauchais, P., Vardelle, M., 2010. Sensors in spray processes. *J. Therm. Spray Technol.* 19 (4), 668–694.
- Fauchais, P., Coudert, J.F., Vardelle, M., 1989. Diagnostics in thermal plasma processing. In: Auciello, O., Flamm, D.L. (Eds.), In: *Plasma Diagnostics*, vol. 1. Academic Press, NY, USA, pp. 349–446.
- Fauchais, P., et al., 1992. Diagnostics of thermal spraying plasma jets. *J. Therm. Spray Technol.* 1 (2), 117–128.
- Fauchais, P., Fukumoto, M., Vardelle, A., Vardelle, M., 2004. Knowledge concerning splat formation: an invited review. *J. Therm. Spray Technol.* 13 (3), 337–360.
- Fauchais, P., Rat, V., Coudert, J.-F., Etchart-Salas, R., Montavon, G., 2008a. Operating parameters for suspension and solution plasma-spray coatings. *Surf. Coat. Technol.* 202, 4309–4317.
- Fauchais, P., Etchart-Salas, R., Rat, V., Coudert, J.F., Caron, N., Wittmann, K., 2008b. Parameters controlling liquid plasma spraying: solutions, sols or suspensions. *J. Therm. Spray Technol.* 17 (1), 31–59.
- Fauchais, P., Montavon, G., Lima, R.S., Marple, B.R., 2011. Engineering a new class of thermal spray nano-based microstructures from agglomerated nanostructured particles, suspensions and solutions: an invited review. *J. Phys. D* 44, 093001.
- Fauchais, P., Heberlein, J., Boulos, M., 2014. *Thermal Spray Fundamentals*. Springer, NY, USA, 1600 pages.
- Floristán, M., Montesinos, J.A., García-Marín, J.A., Killinger, A., Gadow, R., 2012. Robot trajectory planning for high quality thermal spray coating processes on complex shaped components. In: ITSC 2012. ASM International, Materials Park, OH, USA.
- Freslon, A., 1995. Plasma spraying at controlled temperature and atmosphere. In: Berndt, C.C., Sampath, S. (Eds.), In: *Thermal Spray: Science and Technology*. ASM International, OH, USA, pp. 57–63.
- Frey, H., Khan, H.R., 2013. *Handbook of Thin Film Technology*. Springer, NY, USA, 550 pages.

- Friis, M., Persson, C., 2003. Control of thermal spray processes by means of process maps and process windows. *J. Therm. Spray Technol.* 12 (1), 44–52.
- Fukanuma, H., Ohno, N., Sun, B., Huang, R., 2006. In-flight particle velocity measurements with DPV-2000 in cold spray. *Surf. Coat. Technol.* 201, 1935–1941.
- Ganser, G.H., 1993. A rational approach to drag prediction of spherical and non-spherical particles. *Powder Technol.* 77, 143–152.
- Gärtner, F., Stoltenhoff, T., Schmidt, T., Kreye, H., 2006. The cold spray process and its potential for industrial applications. *J. Therm. Spray Technol.* 15 (2), 223–232.
- Gavrilenko, T.P., Yu, A., 2007. Nikolaev, calculation of detonation gas spraying. *Combust. Explos. Shock Waves* 43 (6), 724–731.
- Ghafouri-Azar, R., Mostaghimi, J., Chandra, S., Charmchi, M., 2003. A stochastic model to simulate the formation of a thermal spray coating. *J. Therm. Spray Technol.* 12 (1), 53–69.
- Gladish, G.G., Smurov, I., 2011. *Physics of Laser Materials Processing: Theory and Experiment*. Springer Series in Materials Science, Book 146, Springer, NY, USA.
- Glocker, D.A., Shah, S.I. (Eds.), 2002. In: *Handbook of Thin Film Process Technology*, 2 vol. set. Institute of Physics, Bristol, UK.
- Goutier, S., Vardelle, M., Labbe, J.C., Fauchais, P., 2011. Flattening and cooling of millimeter- and micrometer-sized alumina drops. *J. Therm. Spray Technol.* 20 (1–2), 59–67.
- Grey, J., Jacobs, P.F., Sherman, M.P., 1962. Calorimetric probe for the measurement of extremely high temperatures. *Rev. Sci. Instrum.* 33 (7), 738–741.
- Gu, S., McCartney, D.G., Eastwick, C.N., Simmons, K., 2004. Numerical modeling of in-flight characteristics of Inconel 625 particles during high-velocity oxy-fuel thermal spraying. *J. Therm. Spray Technol.* 13 (2), 200–211.
- Hall, R.J., Eckbreth, A.C., 1984. CARS: application to combustion diagnostics. In: Ready, J.F., Eaf, R.K. (Eds.), *In: Laser Applications*, vol. 5. Academic Press, New York.
- Han, T., Zhao, Z., Gillispie, B.A., Smith, J.R., 2005. Effects of spray conditions on coating formation by the kinetic spray process. *J. Therm. Spray Technol.* 14 (3), 373–383.
- Harding, J.H., Mulheran, P.A., Cirolini, S., Marchese, M., Jacucci, G., 1995. Modeling the deposition of thermal barrier coatings. *J. Therm. Spray Technol.* 4 (1), 34–40.
- Hermanek, F.J., 2001. *Thermal Spray Terminology and Company Origins*. ASM International, Materials Park, OH, USA.
- Ivosevic, M., Cairncross, R.A., Knight, R., 2006. 3D predictions of thermally sprayed polymer splats: modeling particle acceleration, heating and deformation on impact with a flat substrate. *Int. J. Heat Mass Transf.* 49, 3285–3297.
- Jodoin, B., 2002. Cold spray nozzle mach number limitation. *J. Therm. Spray Technol.* 11 (4), 496–507.
- Kadyrov, E., 1996. Gas–particle interaction in detonation spraying process. *J. Therm. Spray Technol.* 5 (2), 185–195.
- Kadyrov, E., Kadyrov, V., 1995. Gas dynamical parameters of detonation powder spraying. *J. Therm. Spray Technol.* 4 (3), 280–286.
- Kamnis, S., Gu, S., Zeoli, N., 2008. Mathematical modelling of Inconel 718 particles in HVOF thermal spraying. *Surf. Coat. Technol.* 202, 2715–2724.
- Kanta, A.-F., Montavon, G., Vardelle, M., Planche, M.-P., Berndt, C.C., Coddet, C., 2008. Artificial neural networks vs. fuzzy logic: simple tools to predict and control complex processes—application to plasma spray processes. *J. Therm. Spray Technol.* 17 (3), 365–376.
- Katanoda, H., Matsuoka, T., Matsuo, K., 2007. Experimental study on shock wave structures in constant-area passage of cold spray nozzle. *J. Therm. Sci.* 16 (1), 40–45.

- Killinger, A., Gadow, R., Mauer, G., Guignard, A., Vaßen, R., Stöver, D., 2011. Review of new developments in suspension and solution precursor thermal spray processes. *J. Therm. Spray Technol.* 20 (4), 677–695.
- Landes, K., 2006. Diagnostics in plasma spraying techniques. *Surf. Coat. Technol.* 201, 1948–1954.
- Lee, Y.C., Chyou, Y.P., Pfender, E., 1985. Particle dynamics and particle heat and mass transfer in thermal plasmas. Part II. Particle heat and mass transfer in thermal plasmas. *Plasma Chem. Plasma Process.* 5 (4), 391–414.
- Legoux, J.-G., Arsenault, B., Leblanc, L., Bouyer, V., Moreau, C., 2002. Evaluation of four high velocity thermal spray guns using Wc-10% Co-4% Cr cermets. *J. Therm. Spray Technol.* 11 (1), 86–94.
- Lewis, J.W., Gauvin, W.H., 1973. Motion of particles entrained in a plasma jet. *AIChE J.* 19 (6), 982–990.
- Li, M., Christofides, P.D., 2005. Multi-scale modeling and analysis of an industrial HVOF thermal spray process. *Chem. Eng. Sci.* 60, 3649–3669.
- Li, H.P., Pfender, E., 2005. Three-dimensional effects inside a dc arc plasma torch. *IEEE Trans. Plasma Sci.* 33 (2), 400–401.
- Li, C.-J., Wu, T., Li, C.-X., Sun, B., 2003. Effect of spray particle trajectory on the measurement signal of particle parameters based on thermal radiation. *J. Therm. Spray Technol.* 12 (1), 80–94.
- Li, W.-Y., Liao, H., Douchy, G., Coddet, C., 2007. Optimal design of a cold spray nozzle by numerical analysis of particle velocity and experimental validation with 316L stainless steel powder. *Mater. Des.* 28, 2129–2137.
- Lima, R.S., Marple, B.R., 2007. Thermal spray coatings engineered from nanostructured ceramic agglomerated powders for structural, thermal barrier and biomedical applications: a review. *J. Therm. Spray Technol.* 16 (1), 40–63.
- Madejski, J., 1976. Solidification of droplets on a cold surface. *Int. J. Heat Mass Transf.* 19, 1009–1013.
- Mahan, J.E., 2000. *Physical Vapor Deposition of Thin Films*. John Wiley & Sons, Hoboken, New Jersey, USA.
- Marchand, C., Vardelle, A., Mariaux, G., Lefort, P., 2008. Modelling of the plasma spray process with liquid feedstock injection. *Surf. Coat. Technol.* 202, 4458–4464.
- Mauer, G., Vaßen, R., Stöver, D., 2007. Comparison and applications of DPV-2000 and accuraspray-g3 diagnostic systems. *J. Therm. Spray Technol.* 16 (3), 414–424.
- Mauer, G., Vaßen, R., Stöver, D., Kirner, S., Marqués, J.L., Zimmermann, S., Forster, G., Schein, J., 2011a. Improving power injection in plasma spraying by optical diagnostics of the plasma and particle characterization. *J. Therm. Spray Technol.* 20 (1–2), 3–11.
- Mauer, G., Vaßen, R., Stöver, D., 2011b. Plasma and particle temperature measurements in thermal spray: approaches and applications. *J. Therm. Spray Technol.* 20 (3), 391–406.
- Meillot, E., Balmigere, G., 2008. Plasma spraying modelling: particle injection in a time-fluctuating plasma jet. *Surf. Coat. Technol.* 202, 4465–4469.
- Meillot, E., Vincent, S., Caruyer, C., Caltagirone, J.-P., Damiani, D., 2009. From DC time-dependent thermal plasma generation to suspension plasma-spraying interactions. *J. Therm. Spray Technol.* 18, 875–886.
- Molz, R., McCullough, R., Hawley, D., Muggli, F., 2007. Improvement of plasma gun performance using comprehensive fluid element modeling II. *J. Therm. Spray Technol.* 16 (5–6), 684–689.
- Moreau, C., Gougeon, P., Burgess, A., Ross, D., 1995. Characterization of particle flows in an axial injection plasma torch. In: Berndt, C.C., Sampath, S. (Eds.), In: *Proc. 8th National Thermal Spray Conference*, Houston, Texas. ASM International, Materials Park, OH, pp. 141–147.

- Moreau, C., Bisson, J.-F., Lima, R.S., Marple, B.R., 2005. Diagnostics for advanced materials processing by plasma spraying. *Pure Appl. Chem.* 77 (2), 443–462.
- Moreau, E., Chazelas, C., Mariaux, G., Vardelle, A., 2006. Modeling of the restrike mode operation of a DC plasma spray torch. *J. Therm. Spray Technol.* 15 (4), 524–530.
- Morishita, T., 1991. Coatings by 250 kW plasma jet spray system. In: Blum-Sandmeier, S., Eschnauer, H., Huber, P., Nicoll, A. (Eds.), In: *Proc. 2nd Plasma Technik Symp.*, Luzern, Switzerland, Plasma Technik, Wohlen, Switzerland, pp. 137–145.
- Muehlberger, E., 1988. Industrial plasma processing technology. In: *Proc. 1st Plasma Technik Symp.*, vol. 3. Plasma Technik, Wohlen, pp. 105–118.
- Muggli, F., Molz, R., McCullough, R., Hawley, D., 2007. Improvement of plasma gun performance using comprehensive fluid element modeling: part I. *J. Therm. Spray Technol.* 16 (5–6), 677–683.
- Nadeau, A., Pouliot, L., Nadeau, F., Blain, J., Berube, S.A., Moreau, C., Lamontagne, M., 2006. A new approach to online thickness measurement of thermal spray coatings. *J. Therm. Spray Technol.* 15 (4), 744–749.
- Neiser, V., Smith, M.F., Dykhuisen, R.C., 1998. Oxidation in wire HVOF-sprayed steel. *J. Therm. Spray Technol.* 7 (4), 537–545.
- Nickel, R., Bobzin, K., Lugscheider, E., Parkot, D., Varava, W., Olivier, H., Luo, X., 2007. Numerical studies of the application of shock tube technology for cold gas dynamic spray process. *J. Therm. Spray Technol.* 16 (5–6), 729–735.
- Pawlowski, L., 2003. *Dépôts physiques*. Presses polytechniques et universitaires romandes, Lausanne, CH.
- Pfender, E., 1985. Heat and momentum transfer to particles in thermal plasma flows. *Pure Appl. Chem.* 57, 1179–1196.
- Pfender, E., 1989. Particle behavior in thermal plasmas. *Plasma Chem. Plasma Process.* 9 (Suppl. 1), 167S–194S.
- Pfender, E., 1999. Thermal plasma technology: where do we stand and where are we going? *Plasma Chem. Plasma Process.* 19 (1), 1–31.
- Planche, M.P., Coudert, J.F., Fauchais, P., 1998. Velocity measurements for arc jets produced by a DC plasma spray torch. *Plasma Chem. Plasma Process.* 18 (2), 263–283.
- Planche, M.P., Bolot, R., Coddet, C., 2003. In-flight characteristics of plasma sprayed alumina particles: measurements, modeling, and comparison. *J. Therm. Spray Technol.* 12 (1), 101–111.
- Proulx, P., Mostaghimi, J., Boulos, M.I., 1985. Computer modeling of the emission patterns for a spectrochemical ICP. *Int. J. Heat Mass Transf.* 28, 1327–1336.
- Roumilhac, P., Coudert, J.-F., Fauchais, P., 1990. Designing parameters of spraying plasma torches. In: Bernecki, T. (Ed.), *Proc. National Thermal Spray Conf.*, Long Beach, CA. ASM International, Materials Park, OH, pp. 11–19.
- Samareh, B., Dolatabadi, A., 2007. A three-dimensional analysis of the cold spray process: the effects of substrate location and shape. *J. Therm. Spray Technol.* 16 (5–6), 634–642.
- Sampath, S., Srinivasan, V., Valarezo, A., Vaidya, A., Streibl, T., 2009. Sensing, control, and in situ measurement of coating properties: an integrated approach toward establishing process-property correlations. *J. Therm. Spray Technol.* 18 (2), 243–255.
- Sevostianov, I., Kachanov, M., 2009. Elastic and conductive properties of plasma-sprayed ceramic coatings in relation to their microstructure: an overview. *J. Therm. Spray Technol.* 18, 822–834.
- Shan, Y., Coyle, T.W., Mostaghimi, J., 2007. Numerical simulation of droplet break-up and collision in solution precursor plasma spraying. *J. Therm. Spray Technol.* 16, 698–704.
- Sørensen, P.A., Kiil, S., Dam-Johansen, K., Weinell, C.E., 2009. Anticorrosive coatings: a review. *J. Coat. Technol. Res.* 6 (2), 135–176.

- Srivatsan, V.R., Dolatabadi, A., 2006. Simulation of particle-shock interaction in a high velocity oxygen fuel process. *J. Therm. Spray Technol.* 15 (4), 481–487.
- Steffens, H.D., Babiak, Z., Wewel, M., 1990. Recent developments in arc spraying. *IEEE Trans. Plasma Sci.* 18 (6), 974–979.
- Stoltenhoff, T., Kreye, H., Richter, H.J., 1994. An analysis of the cold spray process and its coatings. *J. Therm. Spray Technol.* 11 (4), 542–550.
- Streibl, T., Vaidya, A., Friis, M., Srinivasan, V., Sampath, S., 2006. A critical assessment of particle temperature distributions during plasma spraying: experimental results for YSZ. *Plasma Chem. Plasma Process.* 26 (1), 73–102.
- Taylor, K., Jodoin, B., Karov, J., 2006. Particle loading effect in cold spray. *J. Therm. Spray Technol.* 15 (2), 273–279.
- Thorpe, M.L., Richter, H.J., 1992. A pragmatic analysis and comparison of HVOF processes. *J. Therm. Spray Technol.* 1 (2), 161–170.
- Tillmann, W., Vogli, E., Nebel, J., 2007. Development of detonation flame sprayed Cu-base coatings containing large ceramic particles. *J. Therm. Spray Technol.* 16 (5–6), 751–758.
- Tillmann, W., Vogli, E., Abdulgader, M., Gurriss, M., Kuzmin, D., Turek, S., 2008. Particle behavior during the arc spraying process with cord wires. *J. Therm. Spray Technol.* 17 (5–6), 966–973.
- Trelles, J.P., Chazelas, C., Vardelle, A., Heberlein, J., 2009. Arc plasma torch modeling. *J. Therm. Spray Technol.* 18 (5–6), 728–752.
- Trifa, F.-I., Montavon, G., Coddet, C., 2007. Model-based expert system for design and simulation of APS coatings. *J. Therm. Spray Technol.* 16 (1), 128–139.
- TSS, 2014. Thermal Spray Coating Technology White Paper by the ASM International Thermal Spray Association (TSS). <http://tss.asminternational.org/portal/site/tss/>.
- Tucker Jr., C. (Ed.), 2013. ASM Handbook. Thermal Spray Technology, vol. 5A.
- Vaidya, A., Srinivasan, V., Streibl, T., Friis, M., Chi, W., Sampath, S., 2008. Process maps for plasma spraying of yttria-stabilized zirconia: an integrated approach to design, optimization and reliability. *Mater. Sci. Eng. A* 497, 239–253.
- Vardelle, M., Vardelle, A., Li, K.-I., Fauchais, P., Themelis, N.J., 1996. Coating generation: vaporization of particles in plasma spraying and splat formation. *Pure Appl. Chem.* 68 (5), 1093–1099.
- Vardelle, A., Themelis, N.J., Dussoubs, B., Vardelle, M., Fauchais, P., 1997. Transport phenomena in thermal plasmas. *J. High. Temp. Mater. Proc.* 1 (3), 295–317.
- Vardelle, M., Vardelle, A., Fauchais, P., Li, K.-I., Dussoubs, B., Themelis, N.J., 2001. Controlling particle injection in plasma spraying. *J. Therm. Spray Technol.* 10, 267–286.
- Vincent, S., Balmigere, G., Caruyer, C., Meillot, E., Caltagirone, J.-P., 2009. Contribution to the modeling of the interaction between a plasma flow and a liquid jet. *Surf. Coat. Technol.* 203, 2162–2171.
- von Niessen, K., Gindrat, M., 2010. Vapor phase deposition using a plasma spray process. In: *Thermal Spray: Global Solutions, ITSC 2010, DVS, Düsseldorf, Germany*.
- von Niessen, K., Gindrat, M., 2011. Plasma sprayed-PVD: a new thermal spray process to deposit out of the vapor phase. *J. Therm. Spray Technol.* 20 (4), 736–743.
- Wang, H.-T., Li, C.-J., Yang, G.-J., Li, C.-X., Zhang, Q., Li, W.-Y., 2007. Microstructural characterization of cold-sprayed nanostructured FeAl intermetallic compound coating and its ball-milled feedstock powders. *J. Therm. Spray Technol.* 16 (5–6), 669–676.
- Westerweel, J., 1993. Digital particle image velocimetry—theory and application. PhD thesis, Delft University Press.
- Yamada, M., Isago, H., Nakano, H., Fukumoto, M., 2010. Cold spraying of TiO₂ photocatalyst coating with nitrogen process gas. *J. Therm. Spray Technol.* 19 (6), 1218–1223.

-
- Yang, Y.-M., Liao, H., Coddet, C., 2002. Simulation and application of a HVOF process for MCrAlY thermal spraying. *J. Therm. Spray Technol.* 11 (1), 36–43.
- Yoshida, T., Akashi, K., 1977. Particle heating in a radio-frequency plasma torch. *J. Appl. Phys.* 48 (6), 2252–2264.
- Zhang, T., Gawne, D.T., Liu, B., 2000. Computer modelling of the influence of process parameters on the heating and acceleration of particles during plasma spraying. *Surf. Coat. Technol.* 132, 233–243.
- Zhang, Q., Li, C.-J., Li, C.-X., Yang, G.-J., Lui, S.-C., 2008. Study of oxidation behavior of nanostructured NiCrAlY bond coatings deposited by cold spraying. *Surf. Coat. Technol.* 202 (14), 3378–3384.

This page intentionally left blank

Feedstock suspensions and solutions

3

R. Moreno, E. Bannier

3.1 Introduction

There are many different techniques to produce ceramic coatings onto metals and/or ceramics (Reed, 1995; Rahaman, 1995). These techniques can be classified into three categories depending on the physical state of the starting materials (i.e., gas, liquid or solid phase). Gas-phase synthesis leads to thin films (with thicknesses that can be well below 1 μm and can go up to several tenths of micrometres), as it is the case of chemical or physical vapour deposition (CVD or PVD, respectively). The use of particulate sols and suspensions (considered as liquid-phase starting materials) allows us to obtain a broad range of coating thicknesses, from less than 1 μm in the case of precursor solutions to a few tenths of microns when using concentrated suspensions for dipping. Sol-gel technology and polymer pyrolysis are probably the most important representatives for the liquid precursor methods. There are two main groups of techniques for the fabrication of coatings from powders, melting followed by shaping, referred to as melt casting, and firing of compacted powders. In the last case, the coated material needs to be co-sintered, and many times, the thermal expansion coefficient mismatch and the much lower melting temperature of metal substrates are limiting factors. Within the techniques using the melting mechanism, thermal spray is one of the most widely used to apply metallic or non-metallic coatings onto metals, alloys, ceramics, etc. Thermal spray is one of the most economical and viable processes to obtain coatings at industrial scale, given its high deposition rates and that, in most cases, there is no need for special atmospheric or chemical chambers, and the durability and high bond strength of the coatings (Davis, 2004).

In the last decades, nanostructured coatings have been extensively studied as they may significantly enhance the coating properties (Fauchais et al., 2011). In conventional plasma spraying, a micrometre-sized powder is injected within the plasma flow using a carrier gas. The decrease in particle size and weight from micro- to nanoparticles requires an increase in particle injection velocity, making it impossible to inject the nanoparticles into the plasma jet using conventional feeding system. However, these difficulties can be overcome using one of the following approaches:

- (1) Agglomeration of nanometre-sized particles into micrometre-sized feedstock that can be injected conventionally using a carrier gas (atmospheric plasma spraying, APS) (Lima and Marple, 2007; Cao et al., 2000).

- (2) Use of a carrier liquid instead of a carrier gas (suspension plasma spraying, SPS) (Pawlowski, 2009; Fauchais et al., 2008; Fauchais and Vardelle, 2012).

In both APS and SPS, the characteristics of the as-sprayed coatings depend not only on the operational conditions but also on the properties of the feedstock. Then, the control of the characteristics of the feeding material determines the microstructure and properties of the final coating (Knight and Smith, 1998; Killinger et al., 2011).

In the case of APS, the main requirements for powders are free flowability and narrow size distribution (Chuankian et al., 1984; Wigren et al., 1996). A free-flowing powder is necessary to reduce friction effects and to ensure a uniform feeding and a high uniformity. Spray drying is a suitable method to reconstitute the nanoparticles into granules with good flowability and provides a route to safe handling of nanoparticles (Faure et al., 2010). In the spray dryer, a suspension is fed into the drying chamber; then, the slip is atomized by pumping it at high pressure through a multinozzle array; after that, the upward spiralling droplets encounter hot air and are fed through a diffuser into the chamber in a countercurrent flow with respect to that of the droplets (Negre and Sánchez, 1996). The rapid heat and mass transfer and occasionally the presence of processing aids (mainly binders) result in dried granules that can have a large variety of shapes, from uniform solid spheres that are regarded as ideal granules for most ceramic systems to elongated, pancake, doughnut-shaped, needlelike or hollow granules (Masters, 1985; Walton and Mumford, 1999). In order to avoid undesired agglomerates and obtain homogeneous spray-dried granules with high apparent density, it is necessary to prepare and optimize the suspensions (Fauchais et al., 2010; Zainuddin et al., 2011). Maintaining the nanostructure in the final coating is possible due to the high speed of the deposition process.

SPS differs significantly from APS since the feeding suspension is first fragmented into droplets and the liquid phase is vapourized before the solid feedstock is processed, leading to different interaction phenomena between the plasma and the particles and to different thermal routes during spraying (Pawlowski, 2009; Fauchais et al., 2008). However, as in the case of APS of a nanostructured feedstock, the first step consists of obtaining a stable suspension of nanoparticles that can be fed into the plasma stream.

In spite of the clear advantages of using stable suspensions of nanoparticles, its use is not as frequent as desired, mainly due to the low availability of commercial nano-suspensions. Some drawbacks of the current commercially available feeding materials are the low concentration of the suspensions (Santacruz et al., 2008, 2009), the small variety of suspension compositions, and the lack of bimodal or multimodal mixtures of powders with the desired stability. In fact, in the last years, there is a growing tendency to prepare slurries with bimodal or multimodal size distribution in which nanosized powders are mixed with submicron- or micron-sized particles (Vicent et al., 2012a).

All these limitations may be overcome using adequate suspensions of the desired feeding material. Longtime stability of concentrated or diluted suspensions of monophase or multiphase materials with monomodal or multimodal size distributions can be produced by using a colloidal approach in which colloidal stability is controlled by

manipulating the interaction forces existing among the different components of the suspension and by optimizing the rheological behaviour of the suspensions in terms of any parameters affecting the viscosity and the time stability, such as the solids loading, the presence of deflocculants, pH, mixing/milling procedure and time (Lange, 1989; Lewis, 2000; Sigmund et al., 2000). Accordingly, the next section will be devoted to concisely explain the fundamentals of colloid science and rheology of particulate suspensions.

3.2 Stability and rheology of suspensions

3.2.1 Colloidal stability

Colloids are dispersed systems consisting of one or more phases dispersed in a continuous medium with at least one dimension lying within the nanometre to the micrometre scale. In colloidal dispersions, the dispersed phase can be a gas, a liquid or a solid. In this chapter, we will refer to dispersions of solids in liquids, for example, particulate sols and suspensions. Considering the small size of the particles, the surface/volume ratio is high so that a high ratio of molecules lies in the vicinity of the particle/medium interface. Hence, the structure of the interfacial region determines the properties of the system and the tendency of the particles to form aggregate units or to remain as individual particles. In ceramic processing, it is essential to maintain a high dispersion level during all processing stages in order to obtain a uniform microstructure. Agglomeration leads to defects that will remain in the final microstructure, thus decreasing the properties of the sintered material. There are many available books and reviews focusing on the fundamentals of colloid science and surface chemistry. Readers are referred to the excellent books of Hiemenz (1997), Hunter (1987), Israelachvili (1985), Everett (1988), Cosgrove (2005) and Pugh and Bergström (1994) for deeper knowledge in the topic.

There are two types of structures occurring with charged interfaces (i.e., electrical double layers, Figure 3.1) or with adsorbed polymers, respectively. Systems containing double layers or adsorbed polymer layers will develop a repulsive interaction as particles approach each other and the electrical or adsorbed layers start to overlap. However, there is always an attractive interaction due to the London–van der Waals dispersion forces, which try to attract particles to each other at short separation distances. Stable dispersions are obtained when the repulsive forces dominate over the attractive van der Waals forces. The main particle interactions can be classified into four types:

- Hard sphere interaction. Particles are considered as hard, non-compressible spheres. When two particles approach until the centre distance is lower than two times the radius, then the interaction increases towards infinity.
- Attractive interaction arising from the induced dipoles due to fluctuation in the distribution of electronic charges (the London–van der Waals dispersion interaction).

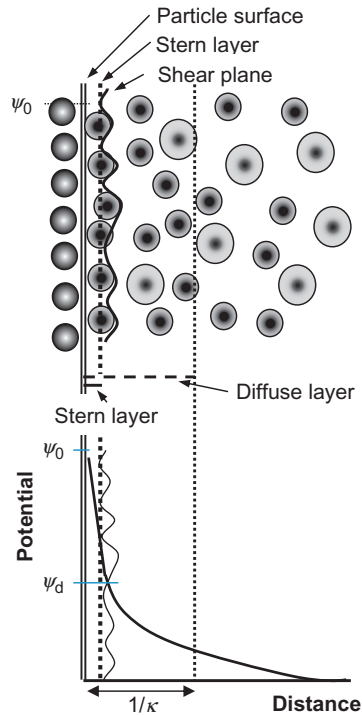


Figure 3.1 Representation of the electrical double layer.

- Soft or electrostatic interaction. Particles have a surface charge, due to either the development of a double layer or the adsorption of charged surfactants. In a soft system, the particle radius (a) is modified by the length of the electrical or the adsorbed layer (δ), the effective radius being $(a + \delta)$.
- Steric interaction. Particles contain adsorbed non-ionic surfactants or polymers that interpenetrate when the particles approach, increasing the density of polymer segments, which results in a steric repulsion.

3.2.1.1 *The attractive interaction*

The attractive term in the interaction potential is generally the result of the London–van der Waals dispersion forces. The van der Waals force is the result of the interaction between a permanent dipole and other permanent dipoles (the Keesom interaction) or a polarizable atom that produces an induced dipole (the Debye interaction), or, when no permanent dipoles are present, instantaneous dipoles are formed arising from fluctuations in the distribution of electronic charge (the London dispersion interaction). The latter is always present and plays a key role in the stability of the colloidal suspension.

The attractive interaction between two similar spherical particles of radius a at a distance x (the distance between the centres being $D=2a+x$), as proposed by Hamaker, is given by Equation (3.1)

$$V_A = -\frac{Aa}{12x} \quad (3.1)$$

being A the Hamaker constant. Values of A for most solvents are in the range $4-8 \times 10^{-20}$ J; for polymers, $6-10 \times 10^{-20}$ J and for metals and ionic solids, $10-30 \times 10^{-20}$ J. A for two particles in a medium is given by Equation (3.2):

$$A = A_{pp} + A_{mm} - 2A_{pm} \quad (3.2)$$

where A_{pp} and A_{mm} are the constants for the particles and for the medium and A_{pm} is associated to the particle/medium interaction and is generally assumed to be $A_{pm} = (A_{pp}A_{mm})^{1/2}$, and hence, $A = (A_p^{1/2} - A_m^{1/2})^2$, where A is always positive. At large separations, a delay in the dipole–dipole interactions is observed and the original model by Hamaker breaks down. Many authors have developed models taking into account the so-called retardation effect. The Hamaker constant can also be calculated based on the dielectric constants and refractive indexes and as a function of the separation between the bodies (Bergström, 1997).

3.2.1.2 The electrostatic interaction

Hydrous oxide surfaces are amphoteric and are subjected to acid–base reactions where protons and hydroxyl ions can specifically adsorb. For this reason, H^+ and OH^- are referred to as potential determining ions. The separation of charge occurring at an interface between two phases is referred to as an electrical double layer because it consists ideally of two regions of opposite charge.

The surface charge (σ_0) is compensated by a distribution of ions with opposite charge to that of the surface (the so-called counterions) and ions with the same charge (co-ions). The surface potential (ψ) decays exponentially with distance (x) according to the Debye–Hückel equation:

$$\psi_x = \psi_0 \exp(-\kappa x) \quad (3.3)$$

where

$$\kappa = \left(\frac{\sum_i \rho_{\infty i} e^2 z_i^2}{\epsilon \epsilon_0 kT} \right)^{1/2} \quad (3.4)$$

where $\rho_{\infty i}$ is the ionic concentration of ions i in the bulk, e is the electronic charge, z_i is the valency of the ions, ϵ is the permittivity of the medium (dielectric constant, 78.6 for water at 25 °C), ϵ_0 is the permittivity of vacuum, k is the Boltzmann constant and T is

the absolute temperature. This equation defines a condenser whose two plates are separated by a distance $1/\kappa$, which is known as the Debye length and gives the thickness of the double layer. Its magnitude depends only on the medium properties and not on the properties of the surface, such as the charge and the potential.

The double-layer formation is explained through the Stern modification of the Gouy–Chapman theory, which assumes that there are a monolayer of counterions specifically adsorbed onto the surface and a diffuse layer in which the concentration of counterions decreases as the separation distance increases. The distance of the closest approach to the surface is x_1 , and the diffuse part of the double layer starts at x_2 , such that for $x > x_2$, specific interaction forces are negligible. If the particle surface is positive, the unhydrated anions are in contact with the surface, and the plane formed by the centres of the anions is called the inner Helmholtz plane (IHP). The cations remain hydrated and the plane crossing their centres is the outer Helmholtz plane (OHP). The potential distribution at an interface is schematically represented in [Figure 3.1](#). For a detailed analysis of the electrostatic interaction, the reader is referred to the textbooks on colloids referred at the end of the chapter.

When a particle moves through the liquid, the Stern and part of the diffuse layer move with the particle. The potential at this plane of shear is referred to as the *zeta potential* (ζ), and it indicates the gradient of electrical potential when the surface potential is constant. The isoelectric point is defined as the pH value at which the zeta potential is zero. In the absence of specific adsorption, the isoelectric point and the zero point of charge are coincident. When specific adsorption occurs, the isoelectric point shifts towards acidic pH when anions are adsorbed and towards basic pH when cations are adsorbed ([Parks and De Bruyn, 1962](#); [Hunter, 1981](#)).

The repulsive electrostatic potential between two particles is given by

$$V_R = \left(\frac{64\pi k T a \rho_\infty \gamma^2}{\kappa^2} \right) \exp(-\kappa x) \quad (3.5)$$

where

$$\gamma = \tanh \left(\frac{ze\psi_0}{4kT} \right) = \frac{\exp(ze\psi_0/2kT) - 1}{\exp(ze\psi_0/2kT) + 1} \quad (3.6)$$

which is the basis of the Gouy–Chapman model. For large potentials, $\gamma \rightarrow 1$, whereas for low potentials, the substitution $\tanh x \sim x$ reduces this equation to Equation (3.3).

The stability of a suspension is widely evaluated by the combination of the different interactions. In the most general case, the stability of charged systems is given by the Derjaguin–Landau–Verwey–Overbeek (DLVO) theory, where the total interaction potential is given by the sum of the repulsive electrostatic potential and the attractive London–van der Waals potential ([Derjaguin and Landau, 1941](#); [Verwey and Overbeek, 1948](#)):

$$V_T = \frac{64\pi k T \rho_\infty \gamma^2}{\kappa^2} \exp(-\kappa x) - \frac{Aa}{12x} \quad (3.7)$$

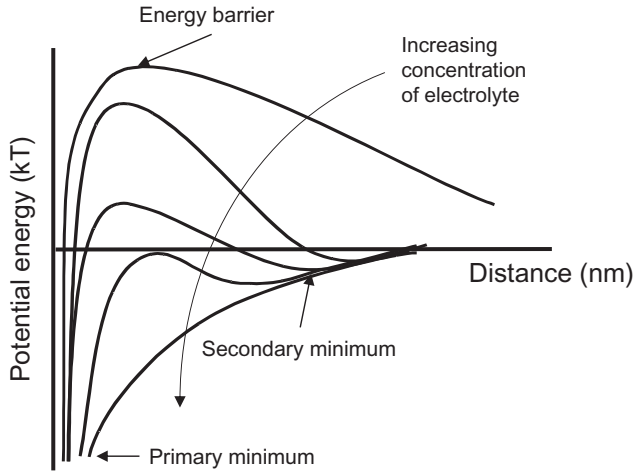


Figure 3.2 Variation of interparticle potentials as a function of separation distance and concentration of electrolyte.

The DLVO interaction can be represented as a function of separation distance between two particles as plotted in [Figure 3.2](#). The van der Waals interaction is always negative, and the combination with the electrostatic repulsion leads to the presence of a deep minimum (referred to as primary minimum) at very short distances where particles touch one another leading to the so-called coagulation. At longer distances, there is a maximum barrier that corresponds to the maximum stability of the system. At even longer distances, there could be a secondary minimum, in which particles flocculate. In this case, particles are together through the action of an intermediate substance (such as liquid molecules or a compressed double layer) so that they can be easily redispersed. On the contrary, coagulated systems are not redispersible. An important feature is that the interaction energy (and the zeta potential) of the suspension strongly depends on the concentration of electrolyte (in general, any ions resulting from the addition of deflocculant or present as impurities).

When more than one type of particle is present, the situation becomes more complex. Interactions between dissimilar particles (in nature or in size) are referred to as heterocoagulation. From the DLVO theory, for spherical particles with $\kappa a > 10$ and $\psi_0 > 50$ mV, the potential energy of repulsion for two particles with radii a_1 and a_2 and potentials ψ_1 and ψ_2 is given by the equation proposed by [Hogg et al. \(1966\)](#):

$$V_R = \frac{2\pi\epsilon\epsilon_0 a_1 a_2}{(a_1 + a_2)} \left[2\psi_1 \psi_2 \ln \left(\frac{1 + \exp(-\kappa x)}{1 - \exp(-\kappa x)} \right) + (\psi_1^2 + \psi_2^2) \ln [1 - \exp(-\kappa x)] \right] \quad (3.8)$$

The preparation of mixtures needs a careful control of pH, since the different species have a different isoelectric point, and hence, there will be a pH region with species of opposite sign that will lead to heterocoagulation. However, this could be advantageous for mixtures of materials with strong differences in shape or size, to obtain core-shell structures and to coat bigger particles with smaller ones by means of strong electrostatic forces.

There are available models and software to evaluate the colloidal stability of suspensions of virtually any kind of suspensions. One such program is the Hamaker 2 toolkit freely provided at the EPFL (Lausanne, Switzerland). In Hamaker 2, a great deal of attention was put into making plotting as flexible as possible. Plots of the potential and the force between dissimilar particles can be done in 2-D as a function of a single variable or in 3-D as a function of two variables. All parameters of the models can be chosen as plotting variable, making it very flexible as the user can add virtually any type of interaction potential (Aschauer et al., 2011).

3.2.1.3 The steric interaction

Another route to provide stability to a suspension is through the adsorption of polymers onto the particles surfaces (Napper, 1983). Attached polymers can be non-ionic or can be charged (this being the case of the so-called polyelectrolytes), in which case the steric hindrance associated to the adsorbed polymer is reinforced by electrostatic repulsion due to the presence of charges. This results in an electrosteric mechanism with the steric effect dominating the stability at short separation distances and the electrostatic repulsion operating at higher distances. A consequence of the polymers adsorption is that surfaces are not free so that they cannot touch one another. This means that there is no primary minimum, so that coagulation does not occur, and consequently, electrosterically stabilized systems are stable thermodynamically, whereas electrostatically stabilized suspensions are only metastable.

To illustrate the potential energy interaction in steric (or electrosteric) systems, Figure 3.3 shows the potential energy plot for suspensions of alumina dispersed with

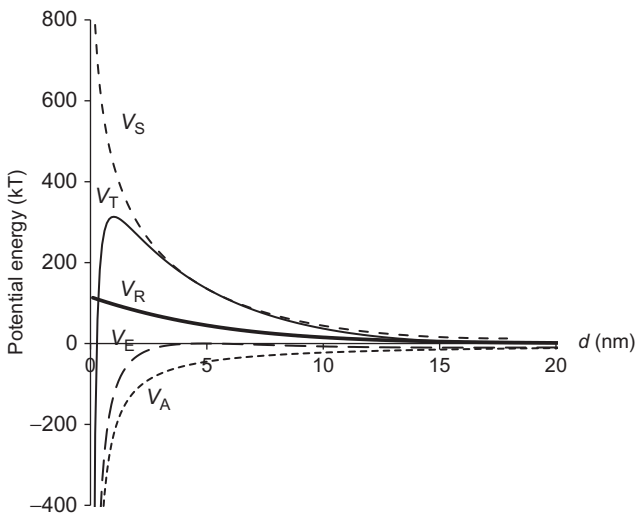


Figure 3.3 Variation of interparticle potentials as a function of separation distance for aqueous alumina suspensions showing the different contributions to the total potential.

a polyacrylic-type polyelectrolyte. The different contributions to the stability are plotted independently, the attractive interaction (V_A), the electrostatic repulsion (V_R), the calculated steric contribution (V_S), and the total interaction potential considering only electrostatic stability ($V_E = V_A + V_R$) or both the electrostatic and the steric effects ($V_T = V_A + V_R + V_S$). It is experimentally observed that this suspension is quite stable and can be prepared with high solids loadings (>40 vol.%) while maintaining very low viscosity. However, the observed stability is only explained considering the steric contribution to the total interaction potential, as there is no primary minimum.

3.2.2 Rheology of ceramic suspensions

The flow behaviour of a suspension depends on many factors, the most characteristic being (1) the physicochemical properties of the particles, that is, particle size distribution (PSD), surface area, shape and density; (2) the magnitude and balance of the various interaction forces; (3) the presence of additives in the suspension, such as deflocculants or binders and plasticizers, frequently used in spray drying and other ceramic processes; (4) the solids loading of the suspension (as the number of particles per unit volume increases, there are more interactions until a limit in which particles reach the theoretical packing density and the system becomes a solid-like structure); (5) the experimental measuring conditions; and (6) the history and shearing conditions at which the suspension has been previously subjected (Goodwin, 1990). This obviously includes most treatment steps of the ceramic process, such as milling, mixing, centrifuging and other separation procedures, frequently used during the industrial granulation process.

General books to understand the basics of rheology are those by Tadros (2010), Moreno (2005), Barnes et al. (1989), Malkin (1994), Schramm (1984) and Larson (1999).

3.2.2.1 Flow behaviour

Rheology is usually defined as the study of the flow and deformation of matter. Its origin must be related to observation of abnormal behaviour of many well-known materials exhibiting both liquid-like and solid-like properties. This makes necessary to introduce a new terminology to describe those particular features of behaviour and properties and to establish the adequate methods to characterize them. A second aspect is the experimental confirmation of a time dependence, which demonstrates that the material changes with time. Thus, rheology can be redefined as a branch of natural sciences considering real materials with changing structure (Malkin, 1994), and it makes use of phenomenological models. The rheological equations of state (or constitutive equations) are those equations relating an applied stress (σ) and the resulting deformation (γ). The simplest models describing the behaviour of solids and liquids are those due to Hooke and Newton. In between, there exist a large variety of rheological effects not explained by these models.

According to Hooke's law, when a stress (σ) is applied to a solid, it deforms elastically:

$$\sigma = G\gamma \quad (3.9)$$

where G is the elastic modulus (Young's modulus) and γ is the strain. When the strain falls to zero, the sample recovers its original shape. If the shear is large, then the structure of the sample can break, and hence, it not only deforms but also starts to flow. This is the case of liquids that follow Newton's law:

$$\sigma = \eta \dot{\gamma} \quad (3.10)$$

where $\dot{\gamma}$ is the velocity gradient (also known as the shear rate) and η is the viscosity. The unit of viscosity is Pa s. In a Newtonian behaviour, the viscosity does not depend neither on the shear rate nor on the shear history. Most simple liquids like water, acetone and oils are Newtonian. Liquids showing any variation from this behaviour are referred to as non-Newtonian. Figure 3.4 illustrates the possible variations of shear stress versus shear rate (referred to as flow curves). Most common colloidal suspensions are shear thinning (also referred to as pseudoplasticity) because the viscosity decreases as the shear rate increases. Shear thickening (dilatancy) occurs when viscosity increases with shear rate.

Table 3.1 summarizes the most common rheological models for the analysis of flow curves. The simplest model describing the non-Newtonian behaviour of samples is the Ostwald–de Waele model (Equation 3.11). This model fits both shear thinning and shear thickening curves through the constants k (consistency index) and n (shear thinning index when $n < 1$ or shear thickening index when $n > 1$). By fitting the experimental data to this equation, the viscosity can be calculated according to Equation (3.12), which is the power-law model.

Some concentrated suspensions cannot flow until a minimum yield stress (σ_0) is exceeded as in the case of the Bingham plastic flow, which means the linear flow

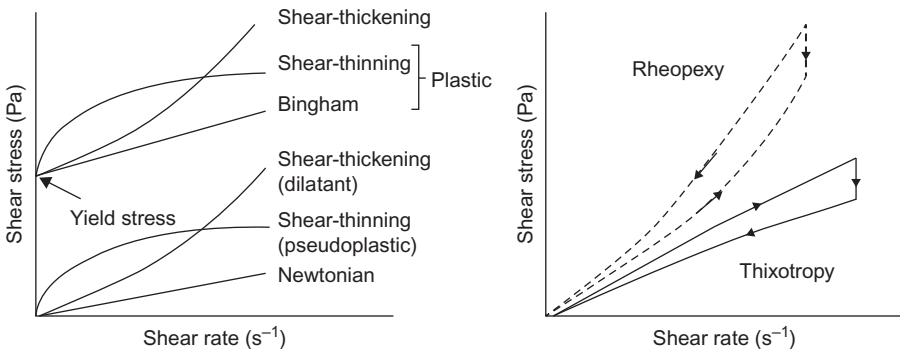


Figure 3.4 Representation of the different types of flow curves (left) and flow curves of time-dependent samples (right).

Table 3.1 Common rheological models to fit the flow curves

Model	Equation
Newton	$\sigma = \eta \dot{\gamma}$ (3.10)
Ostwald–de Waele	$\sigma = K \left(\dot{\gamma} \right)^n$ (3.11)
Power-law model	$\eta = k \left(\dot{\gamma} \right)^{n-1}$ (3.12)
Bingham	$\sigma = \sigma_0 + \eta_p \dot{\gamma}$ (3.13)
Herschel–Bulkley	$\sigma = \sigma_0 + K_1 \left(\dot{\gamma} \right)^n$ (3.14)
Casson	$\sigma^{1/2} = (\sigma_0)^{1/2} + K_1 \left(\dot{\gamma} \right)^{1/2}$ (3.15)
Casson (modified)	$\sigma^{1/2} = (\sigma_0)^{1/2} + K_1 \left(\dot{\gamma} \right)^{n_1}$ (3.16)
Cross	$\frac{\eta_0 - \eta}{\eta - \eta_\infty} = \left(K \dot{\gamma} \right)^m$ (3.17)
Carreau	$\frac{\eta - \eta_\infty}{\eta_0 - \eta_\infty} = \frac{1}{\left(1 + \left(K_1 \dot{\gamma} \right)^2 \right)^{m_1/2}}$ (3.18)
Sisko	$\eta = \eta_\infty + K_2 \left(\dot{\gamma} \right)^{n-1}$ (3.19)

curve is independent of the shear rate above σ_0 (Equation 3.13). When the sample has a yield stress and shows shear thinning behaviour, it is said to be plastic (Bingham, 1922). The most popular models describing this dependence on shearing are those of Herschel–Bulkley (Equation 3.14) and Casson (Equations 3.15 and 3.16). Some systems show a complex behaviour with a limiting viscosity (η_0) in the low-shear-rate regime and another limiting viscosity (η_∞) in the high-shear-rate regime, both separated by a shear thinning behaviour. This is defined by the Cross model (Equation 3.17). A similar equation to fit this complex behaviour is that given by Carreau (Equation 3.18). In all these models, K is a constant parameter with dimension of time, and n or m is a dimensionless constant. Another model that fits a large number

of suspensions is the Sisko model (Equation 3.19), derived from the Cross equation. This model is valid for shear thinning samples where the zero shear viscosity tends to infinity.

In addition to the shear rate dependence, the rheological behaviour of suspensions is often time dependent; the viscosity changes with the time of shearing. Pseudoplastic slurries that show time-dependent viscosities are referred to as thixotropic, whereas time-dependent dilatancy is called anti-thixotropy or rheopexy; see Figure 3.4 (Albertazzi and Rastelli, 1997). The mismatch between the up and the down curves in Figure 3.4 may be associated to a spatial rearrangement of the molecules or particles in the direction of the applied flow field or changes in the structure produced by breaking of weak bonds, alignment of non-spherical particles or agglomerate formation or breakdown.

The yield stress (or yield point) is a parameter of great technological importance. This point defines the minimum stress required to start the flow, and this is strongly dependent on the measuring conditions. If the measurement is done over a long testing time, the yield stress can reduce or disappear. So, although the yield stress is not an intrinsic property of the suspension, the evaluation of an apparent yield stress can give valuable information for comparative purposes (Barnes and Walters, 1985; Barnes, 1999). The easiest method to determine the yield stress for any particular testing conditions is by fitting with the described rheological models, but this requires defining properly the viscosity or shear stress range. Moreover, suspensions may have different behaviours at various shear rates. All these factors can lead to errors in the interpretation of the rheograms. Currently available rheometers have made possible to measure at very low shear rates and low frequencies in the case of oscillatory measurements. They also allow performing measurements under controlled stress conditions. It is usual to plot the stress versus the deformation in a log–log scale, which results in two straight lines whose interception gives the yield stress (Gutiérrez et al., 2000).

3.2.2.2 Rheology of suspensions

The rheology of suspensions depends on the balance between three main forces: the Brownian diffusion, hydrodynamic interaction and interparticle potentials. Those forces are controlled by the volume fraction of particles in the dispersion, their shape and size distribution and the interparticle interactions that can be modulated with the addition of defloculants. When solid fraction increases, the interactions among neighbour particles also increase until they become constrained forming a network structure. This concentration defines the maximum packing fraction (ϕ_m). In some ceramic operations such as near net shaping, it is important to obtain the highest solids content while maintaining good flowability in order to reduce the amount of water to be removed on drying. Therefore, the prediction of the relationship between the reduced viscosity η_r (defined as the suspension viscosity η divided by the medium viscosity η_s) and the volume fraction of particles (ϕ) has great technological interest (Bergström, 1996; Liu, 2000).

Table 3.2 summarizes the most common models relating the viscosity to the volume fraction of solids in suspensions with the corresponding equations. The

Table 3.2 Models describing the relation between viscosity and volume fraction of particles in suspensions

Model	Equation
Einstein	$\eta = \eta_s(1 + 2.5\phi)$ (3.20)
Bachelor	$\eta = \eta_s(1 + 2.5\phi + 6.2\phi^2)$ (3.21)
Krieger–Dougherty	$\eta_r = \left(1 - \frac{\phi}{\phi_m}\right)^{-2.5\phi_m}$ (3.22)
Modified Krieger–Dougherty	$\eta_r = \left(1 - \frac{\phi}{\phi_m}\right)^{-n}$ (3.23)
Quemada	$\eta_r = \left(1 - \frac{\phi}{\phi_m}\right)^{-2}$ (3.24)
Mooney	$\eta_r = \exp\left[\frac{2.5\phi}{1 - \phi/\phi_m}\right]$ (3.25)
Chong	$\eta_r = \left[1 + \frac{0.75(\phi/\phi_m)}{1 - (\phi/\phi_m)}\right]^2$ (3.26)
Liu	$\eta_r = [a(\phi_m - \phi)]^{-n}$ (3.27)
Zhang–Evans	$\eta_r = \left[\frac{(\phi_m - C\phi)}{(\phi_m - \phi)}\right]^2$ (3.28)
Farris	$\eta = \eta_s \prod_{i=1}^n \left(1 - \frac{\phi_i}{\phi_{mi}}\right)^{-[\eta]_i \phi_{mi}}$ (3.29)
Woutersen–de Kruif	$\eta_{r,0} = 1 + 2.5\phi + \left(6.2 + \frac{2.1}{\sigma_B}\right)\phi^2$ (3.30)

first model relating viscosity to particle volume fraction was due to Einstein (Equation 3.20). This model assumes that particles behave as rigid spheres that do not interact, so that it is valid for low volume fractions ($\phi < 0.01$). A further model developed by Bachelor (Equation 3.21) considered the hydrodynamic interactions that become more important as ϕ increases. One of the most popular empirical

models to describe the dependence of viscosity with solid fraction for concentrated suspensions is the Krieger–Dougherty model (Equation 3.22) that introduces the term “intrinsic viscosity” $[\eta]$ and uses the value 2.5 for suspensions of spherical particles. To predict the evolution of viscosity with solid fraction in slurries with non-spherical particles, the exponent factor $[\eta]\phi_m$ is commonly replaced by an exponent n ; then, the Krieger–Dougherty model is referred as the modified Krieger–Dougherty model (Equation 3.23) that allows fitting a big variety of suspensions of different materials. Other models have been used to fit rheological data, such as the models of Quemada (Equation 3.24), Mooney (Equation 3.25), Chong (Equation 3.26), and Liu (Equation 3.27). The independent parameter for these models is ϕ_m while for the Krieger–Dougherty model is $[\eta]$. Zhang and Evans extended Chong’s model with a two-parameter equation (Equation 3.28) that allows describing the behaviour of a great variety of suspensions.

Previous models are valid for systems of monomodal spheres (rigid or soft), but do not account for differences in size and/or shape. The first model for bimodal suspensions was developed by Farris (Equation 3.29). Barnes had reported the influence of the shape of the particles in the suspension rheology, demonstrating that the viscosity increases and ϕ_m decreases as the shape deviates from sphericity from spheres to grains to platelet-like to rod-like shapes. There are also more recent models for describing the behaviour of weakly flocculated suspensions such as the Wouterse–de Kruif model (Equation 3.30).

Figure 3.5 illustrates the effect of particle concentration on viscosity for aqueous suspensions of Al_2O_3 . In Figure 3.5a, the expanded flow curves of suspensions with different solids loading are plotted, as well as the fitting regression to the Cross model that gives the extrapolated values of viscosity to zero and infinite shear rates (η_0 and η_∞). In Figure 3.5b, the variation of viscosity as a function of the volume fraction of solids is plotted. The fitting lines correspond to the predicted behaviour according to the modified Krieger–Dougherty equation (Equation 3.23). The experimental data can be adequately fit in both the high-shear and the low-shear regions (Gutiérrez and Moreno, 2001). However, it must be noted that the coefficient m is different in each region. The Krieger–Dougherty model was developed from Einstein’s theory for diluted suspensions, which are mainly dominated by viscous flow. Hence, the intrinsic viscosity is better represented by the high-shear-rate region (η_∞). The intrinsic viscosity of this system for the high-shear region is $[\eta]=3.6$, higher than the value of 2.5 predicted by Einstein because the particles are not perfectly spherical and monodispersed. The application of the Krieger–Dougherty model provides a maximum packing fraction of 0.66 for this system, which is very close to the packing density (green samples led to a relative density of 64% of theoretical density). This parameter and the arrangement of the particles in the equilibrium structure are necessary for correlating the rheological properties with the pair potential. Earlier studies on hard sphere suspensions have raised a $\phi_m=0.71$ in the high-shear limit for silica slips of different sizes. Other studies have obtained maximum volume fractions of $\phi_m=0.61$ and $\phi_m=0.62$ for Al_2O_3 suspensions and $\phi_m=0.67$ for SiC aqueous suspensions. These differences have been explained considering the contribution taken by the dispersant to the volume.

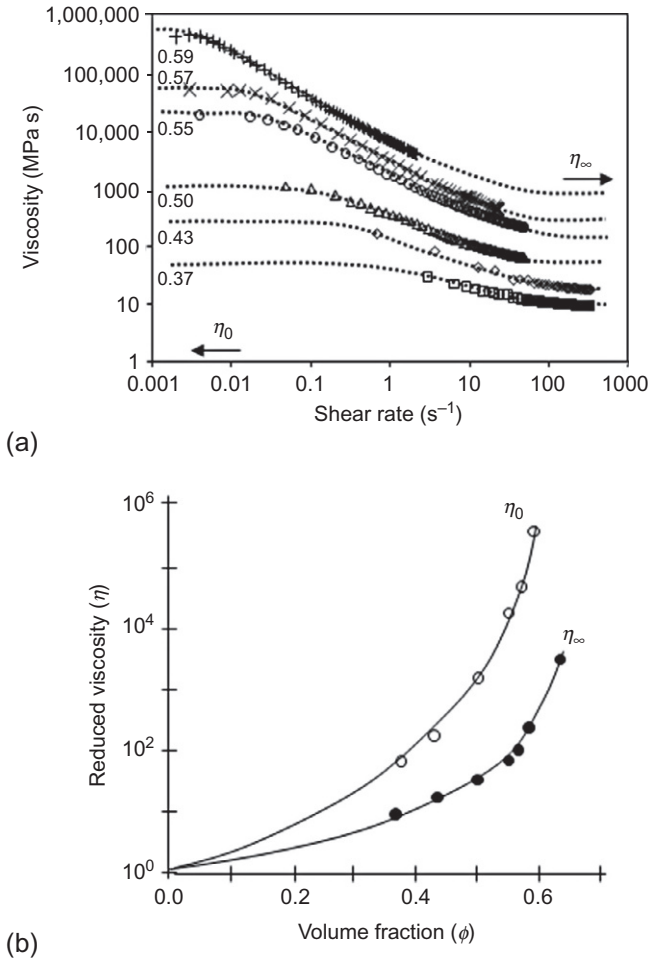


Figure 3.5 Experimental flow curves measured for alumina suspensions dispersed with polyelectrolyte at different volume fractions of solids and fitting to the Cross model (a) and variation of the zero shear viscosity and the high shear viscosity with the volume fraction of solids (symbols) and fitting (solid lines) to the Krieger–Dougherty model (b).

3.3 Requirements for thermal spray suspension and solution feedstocks

In general, two types of liquid feedstocks can be used for plasma spraying: suspensions and solutions. In both cases, the feeding liquids should fulfil the following requirements:

- Very good physical and chemical stability, in order to avoid the modification of the liquid feed characteristics with time and, thus, of the coating properties.
- Low viscosity to facilitate the injection in the plasma jet.

In addition, in the case of solutions, the precursor must be easily decomposed at high temperatures to facilitate the formation of the coating compounds during the deposition process. In the case of a suspension, an adequate dispersion of the particles is also necessary: first to avoid the formation of agglomerate that can block the injector and second to guarantee a homogeneous heating of the particles. In fact, the presence of agglomerates leads to areas less molten in the final structure of the coating and thus to a more heterogeneous microstructure.

Moreover, the liquid feedstock should be fully characterized in order to guarantee the reproducibility of the coating characteristics. This characterization should include not only the measurements of basic properties such as concentration, pH, and density but also the characterization of advanced properties (suspension stability, particles size distribution, surface area and gravitational forces), which are discussed hereinafter on the basis of the theory described in the previous section.

3.3.1 Suspension stability

Suspensions are usually prepared by directly dispersing powders in liquids in the presence or not of adequate dispersing aids (deflocculants) and other processing aids such as temporary binders and plasticizers. When a powder is dispersed into a liquid, different interaction forces are present, including the interparticle interactions and gravitational and inertial forces. All these parameters must be controlled to provide the desired stability:

- The interparticle interactions have been largely described in previous sections. Summarizing, stability can be provided by the manipulation of the colloidal interactions through the formation of an electrostatic double layer or the adsorption of a polymer layer. Both mechanisms can overcome the attractive forces due to London–van der Waals.
- The PSD and the specific surface area. When particle size is large (as in the case of micron-sized particles used frequently as feedstock), the tendency to sedimentation is also high and eventually can dominate over the colloidal interactions.

3.3.2 Particle size distribution

The PSD of a powder determines its properties, processability and applications (Bowen, 2002). The comparison of a PSD with the specific surface area allows assessing the degree of agglomeration. Many powders with nanosized crystals can be so agglomerated that redispersion may be very difficult. A basic statement for particle size analysis is the concept of equivalent sphere, which allows describing a 3-D object (the particle) with just a number. However, different results can be obtained depending on the measuring technique.

The mean size may be calculated in different ways. The first way for a sample containing N particles is the sum of each diameter divided by the number of particles, that is,

$$\bar{d} = \frac{\sum d_i}{N} \quad (3.31)$$

This is a number length mean diameter because the number of particles appears in the equation. It is also represented as $D[1,0]$. The first number in brackets means that the diameter in the top of the equation changes with d_1 , while the second number (0) means that there are no diameter terms in the bottom of the equation. If we consider the particles on the basis of their surface ($S=4\pi a^2$), the mean diameter will be








$$\bar{d} = \sqrt{\frac{\sum d_i^2}{N}} = \frac{\sum d^2}{N} \quad (3.32)$$

This is a number surface mean diameter (N appears in the equation). Since the squares of diameters appear in the top and no diameter appears in the bottom, it is represented by the term $D[2,0]$. If we compare on a weight basis ($w=4/3\pi a^3\rho$), then we have

$$\bar{d} = \sqrt{\frac{\sum d_i^3}{N}} = \frac{\sum d^3}{N} \quad (3.33)$$

which is a number volume mean or number weight mean diameter, represented as $D[3,0]$, the so-called volume mean diameter. For non-spherical particles, the concept of equivalent diameter or volume is used, thus giving the number $D[4,3]$. The different types of mean diameters are summarized in [Table 3.3](#). Considering 10 spherical

Table 3.3 Different types of mean diameter

Type of mean diameter	Term	Equation	Example	
Number-length, X_{NL}	$D[1,0]$	$X_{NL} = \frac{\sum dL}{\sum dN} = \frac{\sum d \cdot dN}{\sum dN}$	5.50	
Number-surface, X_{NS}	$D[2,0]$	$X_{NS} = \sqrt{\frac{\sum dS}{\sum dN}} = \sqrt{\frac{\sum d^2 \cdot dN}{\sum dN}}$	6.21	
Number-volume, X_{NV}	$D[3,0]$	$X_{NV} = \sqrt[3]{\frac{\sum dV}{\sum dN}} = \sqrt[3]{\frac{\sum d^3 \cdot dN}{\sum dN}}$	6.71	
Length-surface, X_{LS}	$D[2,1]$	$X_{LS} = \frac{\sum dS}{\sum dN} = \frac{\sum d^2 \cdot dN}{\sum d \cdot dN}$	7.0	
Length-volume, X_{LV}	$D[3,1]$	$X_{LV} = \sqrt{\frac{\sum dV}{\sum dN}} = \sqrt{\frac{\sum d^3 \cdot dN}{\sum d \cdot dN}}$	7.43	
Surface-volume, X_{SV}	$D[3,2]$	$X_{SV} = \frac{\sum dV}{\sum dS} = \frac{\sum d^3 \cdot dN}{\sum d^2 \cdot dN}$	7.87	
Volume (weight), $X_{V,w}$	$D[4,3]$	$X_{V,w} = \frac{\sum d^4 \cdot dN}{\sum d^3 \cdot dN}$	8.37	

particles with sizes of 1, 2, 3, . . . , 10, the corresponding mean diameters will be those in the last column of [Table 3.3](#): as it can be seen, they are all different. The average of a distribution indicates the central tendency that is not greatly affected by the values at the tails of the distribution. The central tendency can be represented by the mean diameter, the mode and the median. The mean value is the point about which the moments of the distribution are equal. The median is the value that divides the population into two equal halves, that is, 50% of the population is above and 50% is below that value. This is the $d_{v,50}$, extensively used in ceramics and often referred to as mean or average particle size. The mode is the highest point in the frequency curve, that is, the value that occurs most frequently. For a Gaussian (normal) PSD curve, the mean, median and mode are the same.

Measuring systems for PSD may be classified into a few general mechanisms, although many variants have been developed. The first way is by direct observation with microscope (optical microscope, scanning electron microscope or transmission electron microscope as particle size decreases in size). Another way is through indirect methods that relate some physical property of the particle to its size. Indirect methods may be classified in the following mechanisms: (1) sieving, based on a mechanical mechanism; (2) sedimentation, involving fluids; (3) electrical sensing zone, based on the action of an electric field; and (4) light diffraction, based on the optical mechanisms. There is another classification of measuring techniques that differentiates methods that count and measure particles, methods that relate some signal to a continuous distribution, and those that divide particles into discrete fractions. Information about this classification can be found at Allen's textbook ([Allen, 1997](#)).

Microscopy observations and light scattering techniques are the most commonly used to analyse PSD. For nanoparticles, transmission electron microscopy (TEM) is preferred. Since the particle size produces different light scattering behaviours, different measuring techniques have been developed to cover the widest range of particle sizes. In the last years, the developments in lasers, optical fibre and computing have favoured the construction of the increasingly demanded laser measuring techniques. There are four types of laser instruments:

- (1) Laser diffraction instrument. It detects the forwarded scattered diffraction pattern from a stream of particles and a deconvolution routine is necessary.
- (2) Aerosol particle counters, where a stream of particles passes through a focused beam. The scattered light is recorded at certain angle for each particle.
- (3) Dynamic light scattering that detects the fluctuation frequency of the light scattered from a beam passing through a suspension. This frequency is related to the Brownian motion of their particle and, therefore, their average size.
- (4) Laser Doppler, in which the velocity of the particle is recorded from the point of intersection of two laser beams.

Static light scattering (conventional laser diffraction) is useful to measure PSD in a broad size margin from a few millimetres down to about 0.2 μm . For lower sizes, the most useful technique is dynamic light scattering (also referred to as photon correlation spectroscopy, PCS).

3.3.3 Surface area

Surface area is important since it is related to the particle size, and thus, it is an indicator of the surface activity of the powder. It offers overall information regarding the combined effects of particle size and shape, surface texture and open porosity within a particle or agglomerate. Surface area (S_s) is given in (m^2/g) units. A larger surface area means a higher surface activity, that is, a stronger tendency of particles to agglomerate. Powders for conventional ceramic processing have typical surface areas lower than $20 \text{ m}^2/\text{g}$. In general, reactive aluminas and other oxides have surface areas ranging from 2 to $10 \text{ m}^2/\text{g}$, while other materials are more difficult to sinter due to the increased covalence of their bonds, as in the case of non-oxide ceramics, so powders with higher surface area, $\sim 15 \text{ m}^2/\text{g}$, are preferred. In thermal spray, the size and morphology of the powder strongly influence the heating and acceleration of the feed into the torch, thus determining the efficiency of the deposition and the quality of the coating. In general, a narrow PSD is preferred for thermal spray. Although this makes the cost to increase, greater deposition efficiency is reached. Milled and spray-dried powders have a broad size distribution; thus, it is usual to sieve them before thermal spraying. Typical particle (or granule) sizes for a suitable spraying are those ranging from 20 to $200 \mu\text{m}$, depending on the material and application process. Regarding the morphology, the use of spherical particles or granules is usually preferred in order to avoid irregular shapes and edges than can modify their flowability.

Specific surface area is defined as the total area per unit mass of material. Many materials present irregularities at different structural levels, and hence, the surface area is much higher than the apparent geometric area.

The most extensively used method for measuring the specific surface area is that of gas adsorption at cryogenic temperatures, which is known as the BET method. Usually, liquid nitrogen is used (77.4°K), although other gases and temperatures can be used. The surface area is calculated from the amount of gas needed to coat the surface with a monolayer of gas molecules, provided that the area occupied by a single molecule is known. The volume of gas adsorbed depends on the nature of the gas, the size of the adsorbed molecule relative to the pores size, and the gas pressure. The specific surface area S_s is related with the particle diameter d by Equation (3.34):

$$S_s = \frac{A}{w} = \frac{A}{\rho V} = \frac{4\pi a^2}{(4/3\pi a^3)\rho} = \frac{3}{a\rho} = \frac{6}{d\rho} \quad (3.34)$$

where ρ is the powder density. The evaluation of the BET diameter is particularly interesting for nanosized particles, which have a high tendency to agglomerate. It is possible to define an agglomeration factor f_{agg} that relates the measured to the BET particle size:

$$f_{\text{agg}} = \frac{d_{v,50}}{d_{\text{BET}}} \quad (3.35)$$

3.3.4 Gravitational forces

When a particle with mass m and radius a in a fluid starts to fall, it achieves the so-called terminal velocity v_t in a short time, and the gravitational force ($F_G = mg$, with g being the gravity constant) is balanced by the buoyancy ($F_B = mg$), due to the displaced liquid, and the frictional force ($F_D = Bv_t$, where $B = 6\pi a\eta v$ is the friction coefficient), which is related to the drag of the surrounding liquid. Then,

$$(\rho_s - \rho_l) \frac{4}{3} \pi a^3 g = 6\pi a\eta v_t \quad (3.36)$$

which can be rewritten as

$$v = \frac{2(\rho_s - \rho_l)ga^2}{9\eta} \quad (3.37)$$

where ρ_s and ρ_l are the densities of the solid and the liquid, respectively, and η is the viscosity of the liquid. This equation is normally referred to as the Stokes equation. The time t required for setting a height H is then

$$t = \frac{9\eta H}{2(\rho_s - \rho_l)ga^2} \quad (3.38)$$

The Stokes law is valid for laminar flow and assumes that there are no collisions or interactions between the particles. The transition from laminar to turbulent flow occurs at some critical velocity v_c , given by

$$v_c = \frac{N_R \eta}{\rho_l a} \quad (3.39)$$

where N_R is a dimensionless number called the Reynolds number. The transition from laminar to turbulent flow occurs when its value is ~ 0.2 . When particles are sufficiently small, the Brownian motion resulting from collisions with the molecules of the liquid may displace the particle so the lower limit to the use of gravitational settling in water is $\sim 1 \mu\text{m}$.

Table 3.4 shows the typical energies associated to different interaction forces for different particle sizes. Surface and colloidal interactions dominate over the inertial and gravitational forces only when particle size is small. When particle size increases by one order of magnitude, the Brownian motion maintains constant and the van der Waals and electrostatic forces increase by one order of magnitude, also. However, the kinetic energy promoted by mixing can increase by three orders of magnitude and, still more relevant, the kinetic energy of sedimentation increases by six orders of magnitude (Table 3.4).

Table 3.4 Energies associated to the various interaction forces as a function of particle size

Particle size	0.1 μm	1 μm	10 μm
The van der Waals attraction	10	10^2	10^3
Electrostatic repulsion	$0-10^2$	$0-10^3$	$0-10^4$
Brownian motion	1	1	1
Kinetic energy of sedimentation	10^{-13}	10^{-6}	10
Kinetic energy of mixing	1	10^3	10^6

3.4 Suspensions feedstock for thermal spray: types and preparation

In order to obtain a coating of a given material by SPS, a wide variety of suspensions can be used as a feedstock, which can be classified as a function of the solvent nature or of the primary PSD.

The later characteristic has been extensively commented in the previous section, and the suspensions used in thermal spraying can be classified as:

- nanosuspensions, which present a monodal size distribution of nanoparticles;
- submicron suspensions, which exhibit a monodal size distribution of submicron-sized particles;
- submicron suspensions–nanosuspensions, which display a bimodal PSD formed by a mixture of submicronic and nanometric particles.

With respect to solvent nature, the suspensions can be classified into aqueous suspension and organic ones. It should be mentioned that not all organic solvents are adequate for plasma spraying: characteristics such as flash point, flammability range or explosive limits should be taken into account in order to avoid accidents during plasma spraying.

Nowadays, water and ethanol are the most commonly used solvents to prepare SPS feedstock. The main advantage of using an aqueous suspension consists of a safer handling and storage. However, water vapourization tends to cool down the plasma jet during spraying leading to a lower melting of the initial particles. On the contrary, ethanol vapourization leads to an increase in the plasma jet temperature and thus to a more effective particles heating and melting during coating deposition (Pawlowski, 2009).

Independently of the solvent nature, suspension preparation is usually done by the slurry route that consists of dispersing solid particles in a solvent. This process is especially critical in the case of nanosuspensions and should be well controlled in order to obtain well-dispersed suspensions with a low viscosity, a high stability and an adequate solid content (Fazio et al., 2008). Table 3.5 shows a general list of the various types of substances that can be used for dispersing powders.

Table 3.5 Different types of stabilizing agents

Substance	Mechanism	Examples
Potential-determining ions (pH)	Electrostatic repulsion	Acids (HCl), bases (NaOH and KOH)
Electrolyte (inorganic salts)	Electrostatic repulsion	Na ⁺ salts, hydroxides of NH ₄ ⁺ salts
Non-ionic surfactants	Adsorption	Oils, fatty acids, triglycerides, PEO
Ionic surfactants	Adsorption + electrostatic repulsion	Phosphate esters, quaternary NH ₄ ⁺
Adsorbed polymers	Steric hindrance	Block copolymers (PVB, PEO and PIB)
Adsorbed charged polymers	Steric hindrance + electrostatic repulsion	PAA, PMMA, PEI
Coupling agents	Adsorption + electrostatic repulsion	Alkoxides (TEOS, MTES, etc.)
Non-adsorbing polymers	Depletion stabilization	Non-ionic polymers

PEO, poly(ethylene oxide); PVB, poly(vinyl butyral); PIB, poly(isobutylene); PAA, poly(acrylic acid); PMMA, poly(methyl methacrylate); PEI, poly(ethylene oxide); TEOS, tetraethyl orthosilicate; MTES, methyltriethoxysilane.

Looking at the theoretical knowledge of the previous sections, a general and efficient methodology to optimize the suspension preparation should include the following steps (Vicent et al., 2011):

- (1) Starting raw material characterization (particles size, specific surface, crystalline phase composition, etc.).
- (2) Colloidal behaviour characterization. This step is necessary in order to optimize the dispersant nature and content as well as the suspension pH, and it is done through zeta potential measurements.
- (3) Rheological study. This study includes first the fabrication of different solid content suspensions, using the optimum dispersant content determined in the previous step and applying different homogenization times. Then the rheological behaviour of the different slurries is measured in order to determine the best preparation conditions.

This methodology has been successfully used to obtain highly concentrated suspension for spray drying, obtaining free-flowing nanostructured powders that can be successfully deposited by APS (Bordes et al., 2013; Vicent et al., 2013). These studies demonstrate the strong influence of rheology on the characteristics of the spray-dried granules and thus on the final coatings properties. A similar methodology should be used to develop optimized SPS feedstock and thus higher-performance SPS coatings.

Another efficient route to prepare concentrated nanosuspensions suitable for spray drying is the use of colloidal commercial suspensions as a dispersing medium to which dry particles are added. These particles can be of any particle size range, from micronic to submicronic or nanometric (Vicent et al., 2012b; Benavente et al., 2012). In general,

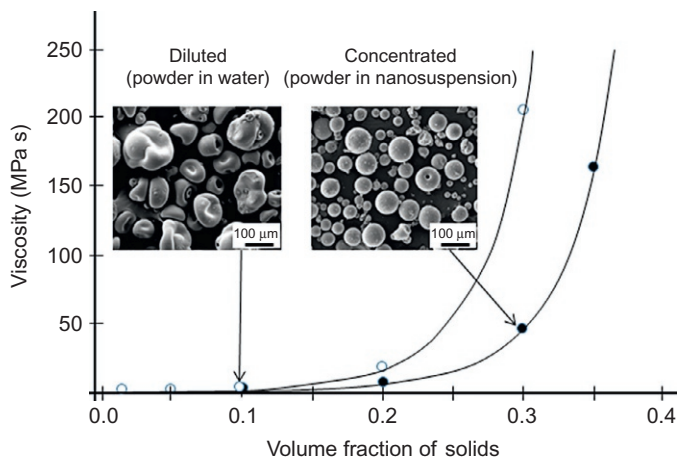


Figure 3.6 Evolution of viscosity with volume fraction of solids for suspensions prepared by dispersing a TiO_2 nanopowder (P25, Degussa-Evonik, Germany) in water, labelled as diluted or, in a colloidal TiO_2 suspension (W740X, Degussa-Evonik, Germany), labelled as concentrated. The microstructure of spray-dried granules obtained from these two suspensions is also shown.

commercial suspensions have solids loadings not higher than 10 vol.%. Concentrated suspensions are then prepared by adding new dry powders to the commercial colloidal suspension, which acts as a dispersing medium. This requires the previous dispersion of those powders by proper incorporation of deflocculants when needed. To illustrate the effect of this route, Figure 3.6 shows the viscosity versus volume fraction of solids curves of diluted, commercial suspensions of TiO_2 and concentrated suspensions prepared adding TiO_2 dry nanopowders to the commercial suspension. These concentrated suspensions maintain viscosity values low enough to be easily spray-dried. The resulting granules are also shown in Figure 3.6, where it can be seen that those obtained from the concentrated suspensions have much higher uniformity and less number of irregular and doughnut-shaped granules. The granules are micrometric but they are formed by nanoparticles, which have been reconstituted through a spray-drying process after optimization of the suspensions. The coatings produced from these granules maintain the nanostructure, combining the presence of molten zones, with semimolten ones together with some nanocrystals, as can be observed in Figure 3.7. The microstructure of the granules and the coatings obtained thereof are clearly influenced by the rheological properties of the feedstock, whose optimization can lead to the desired microstructural features.

3.5 Solution precursor feedstock for thermal spray: types and preparation

It has been demonstrated the suitability of using molecularly mixed amorphous powders as feedstock for the deposition of homogeneously distributed multicomponent ceramic coatings (Chen et al., 2009). Sometimes, colloidal suspensions are referred to as solutions, but this is not accurate; although particles in the suspension are very

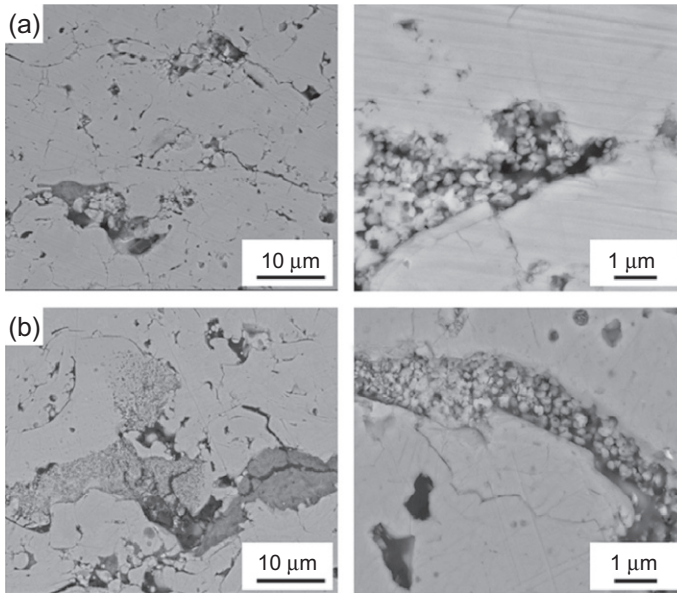


Figure 3.7 SEM microphotographs taken at two different magnifications showing the microstructure of coatings obtained from granules prepared at similar conditions using diluted (a) and concentrated (b) suspensions of nanoparticles. The melted zones co-exist with regions in which the nanoparticles have been retained, as observed in the larger magnification pictures.

small, they are completely developed. Solutions imply chemical precursors diluted in a medium and the further reaction to get the solid particles. Among these routes, the most common are co-precipitation reactions, hydrothermal routes and specific variations such as the citrate route or the use of nitrates. All these techniques are suitable for synthesizing nanoparticles that remain dispersed in the liquid (i.e., they are suspensions). Another route is the use of precursor solutions that need a thermal treatment before or after the deposition process to promote the interpenetration of the molecules until a network (gel) is formed. This is the basis of the sol–gel route, which can be used as a source of metals to produce core-shell-coated particles or as a continuous medium where particles can be incorporated.

In the case of solution precursor plasma spraying (SPPS), the feedstock solutions can be classified as a function of the solvent nature or of the kind of precursor used. In general, the liquid precursors are made of inorganic salts or metallo-organic compounds, which are dissolved in water, in an organic solvent (ethanol, isopropanol, etc.) or in a mixture of both. When water is used as solvent, it is generally possible to obtain higher precursor concentration (Tikkanen et al., 1997). Moreover, aqueous suspensions are cheaper and safer (from handling and storing point of view) than organic ones.

Some examples of solutions used to obtain SPPS coatings are given in Table 3.6. As can be observed in this table, SPPS process has been used to obtain coatings of a wide variety of material and the applications of SPPS include, among others, thermal barrier coatings, fuel cell and biomedical coatings.

Table 3.6 Examples of precursor solutions used in SPPS

Coating	Precursor	Solvent	Reference
TiO ₂	Titanium isopropoxide	Water	Chen et al. (2008)
NiO/YSZ	Nickel nitrate, yttrium nitrate, zirconyl nitrate	Ethanol	Michaux et al. (2010)
ZnO	Zinc acetate	Water + ethanol	Tummala et al. (2011)
Hydroxyapatite	Ca(NO ₃) ₂ , (NH ₄) ₂ HPO ₄	Water	Huang et al. (2011)
Bioglass	Tetraethyl orthosilicate, triethyl phosphate, calcium nitrate, sodium nitrate	Ethanol	Xiao et al. (2011)
YSZ	Zirconium acetate, yttrium nitrate	Water	Govindarajan et al. (2011)
La _{0.8} Sr _{0.2} MnO ₃	Lanthanum nitrate, strontium nitrate, magnesium nitrate	Water	Wang et al. (2011)
Lu ₂ Si ₂ O ₇	Lutetium nitrate, tetraethyl orthosilicate	Ethanol	Darthout and Gitzhofer (2011)
ZnFe ₂ O ₄	Zinc nitrate, ferric nitrate	Water	Dom et al. (2012)
Sm _{0.7} Sr _{0.3} Co _{3-d}	Samarium nitrate, strontium nitrate, cobalt nitrate	Water + ethanol	Li et al. (2012)
Eu:Y ₂ O ₃	Yttrium nitrate, europium nitrate	Water + isopropanol	Chen et al. (2012)
CdS	Cadmium chloride, thiourea	Water	Tummala et al. (2012)

3.6 Conclusions and further developments of suspension and solution precursor feedstock for thermal spray

In summary, engineering aspects of thermal spraying have attracted the interest of scientists, but the studies concerning the optimization of the feedstock have received less attention. In general, thermal spraying is largely performed using particulate feedstocks, with typical particle sizes in the range of micrometres. It is generally accepted that not only particles must have a relatively large size but also the shape is very important, as any edges and irregularities make the free flowing difficult and, thus, the spraying process. Consequently, spray drying offers clear advantages to prepare thermal spray feedstocks. Moreover, in the last years, the development of nanostructured materials has attracted great attention due to their improved mechanical and chemical properties. This is valid in many applications, products and shaping techniques, including the production of coatings by thermal spray. The possibility to retain

the nanostructure in the final coating is expected to lead to enhanced properties, as observed for bulk materials. Such growing interest for nanostructured thermally sprayed coatings has led to the development of nanostructured feedstocks. As the nanoparticles cannot be directly injected in the flame using conventional feeding systems, a usual technique to deposit them by thermal spray consists of preparing a suspension of nanoparticles and spray-dry it. In such case, the preparation of the feedstock needs special attention, since the dispersion of nanoparticulate systems is more difficult to achieve because of the high surface/volume ratio. This limits the solids loading of the suspension with low viscosity enough to allow an easy injection in the plasma when using suspensions or in the spray drier when using solid particles. Furthermore, the production conditions of the feedstock can have a strong effect in the characteristics of the resulting spray-dried powders. As a result, an adequate control and optimization of the rheological properties of the suspensions used for spray drying is crucial in order to increase the solids loading of those suspensions and thus to obtain spray-dried granules with much larger homogeneity, lower defects (being a classical example the formation of doughnut-shaped granules) and narrower size distribution, with the final objective to enhance the free flowing of the feedstock and improve the microstructural uniformity of the final coating.

Actually, in recent years, the efforts are being devoted to the development of nanoparticles suspensions, not only for spray drying but also for SPS, in which the feedstock is a suspension instead of a dry powder. This technique is especially interesting for nanometric- or submicron-sized feeding particles, as a stable, well-dispersed slurry is directly used as feedstock without any necessity for an intermediate and highly energy-consuming spray-drying stage. However, although some work is being carried out in this line, the interest usually lies on the product characteristics and the optimization of the slurry is not always considered as a key parameter to be controlled. However, an adequate control of the solids loading of the slurry, the type and content of deflocculant allowing the stability for long times, the pH, the uniformity in size and shape and the microstructure are required. Indeed, the adjustment of all these parameters will lead to a proper control of the characteristics of the thermal spray coatings.

In conclusion, the rheological behaviour of the suspensions and solutions used in thermal spray should always be carefully characterized. In fact, the final coating properties are influenced by the feedstock characteristics. As a consequence, thermal spray operators should be aware that an adequate control of properties such as viscosity and solids loading is necessary in order to guarantee a good reproducibility of the process and thus of the final coating properties.

Acknowledgments

This work has been supported by MINECO (Spain, contract MAT2012-38364-C03-1). Drs. Enrique Sánchez and Mónica Vicent (ITC-AICE, Spain) are gratefully acknowledged for their useful suggestions.

References

- Albertazzi, A., Rastelli, E., 1997. Evaluation of the thixotropy and yield stress of industrial ceramic slips using a torque-type viscometer. *Ceram. Acta* 9 (4), 5–11.
- Allen, T., 1997. Particle size measurement, Vol. 1. Powder Sampling and Particle Size Measurement, Chapman & Hall, London, UK.
- Aschauer, U., Burgos-Montes, O., Moreno, R., Bowen, P., 2011. Hamaker 2: a toolkit for the calculation of particle interactions and suspension stability and its application to mullite synthesis by colloidal methods. *J. Dispers. Sci. Technol.* 32, 470–479.
- Barnes, H.A., 1999. The yield stress—a review or “panta rei”—everything flows? *J. Non-Newtonian Fluid Mech.* 81, 133–178.
- Barnes, H.A., Walters, K., 1985. The yield stress myth? *Rheol. Acta* 24 (4), 323–326.
- Barnes, H.A., Hutton, J.F., Walters, K., 1989. *An Introduction to Rheology*. Elsevier, Amsterdam, Netherlands.
- Benavente, R., Salvador, M.D., Alcázar, C., Moreno, R., 2012. Dense nanostructured zirconia compacts obtained by colloidal filtration of binary mixtures. *Ceram. Int.* 38, 2111–2117.
- Bergström, L., 1996. Rheological properties of concentrated, non-aqueous silicon nitride suspensions. *J. Am. Ceram. Soc.* 79 (12), 3033–3040.
- Bergström, L., 1997. Hamaker constants of inorganic materials. *Adv. Colloid Interface Sci.* 70, 125–169.
- Bingham, E.C., 1922. *Fluidity and Plasticity*. McGraw-Hill Book Co, New York.
- Bordes, M.C., Vicent, M., Moreno, A., Moreno, R., Borrell, A., Salvador, M.D., Sánchez, E., 2013. Microstructure and photocatalytic activity of APS coatings obtained from different TiO₂ nanopowders. *Surf. Coat. Technol.* 220, 179–186.
- Bowen, P., 2002. Particle size distribution measurement from millimeters to nanometers and from rods to platelets. *J. Dispers. Sci. Technol.* 23, 631–662.
- Cao, X.Q., Vassen, R., Schwartz, S., Jungen, W., Tietz, F., Stöver, D., 2000. Spray-drying of ceramics for plasma-spray coating. *J. Eur. Ceram. Soc.* 20, 2433–2439.
- Chen, D., Jordan, E.H., Gell, M., Ma, X., 2008. Dense TiO₂ coating using the solution precursor plasma spray process. *J. Am. Ceram. Soc.* 91 (3), 865–872.
- Chen, D., Jordan, E.H., Gell, M., 2009. Suspension plasma sprayed composite coating using amorphous powder feedstock. *Appl. Surf. Sci.* 255 (11), 5935–5938.
- Chen, D., Gell, M., Jordan, E.H., Renfro, M.W., 2012. Solution precursor plasma spray Eu: Y₂O₃ phosphor coating. *Int. J. Appl. Ceram. Technol.* 9 (3), 636–641.
- Chuankian, D., Zatorski, R.A., Herman, H., Ott, D., 1984. Oxide powders for plasma spraying. The relationship between powder characteristics and coating properties. *Thin Solid Films* 118, 467–475.
- Cosgrove, T. (Ed.), 2005. *Colloid Science. Principles, Methods and Applications*. Blackwell Publishing Ltd., Oxford, UK.
- Darthout, E., Gitzhofer, F., 2011. Lutetium disilicate nanostructured coatings for environmental barrier application produced by solution plasma spraying. In: *Proceedings of the 20th International Symposium on Plasma Chemistry*. Available from: http://ispc20.plasmainstitute.org/my_ispc/papers/60.pdf (accessed 15.01.13).
- Davis, J.R. (Ed.), 2004. *Handbook of Thermal Spray Technology*. ASM International, Materials Park, OH, USA.
- Derjaguin, B., Landau, L., 1941. Theory of the stability of strongly charged lyophobic sols and of the adhesion of strongly charged particles in solutions of electrolytes. *Acta Physicochim. URSS* 14, 633.

- Dom, R., Sivakumar, G., Hebalkar, N.Y., Joshi, S.V., Borse, P.H., 2012. Deposition of nanostructured photocatalytic zinc ferrite films using solution precursor plasma spraying. *Mater. Res. Bull.* 47 (3), 562–570.
- Everett, D.H., 1988. *Basic Principles of Colloid Science*. The Royal Society of Chemistry, London, UK.
- Fauchais, P., Vardelle, A., 2012. Solution and suspension plasma spraying of nanostructure coatings. In: Jazi, H.S. (Ed.), *Advanced Plasma Spray Applications*. Available from: http://cdn.intechopen.com/pdfs/32980/InTech-Solution_and_suspension_plasma_spraying_of_nanostructure_coatings.pdf (accessed 14.01.13).
- Fauchais, P., Etchart-Salas, R., Rat, V., Coudert, J.F., Caron, N.K., Wittmann-Ténèze, K., 2008. Parameters controlling liquid plasma spraying: solutions, sols, or suspensions. *J. Therm. Spray Technol.* 17 (1), 31–59.
- Fauchais, P., Montavon, G., Bertrand, G., 2010. From powders to thermally sprayed coatings. *J. Therm. Spray Technol.* 19, 56–80.
- Fauchais, P., Montavon, G., Lima, R., Marple, B.R., 2011. Engineering a new class of thermal spray nano-based microstructures from agglomerated nanostructured particles, suspensions and solutions: an invited review. *J. Phys. D Appl. Phys.* 44, 093001.
- Faure, B., Lindeløv, J.S., Wahlberg, M., Adkins, N., Jackson, P., Bergström, L., 2010. Spray drying of TiO₂ nanoparticles into redispersible granules. *Powder Technol.* 203, 384–388.
- Fazio, S., Guzmán, J., Colomer, M.T., Salomoni, A., Moreno, R., 2008. Colloidal stability of nanosized titania aqueous suspensions. *J. Eur. Ceram. Soc.* 28, 2171–2176.
- Goodwin, J.W., 1990. Rheology of ceramic materials. *Am. Ceram. Soc. Bull.* 69 (11), 1694–1698.
- Govindarajan, S., Dusane, R., Vi, S., Joshi, S.V., 2011. In situ particle generation and splat formation during solution precursor plasma spraying of yttria-stabilized zirconia coatings. *J. Am. Ceram. Soc.* 94 (2), 4191–4199.
- Gutiérrez, C.A., Moreno, R., 2001. Influence of slip preparation and casting conditions on aqueous tape casting of Al₂O₃. *Mater. Res. Bull.* 36 (6), 2059–2072.
- Gutiérrez, C.A., Sánchez-Herencia, A.J., Moreno, R., 2000. Plástico o pseudoplástico? Métodos de determinación y análisis del punto de fluidez de suspensiones cerámicas. *Bol. Soc. Esp. Ceram. Vidrio* 39 (1), 105–117.
- Hiemenz, P.C., 1997. *Principles of Colloid and Surface Chemistry*, third ed. Marcel Dekker, New York.
- Hogg, R., Healy, T.W., Fuerstenau, D.W., 1966. Mutual coagulation of colloidal dispersions. *Trans. Faraday Soc.* 62, 1638.
- Huang, T., Xiao, Y., Wang, S., Huang, Y., Liu, X., Wu, F., Gu, Z., 2011. Nanostructured Si, Mg, CO₃²⁻ substituted hydroxyapatite coatings deposited by liquid precursor plasma spraying: synthesis and characterization. *J. Therm. Spray Technol.* 20 (4), 829–836.
- Hunter, R.J., 1981. *Zeta Potential in Colloid Science*. Academic Press, New York.
- Hunter, R.J., 1987. *Foundations of Colloid Science*, vol. 1. Clarendon Press, Oxford, UK.
- Israelachvili, J.N., 1985. *Intermolecular and Surface Forces*. Academic Press, London, UK.
- Killinger, A., Gadow, R., Mauer, G., Guignard, A., Vaßen, R., Stöver, D., 2011. Review of new developments in suspension and solution precursor thermal spray processes. *J. Therm. Spray Technol.* 20 (4), 677–695.
- Knight, R., Smith, R.W., 1998. Thermal spray forming of materials. In: *Powder Metal Technologies and Applications*. ASM Handbook, vol. 7. ASM International, Materials Park, OH, USA, pp. 408–419.
- Lange, F.F., 1989. Powder processing science and technology for increased reliability. *J. Am. Ceram. Soc.* 72 (1), 3–15.

- Larson, R.G., 1999. *The Structure and Rheology of Complex Fluids*. Oxford University Press, New York, USA.
- Lewis, J.A., 2000. Colloidal processing of ceramics. *J. Am. Ceram. Soc.* 83, 2341–2359.
- Li, C.X., Liu, S., Zhang, Y., Li, C.J., 2012. Characterization of the microstructure and electrochemical behaviour of $\text{Sm}_{0.7}\text{Sr}_{0.3}\text{Go}_{3-\delta}$ cathode deposited by solution precursor plasma spraying. *Int. J. Hydrog. Energy* 37, 13097–13102.
- Lima, R.S., Marple, B.R., 2007. Thermal spray coatings engineered from nanostructured ceramic agglomerated powders for structural, thermal barrier and biomedical applications: a review. *J. Therm. Spray Technol.* 16 (1), 40–63.
- Liu, D.M., 2000. Particle packing and rheological property of highly-concentrated ceramic suspensions: ϕ_m determination and viscosity prediction. *J. Mater. Sci.* 35, 5503–5507.
- Malkin, A.Y., 1994. *Rheology Fundamentals, Fundamental Topics in Rheology*. ChenTech Publ, Ontario, Canada.
- Masters, K., 1985. *Spray Drying Handbook*, fourth ed. Wiley, New York.
- Michaux, P., Montavon, G., Grimaud, A., Denoirjean, A., Fauchais, P., 2010. Elaboration of porous NiO/8YSZ layers by several SPS and SPPS routes. *J. Therm. Spray Technol.* 19 (1–2), 317–327.
- Moreno, R., 2005. *Reología de Suspensiones Cerámicas*. CSIC, Madrid, Spain.
- Napper, D.H., 1983. *Polymeric Stabilization of Colloidal Dispersions*. Academic Press, London, UK.
- Negre, F., Sánchez, E., 1996. Advances in spray-dried pressing powder processes in tile manufacture. In: Henkes, V.E., Onoda, G.Y., Carty, W.M. (Eds.), *Science of Whitewares*. American Ceramic Society, Ohio, pp. 169–181.
- Parks, G.A., De Bruyn, P.L., 1962. The zero point of charge of oxides. *J. Phys. Chem.* 66, 967–972.
- Pawlowski, L., 2009. Suspension and solution thermal spray coatings. *Surf. Coat. Technol.* 203, 2807–2829.
- Pugh, R.J., Bergström, L. (Eds.), 1994. *Surface and Colloid Chemistry in Advanced Ceramics Processing*. Marcel Dekker Inc, New York, USA.
- Rahaman, M.N., 1995. *Ceramic Processing and Sintering*, second ed. Marcel Dekker Inc, New York.
- Reed, J.S., 1995. *Introduction to the Principles of Ceramic Processing*, second ed. John Wiley & Sons, New York.
- Santacruz, I., Annapoorani, K., Binner, J., 2008. Preparation of high solids content nano zirconia suspensions. *J. Am. Ceram. Soc.* 91, 398–405.
- Santacruz, I., Nieto, M.I., Binner, J., Moreno, R., 2009. Wet forming of concentrated nano BaTiO₃ suspensions. *J. Eur. Ceram. Soc.* 29, 881–886.
- Schramm, G., 1984. *A Practical Approach to Rheology and Rheometry*. Haake GmbH, Karlsruhe, Germany.
- Sigmund, W.M., Bell, N.S., Bergström, L., 2000. Novel powder-processing methods for advanced ceramics. *J. Am. Ceram. Soc.* 83, 1557–1574.
- Tadros, T.F., 2010. *Rheology of Dispersions*. Wiley-VCH Verlag & Co, Germany.
- Tikkanen, J., Gross, K.A., Berndt, C.C., Pitkänen, V., Keskinen, J., Ragha, S., Rajala, M., Karthikeyan, J., 1997. Characteristics of the liquid flame spray process. *Surf. Coat. Technol.* 90, 210–216.
- Tummala, R., Guduru, R.K., Mohanty, P.S., 2011. Nanostructured zinc oxide coatings via solution precursor plasma spray technique. *Mater. Res. Bull.* 46, 1276–1282.
- Tummala, R., Guduru, R.K., Mohanty, P.S., 2012. Solution precursor plasma deposition of nanostructured CdS thin films. *Mater. Res. Bull.* 47 (3), 700–707.

- Verwey, E.J.W., Overbeek, J.Th.G., 1948. *Theory of the Stability of Lyophobic Colloids*. Elsevier, Amsterdam.
- Vicent, M., Sánchez, E., Santacruz, I., Moreno, R., 2011. Dispersion of TiO₂ nanopowders to obtain homogeneous nanostructured granules by spray-drying. *J. Eur. Ceram. Soc.* 8, 1413–1419.
- Vicent, M., Molina, T., Sánchez, E., Moreno, R., 2012a. Dispersion and reaction sintering of alumina–titania mixtures. *Mater. Res. Bull.* 47, 2469–2474.
- Vicent, M., Sánchez, E., Moreno, A., Moreno, R., 2012b. Preparation of high solids content nanotitania suspensions to obtain nanostructured spray-dried powders for atmospheric plasma spraying. *J. Eur. Ceram. Soc.* 32, 185–194.
- Vicent, M., Bannier, E., Benavente, R., Salvador, M.D., Molina, T., Moreno, R., Sánchez, E., 2013. Influence of the feedstock characteristics on the microstructure and properties of Al₂O₃–TiO₂ plasma-sprayed coatings. *Surf. Coat. Technol.* 220, 74–79.
- Walton, D.E., Mumford, C.J., 1999. Spray dried products—characterization of particle morphology. *Trans. Inst. Chem. Eng.* 77, 21–38.
- Wang, X., Li, C.X., Li, C.J., Tian, L., Yang, G., 2011. Microstructure and electrochemical behavior of La_{0.8}Sr_{0.2}MnO₃ deposited by solution precursor plasma spraying. *Rare Met. Mater. Eng.* 40 (11), 1881–1886.
- Wigren, J., de Vries, J.-F., Greving, D., 1996. Effect of powder morphology, microstructure, and residual stresses on thermal barrier coating thermal shock performance. In: Berndt, C.C. (Ed.), *Thermal Spray: Practical Solutions for Engineering Problems*. ASM International, USA, pp. 855–861.
- Xiao, Y., Song, L., Liu, X., Huang, Y., Huang, T., Chen, J., Wu, Y., Wu, F., 2011. Bioactive glass-ceramic coatings synthesized by the liquid precursor plasma spraying process. *J. Therm. Spray Technol.* 20 (3), 560–568.
- Zainuddin, M.I., Tanaka, S., Furushima, R., Uematsu, K., 2011. Influence of particles packing in granules on the particles orientation in compacts. *J. Eur. Ceram. Soc.* 31, 3–11.

Status and future trends in suspension spray techniques

4

A. Killinger

Abbreviations

APS	atmospheric plasma spraying
CVD	chemical vapor deposition
DC	direct current
DE	deposition efficiency
DEG	diethylene glycol
EB-PVD	electron beam physical vapor deposition
GDC	gadolinia-doped ceria
HVOF	high-velocity oxygen fuel spraying
HVSFS	high-velocity suspension flame spraying
HA	hydroxyapatite $\text{Ca}_5(\text{PO}_4)_3(\text{OH})$
ICP	inductively coupled plasma
IFKB	Institut für Fertigungstechnologie keramischer Bauteile
LSM	lanthanum strontium manganite
<i>Oh</i>	the Ohnesorge number
PEM	polymer electrolyte membrane
<i>Re</i>	the Reynolds number
RF	radio frequency
ScSZ	scandia-stabilized zirconia
SDC	samarium-doped ceria
SEM	scanning electron microscope
SBF	simulated body fluid
SOFC	solid oxide fuel cell
SPS	suspension plasma spraying
SPPS	solution precursor plasma spraying
<i>St</i>	the Stokes number
TBC	thermal barrier coating
TCP	tricalcium phosphate $\text{Ca}_3(\text{PO}_4)_2$
TTCP	tetracalcium phosphate $\text{Ca}_4(\text{PO}_4)_2\text{O}$
TS	thermal spraying
VPS	vacuum plasma spraying
<i>We</i>	the Weber number
YSZ	yttria-stabilized zirconia

4.1 Introduction: Suspension spraying

Ordinary thermal spray techniques use feedstocks in a solid form. Following modern practice and common standards, these are powders, wires, or rods. However, thermal spray techniques are not at all restricted to solid feedstocks. Plasma CVD processes (also named reactive plasma spraying) were introduced in the 1980s to synthesize diamond films on various high-temperature substrates like cemented carbides. Reactive gases (H_2 and CH_4) were inserted into a DC plasma torch working under vacuum conditions (Deuerler et al., 1999). As soon as chemical precursors were available on the market, liquid precursor plasma and combustion spray techniques were evaluated to produce ceramic coatings. Bouyer et al. (1999) used silanes as a precursor material to deposit SiC coatings using RF inductive plasma spraying technique.

Suspension spraying expands the thermal spray techniques by using a liquid feedstock in form of a suspension. Regarding the process route, it is closely linked to the solution spraying where a liquid containing a chemical precursor is used as a feedstock (Pawlowski, 2009). An essential motivation and attraction for suspension spraying lies in the degree of freedom in the choice of particle sizes, mixtures, and chemical composition of the liquid phase and the solid phase and their combinations. Suspension properties play, as any feedstock in thermal spraying (TS), a crucial role for the spray process itself and the resulting coating structure. However, the complex nature of a suspension consequently leads to a rather manifold interaction when introduced into a hot gas stream of a combustion or plasma spray torch. Liquid and solid phases show distinguishable effects and hot gas interactions such as evaporation and postcombustion (when organic liquids are involved), agglomeration, melting, and evaporation of the solid particles.

Especially the liquid phase significantly alters and disturbs the spray process, that is, the thermal and kinetic characteristics of the expanding gas jet after injection has taken place. This interference is one of the key problems that developers have to deal with and that also concern the field of solution spraying (this chapter in this book). The in-flight behavior of a suspension significantly differs from ordinary spray materials, for instance, solid powders. Whereas in an ordinary spray process any powder particle more or less converts into a single molten droplet, in suspension spraying, many effects contribute to the final droplet formation.

Suspension properties play an important role in the spray process and are closely linked to their fabrication procedure. All aspects concerning this subject will be described in Chapter 8 of this book. Particle size is another important factor that strongly influences suspension properties. One of the great potentials of suspension spraying is the possibility to use very small particle sizes that can easily reach nanometer scale. The active surface of nanopowders can tremendously favor the formation of very stable agglomerates that cannot be destroyed by means of ordinary milling techniques. In fact, such suspensions do not carry nanoparticles at all, but agglomerates whose volume is some orders of magnitude larger than the originating particles. For further reading, please refer to Chapter 8 in Part II of this book.

Probably the strongest motivation in developing suspension and solution spray techniques is the aim to process submicron powders and nanopowders (particles

diameter < 100 nm) to form finely structured or even nanostructured coatings with an improvement of their mechanical, thermal, and chemical properties for numerous technical and industrial applications; see given example in [Figure 4.1](#). As soon as nanomaterials became available through several synthesis technologies in the early 1990s of the last century ([Gell, 1995](#)), thermal spray engineers and scientists were searching for technical solutions to successfully process this kind of materials. One approach was the development of nanoagglomerated spray powders using the spray-dry agglomeration route. Cermet materials like tungsten carbide–cobalt (WC–Co) containing nanocarbides could be successfully sprayed to form nanostructured coatings revealing superior mechanical properties. The advantage of this approach was the fact that no changes in the feeder design had to be developed.

However, suspension plasma spraying (SPS) processes were rapidly developing in parallel. [Gitzhofer et al. \(1994\)](#) published their SPS patent based on an inductively coupled plasma (ICP) spray device. The process was dedicated for coating deposition

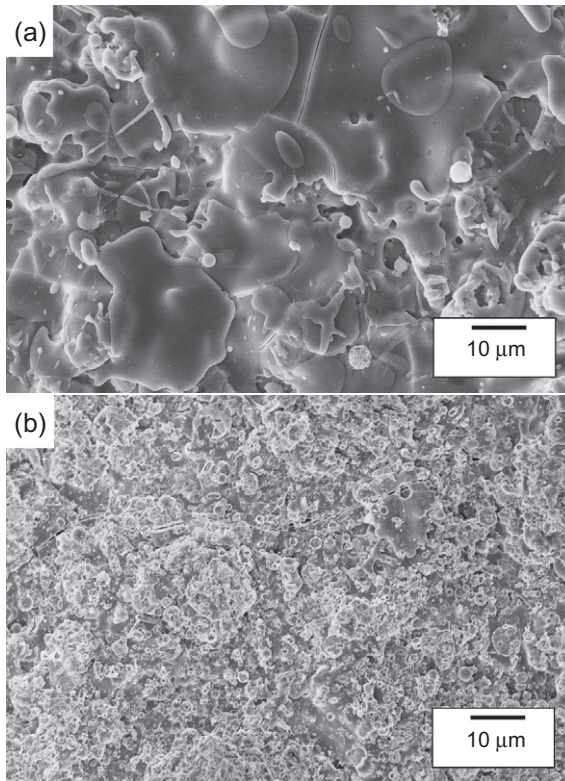


Figure 4.1 Comparison of coating surface of APS and HVSFS HA coatings in SEM. (a) APS process using HA powder with $d_{50} = 40$ μm. (b) HVSFS coating using a nanosized HA feedstock with $d_{50} = 50$ nm.

Courtesy of IFKB, University of Stuttgart, Germany.

as well as for powder production. The manufacturing of calcium phosphate-based bio-ceramic powders like hydroxyapatite for biomedical applications is described as a possible application, for instance, in [Bouyer et al. \(1997a\)](#). The motivation for using the RF plasma discharge process was the absence of any contamination risks stemming from electrodes (tungsten and copper) as it may occur in DC plasma spraying.

Since then, numerous activities have been undertaken to evaluate SPS and SPPS processes, mainly in the field of TBC and SOFC research. Soon, it was recognized that SPS coatings revealed a unique microstructure that could not be achieved by ordinary spray processes like plasma and combustion flame spraying. In parallel, spraying of liquid precursors for the fabrication of nanoscale powders and deposits was investigated, for example, by [Karthikeyan et al. \(1997\)](#) and [Tikkanen et al. \(1997\)](#).

At the beginning of the new millennium, suspension spraying—based on the HVOF process—came into the focus of several research groups. [Gadow et al. \(2005\)](#) filed their patent about an HVOF torch featuring an axial suspension injection system, and they were among the first to introduce the high-velocity suspension flame spraying (HVSFS) process and to spray nanosized oxide ceramic feedstocks using this technique ([Killinger et al., 2006](#)). Since then, SPS and HVSFS were further developing in parallel.

4.2 The suspension spray process

During the last decades, numerous review articles have been worked out by several authors discussing virtually any aspect of suspension and solution spraying. The following reviews have been considered for this chapter and should be consulted if a further study of the subject is required.

[Fauchais \(2008\)](#) and [Pawlowski \(2008, 2009\)](#) presented their reviews and discussed physical principles of suspension and solution spraying with nanosized feedstocks, mainly based on oxide ceramics. Especially phenomena occurring in SPS processes are discussed in depth by [Fauchais and Vardelle \(2012\)](#). The publication presents experimental data about the liquid plasma interaction during injection, including droplet fragmentation and vaporization using imaging techniques. General review papers covering SPS and HVSFS processes along with their potential applications were given by [Fauchais et al. \(2011\)](#) and [Killinger et al. \(2011\)](#). To describe the suspension spray process in more detail, a breakup of the process in single process steps is reasonable. These process steps include (a) injection of the suspension, (b) suspension flame interaction, and (c) coating formation and coating structure. These steps will be discussed in the following sections.

4.2.1 Suspension injection

Injection of the suspension into a high enthalpic plasma jet or a flame current is the first crucial step in the spray process. Unlike in powder spraying where solid particles, accelerated in a feeder gas, enter the gas stream, suspension injection basically offers

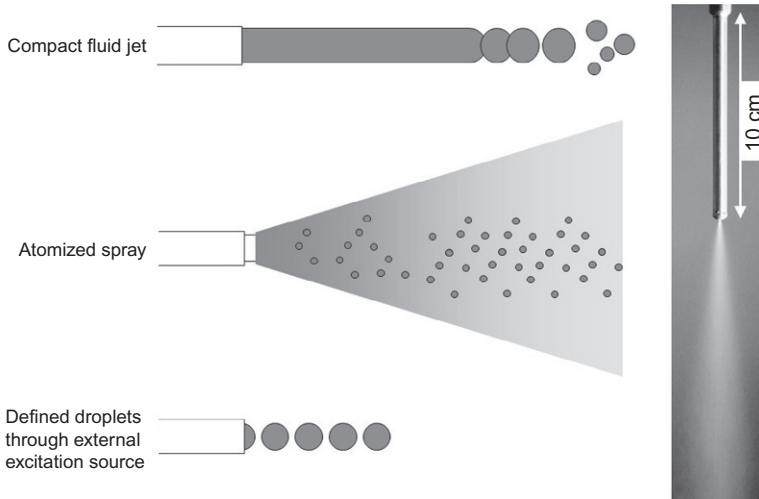


Figure 4.2 (left) Basic concepts of suspension injection due to the application of suitable injection nozzles. (right) HVSFS injector with conical nozzle atomizing water. Courtesy of IFKB, University of Stuttgart, Germany.

several alternative ways to inject the liquid into the gas stream. Basically controlled by the liquid pressure and the nozzle geometry, either the liquid stream may form a compact liquid jet or it may be atomized to form small droplets or it is fragmented into distinct droplets of equal size at a constant frequency by means of an external mechanical excitation source; refer to [Figure 4.2](#). The concept of using a continuous jet printer device driven by a piezoelement to form single droplets was already demonstrated by [Blazdell and Kuroda \(2000\)](#) for the SPS process.

The ordinary injector geometry comprises a tube with a small bore forming the nozzle exit (turbulent nozzle). Under laminar operation conditions, a compact liquid jet is formed. By either reducing the nozzle diameter or increasing liquid pressure to critical values (the Reynolds number Re typically exceeds values of 1000 – 3000), a turbulent stream is formed implying high shear forces that lead to an atomization of the liquid. It should be pointed out that for a given nozzle geometry, the degree of atomization is a function of the liquid pressure. More sophisticated nozzles allow a more precise control of the degree of atomization by including a control cone or needle. Using this configuration, the degree of atomization can be independently adjusted within a certain mass flow range. By using two fluid nozzles, the degree of atomization is controlled by separately feeding an atomization gas in parallel to the suspension feeding line. Thus, the degree of atomization can be chosen independently from liquid pressure. However, the fabrication of such miniaturized injectors showing complex geometries is rather elaborate.

The theory of spray formation and liquid atomization distinguishes two types of atomization in a spray: primary atomization, in or near the nozzle exit, and secondary atomization, which is the aerodynamic breakup further downstream (discussed in the

following section). Primary atomization basically depends on liquid geometry, relative velocity of liquid to surrounding gas and gas/liquid properties such as density, viscosity, and (liquid) surface tension. The main forces acting on the liquid are inertia, viscosity, and surface tension. Their interaction is described by two important dimensionless numbers, the Reynolds (Re) and the Weber (We) number. The We number expresses the ratio of the deforming inertia force of the medium to surface tension of the droplet. In general, high values for both (Re and We) promote a more rapid and finer atomization. For water (w) and ethanol (e), typical values can be found in the literature; they are in the range of $Re = 1500$ (w), 3300 (e) and $We = 15$ (w), 150 (e) (Dai and Faeth, 2001). A third dimensionless number, the Ohnesorge (Oh) number, which relates viscous and surface tension forces, allows a more precise discussion when considering highly viscous fluids. For further reading, refer to Nasr et al. (2002) and Richter (2004).

Depending on the nature of the gas stream, atomization of the suspension is not always reasonable. Considering high enthalpic plasma jets, as it is the case in standard SPS processes with radial suspension injection, gas viscosity of the ionized gas is reasonably high, and small droplets will not be able to enter into the center of the plasma stream due to their low inertial forces. Those droplets will thus follow the gas stream in the comparatively cold fringe, not sufficiently heating the solid particles within the liquid. They will end up as overspray dust or will be incorporated in the coating in form of unmolten or resolidified agglomerates, mainly increasing the porosity level of the coating.

Cooling of the suspension nozzle, by either a gas or a closed water circuit, can significantly increase operational stability in SPS and HVSFS. Especially in HVSFS applications, where an internal axial injection of the suspension into a combustion chamber is required, an independent jacket cooling will prevent the suspension from clogging due to overheating of the nozzle, which is directly facing the combustion chamber entrance. This may also occur in high-power plasma spray devices where the (plasma facing) feeder nozzle heats up to a critical level.

4.2.2 Suspension–gas interaction

Interaction of a suspension with the hot gas current in a combustion or plasma jet is much more complex than particle flame interaction observed in ordinary powder combustion/plasma spray processes. The presence of the liquid dispersant has a tremendous impact on the hot gas stream. First of all, evaporation will take place, leading to a significant energy consumption within the flame/plasma jet depending on the evaporation enthalpy of the liquid. As evaporation occurs rather rapidly, disturbance of the gas stream will take place. In case of organic liquids, its combustion will occur farther downstream in the flame or plasma jet. This way some of the energy, consumed during evaporation process, is fed back into the process. No doubt, the role of the solvent is eminent for spray and particle forming in both combustion and plasma spray processes.

Droplet formation is the second phenomenon that has to be considered in suspension spray processes. As the liquid enters the hot gas stream, a further fragmentation, called the aerodynamic breakup, will occur. Due to aerodynamic forces acting on the

liquid, the droplet is dynamically deformed and excited to oscillation until a further defragmentation may occur. Mainly depending on the value of the We number (refer to previous section), a liquid droplet typically encounters the following breakup mechanisms:

$We \approx 12$:	Vibrational breakup
$12 < We < 50$:	Bag breakup. Deformation of the droplet to a bag-like structure that is stretched in flow direction
$50 < We < 100$:	Umbrella breakup. Very similar to bag breakup
$100 < We < 350$:	Sheet stripping breakup. Thin sheets are drawn from the periphery of the deforming droplet
$We > 350$:	Catastrophic breakup. Droplet is instantly fragmented in multiple stages

Some of the breakup mechanisms are illustrated in [Figure 4.3](#). Especially in highly ionized plasma gases, more complex interaction occurs due to the acting of electrostatic and electrodynamic forces of ionized gas atoms/molecules with the droplet surface.

Parallel to droplet formation, several processes within the suspension droplet body take place. Temperature gradients lead to thermodiffusion effects; density and surface tension gradients can lead to microcirculation of the liquid within the droplet. At lower solid content levels, this microcirculation can lead to a concentration of solid particles near the outer boundary. This way, liquid and vapor transport outward from the droplet center can be hindered favoring the formation of hollow spheres. This can be especially observed in suspensions containing submicron particles/agglomerates or nanoparticles/agglomerates (also refer to next section and [Figure 4.6](#)).

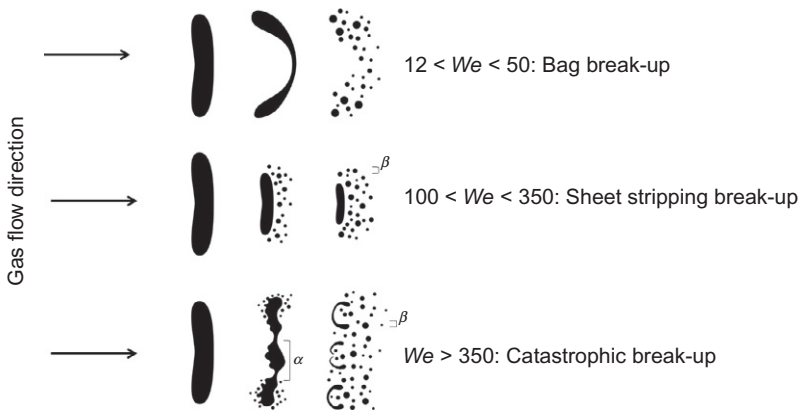


Figure 4.3 Examples of droplet breakup mechanisms due to aerodynamic forces acting on the droplet plotted for different We numbers, according to Ashgriz (2011). α , The *Rayleigh–Taylor instability*: inertia of the denser fluid opposes the system acceleration. β , The *Kelvin–Helmholtz instability*: viscous forces caused by the relative motion of the fluids.

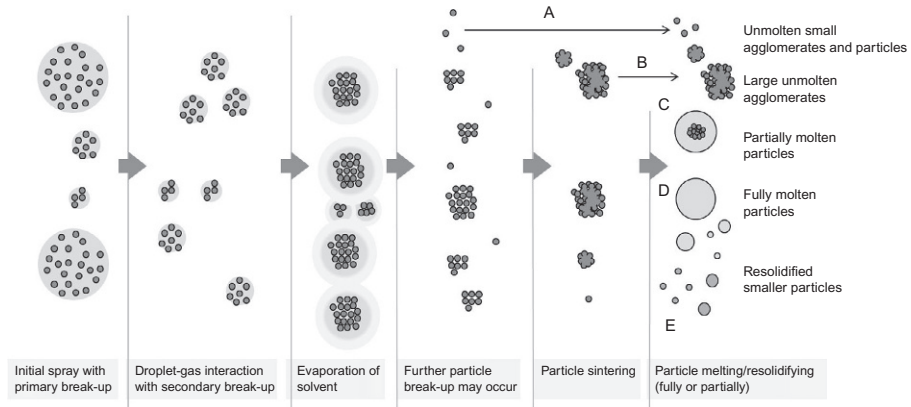


Figure 4.4 General conception of the droplet formation process in thermal suspension spraying.

Eventually, all liquid has evaporated and only the solid particles remain from the former droplet, forming an agglomerate. Melting of the particle material starts from the outer zone of the particle. Depending on the heat flux and time of flight that is available for further particle heating, a complete or partial melting will occur. This will basically lead to several types of droplets/particles hitting the surface of the substrate. In [Figure 4.4](#), some of the possible formation paths are illustrated schematically: (A) unmelted particles and small agglomerates, (B) “spray-dried” large agglomerates that did not melt at all, (C) partially molten droplets still containing solid particles/agglomerates within the melt, (D) fully molten droplets, and (E) resolidified particles. Which formation path a particle will follow depends on the injection system and the way the suspension is atomized (or not), determining the initial droplet size distribution as well as the flight path the droplet follows within the combustion flame/plasma jet. The resulting coating structure is discussed in the following section.

4.2.3 Coating formation and achieved microstructures

Basically, coating formation works similarly as in ordinary thermal spray processes, as it mainly consists of molten droplets deforming during impact and building up the layered structure. However, due to the fact that size of the droplet volume can be a factor of 10^3 – 10^4 smaller than in ordinary TS processes, a number of phenomena are observed, not known from ordinary TS. As discussed in the last section, the spray jet may contain many different types of molten, semimolten, unmolten, or resolidified particle types. Large agglomerates that are fully molten may behave more or less as in a standard TS process, forming a solid and flattened splat structure. An example is given in [Figure 4.5](#) where nanosized TiO_2 (P25, 21 nm; ethanol, 10 wt%) was sprayed on glass-ceramic substrate in a kind of wipe test using HVFSF: Small particles (in the diameter range of 100 nm), however, having a low inertia will not deform when hitting the surface but keep their spherical shape due to the dominating surface tension.

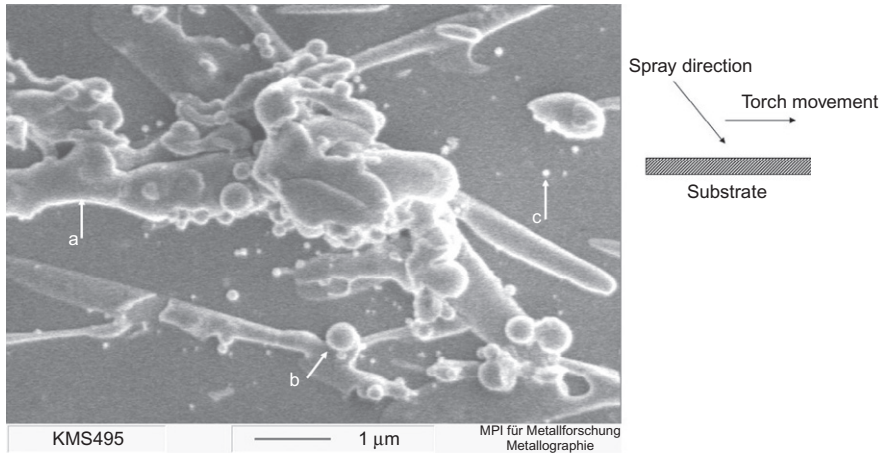


Figure 4.5 Wipe testing using HVSFS to spray a suspension containing nanosized TiO₂ (P25, 21 nm; ethanol, 10 wt%) onto a glass-ceramic substrate in order to visualize single particle morphology: a, large flattened irregular splats; b, small disk-shaped splats; c, very small globular particles, probably stemming from primary nanograins or small aggregates. Courtesy of IFKB, University of Stuttgart, Germany.

Larger particles (in the diameter range of 500 nm) will deform to a rather regular disk without any splashing. Only larger droplets (having diameters $>1\ \mu\text{m}$), stemming from large agglomerates, show the irregular nature of splashed splats.

As described at the end of the previous section, many different types of particles are formed in the hot gas jet, hitting the substrate surface and contributing to the microstructure. Depending on process parameters and suspension properties, a nonnegligible amount of resolidified or semimolten particles can be incorporated in the coating. Semimolten droplets and molten hollow spheres can lead to a doughnutlike splat structure exhibiting either a cavity in the center or residuals of unmolten primary particle agglomerates as discussed, for instance, by [Pawłowski \(2008\)](#). This is illustrated in [Figure 4.6](#) together with an example of single lamellae formed on a glass surface (suspension, TiO₂; particle size, 20 nm; 20 wt% in isopropanol/water 30/70 wt%; sprayed via HVSFS).

In suspension spraying, particles commonly are much smaller than in ordinary spray processes, especially when submicron or nanosized powders are used. As a consequence, they show a different behavior in gas currents not observed in ordinary spray processes, described, for instance, by the dimensionless Stokes number St . Small particles with $St \ll 1$ tend to follow the gas current very easily. This can lead to several phenomena during coating formation. Observed mainly in HVSFS processes, distinct defects in the coating may occur like the one displayed in [Figure 4.7](#). These defects grow near asperities, like surface roughness or agglomerate deposits, during spray process. Small particles follow the gas stream tangentially to the surface, eventually colliding with the asperity and forming a deposit. The defect grows and collects more and more particles traveling in parallel to the substrate

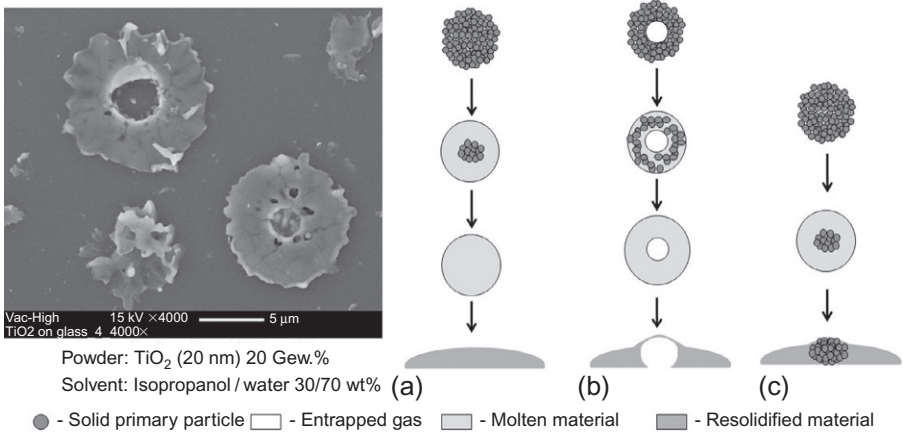


Figure 4.6 Suggested formation mechanisms of donut-shaped splats. (left) SEM image of collected individual TiO₂ splats on a glass substrate, having a central void sprayed using HVSFS. (right) Suggested formation paths of splats: full melting (case a); voids formed due to entrapped gas (case b: air, solvent vapour); remaining unmolten particles that are rebound from surface (case c). SEM image courtesy of University of Stuttgart, Germany.

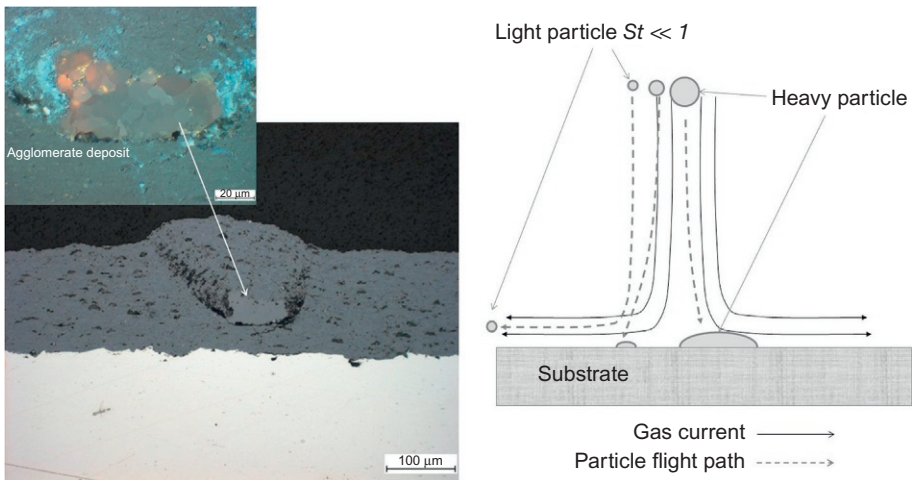


Figure 4.7 Formation of a cone-shaped defect in an HVSFS coating. (left) Defect is initiated at an agglomerated deposit. Suspension: TiO₂ (25 nm, 10 wt%, solvent: ethanol). Substrate: mild steel. Courtesy of IFKB, University of Stuttgart, Germany. (right) Suggested formation mechanism.

surface finally forming the conical defect through the entire coating. As an extreme case, coatings with a columnar structure can be formed resembling those observed in PVD processes. Especially in SPS when high-power torches like Triplex (Sulzer Metco, Wohlen, Switzerland) and Mettech Axial III (Northwest Mettech Corp., Vancouver, Canada) are used, it was demonstrated by several research groups that by varying the plasma parameters, all kinds of coating morphologies can be achieved, ranging from columnar PVD-like structures to dense structures with high segmentation crack densities (Kaßner et al., 2008a; Tang et al., 2011). Examples for SPS coatings showing this features are given in Section 4.4.1; refer to Figure 4.13.

Overall porosity structure of SPS and HVSFS ceramic coatings strongly depends on operational conditions and involved materials. Any porosity level, from dense coating layers to open porous structures, can be produced. In general, with HVSFS, it is possible to form fully dense coatings, due to the high particle velocity that can be achieved. However, high-power plasma torches like the Mettech Axial III (Northwest Mettech Corp., Vancouver, Canada) also achieve reasonable particle velocities and form dense coatings (see HVSFS and SPS application examples in Section 4.4.3). On the other hand, SPS is capable to form coatings showing a submicron porosity network. However, depending on substrate geometry and process characteristics, it is often observed in both processes (SPS and HVSFS) that overspray effects can lead to the formation of pronounced interlayered porosity zones, a phenomenon that is not always desired. Two examples of suspension-sprayed alumina coatings are given in Figure 4.8. The dense coating was sprayed using HVSFS with axial injection. Same suspension was sprayed with SPS using an F6 torch with radial injection, exhibiting a fine porosity structure.

In SPS processes, when spraying nanosized feedstocks, it has been found that a shorter spraying distance as compared to APS favors postsintering of small particles in the coating due to the increased heat flux. This often leads to an overall stabilization of the rather porous coating structure. The effects of postsintering are discussed in depth, for instance, by Latka et al. (2010) in case of plasma-sprayed titanium oxide and hydroxyapatite. It was found that it is possible to develop sinter necks having the relative size of 10% of particle diameter during the thermal cycles that typically occur in SPS.

Regarding deposition efficiency (DE) and deposition rates, SPS and HVSFS can reach comparable values compared to their standard process counterparts (APS and HVOF) but are lower in many practical cases (so far). However, DE strongly depends on many details of the spray process, that is, properties of the suspension (solid content, chemical composition of the solid and the solvent, injection method, torch type used, etc.).

4.2.4 Coating properties

Concerning achievable coating thickness of SPS and HVSFS coatings, at least for oxide ceramics and phosphate-based biomaterials (hydroxyapatite, tricalcium phosphate, and others), it can be stated that a closed coating structure already starts at 10 μm or so. However, it is difficult to define an upper limit. SPS coatings (for

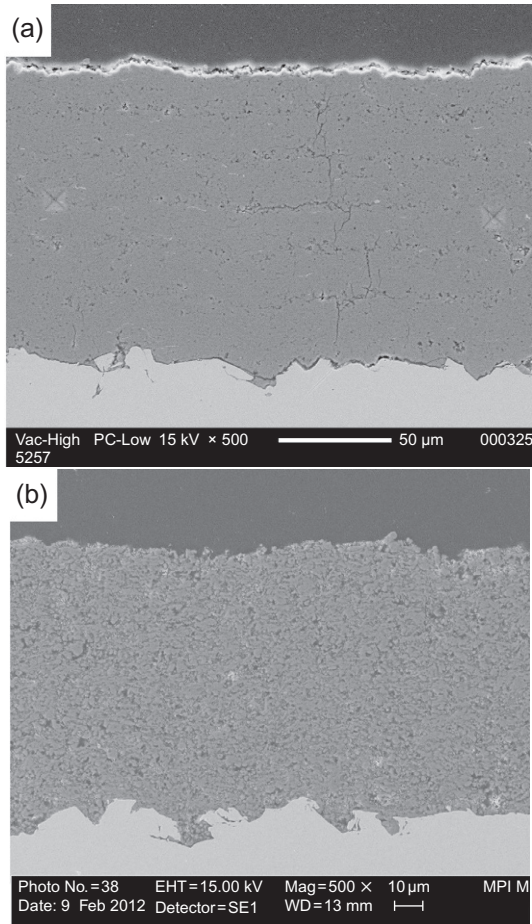


Figure 4.8 Al₂O₃ coating sprayed using a water-based suspension (particle size, $d_{50} = 1.26 \mu\text{m}$; solid content, 20 wt%). (a) Coating achieved by HVSFS using a TopGun system with axial injection. (b) Same suspension sprayed with SPS using an F6 torch with radial injection. Courtesy of IFKB, University of Stuttgart, Germany.

instance, TBCs) can reach significantly higher values. HVSFS-based coatings with a dense structure are typically fabricated in the range of 100–300 μm. The process is often limited by the increasing residual stress values induced by the higher thermal flux of the process (especially in the case of organic solvents and due to reduced spraying distance). Only few data are available from literature dealing with metal or cermet systems, for instance, SPS of WC–Co by [Oberste Berghaus et al. \(2006\)](#) and SPS of cast iron by [Tekmen et al. \(2010\)](#).

Coating adhesion levels are also comparable to standard TS coatings with typical values ranging from 20 to 40 MPa for SPS and 50–80 MPa for HVSFS coatings. As

already mentioned, the substrate topography can affect overall coating morphology, especially when fine particles are involved in the spray process. Therefore, surface activation should be adapted to the reduced splat size by reducing the initial roughness of the grit-blasted substrate.

So far, suspension spraying has been preferentially used to spray micron- and nano-sized oxide ceramics. Interestingly, phase composition of SPS and HVSFS ceramic coatings can significantly differ from standard TS coatings. This has been observed and intensively investigated for TiO_2 (anatase). It was found that SPS nanosized feedstocks of anatase reveal coatings with a high anatase content as described by [Toma et al., 2008](#); also, refer to [Section 4.4.4](#). Similar observations can be found when spraying alumina nanosized feedstocks with SPS and HVSFS. In SPS, the highest amount of alumina α -phase can be found, as described by [Müller et al., 2012](#). When alumina is sprayed by standard TS processes, most of the coating consolidates in the alumina γ -phase. These results cannot be achieved by standard TS techniques, neither APS nor HVOF. Although underlying mechanisms are not fully clarified yet, it is obvious that particle size and corresponding cooling rates are the main reasons for this different behavior.

Due to their refined microstructure, mechanical properties of SPS and HVSFS coatings can show several improvements with respect to APS and HVOF. It has been observed by [Tingaud et al. \(2010\)](#) that SPS alumina and alumina-zirconia nanosized feedstocks revealed higher wear resistance and microhardness than their conventionally sprayed counterparts (also refer to [Section 4.4.5](#)). Another interesting aspect concerns fractural toughness of suspension-sprayed coatings in general, measured by crack propagation by microindentation on coating cross sections. It was observed that crack propagation is significantly lower in suspension-sprayed coatings, and therefore, better fracture toughness is achieved. Similar results are reported in conventionally (HVOF) sprayed coatings as described by [Lima et al. \(2007\)](#). They compared fracture toughness of alumina-titania coatings sprayed with conventional and agglomerated (nano)spray powders. The Vickers indentation method on polished cross-sectional samples was used to provoke crack propagation. Significantly shorter crack length was observed in the nanostructured coating. The results are interpreted by the authors as follows: it is thought that crack deflection and arresting in dense nanozones of the coatings are the responsible mechanisms.

4.3 Equipment for suspension spraying

Suspension spraying can be operated using standard thermal spray device. However, it requires a suspension feeding line and a suitable injection system as already discussed in [Section 4.2.2](#). For plasma spraying with radial injection, a modification of the plasma torch itself (without injector) is not mandatory. In case of HVSFS with internal injection, a modification of the torch internal design may become indispensable, depending on the torch type, especially when water-cooled injectors are mounted, due to a higher space consumption compared to simple powder injectors. The basic setup for suspension spraying is shown in [Figure 4.9](#).

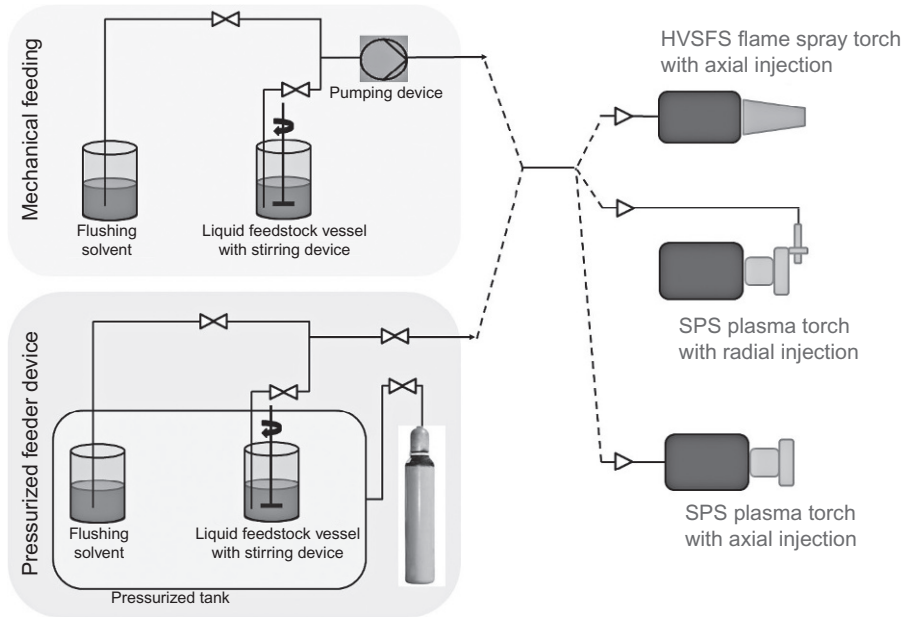


Figure 4.9 Basic setup scheme for suspension spraying for HVSFS and SPS.

4.3.1 Feeder concepts

Suspension feeders are designed to deliver nanoscale, fine micron, or submicron powders in dispersed form to a thermal spray torch. Ideally, injection mass flow and injection pressure can be controlled separately. Typical feeder data comprise a powder size range between 10 nm and 10 μm , feeding rates up to 0.5 l/min, and a solid content range in suspension up to 40%.

Two feeder concepts are commonly in use: (1) the pressure-based concept using a pressurized vessel containing the suspension and (2) a mechanical feeding by appropriate mechanical pumping devices. Both concepts have their own benefits and drawbacks. A pressure-based feeding device offers pulsation-free feeding; there are no moving parts (except steering devices) that may suffer from erosive or abrasive wear that especially occurs when ceramic suspensions are in use. However, exact control of suspension mass flow is rather expensive as external mass flow controllers or scale units have to be implemented. Appropriate mechanical pumping devices either eccentric screw pump or peristaltic pumps are commonly used. However, both systems lead to a certain pulsation of the suspension stream that cannot be fully avoided. Flow control on the other hand is technically simple. Several institutes and companies have started to publish concepts and offer commercial feeder systems that can be used as a stand-alone system or can be fully integrated into modern thermal spray control systems. Two examples of commercially available systems are given in [Figure 4.10a and b](#) (refer to [Cotler et al., 2011](#)).



Figure 4.10 Suspension feeder concepts: (a) NanoFeed from Northwest Mettech Corp., Vancouver, Canada; (b) pressurized feeder prototype from Sulzer AG, Wohlen, Switzerland (Cotler et al., 2011).

With permission from the manufacturers.

4.3.2 Plasma torches for SPS

Numerous plasma torch types have been successfully used for suspension spraying based on either ICP or direct current (DC) plasma jets. First approaches date back to 1997 using ICP plasma torches. ICP torches allow axial injection of powders, suspension, and liquid precursors. As there are no electrodes present, injection of any kind of feedstock is straightforward. ICP torches feature a rather voluminous plasma jet that efficiently vaporizes any solvent. One big advantage of ICP torches is the possibility to use virtually any plasma medium, reactive or nonreactive. However, ICP torches generate a rather slow plasma gas flow velocity below 100 m/s, inefficiently fragmenting liquid droplets and thus making it impossible to generate nanostructured coatings as stated by Fauchais et al. (2011). Schiller et al. (1997) used a PL-50 induction plasma torch from TEKNA Plasma Systems Inc. operated at 3 MHz to spray cobalt spinel. The same system was used by Bouyer et al. (1997b) to spray nanosized hydroxyapatite suspensions.

DC-based plasma torches are operated using a high-current arc as energy source. The torch design restricts the usage of plasma gases to those that do not chemically attack the electrode material like argon (Ar), helium (He), nitrogen (N₂), and hydrogen (H₂). DC plasma torch systems are industrially widespread, and they exist in various designs and have been consequently used for SPS. A well-established torch design is represented by the stick-type single-cathode torch with a nozzle forming the anode and an externally mounted radial injection tube. These torches feature high plasma gas velocities typically in the range of 800–2000 m/s, depending on the individual torch design. This leads to an intensive interaction with the liquid and thus to a strong droplet breakup. Radial injection in the free expanding plasma jet however involves significant cooling of the gas stream, consuming nearly a third of the mass enthalpy (Fauchais, 2011). Probably, the most common plasma torch design is represented by the so-called F-series (F4 and F6) distributed by several companies (for instance, Sulzer Metco, Wohlen, Switzerland; GTV, Luckenbach, Germany; Saint-Gobain Coating Solutions, Avignon, France; and others). It features a standardized electrode design and is regarded as the industrial standard for APS since the 1980s. However, several improved torch designs are available on the market offered by the same manufacturers.

A three-cathode-type plasma torch design has been developed and introduced to the market at the end of the last century. The torch is operated with three electrically separated cathodes distributing the electrical energy through three parallel arcs striking at a single anode preceded by insulating rings. As they are operated in low-current but high-voltage arc mode, these torches achieve higher thermal efficiencies compared to their single stick-type counterpart (i.e., the F-series). In this new design, the torches feature extended electrode lifetime, as well as higher deposition rates and efficiencies. Standard designs require an Ar–He gas mixture for stable operation. The most commonly used commercial torch is the Triplex II system, distributed by Sulzer Metco, Wohlen, Switzerland. Following the threefold symmetry of the generated plasma jet, the torch can be operated with three simultaneous working radial feedstock injection lines. Of importance (especially for SPS) is the radial injection position where the feedstock enters the plasma jet. Injection should be performed in such a way that the feedstock is “caged” in the interstice between the three plasma flows.

A DC torch featuring an axial injection has been developed and commercialized by Northwest Mettech Corp., Vancouver, Canada (Mettech Axial III). The torch comprises three independently operated cathode–anode pairs. The three created plasma jets are converged before entering the nozzle creating a powerful plasma jet. This design allows axial injection of the feedstock materials from the rear into the converging individual plasma jets. Particle trajectory in the hot plasma zone is therefore two to three times longer compared to single-stick types with radial injection. For SPS applications, this design is especially advantageous, as cooling effects from the solvent get less denotative and particles experience an efficient heat and impulse transfer. A collection of commonly used plasma torches is shown in Figure 4.11.

4.3.3 HVOF torches for HVSFS

HVOF has been designed to achieve high particle velocities by means of combustion of a gaseous or liquid fuel inside a chamber and its expansion through a barrel. To achieve an optimum in heat and impulse transfer, feedstock injection should occur

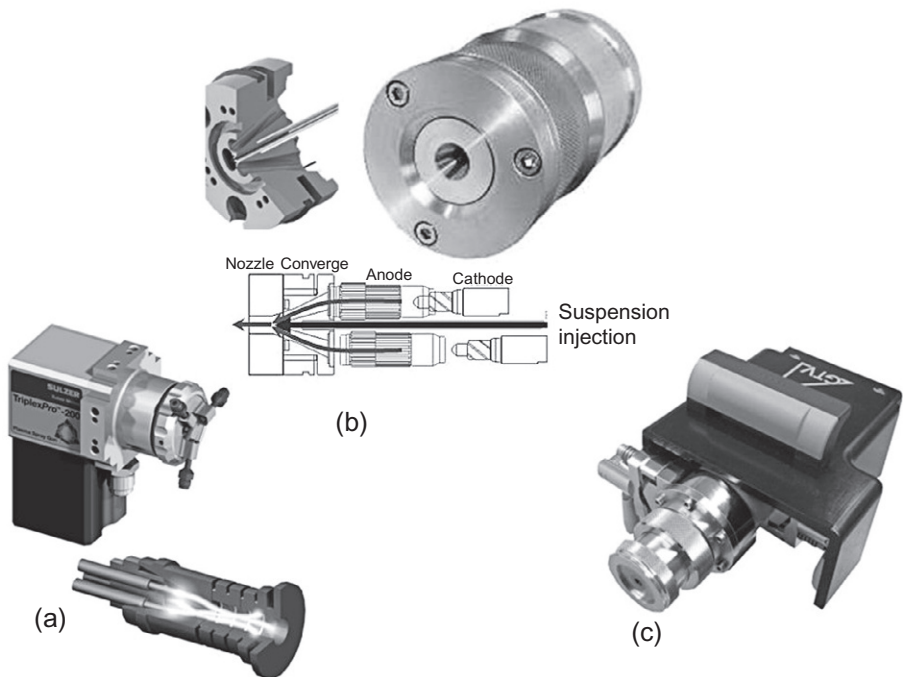


Figure 4.11 Selection of suitable plasma torches to perform SPS: (a) Triplex II (Sulzer AG, Wohlen, Switzerland); (b) Mettech Axial III (Northwest Mettech Corp., Vancouver, Canada); and (c) F6 single-cathode torch.

GTV Verschleißschutz GmbH, Luckenbach, Germany, with permission from the manufacturers.

axially into the rear of the combustion chamber. So far, this is accomplished for HVOF torches operated with gaseous fuels. In HVFSFS, suspension injection is done accordingly, making the process more complex as combustion is strongly influenced by solvent vaporization and—in case of organic solvents—subsequent combustion. The most commonly used HVOF torches operated with fuel gases are the Diamond Jet DJ 2700 hybrid (distributed, for instance, by Sulzer Metco, Wohlen, Switzerland) and TopGun-G (distributed, for instance, by GTV, Luckenbach, Germany). The development of both HVOF torches dates back to the 1980s. Due to the historical development path, both torch designs show some distinct differences. The TopGun system comprises a fully water-cooled jacket, whereas the Diamond Jet system combines compressed air cooling of the combustion chamber with a water cooling of the barrel. Further differences concern design details of nozzle geometry, gas injection, and mixing. This allows the exclusive usage of acetylene in case of the TopGun-G system, making it possible to spray oxide ceramics with hypersonic speed. Apart from that, both torches can be operated using propane, propylene, and ethane.

Both torches have been used for spraying suspensions containing micron-, submicron-, and nanosized feedstocks (HVFSFS). Although feasibility has been demonstrated and suspension spraying with HVOF has proved its clear potential, a future torch design will need distinct adaptations to improve long-term process stability and efficiency of the process. Major improvements concern the internal suspension injection system and an adaptation of the combustion chamber and the expansion nozzle geometry.

Like in powder spraying, the suspension liquid is injected directly into the combustion chamber of the operating torch. The suspension is fed against the combustion chamber pressure, just like in conventional HVOF. Especially the use of an organic liquid phase can improve the spray performance as vaporization enthalpies are lower than that of water, and reaction enthalpies should contribute to the combustion process. However, in a first step, vaporization deprives energy from the combustion process. To really take advantage out of the organic solvent combustion, ideally, it should take place in the combustion chamber to fully feedback combustion enthalpy into the process. The degree of atomization of the suspension is one important parameter that controls combustion as well as accompanying droplet and particle forming. Unlike in DC plasma spraying, direct observation of these processes is not possible. Commonly used HVOF torches are shown in [Figure 4.12](#).

Therefore, numerical modeling of the combustion process along with suspension atomization and droplet forming is especially of importance to understand and improve the HVFSFS process. Both processes, SPS and HVFSFS, are subject of numerical modeling efforts. Modeling of spray atomization by one or two fluid injectors is the first important step when describing the suspension spray process. A fluid dynamic model for suspension atomization was presented by [Esfarjani and Dolatabadi \(2009\)](#).

Extensive CFD modeling using advanced turbulence models has been performed to better understand the SPS process. [Meillot et al. \(2009\)](#) have modeled plasma source characteristics along with the plasma gas dynamics. Gas droplet interaction, followed by a droplet breakup, is modeled, for instance, by [Caruyer et al. \(2010\)](#). In case of HVFSFS, CFD modeling is performed based on existing CFD models already available

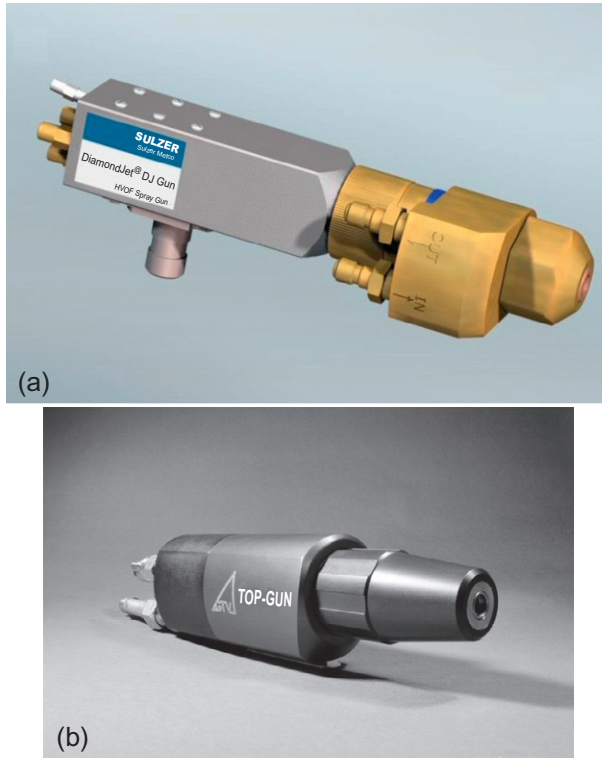


Figure 4.12 Selection of suitable HVOF torches to perform HVSFS: (a) Diamond Jet hybrid (Sulzer Metco, Wohlen, Switzerland) and (b) TopGun-G. GTV Verschleißschutz GmbH, Luckenbach, Germany, with permission from the manufacturers.

for HVOF, adding vaporization and combustion of the solvent into the initial combustion process of the fuel. However, it is not yet possible to calculate all aspects of droplet breakup and particle forming in these models. A promising approach in this direction was suggested by [Dongmo et al. \(2009\)](#). In this study, HVSFS combustion and flow dynamic system on the basis of a three-dimensional CFD model is introduced. The model considers the following phenomena: combustion of the fuel gas (premixed), energy transfer between the flame and the suspension droplets (organic solvent and particles), and the injection, vaporization, and combustion of the suspension organic solvent (nonpremixed).

4.4 Applications

The following sections will discuss some important applications in which suspension-sprayed coatings are under consideration. These applications are thermal barrier coatings (TBCs), biofunctional coatings, coatings for high-temperature fuel cell, catalytic

coatings, as well as wear-resistant and tribological coatings. Most suspension-sprayed applications are still under evaluation, and although there are many promising results, it will need more time to convince industry to implement suspension spray processes as a supplement or even as an alternative to standard spray processes.

4.4.1 Thermal barrier coatings

Protective coatings in gas turbines are one of the most challenging applications in thermal spray technology. This is particularly true for thermal protection of turbine parts that are in direct contact with the hot combustion gases, as it is the case for the rear section of the turbine, where the conversion of thermal to mechanical energy takes place.

Zirconia-based TBCs have been used for decades to protect combustion chamber walls and stator and rotator blades. Especially in aircraft turbines, for dynamically highly loaded components like rotator blades, another coating technology has been favored: EB-PVD. Although EB-PVD coatings exhibit a slightly higher thermal conductivity, they show a better performance related to thermal cycling and erosion resistance. In [Figure 4.13a and b](#), cross-sectional images of state-of-the-art APS and EB-PVD coatings are displayed showing their distinct microstructures: being lamellar with closed micropores in case of APS and columnar in case of EB-PVD.

Improving thermal efficiency of modern gas turbines is the main technological driver for coating development. This is mainly achieved by increasing the turbine entry temperature; therefore, TBCs have to withstand higher temperature gradients and should exhibit improvements in terms of low thermal conductivity and low infrared transparency values, high thermal cycling and erosion resistance, and reduced sinter activity. It is well known that nearly all aspects of the coating microstructure affect thermophysical properties (i.e., thermal and radiative conductivity): coating thickness, grain size and related grain boundary volume density, phase composition, pore volume, and pore size distribution. Especially the radiative contribution becomes more pronounced at higher gas temperatures.

New developments in TBCs are the following three main strategies:

- (1) Using new ceramic materials that complement or replace the standard yttria-stabilized zirconia (YSZ) material. They show lower thermal conductivities, do not undergo phase transitions due to the existence of metastable phases, and show less postsintering effects during their operational lifetime ([Vaßen et al., 2010](#)).
- (2) Applying new coating technologies that allow for cost reduction and/or improved microstructures resembling those achieved in EB-PVD processes ([von Niessen et al., 2010](#)).
- (3) Improving the microstructure of a TBC by modifying and improving existing spray methods ([Mauer and Vaßen, 2011](#)). Nanostructured coatings are one strategy to improve thermal performance of TBCs by using SPPS or SPS methods. Both methods enable fabrication of coatings with a high density of grain boundaries and a nanosized pore structure (ideally < 100 nm) that significantly lowers thermal conductivity.

Numerous research activities are engaged in the development of TBC using the SPS process. It was demonstrated that SPS TBC can be fabricated exhibiting a high porosity level ([Vaßen et al., 2008](#)). In further studies, it was found that SPS coatings can be produced featuring a high density of vertical segmentation cracks

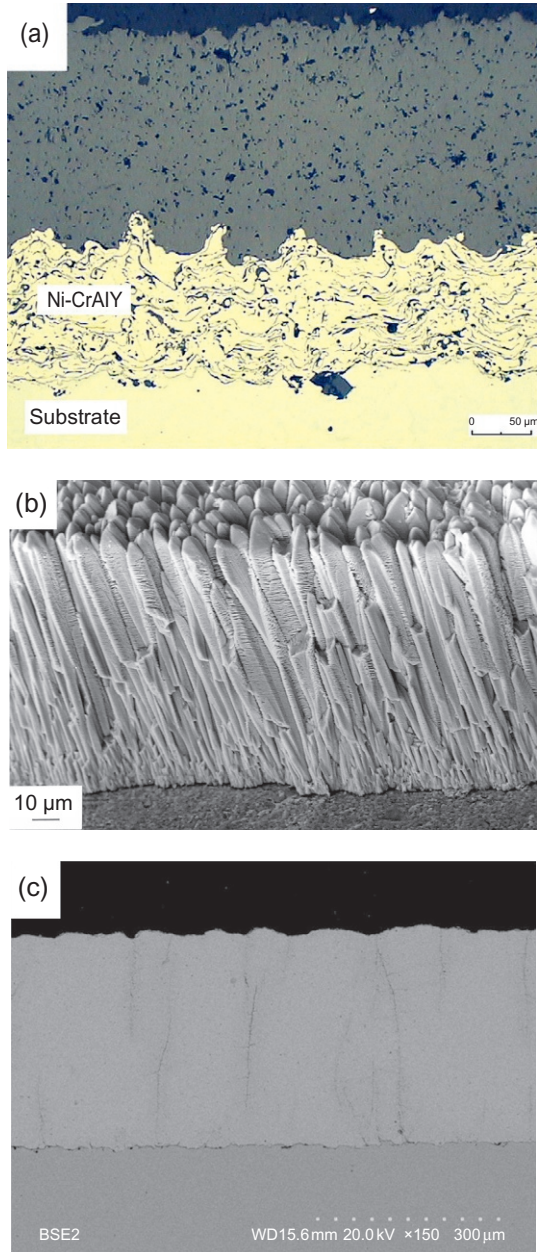


Figure 4.13 Examples of TBCs fabricated using different coating technologies: (a) cross-sectional optical micrograph of YSZ TBC fabricated by APS, (b) SEM cross-sectional image of YSZ TBC fabricated by EB-PVD, (c) SEM cross-sectional image of dense YSZ TBC with vertical cracking fabricated by SPS using a Mettech Axial III,

(Continued)

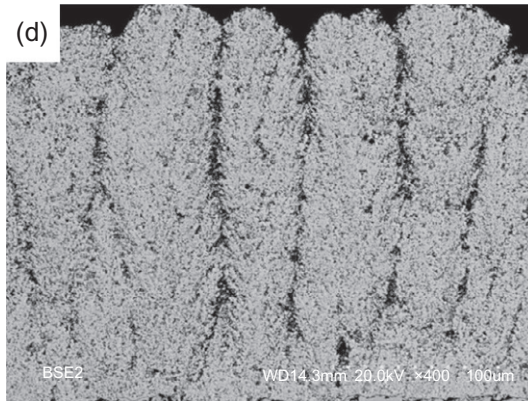


Figure 4.13, cont'd and (d) SEM cross-sectional image of YSZ TBC with columnar structure fabricated by SPS using a Mettech Axial III.

(a) Courtesy of IFKB, University of Stuttgart, Germany. (b) Courtesy of U. Schulz, DLR, Germany. (c and d) Courtesy of Z. Tang, Northwest Mettech Corp., Vancouver, Canada.

(Kaßner et al., 2008a). This crack network is considered to increase the coating's strain tolerance and provide a low Young's modulus. This is especially of benefit in aircraft turbines, where turbine components in the hot section are exposed to high thermal cycling fatigue levels during each start/stop sequence. The increased density of segmentation cracks compared to APS coatings is related to different relaxation processes during spraying. Compared to APS TBCs, the unique microstructure of the SPS process (large number of grain boundaries and high porosity level) leads to superior properties in terms of thermal conductivity and favorable optical properties in the IR radiation regime, that is, a reduced infrared transparency and increased reflectance in the relevant IR wavelength band ($\sim 0.5\text{--}5\ \mu\text{m}$). On the other hand, sintering behavior of SPS coatings seems to exhibit higher sintering rates than comparable APS coatings, which is also related to the refined microstructure and large fraction of submicrometric pore volumes. The sintering behavior of SPS YSZ coatings has been investigated and discussed in numerous publications, for instance, by Kaßner et al. SPS coatings can feature high porosity levels as 40% and more and their sintering behavior directly correlates with their porosity volume (for instance, sintering rate of 0.42% at 40% porosity), as described in Kaßner et al. (2008c).

First attempts for fabrication of finely structured TBCs were in the field of SPPS using liquid precursors by Bathia et al. (2002) and Xie et al. (2004). Spraying of YSZ using the SPS process was first introduced in Section 4.4.3. The research center Jülich in Germany was among the first that reported activities on using the SPS process for the fabrication of TBCs (Vaßen et al., 2008; Kaßner et al., 2008a). F4 and Triplex II plasma torches were employed, both equipped with radial suspension injection. Submicron- and nanosized YSZ feedstocks ($d_{50} = 300\ \text{nm}$ and $25\ \text{nm}$, respectively) were dispersed in ethanol solvent with a mass content of 10–30 wt%. Results were

compared to APS YSZ in terms of coating morphology. Splat diameters found in SPS coatings were up to 20 times smaller compared to those in conventional APS coatings. Coatings containing a porosity volume up to 54% were fabricated. The authors emphasize the importance of the injection system. In the presented work, a specially designed two-phase atomizer was developed to control droplet size prior to entering the plasma jet. This way, YSZ coatings with high segmentation crack densities (7 cracks/mm) were achieved. By changing spray parameters, a columnar-type coating structure, resembling those of EB-PVD coatings, can be achieved as described in [Vaßen et al. \(2009b\)](#). A 70% open pore volume was measured using mercury intrusion technique. An in-depth analysis of the optical properties of APS and SPS TBCs revealed significantly better results of thermal conductivity and infrared scattering for SPS coatings. High reflectance values greater than 90% are obtained for the SPS films over a large spectral range ([Kaßner et al., 2008b](#); [Stuke et al., 2012](#)).

Demonstrating the versatility of SPS, [Tang et al. \(2011\)](#) had shown that fabrication of dense or columnar structured coatings is possible. TBCs were sprayed using a Met-tech Axial III plasma torch with axial injection employing a submicron 8YSZ-based suspension. Exemplarily, [Figure 4.13c and d](#) shows achievable coating microstructures. Both a dense coating with vertical cracking and a columnar structure, more resembling the nature of EB-PVD coatings, can be achieved, depending of the spray parameters that are used. It was also found that surface roughness of the underlying bond coat strongly influences the shape of the columnar structure in terms of open porosity and column thickness. Spray parameters like standoff distance and spray angle influence the amount of intercolumnar porosity and angular orientation of the columns. Finally, a complete turbine blade was coated, demonstrating that uniform and well-adhered coatings can be achieved.

It is believed that insertion of Nd^{3+} and Yb^{4+} ions into the YSZ lattice increases phonon scattering, thus leading to lower thermal conductivity of the YSZ. This could either be done by preparing agglomerated powders with dopant salts and perform a heat treatment to achieve the desired reactions. A direct method through in situ alloying of YSZ material by means of the SPS process has been presented by [VanEvery et al. \(2011\)](#). Therefore, a suspension was prepared, containing nanosized YSZ powder ($d_{50} \approx 80$ nm) and hydrated Nd and Yb nitrates, which were additionally dissolved in the suspension. During spraying, doping of the YSZ material through diffusion of Yb^{4+} and Nd^{3+} ions occurred, significantly lowering the thermal conductivity (determined by laser flash measurements at elevated temperatures on the freestanding SPS coatings) of the doped coatings from 1.4 (undoped) to 0.8 (doped) W/mK.

4.4.2 Coatings for biomedical applications

In biomedical applications, coating technology plays an important role, as surface functionalization is indispensable in order to ensure a proper and durable integration of artificial materials into the human body. Today, many surface coating and modification methods are employed: thin film deposition techniques like PVD as well as anodizing of metal surfaces and thermal spray methods ([Repenning, 2006](#)).

Biocompatible coatings on endoprosthetic implants replacing pathological human bone hip, shoulder, and knee joints using thermal spray technique have been practiced since the 1990s. Especially for hip and knee joint implants, conventional plasma spraying (APS and VPS) of biocompatible biomaterials like hydroxyapatite ($\text{Ca}_5(\text{PO}_4)_3\text{OH}$), titania, and titanium onto metal implants made from CoCr and titanium alloys has become a well-established and clinically accepted technique. The aim in mind is to enhance biointegration of the implant and favor bone ingrowth to the implant surface. It should be noted that in case of hip joint implants, coatings are involved in case of the so-called press-fit or cementless implants, where the initial fixation is of a pure mechanical nature. In contrast, the so-called cemented implants use special bone cement, which undergoes in situ polymerization immediately after implantation, thus forming a chemical fixation between the bone and implant surface. In case of press-fit fixation, bone ingrowth is a prerequisite to ensure a durable mechanical interlock between the bone tissue and the implant surface. Therefore, the coating plays a crucial role in favoring this ingrowth and ensuring a direct contact between bone tissue and implant surface without the adverse formation of connective tissue. This ingrowth process has to be fast and can be induced by a certain amount of mechanical strain. An extensive review of the subject can be found in [Heimann \(1999, 2002\)](#).

HA is one of the most investigated and widespread coating materials fulfilling these requirements to the best of knowledge. It is regarded as bioactive as it stimulates a chemically induced direct cell growth in vivo. HA in its pure and crystalline form does not or only rarely undergo resorption in the human body. The material has undergone intensive studies, elaborately described by [McPherson et al. \(1995\)](#), [Heimann \(1999\)](#), and [Gruner \(2001\)](#). From these studies, it is well known that phase composition, microstructure of the sprayed materials, and surface topography strongly influence the ingrowth behavior of the coated implant. Concerning phase composition, a high amount of crystalline phase is essential and governs the resorption behavior of the HA coating in vivo. Unfortunately, HA is thermodynamically not stable in the fully molten state, which demands certain dispositions when plasma-sprayed, that is, use of coarse powders, a short dwell time to only partially melt the feedstock material, and a high particle velocity to ensure good adhesion of the softened particles. This way, the amount of crystallinity can be kept as high as possible and the decomposition of HA is minimized.

Bioactive glass materials, so-called bioglasses, were proposed by L. Hench in the late 1960s and have been intensively studied since the first publication from [Hench \(1991\)](#). These materials are bioactive and favor precipitation processes that lead to the formation of HA on the implant surface when immersed in simulated body fluid (SBF). It has been found that this mineralization process is more efficient compared to HA; thus, bioglasses are regarded as an interesting alternative to HA ([Hench and Andersson, 1993](#); [Ha and Wintermantel, 2003](#)).

Suspension spraying of biomaterials has been performed employing SPS and HVSPS processes. As suspension-sprayed coatings feature a refined microstructure, even coatings with a reduced layer thickness compared to industrially established spray processes (mainly APS) can be fabricated. The main motivation for suspension

spraying is to improve the mechanical properties and to properly control biodegradability in the body by tuning the amount of crystallinity. In case of bioglasses, spraying via APS leads to rather porous coatings with insufficient mechanical properties. HA, TCP, and bioglass coatings produced by suspension spray techniques have been investigated for this purpose.

The single-anode torch SPS process has been used to spray HA suspensions in several studies by [Jaworski et al. \(2007, 2008, 2010\)](#). HA was synthesized from aqueous solutions to form particles in the size range of 1–10 μm . Suspensions were prepared using distilled water and an HA solid content of 10 wt%. Spraying was performed with a Praxair SG-100 single-cathode plasma torch. Thin coatings in the thickness range of 10–30 μm were achieved. Results confirm that during SPS, HA undergoes partial decomposition with the formation of crystalline TCP, TTCP, and calcium oxide phases, with HA and TCP found to be the most predominant. Particle size in the suspension has a strong impact on the remaining HA content in the coating. It is commonly assumed that in case of large particles, incomplete melting is responsible for this circumstance, as the unmolten material remains in its original phase. The same authors present a method to deposit graded TiO_2/HA coatings ([Jaworski et al., 2010](#)) by coupling two peristaltic feeder devices and appropriately mixing the two suspension feeding streams to form a TiO_2/HA mixed suspension prior to plasma injection. An example for SPS HA coating is given in [Figure 4.14](#).

[Gadow et al. \(2010\)](#) performed a comparative study to spray HA by means of APS, HVOF, and HVSFS onto titanium substrates. Standard spray powders were used in case of APS and HVOF, and an HA nanopowder (Ce.Ri.Col., Italy) dispersed in either water or diethylene glycol (DEG) was sprayed via HVSFS using a modified TopGun system. The study revealed distinct properties in terms of splat size, coating porosity, and crystallinity of the sprayed coatings. XRD measurements indicated the highest amount of crystallinity in case of HVOF coating, closely followed by HVSFS, and the lowest amount for the APS coating. It turned out that, in case of HVSFS, the solvent (water or DEG) has a strong impact on coating morphology, that is, achieved porosity and splat size. The lowest porosity was achieved using the DEG suspension, and the smallest spray particles were formed using the water-based suspension. The same research group continued investigations ([Stiegler et al., 2012](#)) and performed SBF immersion tests on HVSFS HA using same suspensions as described in [Gadow et al. \(2010\)](#). In this study, a new spray torch design was introduced, exhibiting a new combustion chamber design with higher volume and shape. The new torch design led to a remarkable increase of deposition rates and efficiency, along with an increase of substrate temperature. In this new design, the coatings sprayed with DEG-based suspensions showed the highest crystallinity and thus low resorption rates when immersed in SBF. However, when spraying a coating in several passes, the phase composition of the single deposition layers that build up the coating can be analyzed and compared to each other. A change in the amount of crystallinity can be found in the subsequent layers, starting with a more or less amorphous material in the layer close to the substrate, changing to higher crystallinity in the subsequent deposition layers. In a further study ([Stiegler, 2012](#)), upon the introduction of a titania bond coat sprayed via APS on the titanium substrate, crystallinity and adhesion could be increased and no amorphous interlayers were formed.

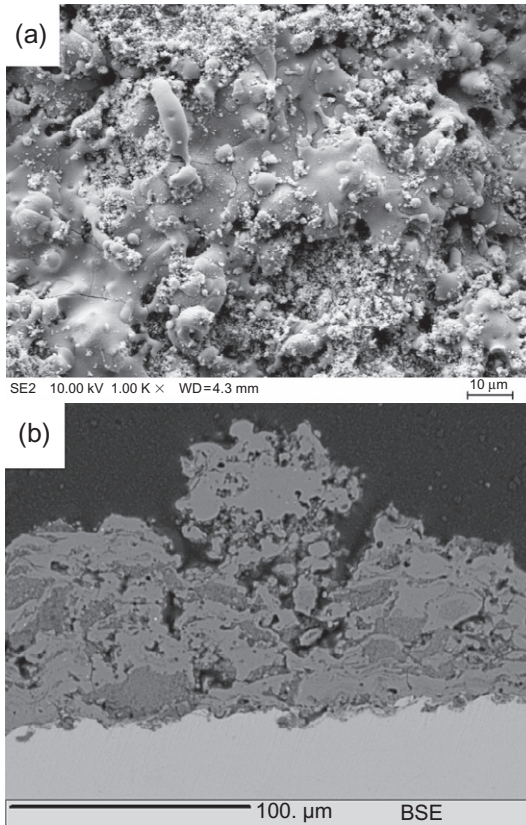


Figure 4.14 Structure of SPS HA coating derived from a micron-sized HA suspension feedstock (20 wt% solid, 40% ethanol+40% water) in SEM: (a) surface structure and (b) cross-sectional image in SEM.

Courtesy of L. Pawlowski, University of Limoges, France.

Analogous studies were performed by the same group using bioglass materials and spraying them on titanium substrates, for instance, the recently developed so-called Bio-K ($\text{SiO}_2\text{-P}_2\text{O}_5\text{-CaO-K}_2\text{O}$) material (Cannillo et al., 2010). Suspensions were prepared using water-isopropanol mixtures and an adequately milled Bio-K glass powder with a resulting grain size in the μm range. Bioglasses do not show serious structural or compositional changes when sprayed via HVSFS. Compared to SPS, HVSFS coatings usually feature higher bond strengths and significantly denser microstructures, which is desired especially in bone implant applications. SBF studies revealed high dissolubility of the bioglass coating in the SBF fluid, leading to solution and precipitation phenomena. High precipitation rates of crystalline HA on the sprayed bioglass surface were observed; and after one day in SBF, a continuous and crystalline HA layer is formed on the surface, making the material particularly promising for applications where fast osseointegration is desired. The bond strength of HVSFS bioglass coatings

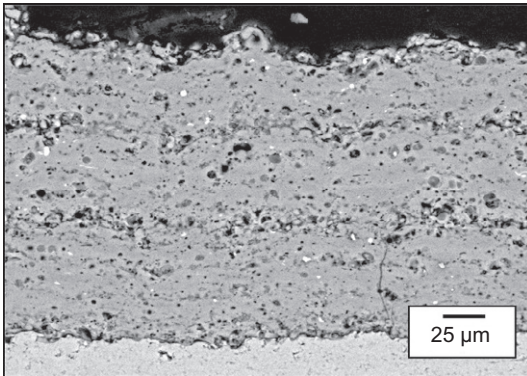


Figure 4.15 HVFSFS bioglass (Bio-K) coating derived from micron-sized glass powders.

Adapted from [Bellucci et al. \(2012\)](#).

could be improved by introducing a plasma-sprayed ceramic bond coat ([Bellucci et al., 2012](#)). An example for HVFSFS bioglass coating is given in [Figure 4.15](#).

4.4.3 SOFC development

Fuel cells are electrochemical devices that directly convert chemical energy of a reaction into electrical energy. In general, fuel cells provide many advantages over traditional energy conversion systems including high efficiency, reliability, modularity, fuel adaptability, and very low levels of emissions.

Numerous concepts of fuel cell designs have been developed in the past decades or are still under development ([Singhal, 2000](#)). Their use in aerospace applications in the 1960s was one of the first important milestones for the current development. Meanwhile, several types of fuel cells have reached an industrial design level that allowed this technology to enter a broad commercial market. One important representative, the polymer electrolyte membrane fuel cell (PEM-FC), has been successfully introduced in lightweight and compact energy storage modules for electrically driven passenger cars and public transport systems. Another type, the solid oxide fuel cell (SOFC), has been primarily developed for stationary power generation. Typically operating at temperature ranges between 800 and 1000 °C, this cell type accepts natural fuel gas without the need of external reformers. Meanwhile, mobile systems are available as so-called auxiliary power units (APU) serving as a powerful onboard voltage source in trucks and large passenger limousines.

A SOFC essentially consists of two porous electrodes separated by a dense, oxygen ion conducting electrolyte. Different planar and tubular designs have been developed and successfully introduced in various applications, for instance, by Westinghouse (stationary power systems) and Delphi (gasoline-fueled APU); more information can be found, for instance, in [Williams et al. \(2004\)](#). Among the different designs and manufacturing concepts, the so-called anode-supported type represents one of the most favored and will be considered here. This type basically consists of a self-standing porous metal structure that works as the gas distributor on the anode site

as well as the mechanical support for the entire cell. The anode, electrolyte, and cathode structures are sequentially deposited on this porous metal to form a trilayer system. Most recent applications work with planar geometries.

In the anode material, where hydrogen is formed, catalytically active Ni/YSZ-based composite materials are well established. For the cathode, where the decomposition of the oxygen molecule takes place, lanthanum strontium manganite (LSM, $\text{La}_{1-x}\text{Sr}_x\text{MnO}_3$)-based perovskites are commonly used in commercial systems. It should be emphasized that, in order to achieve a high electrical efficiency of the cell, the electrodes should exhibit a porous structure with a high amount of reactive surface and a high density of metal-ceramic phase boundaries, whereas the electrolyte itself should represent a preferably thin and gastight structure without any cracks and pores.

Originally, for the electrolyte material, YSZ was found to be the best working material, exhibiting excellent oxygen ion conductivity at a reasonable technical and economical effort in manufacturing (Möbius, 1997). However, operational temperature is near 1000 °C, and the cell components are exposed to numerous thermal and chemical degradation effects, which limits the overall cell lifetime. This fact can be regarded as the main drawback of the present cell design. Therefore, SOFC design is still under development, and one major focus in present research activities focuses on new electrolyte materials that allow a decrease of the operational temperature without lowering the overall performance of the cell.

A generally followed direction to increase ion conductivity at an intermediate temperature range between 600 and 800 °C is to use materials with a higher ionic conductivity, such as scandia-stabilized zirconia (ScSZ), gadolinia-doped ceria (GDC), or samarium-doped ceria (SDC), for instance, $\text{Ce}_{0.8}\text{Gd}_{0.2}\text{O}_{2-\delta}$ and $\text{Ce}_{0.8}\text{Sm}_{0.2}\text{O}_{2-\delta}$, respectively. However, these materials often show quite complex thermodynamic behavior, phase instabilities, etc., often leading to a loss of the desired advantageous properties (Spirin et al., 2012).

To move toward a cost-saving and economically satisfying production process of SOFCs, numerous manufacturing methods have been evaluated, like screen printing techniques and wet spraying of liquid suspensions (Steinberger-Wilckens et al., 2003). However, all these techniques require a subsequent heat treatment step, to sinter and consolidate each functional layer or several layers together (the so-called cofiring). Thermal spray techniques represent an interesting alternative to these methodologies as they allow a one-step manufacturing of each layer, basically avoiding any posterior heat treatment. VPS-, APS-, and HVOF-based spray methods have been intensively investigated concerning their applicability (Henne et al., 1999; Stöver et al., 2006; Gadow et al., 2007). As soon as liquid precursor and suspension spray techniques have become available, numerous scientific activities have started to evaluate these techniques. For electrodes, the use of a liquid feedstock containing a precursor or ultrafine powder leads to a refined coating structure with a high density of micro- and nanopores. It is expected that these micro- and nanopores increase the inner surface volume and thus the number of catalytically active reaction sites. For electrolyte fabrication, suspension spraying of electrolyte materials using HVSFS or SPS is of interest, because thin (down to $\sim 10 \mu\text{m}$) and dense coatings can be fabricated.

Manufacturing of thin and dense electrolyte layers by means of SPS and HVSFS was subjected to intense research. Numerous efforts have been reported using the SPS

process with different plasma torches and submicron- or nanobased suspensions to produce YSZ-, GDC-, and SDC-based electrolyte layers. [Delbos et al. \(2003\)](#) were among the first who investigated SPS as a promising method to fabricate a thin (lower than 50 μm) YSZ electrolytes from nanosized feedstocks using a standard DC plasma torch with radial injection. Experiments revealed a strong influence of operating parameters (i.e., spraying distance, electric power, and torch type) on microstructure (porosity level) and deposition efficiency. Interestingly, fabrication of dense and porous coatings was both feasible. [Oberste Berghaus et al. \(2007\)](#) employed a Mettech Axial III plasma torch to spray dense, thin (<10 μm), and nanostructured SDC electrolyte coatings for intermediate temperature SOFC. A suspension consisting of 5 wt% solids in ethanol was prepared using a $\text{Sm}_{0.2}\text{Ce}_{0.8}\text{O}_{1.9-x}$ nanopowder (20 nm). A high plasma heat flux and short standoff distances were generally required to create a dense coating structure. The same research group ([Oberste Berghaus et al., 2008](#)) successfully used an HVSFS system (based on a Diamond Jet DJ 2700) to spray the same suspension system as in [Oberste Berghaus et al. \(2007\)](#) and achieved fully densified coatings. Electrochemical testing revealed rather high cell performances. [Rauch et al. \(2009\)](#) fabricated dense YSZ coatings on anode-supported half-cells using a modified TopGun system; refer to [Figure 4.16](#).

[Brousse et al. \(2009\)](#) used an F4MB torch (Manufacturer: Sulzer Metco, Wohlen, Switzerland) and found best results at a reduced spraying distance of 30 mm to spray 60 μm thick of YSZ layers. However, coating structure showed a rather high porosity with columnar defects. So it was found that gas permeability was still higher compared to coatings produced using the standard APS process. [Waldbillig and Kesler \(2009\)](#) employed a Mettech Axial III plasma torch to fabricate a full SOFC cell structure. A standard APS procedure with a powder feedstock was used to spray the electrodes (LSM/YSZ and NiO/YSZ powders, respectively), and a suspension containing micrometer-based YSZ feedstock was used as a feedstock for electrolyte fabrication. [Wang et al. \(2010\)](#) reported fabrication of a half-cell structure using micrometer-sized NiO/YSZ containing suspension feedstock for anode fabrication and a YSZ suspension

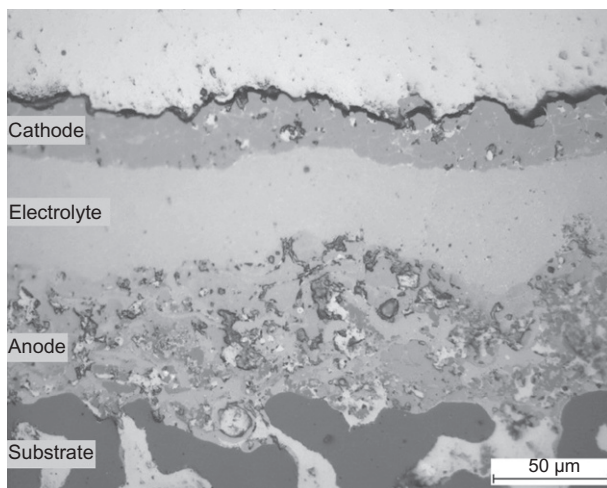


Figure 4.16 Light microscope image of an HVSFS YSZ electrolyte. Anode and cathode plasma-sprayed by DLR Stuttgart. Courtesy of IFKB, University of Stuttgart, Germany.

feedstock for the electrolyte using the same torch system as [Waldbillig and Kesler \(2009\)](#) and [Jia and Gitzhofer \(2012\)](#) employed a PL-50 inductive plasma torch from Tekna Plasma Systems with axial injection to deposit thin and dense GDC electrolyte layers with an insignificantly low gas permeability. GDC nanometer-sized powders were synthesized by the authors and dispersed in ethanol to achieve a 10 wt% suspension. Results of this work demonstrated that SPS-fabricated electrolyte layers show lower residual stresses with no apparent crack formation leading to highly gastight coatings.

SPS was also intensively evaluated regarding anode and cathode fabrication—often in combination with electrolyte deposition—using the same spray method, but in this case, a highly porous structure containing a high amount of three phase boundaries is desired. Spraying of LSM-based suspensions for cathode fabrication was carried out by [Monterrubio-Badillo et al. \(2006\)](#) and [Marchand et al. \(2010\)](#); YSZ/NiO-based suspensions were used by [Wang et al. \(2010\)](#) and [Marchand et al. \(2010\)](#) to fabricate corresponding anode structures. [Marchand et al. \(2010\)](#) deposited optimized electrodes onto a ferritic substrate and performed open-circuit voltage and impedance tests at a temperature around 800 °C with promising results, demonstrating the feasibility of the fabrication method.

4.4.4 Catalytically active coatings

Titanium oxide coatings have been intensively studied because of their interesting physical, chemical, and electrical properties. The application of TiO₂ coatings not only as hydrogen and oxygen sensors and self-cleaning and photocatalytic surfaces to degrade organic pollutants but also as electron emitters for light-emitting devices has been considered by [Jaworski et al. \(2010\)](#). The critical point for most applications, where TiO₂ is involved, is the formation of the appropriate phase. For photocatalytic applications, it is generally assumed that anatase has the higher photocatalytic activity than rutile. Furthermore, microstructural features such as porosity and specific surface are of importance. Suspension TS has proved to offer a large potential to manufacture efficient TiO₂ coatings.

[Toma et al. \(2006, 2008\)](#) compared the photocatalytic behavior of TiO₂ coatings deposited by SPS and HVSFS. The feedstock material contained about 80% anatase with a 25 nm average particle size. The largest anatase content (up to 80 vol.%) was found in the SPS coatings, while 26–41 vol.% was identified in the HVSFS deposits. Based on the dye degradation experiments, the authors proposed a minimum concentration threshold of 65 vol.% anatase to achieve a sufficient photocatalytic performance. In the case of SPS, the coatings consisted to a great extent of nonmelted regions. Thus, the authors assumed that the high anatase content was due to the fact that anatase was retained from the feedstock. However, as a consequence, they also found poor adhesion of the coatings to the substrate. [Figure 4.17](#) shows an SPS TiO₂ coating and compares anatase content for different spray methods, namely, SPS (labeled as suspension APS), HVSFS (labeled as suspension HVOF), and standard HVOF (labeled as HVOF with granules) indicating that SPS process reveals the highest anatase content in the coating.

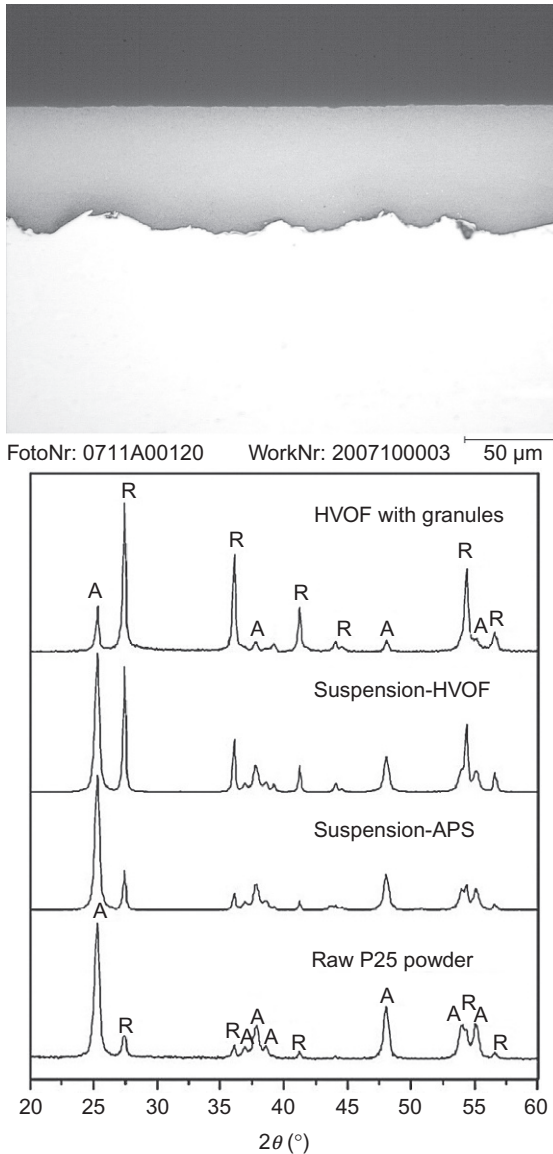


Figure 4.17 (a) SPS TiO₂ coating derived from nanosized feedstock for photocatalytic application (courtesy of F.-L. Toma, IWS, Fraunhofer-Institute, Dresden, Germany). (b) Comparative XRD analysis showing anatase content for HVSFS and SPS (denoted as suspension HVOF and APS, respectively) (adapted from [Toma et al., 2009](#)). Peak labels refer to anatase (A) and rutile (R).

A comparison between external atomization and internal continuous stream injection in SPS when spraying water–ethanol-based TiO₂ suspensions is presented in [Kozerski et al. \(2010\)](#). The feedstock material mainly consisted of rutile. The external atomizer produced distinctly smaller droplets than the continuous jet breakup occurring when an internal injector was used. Therefore, considerably smaller agglomerates are expected to form upon evaporation of the liquid. For such conditions, higher anatase content was detected. The authors suggest that particle size-dependent solidification conditions on the substrate are mainly responsible for the amount of anatase.

Spraying of TiO₂ via SPS was also evaluated for manufacturing the Grätzel cells, as described by [Vaßen et al. \(2009a\)](#). The feedstock material was anatase with a mean particle size of 60 nm. SPS was performed on hot substrates using rather cold spraying parameters, since it was assumed that the phase transformation from anatase to rutile mainly took place on the hot substrates. The results were highly porous TiO₂ coatings with an anatase content of about 90% and crystallite sizes well below 50 nm. However, the photovoltaic cell design still has to be optimized to achieve sufficient photoelectric efficiencies.

4.4.5 Suspension-sprayed tribological and wear-resistant coatings

Wear resistance and tribofunctionality are denotative application fields in TS. Several oxide ceramics in the system Al, Zr, Ti, and Cr have been suspension-sprayed for this purpose preferentially using nanosized feedstocks. Well-known application fields are paper and printing machines (rollers), textile machine elements (for instance, yarn carriers), pump and valve parts, and engine parts only to mention a few examples.

Feedstocks using submicron- and nanosized alumina and alumina-zirconia have been sprayed (SPS) by several authors, as described in [Tingaud et al. \(2010\)](#). It was found that coating microstructure and hence wear resistance and tribological properties strongly depend on plasma spray parameters such as spray distance, suspension solid content, DC plasma torch nozzle geometry, and plasma parameters. A dense microstructure can only be achieved by rather short spraying distances of 30 mm and low solid content in the range of 10 wt%. Suspension-sprayed oxide layers also show superior performance under dry sliding conditions. This was demonstrated by [Darut et al. \(2010\)](#) spraying nanosized Al₂O₃ using SPS and by [Rempp et al. \(2012\)](#) spraying nanosized TiO₂/TiC suspensions using HVSFS.

The potential of HVSFS TiO₂/TiC coatings for automotive engine applications has been proposed by Manzat et al., described in [Manzat et al. \(2010\)](#) and [Killinger et al. \(2010\)](#). The suspension is composed of a nanosized titania and a submicron-sized TiC dispersed in isopropanol. The material was successfully deposited onto inner liner surfaces of light-metal cylinder blocks as well as gray cast cylinder liners. The process is performed by applying an external kinematic using the TopGun-G system as shown in [Figure 4.18](#). Mechanical posttreatment of the HVSFS titania coating was successfully performed by honing. XRD analysis of the as-sprayed coating revealed rutile as the main phase with a measurable amount of substoichiometric Ti₃O₅ phase, which could

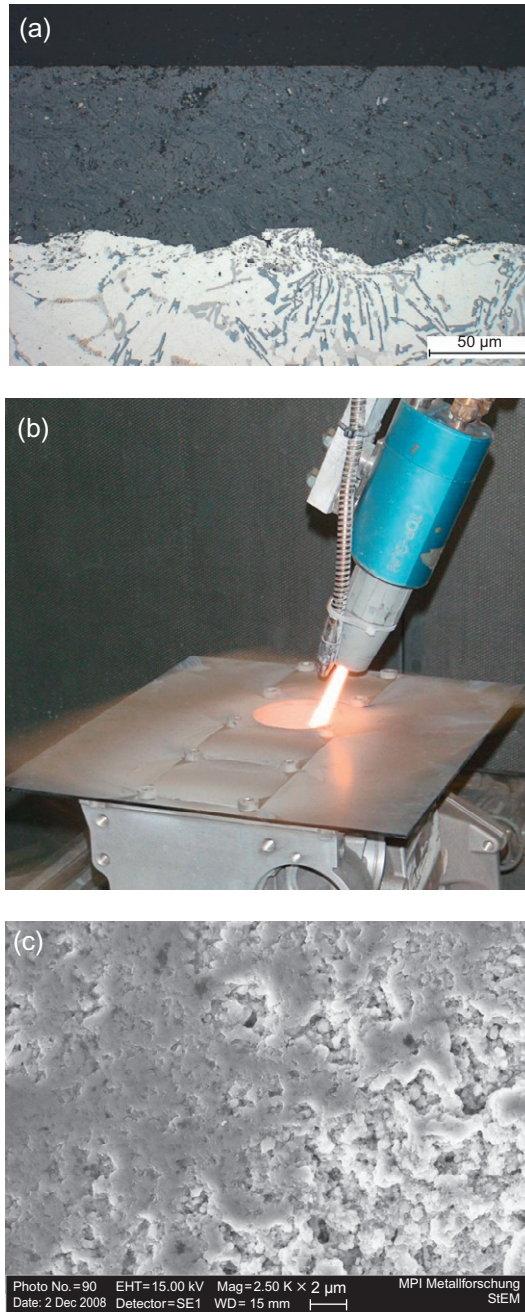


Figure 4.18 (a) Light microscope image of HVSFs coating of a nanosized TiO_2 feedstock for cylinder liner surface after honing operation; (b) photograph of the coating process with rotating light-metal crankcase; (c) SEM image of the honed surface revealing porosity on a micron and submicron level;

(Continued)



Figure 4.18, cont'd and (d) coated components: four cylinder light-metal crankcases and single light-metal bush.

Courtesy of IFKB, University of Stuttgart, Germany.

be favored by the presence of TiC via partial reduction of TiO_2 . Coatings were tested under dry sliding conditions (ball-on-disk tribometer) and under lubricated conditions (piston ring segment test) and revealed improved wear resistance when compared to gray cast iron at comparable friction coefficients. The same authors applied Cr_2O_3 on steel substrates by HVSFS using a submicron Cr_2O_3 powder dispersed in isopropanol with a solid content of 20 wt%. Microindentation measurements revealed hardness values exceeding 2000 $\text{HV}_{0.1}$; refer to Killinger et al. (2010). A typical microstructure of the HVSFS coating is shown in Figure 4.19.

4.4.6 Suspension spraying of metals and cermets

Only few articles present data about suspension spraying of metal- or cermet-based materials. Directly spraying these materials in form of suspensions could bring down production costs, as the production of agglomerated spray powders is still expensive. Although spraying of metals, carbides, and cermets is basically possible by means of suspension spraying, benefits are not yet clearly visible, as those materials undergo transitions and oxidation reactions in most cases. This is simply due to the high surface reactivity of the small particles, which are separately subjected to the hot gas stream. Further research is necessary to solve this issue and it is not yet clear if suspension spraying of cermet materials can produce coatings with superior performance compared to HVOF coatings produced with high-quality standard powders.

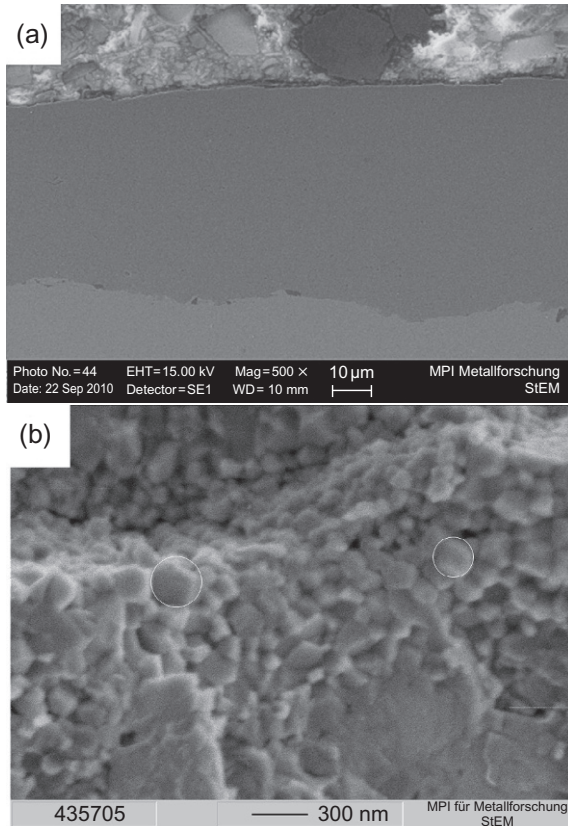


Figure 4.19 Microstructure of HVSFS Cr_2O_3 coating: (a) SEM cross-sectional image and (b) SEM fracture surface revealing the nanograin structure. Courtesy of IFKB, University of Stuttgart, Germany.

[Oberste Berghaus et al. \(2006\)](#) presented data about SPS WC–Co coatings. Suspensions were prepared using nanoagglomerated feedstocks. A Northwest Mettech spray torch with axial injection of the feedstock was used. A similar approach was followed by [Rauch \(2012\)](#) using HVSFS and micron-sized feedstocks of tungsten carbide (WC) and cobalt (Co) dispersed in isopropanol. [Wittmann-Ténéze et al. \(2011\)](#) combined APS and SPS processes to spray a nanosized WC in 316L stainless steel matrix. 316L was injected as a regular powder feedstock; simultaneously, the WC powder was injected in the form of an aqueous suspension containing 20 wt% of carbide. Injection was performed radially using an F4 plasma torch. Although these approaches revealed interesting results, carbide concentration in the coatings was not satisfyingly high. Suspension spraying of WC–Co cannot yet reach the superior quality of HVOF-sprayed coatings using nanoagglomerated powder feedstocks, at least as long degradation and oxidation of the carbide phase cannot be efficiently inhibited.

4.5 Summary and conclusion

Discussed and practiced since the 1990s, suspension spraying is a spray method that is still under development. Research work is closely linked to precursor solution spraying, sharing many of the involved phenomena. Whereas in the first decade of development the focus was more on SPS, HVSFs joined a decade ago and even enhanced the possibilities of suspension spraying. The research work in suspension techniques has clearly shown that liquid injection, gas/liquid interaction, and subsequent droplet formation and breakup are the critical phenomena that need to be understood and tuned in order to gain full control of the process. Besides the application of various diagnostic methods that may not always be capable of fully monitoring the process due to a decreased particle size or for other reasons, numerical modeling and dynamic simulations of these phenomena are important key tools for ongoing research efforts.

Any successful spray method starts with a good feedstock. Suspension fabrication requires an in-depth knowledge in powder processing, in surface chemistry, and in rheology in order to fabricate a stable feedstock featuring a good flowability and processability.

Properties of suspension-sprayed coatings clearly differ from standard TS coatings leading to a change in their electrical, mechanical, and thermal properties when compared to their ordinarily sprayed counterparts. Responsible for this are the strongly refined microstructure and altered phase compositions not observed in standard spray coatings.

The use of nanosized feedstocks gained major interest among the research community, although it turned out that it is not always beneficial. Spraying of nanopowder containing suspensions is challenging in the sense that fully preserving the nanostructure during the whole process—starting from suspension injection—until finalization of coating formation is difficult.

Suspension spraying will for sure not replace the well-established standard thermal spray methods, but it can give an add-on in several application fields such as TBC development, fuel cell development, biofunctional coatings, tribofunctional and wear-resistant coatings, catalytically active surfaces, and much more applications that may come in the near future.

The immense potential of spraying with suspensions and liquid feedstocks in general has just been discovered. Feedstock creation in the liquid phase gives a high degree of freedom in combining powders, powder and liquid precursors, and so on. Any limitation of particle size has been removed. Where nanosized particles may be of advantage, they can be used.

For industry, however, the most important issue is the availability of stable suspensions, as well as their safe handling and storage capability. Spraying torches should be designed and optimized towards suspension spraying, ensuring safe handling, high robustness, and long-term process stability. Suspension feeders should combine robustness and high accuracy in terms of mass flow control and reproducibility. Last but not the least, feedstock and production costs will also decide about the future success of this spray method.

References

- Ashgriz, N. (Ed.), 2011. *Handbook of Atomization and Sprays: Theory and Applications*. Springer, p. 224. ISBN-10: 1441972633 (Chapter 9).
- Bathia, T., Ozturk, A., Xie, L., Jordan, E., Cetegen, B., Gell, M., Ma, X., Padture, N., 2002. Mechanisms of ceramic coating deposition in solution-precursor plasma spray. *J. Mater. Res.* 17 (9), 2363–2372.
- Bellucci, D., Bolelli, G., Cannillo, V., Gadow, R., Killinger, A., Lusvardi, L., Sola, A., Stiegler, N., 2012. High velocity suspension flame sprayed (HVSFS) potassium-based bioactive glass coatings with and without TiO₂ bond coat. *Surf. Coat. Technol.* 206, 3857–3868.
- Blazdell, P., Kuroda, S., 2000. Plasma spraying of submicron ceramic suspensions using a continuous ink jet printer. *Surf. Coat. Technol.* 123, 239–246.
- Bouyer, E., Gitzhofer, F., Boulos, M.I., 1997a. The suspension plasma spraying of bioceramics by induction plasma. *JOM* 1047-4838, 49 (2), 58–62.
- Bouyer, E., Müller, M., Dignart, N., Gitzhofer, F., Boulos, M., 1997b. Suspension plasma spraying for powder preparation. In: P. Fauchais (Ed.), *Progress in Plasma Processing of Materials*. Begell House Publishers. ISBN-13: 978-1-56700-093-1, ISBN: 1-56700-093-2.
- Bouyer, E., Müller, M., Schiller, G., Henne, R., 1999. Conversion of silanes into SiC by RF plasma technology. In: *Proceedings of the UTSC99*. ASM International, Materials Park, OH, USA.
- Brousse, E., Montavon, G., Denoirjean, A., Fauchais, P., Wittmann-Teneze, K., 2009. Gastight yttria-partially stabilized zirconia layers manufactured by suspension plasma spraying for SOFC electrolyte functional layers. In: Marple, B.R., Hyland, M.M., Lau, Y.-C., Li, C.-J., Lima, R.S., Montavon, G. (Eds.), *Proceedings of the International Thermal Spray Conference & Exposition 2009: Expanding Thermal Spray Performance to New Markets and Applications, May 4–7, 2009 (Las Vegas, NV, USA)*. ASM International, Materials Park, OH, USA, pp. 120–125.
- Cannillo, V., Bolelli, G., Gadow, R., Killinger, A., Lusvardi, L., Sola, A., Stiegler, N., 2010. Microstructure and in-vitro behaviour of a novel High Velocity Suspension Flame Sprayed (HVSFS) bioactive glass coating. *Surf. Coat. Technol.* 205, 1145–1149.
- Caruyer, C., Vincent, S., Meillot, E., Caltagirone, J.-P., 2010. Modeling the first instant of the interaction between a liquid and a plasma jet with a compressible approach. *Surf. Coat. Technol.* 205 (4), 974–979.
- Cotler, E.M., Chen, D., Molz, R.J., 2011. Pressure-based liquid feed system for suspension plasma spray coatings. *J. Therm. Spray Technol.* 20 (4), 967–973.
- Dai, Z., Faeth, G.M., 2001. Temporal properties of secondary drop breakup in the multimode breakup regime. *Int. J. Multiphase Flow* 27, 217–236.
- Darut, G., Ben-Ettouil, F., Denoirjean, A., Montavon, G., Ageorges, H., Fauchais, P., 2010. Dry sliding behavior of sub-micrometer-sized suspension plasma sprayed ceramic oxide coatings. *J. Therm. Spray Technol.* 19 (1–2), 275–285.
- Delbos, C., Fazilleau, J., Coudert, J.-F., Fauchais, P., Bianchi, L., Wittmann-Ténéze, K., 2003. Plasma spray elaboration of finely structured YSZ thin coating by liquid suspension injection. In: *Proceedings of the International Thermal Spray Conference & Exposition 2003, Advancing the Science and Applying the Technology*, ASM International, pp. 661–669.
- Deuerler, F., Buck, V., Peterseim, J., Gruner, H., 1999. Effect of hidden parameters for the plasma CVD synthesis of diamond films. *Surf. Coat. Technol.* 116–119, 428–439.

- Dongmo, E., Gadow, R., Killinger, A., Wenzelburger, M., 2009. Modeling of combustion as well as heat, mass, and momentum transfer during thermal spraying by HVOF and HVSF. *J. Therm. Spray Technol.* 18 (5–6), 896–908.
- Esfarjani, S.A., Dolatabadi, A., 2009. A 3D simulation of two-phase flow in an effervescent atomizer for suspension plasma spray. *Surf. Coat. Technol.* 203 (15), 2074–2080.
- Fauchais, P., 2008. Suspension and solution plasma or HVOF spraying. *J. Therm. Spray Technol.* 17 (1), 1–3.
- Fauchais, P., Vardelle, A., 2012. Solution and suspension plasma spraying of nanostructure coatings. In: Jazi, H. (Ed.), *Advanced Plasma Spray Applications*. InTech, ISBN 978-953-51-0349-3. Available from: www.intechopen.com/books/advanced-plasma-spray-applications/solution-and-suspension-plasmaspraying-of-nanostructure-coatings.
- Fauchais, P., Montavon, G., Lima, R.S., Marple, B.R., 2011. Engineering a new class of thermal spray nanobased microstructures from agglomerated nanostructured particles, suspensions and solutions: an invited review. *J. Phys. D.: Appl. Phys.* 44 (093001), 53.
- Gadow, R., Killinger, A., Kuhn, M., Lopez, D., 2005. Verfahren und Vorrichtung zum thermischen Spritzen von Suspensionen. German Patent DE102005038453A1.
- Gadow, R., Killinger, A., Candel Ruiz, A., Weckmann, H., Öllinger, A., Patz, O., 2007. Investigation on HVOF-technique for fabrication of SOFC's (solid oxide fuel cells) electrolyte layers. In: Marple (Hrsg.), B. (Ed.), *Proceedings of the International Thermal Spray Conference, ITSC 2007, Beijing China*. ASM International, Materials Park, OH, ISBN 978-0-87170-855-7.
- Gadow, R., Killinger, A., Stiegler, N., 2010. Hydroxyapatite coatings for biomedical applications deposited by different thermal spray techniques. *Surf. Coat. Technol.* 205, 1157–1164.
- Gell, M., 1995. Application opportunities for nanostructured materials and coatings. *Mater. Sci. Eng.* A204, 246–251.
- Gitzhofer, F., Bouyer, E., Boulos, M.I., 1994. Suspension plasma spraying. US Patent 8,296,674.
- Gruner, H., 2001. Thermal spray coatings on titanium. In: Brunette, D.M., Tengvall, P., Textor, M., Thomson, P. (Eds.), *Titanium in Medicine: Material Science, Surface Science, Engineering, Biological Responses & Medical Applications*. Springer, Berlin, pp. 376–416, ISBN-10: 3540669361.
- Ha, S.-W., Wintermantel, E. (Eds.), 2003. *Medizintechnik mit biokompatiblen Werkstoffen und Verfahren*. Springer Verlag, Berlin, ISBN 3-540-41261-1.
- Heimann, R.B., 1999. Recent trends towards improved plasma-sprayed advanced bioceramic coatings on Ti₆Al₄V implants. *Mater. Werkst.* 30 (12), 775–782.
- Heimann, R.B., 2002. Materials science of crystalline bioceramics: a review of basic properties and applications. *CMU J.* 1 (1), 23–46.
- Hench, L.L., 1991. Bioceramics: from concept to clinic. *J. Am. Ceram. Soc.* 74 (7), 1487–1510.
- Hench, L.L., Andersson, Ö., 1993. Bioactive glasses. In: Hench, L.L., Wilson, J. (Eds.), *An Introduction to Bioceramics*. World Scientific Publishing Co. Pte. Ltd., Singapore, ISBN 9789810214005.
- Henne, R., Schiller, G., Ruckdäschl, R., Lang, M., Müller, M., 1999. Plasmaspritzen von Komponenten für Hochtemperaturbrennstoffzellen (SOFC); VII. In: Nutsch (Hrsg.), G. (Ed.), *Workshop Plasmatechnik*. Verlag ISLE, Ilmenau.
- Jaworski, R., Pierlot, C., Tomaszek, R., Pawlowski, L., Znamirovski, Z., Zdanowski, J., 2007. Optimization of dielectric properties of suspension plasma sprayed hydroxyapatite coatings. *Mat.-wiss. u. Werkstofftech* 2, 125–130.
- Jaworski, R., Pierlot, C., Pawlowski, L., Bigan, M., Quivrin, M., 2008. Synthesis and preliminary tests of suspension plasma spraying of fine hydroxyapatite powder. *J. Therm. Spray Technol.* 17 (5–6), 579–584.

- Jaworski, R., Pawlowski, L., Pierlot, C., Roudet, F., Kozerski, S., Petit, F., 2010. Recent developments in suspension plasma sprayed titanium oxide and hydroxyapatite coatings. *J. Therm. Spray Technol.* 19 (1–2), 240–247.
- Jia, L., Gitzhofer, F., 2012. Induction plasma synthesis of nano-structured SOFCs electrolyte using solution and suspension plasma spraying: a comparative study. *J. Therm. Spray Technol.* 19 (3), 566–574.
- Karthikeyan, J., Berndt, C.C., Tikkanen, J., Wang, J.Y.K., Herman, A.H.H., 1997. Nanomaterial powders and deposits prepared by flame spray processing of liquid precursors. *Nanostruct. Mater.* 8 (1), 61–74.
- Kaßner, H., Siegert, R., Hathiramani, D., Vaßen, R., Stöver, D., 2008a. Application of suspension plasma spraying (SPS) for manufacture of ceramic coatings. *J. Therm. Spray Technol.* 17 (1), 115–123.
- Kaßner, H., Stuke, A., Vaßen, R., Stöver, D., 2008b. Influence of microstructure on thermal and optical properties of suspension plasma sprayed (SPS) and atmospheric plasma sprayed (APS) coatings. In: Lugscheider, E. (Ed.), *Thermal Spray 2008: Crossing Borders: Proceedings of the International Thermal Spray Conference & Exposition 2008*, pp. 573–577.
- Kaßner, H., Stuke, A., Rödiger, M., Vaßen, R., Stöver, D., 2008c. Influence of porosity on thermal conductivity and sintering in suspension plasma sprayed thermal barrier coatings. In: *Advanced Ceramic Coatings and Interfaces III*. In: *Ceram. Eng. Sci. Proc.* 29 (4), pp. 147–155.
- Killinger, A., Kuhn, M., Gadow, R., 2006. High velocity suspension flame spraying (HVSFS), a new approach for spraying nanoparticles with hypersonic speed. *Surf. Coat. Technol.* 201 (5), 1922–1929.
- Killinger, A., Gadow, R., Rempp, A., Manzat, A., 2010. Advanced ceramic tribological layers by thermal spray routes. *Adv. Sci. Technol.* 66, 106–119.
- Killinger, A., Gadow, R., Mauer, G., Guignard, A., Vaßen, R., Stöver, D., 2011. Review of new developments in suspension and solution precursor thermal spray processes. *J. Therm. Spray Technol.* 20 (4), 677–695.
- Kozerski, S., Toma, F.-L., Pawlowski, L., Leupolt, B., Latka, L., Berger, L.-M., 2010. Suspension plasma sprayed TiO₂ coatings using different injectors and their photocatalytic properties. *Surf. Coat. Technol.* 205, 980–986.
- Latka, L., Goryachev, S.B., Kozerski, S., Pawlowski, L., 2010. Sintering of fine particles in suspension plasma sprayed coatings. *Materials* 3, 3845–3866, ISSN 1996-1944, www.mdpi.com/journal/materials.
- Lima, R.S., Moreau, C., Marple, B.R., 2007. HVOF engineered from mixtures of nanostructured and submicron Al₂O₃-TiO₂ powders: an enhanced wear performance. *J. Therm. Spray Technol.* 16 (5–6), 866–872.
- Manzat, A., Killinger, A., Gadow, R., 2010. Application of supersonic flame spraying for next generation cylinder liner coatings. In: Wellnitz, J. (Ed.), *Sustainable Automotive Technologies*. Springer, Heidelberg, Berlin, ISBN 9783642107962, pp. 175–181.
- Marchand, O., Bertrand, P., Mougín, J., Comminges, C., Planche, M.-P., Bertrand, G., 2010. Characterization of suspension plasma-sprayed solid oxide fuel cell electrodes. *Surf. Coat. Technol.* 205 (4), 993–998.
- Mauer, G., Vaßen, R., 2011. Current developments and challenges in thermal barrier coatings. *Surf. Eng.* 27 (7), 477–479.
- McPherson, E.J., Dorr, L.D., Gruen, T.A., Saberi, M.T., 1995. Hydroxyapatite-coated proximal ingrowth femoral stems. A matched pair control study. *Clin. Orthop. Relat. Res.* 315, 226–230.

- Meillot, E., Vincent, S., Caruyer, C., Caltagirone, J.P., Damiani, D., 2009. From DC time-dependent thermal plasma generation to suspension plasma-spraying interactions. *J. Therm. Spray Technol.* 18 (5–6), 875–886.
- Möbius, H.-H., 1997. On the history of solid electrolyte fuel cells. *J. Solid State Electrochem.* 1, 2–16.
- Monterrubio-Badillo, C., Ageorges, H., Chartier, T., Coudert, J.F., Fauchais, P., 2006. Preparation of LaMnO_3 perovskite thin films by suspension plasma spraying for SOFC cathodes. *Surf. Coat. Technol.* 200, 3743–3756.
- Müller, P., Killinger, A., Gadow, R., 2012. Comparison between high-velocity suspension flame spraying and suspension plasma spraying of alumina. *J. Therm. Spray Technol.* 21 (6), 1120–1127.
- Nasr, G.G., Yule, A.J., Bendig, L., 2002. *Industrial Sprays and Atomization: Design, Analysis and Applications*. Springer-Verlag, Berlin, ISBN 1852334606, 9781852334604.
- Oberste Berghaus, J., Marple, B., Moreau, C., 2006. Suspension plasma spraying of nanostructured WC-12Co coatings. *J. Therm. Spray Technol.* 15 (4), 676–681.
- Oberste Berghaus, J., Legoux, J.-G., Moreau, C., Hui, R., Ghosh, D., 2007. Suspension plasma spraying of intermediate temperature SOFC components using an axial injection DC torch. *Mater. Sci. Forum* 539–543, 1332–1337.
- Oberste Berghaus, J., Legoux, J.-G., Moreau, C., Hui, R., Dece's-Petit, C., Qu, W., Yick, S., Wang, Z., Maric, R., Ghosh, D., 2008. Suspension HVOF spraying of reduced temperature solid oxide fuel cell electrolytes. *J. Therm. Spray Technol.* 17 (5–6), 700–707.
- Pawlowski, L., 2008. Finely grained nanometric and submicrometric coatings by thermal spraying: a review. *Surf. Coat. Technol.* 202, 4318–4328.
- Pawlowski, L., 2009. Suspension and solution thermal spray coatings. *Surf. Coat. Technol.* 203, 2807–2829.
- Rauch, J., 2012. Hochgeschwindigkeitsflammspritzen mit keramischen Suspensionen, Doctor thesis, University of Stuttgart. In: Gadow, R. (Ed.), *Forschungsberichte des IFKB*. Shaker Verlag, Aachen, Germany, ISBN 978-3-8440-1160-9.
- Rauch, J., Stiegler, N., Killinger, A., Gadow, R., 2009. High velocity suspension flame spraying (HVSFS): process development and industrial applications. In: Marple, B.R., Hyland, M.M., Lau, Y.-C., Li, C.-J., Lima, R.S., Montavon, G. (Eds.), *Proceedings of the ITSC 2009, Las Vegas, Nevada, USA*. TSS, ASM International, Materials Park, OH, pp. 150–155.
- Rempp, A., Killinger, A., Gadow, R., 2012. New approach to ceramic/metal-polymer multilayered coatings for high performance dry sliding applications. *J. Therm. Spray Technol.* 21 (3–4), 659–667.
- Repenning, D., 2006. Oberflächenbeschichtung, Beschichtungen auf Implantaten. In: Gradinger, R., Gollwitzer, H. (Eds.), *Ossäre Integration*. Springer Medizin Verlag, Heidelberg, Germany, ISBN 3-540-22721-0 (Chapter 3.1).
- Richter, T., 2004. *Zerstäuben von Flüssigkeiten*. Expert-Verlag, Renningen, Germany, ISBN 3-8169-2309-7.
- Schiller, G., Müller, M., Gitzhofer, F., Boulos, M.I., Heimann, R.B., 1997. Suspension plasma spraying (SPS) of cobalt spinel. In: Berndt, C.C. (Ed.), *Proceedings of the 1st United Thermal Spray Conference: Thermal Spray: A United Forum for Scientific and Technological Advances*. ASM International, Materials Park, OH, USA.
- Singhal, S.C., 2000. Advances in solid oxide fuel cell technology. *Solid State Ion.* 135, 305–313. [http://dx.doi.org/10.1016/S0167-2738\(00\)00452-5](http://dx.doi.org/10.1016/S0167-2738(00)00452-5).
- Spirin, A., Ivanov, V., Nikonov, A., Lipilin, A., Parandin, S., Khrustov, V., Spirina, A., 2012. Scandia-stabilized zirconia doped with yttria: synthesis, properties, and ageing behavior. *Solid State Ion.* 225, 448–452.

- Steinberger-Wilckens, R., de Haart, L.G.J., Vinke, I.C., Blum, L., Cramer, A., Rimmel, J., Blaß, G., Tietz, F., Quadackers, W.J., 2003. Recent results of stack development at forschungszentrum Jülich. In: Proceedings of the 8th Int. Symposium on Solid Oxide Fuel Cells (SOFC VIII), Paris, France.
- Stiegler, N., 2012. Biokeramische Schichten auf Implantaten durch thermokinetische Beschichtungsverfahren, Doctor thesis, University of Stuttgart. In: Gadow, R. (Ed.), Forschungsberichte des IFKB. Shaker Verlag, Aachen, Germany, ISBN 978-3-8440-1479-2.
- Stiegler, N., Bolelli, G., Cannillo, V., Gadow, R., Killinger, A., Lusvarghi, L., Sola, A., 2012. High-velocity suspension flame sprayed (HVSFS) hydroxyapatite coatings for biomedical applications. *J. Therm. Spray Technol.* 21 (2), 275–287.
- Stöver, D., Hathiramani, D., Vaßen, R., Damani, R.J., 2006. Plasma-sprayed components for SOFC applications. *Surf. Coat. Technol.* 0257-8972201 (5), Elsevier.
- Stuke, A., Kaßner, H., Marques, J.-L., Vaßen, R., Stöver, D., 2012. Suspension and air plasma-sprayed ceramic thermal barrier coatings with high infrared reflectance. *Int. J. Appl. Ceram. Technol.* 9 (3), 561–574.
- Tang, Z., Kim, H., Yaroslavski, I., Masindo, G., Celler, Z., Ellsworth, D., 2011. Novel thermal barrier coatings produced by axial suspension plasma spray. In: Proceedings of International Thermal Spray Conference & Exposition 2011, DVS, pp 571–575.
- Tekmen, C., Iwata, K., Tsunekawa, Y., Okumiya, M., 2010. In situ particle behavior of cast iron powder by suspension plasma spraying. *J. Therm. Spray Technol.* 19 (1–2), 255–261.
- Tikkanen, J., Gross, K.A., Berndt, C.C., Pitkänen, V., Keskinen, J., Raghu, S., Rajala, M., Karthikeyan, J., 1997. Characteristics of the liquid flame spray process. *Surf. Coat. Technol.* 90, 210–216.
- Tingaud, O., Bertrand, P., Bertrand, G., 2010. Microstructure and tribological behavior of suspension plasma sprayed Al_2O_3 and Al_2O_3 -YSZ composite coatings. *Surf. Coat. Technol.* 205 (4), 1004–1008.
- Toma, F.-L., Bertrand, G., Chwa, S.-O., Meunier, C., Klein, D., Coddet, D., 2006. Comparative study on the photocatalytic decomposition of nitrogen oxides using TiO_2 coatings prepared by conventional plasma spraying and suspension plasma spraying. *Surf. Coat. Technol.* 200, 5855–5862.
- Toma, F.-L., Berger, L.-M., Naumann, T., Langner, S., 2008. Microstructures of nanostructured ceramic coatings obtained by suspension thermal spraying. *Surf. Coat. Technol.* 202, 4343–4348.
- Toma, F.-L., Berger, L.M., Jacquet, D., Wicky, D., Villaluenga, I., de Miguel, Y.-R., Lindelø, J.-S., 2009. Comparative study on the photocatalytic behaviour of titanium oxide thermal sprayed coatings from powders and suspensions. *Surf. Coat. Technol.* 203, 2150–2156.
- VanEvery, K., Krane, M.J.M., Trice, R.W., Porter, W., Wang, H., Besser, M., Sordelet, D., Ilavsky, J., Almer, J., 2011. In-flight alloying of nanocrystalline yttria-stabilized zirconia using suspension spray to produce ultra-low thermal conductivity thermal barriers. *Int. J. Appl. Ceram. Technol.* 8 (6), 1382–1392.
- Vaßen, R., Kaßner, H., Stuke, A., Hauler, F., Hathiramani, D., Stöver, D., 2008. Advanced thermal spray technologies for applications in energy system. *Surf. Coat. Technol.* 202 (18), 4432–4437.
- Vaßen, R., Yi, Z., Kaßner, H., Stöver, D., 2009a. Suspension plasma spraying of TiO_2 for the Manufacture of photovoltaic cells. *Surf. Coat. Technol.* 203 (15), 2146–2149.
- Vaßen, R., Stuke, A., Stöver, D., 2009b. Recent developments in the field of thermal barrier coatings. *J. Therm. Spray Technol.* 18 (2), 181–186.
- Vaßen, R., Jarligo, M.O., Steinke, T., Mack, D.E., Stöver, D., 2010. Overview on advanced thermal barrier coatings. *Surf. Coat. Technol.* 205 (4), 938–942.
- von Niessen, K., Gindrat, M., Refke, A., 2010. Vapor phase deposition using plasma Spray-PVD™. *J. Therm. Spray Technol.* 19, 502–509.

- Waldbillig, D., Kesler, O., 2009. Characterization of metal-supported axial injection plasma sprayed solid oxide fuel cells with aqueous suspension plasma sprayed electrolyte layers. *J. Power Sources* 191, 320–329.
- Wang, Y., Legoux, J.-G., Neagu, R., Hui, R., Maric, R., Marple, B.R., 2010. Deposition of Nio/YSZ composite and YSZ by suspension plasma spray on porous metal. In: *Proceedings of the International Thermal Spray Conference & Exposition 2010, Thermal Spray: Global Solutions for Future Application*, DVS-ASM, pp 431–438.
- Williams, M.C., Strakey, J.P., Singhal, S.C., 2004. U.S. distributed generation fuel cell program. *J. Power Sources* 131, 79–85.
- Wittmann-Ténéze, K., Pereira, J.M., Brelivet, P., Bianchi, L., 2011. Development of composite coatings composed of a stainless steel matrix and tungsten carbide nano-inclusions by plasma spraying. In: *Proceedings of International Thermal Spray Conference & Exposition 2011*, DVS, pp. 152–156.
- Xie, L., Ma, X., Jordan, E., Pasture, N., Xiao, D., Gell, M., 2004. Deposition mechanisms of thermal barrier coatings in the solution precursor plasma spray process. *Surf. Coat. Technol.* 177–178, 103–107.

Application of solution precursor spray techniques to obtain ceramic films and coatings

5

L. Pawłowski

Abbreviations

ALE	atomic layer epitaxy
APS	atmospheric plasma spraying
CVD	chemical vapor deposition
CZTS	$\text{Cu}_2\text{ZnSnS}_4$
d.c.	direct current
DTA	differential thermal analysis
GLR	gas-to-liquid ratio
HA	hydroxyapatite
HVOF	high-velocity oxygen fuel
LSA	laser surface alloying
LSM	$\text{La}_{0.8}\text{Sr}_{0.2}\text{MnO}_3$
PECVD	plasma-enhanced chemical vapor deposition
PLD	pulsed laser deposition
PVD	physical vapor deposition
SOFC	solid oxide fuel cell
SPFS	solution precursor flame spray
SPHVOF	solution precursor high-velocity oxygen fuel
SPS	suspension plasma spraying
SPPS	solution precursor plasma spray
TBC	thermal barrier coating
TG	thermogravimetry
YBCO	$\text{YBa}_2\text{Cu}_3\text{O}_{7-x}$
YIG	yttrium iron garnet
YSZ	yttria-stabilized zirconia

Symbols

v	velocity
η	dynamic viscosity
ρ	density
σ	surface tension

Subscripts

pl plasma

s solution

5.1 Introduction

5.1.1 Definitions

Ceramic films and coatings can be obtained using chemical processes with the help of gaseous, liquid, and solid feedstock. [Table 5.1](#) shows some of the processes applying these techniques. The gaseous feedstock is very frequently applied to obtain the films using a CVD process, which consists of the “deposition of solids on a heated surface from a chemical reaction in the vapor phase,” after [Pierson \(1999\)](#). The CVD process has many variations, such as PECVD, in which reacting gases occur in a state of plasma that enhances their reactivity and enables lowering of coated substrate ([Reif and Kern, 1991](#)). The ALE process enables a growth of epitaxial single crystals by a chemical superficial reaction between the substrate and the adsorbed gas. The process was developed initially to form electroluminescent ZnS thin films by using the following reaction ([Suntola, 1989](#)):



The liquid feedstock is also used in the sol–gel film deposition process. The process consists of the preparation of an appropriate liquid precursor and its application at room temperature onto a substrate of any kind of material including metals, ceramics, and polymers by spinning, dipping, draining, or spraying. The latter is rarely applied. The solution is transformed into a sol in a process of peptization with the use of

Table 5.1 Chemical process used in manufacturing films and coatings using different feedstocks (in bold are shown the processes discussed in this chapter)

Feedstock	Process	References
Gaseous	Atomic layer epitaxy (ALE)	Suntola (1989)
	Chemical vapor deposition (CVD)	Pierson (1999)
Liquid	Sol–gel	Klein (1991)
	Electrolytic anodization	Campbell (1974)
	Solution precursor thermal spraying	Karthikeyan et al. (1997) and Pawłowski (2009)
	Spray pyrolysis	Perednis and Gauckler (2005)
Solid	Plasma or laser surface alloying (LSA)	Pawłowski (2003)

a peptizing agent such as nitric acid. After the gelation, the films, having typical thickness of around 1 μm , are heated to be densified (Pawłowski and Blanchart, 2015). The process of electrolytic anodization consists of oxidation accelerated by the presence of an electrolyte and an electric field and is traditionally used to grow alumina coatings (Campbell, 1974). The processes of spray pyrolysis and solution precursor thermal spraying with flame or with plasma will be described in a more detailed way in the next section.

Finally, the solid feedstock in the form of wire or powder is typically used in laser or plasma alloying. In such process, plasma or laser is used to melt the substrate and the powder feedstock is then injected into a liquid spot to form an alloy with the substrate (Pawłowski, 2003).

The present review focuses on the manufacturing of film coatings sprayed using liquid feedstock. In particular, the methods using the flame (low and high velocity) and plasma torches are considered. These methods are probably the newest to be studied intensively and are, under many aspects, similar to spray pyrolysis. That is why, some notions and examples of the application of the latter, being one of the first methods to use liquid feedstock for manufacturing of films and coatings, are also given.

5.1.2 History

The spray pyrolysis started to be used as early as in the 1960s of the last century (Tomar and Garcia, 1981). The method was used to synthesize films of metal oxides, sulfides, and selenides. The use of the torches generating combustion flames and plasma jets to process liquid solutions was applied at the end of the twentieth century (Karthikeyan et al., 1997). The authors were inspired by the spray pyrolysis process. The torches generating high-velocity flames (HVOF) have started to be used more recently (Killinger et al., 2011).

5.1.3 Advantages and usefulness

The use of liquid feedstock in thermal spraying instead of usual solid powders was inspired by an interest in obtaining coatings having fine microstructure. Such coatings were easier to be sprayed with liquid feedstock (solution or suspensions) than with fine solid powders (Pawłowski, 2008a). In addition, thermal spraying is a well-established technology. The use of this technology for producing such coatings is industrially advantageous because of a dense network of job shops having expertise in coating deposition, high productivity of coatings manufacturing, and also a dynamic and well-organized community of involved professionals.

5.2 Solution spray techniques

The techniques of spray discussed in this section include spray pyrolysis and thermal spray methods, that is, plasma and high- and low-velocity flame spraying. Thermal spray methods are carefully described elsewhere, and the interested reader can find additional information in such textbooks as that of Pawłowski (2008b).

5.2.1 Spray pyrolysis

The sketch of spray pyrolysis is shown in [Figure 5.1](#). The technique consists of atomizing the solution directed toward a hot substrate. The solutions of metal salts dissolved in organic or water are used generally to obtain coating of metal oxides. The atomized droplets impact the heated substrate to form lamellae and undergo a thermal decomposition. The substrate temperature is the main parameter, which influences the morphology and properties of coatings ([Perednis and Gauckler, 2005](#)). The final coating is a superposition of overlapping lamellae. The deposited coatings undergo frequently a postspray heat treatment to reach their final chemical composition.

5.2.2 Solution precursor plasma spray

The d.c. torches generate arc that heats working gases to form plasma jets. The jet's temperature, in a conventional plasma torch, reaches 14,000 K and its velocity on the nozzle exit reaches 800 m/s. The torches used in SPPS process are ([Fauchais et al., 2013](#)): (i) conventional one-cathode torches having radial introduction of solution, (ii) three-cathode torches having axial introduction of solution, and (iii) segmented anode torches. The injection of solution can be made by an atomizer or by a nozzle ([Figure 5.2](#)). The working gases used to generate the plasma are usually argon with a molecular gas such as hydrogen or nitrogen. The molecular gases are added in order to increase the thermal conductivity of the plasma. The conventional one-cathode torches have important fluctuations and instabilities depending on the kind of working gas ([Coudert and Rat, 2010](#)). The molecular gases contribute considerably the voltage

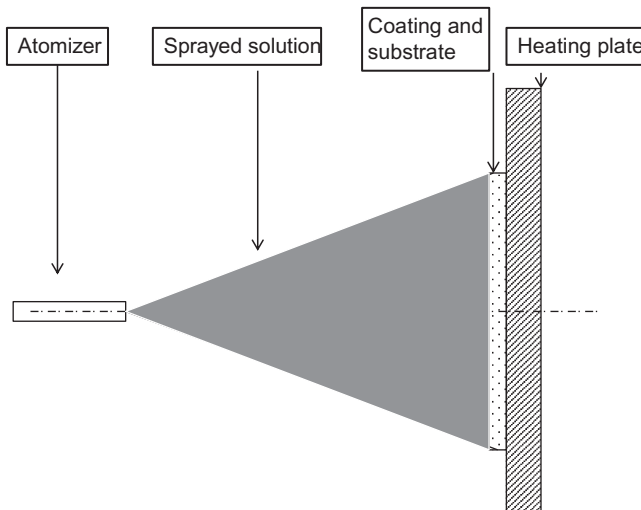


Figure 5.1 Sketch of spray pyrolysis process (inspired by [Perednis and Gauckler, 2005](#)).

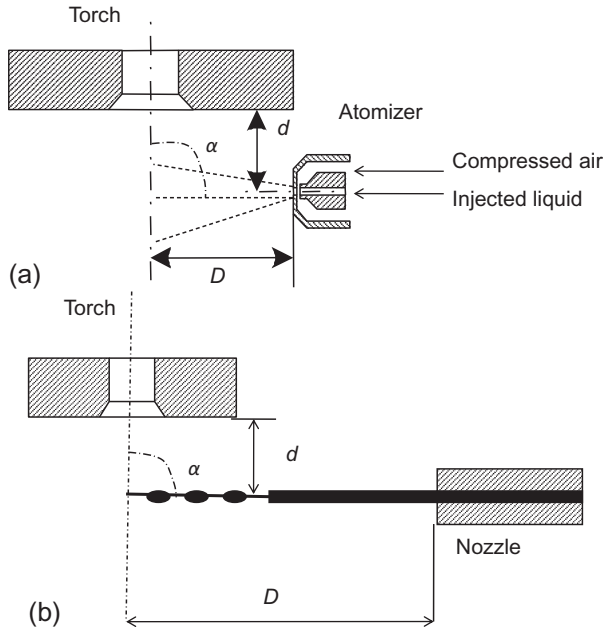


Figure 5.2 Modes of liquid feedstock injection (Pawłowski, 2009): (a) atomizer and (b) mechanical injector.

arc fluctuations in the kilohertz frequency range. The use of three-cathode torches without the use of molecular (or at least with its reduced quantity) gases may be a solution of the fluctuation problem (Vassen et al., 2010).

5.2.3 Flame spray (solution precursor flame spray, SPFS)

The flame spray torch works on a principle of combustion of a fuel gas (e.g., acetylene) in oxygen. The temperature of flame can reach 3350 K, and its velocity is in the range 80–100 m/s (Pawłowski, 2008b). The solution can be introduced axially to the flame using an atomizer, and atomizing gas may promote combustion. For example, Saremi and Valefi (2013) used hydrogen and oxygen as atomizing gases.

5.2.4 High-velocity oxygen fuel (solution precursor HVOF, SPHVOF)

The HVOF torch is fueled by a combustion hydrocarbon gases as ethylene, propylene, and many others or hydrocarbon liquids as kerosene, which is atomized prior to combustion. The combustion takes place in a chamber under high pressure, which varies from 0.3 to 4 MPa. The resulting jet issuing from a nozzle may reach temperature of about 3000 K and supersonic velocity by 2000 m/s. The solution can be injected radially using injector external to the gun, directly into the HVOF flame (as in the

suspension plasma spraying (SPS) processes shown in [Figure 5.2](#)), or axially, directly into the combustion chamber ([Killinger et al., 2011](#)).

5.3 Preparation of solutions

The precursors used for solution spraying of metal oxides films and coatings are generally the salts of metals and very frequently nitrates and acetates (see [Table 5.2](#)). The salts are mixed in a way to keep the desired stoichiometry. In this way, it is possible to obtain coatings of multioxide compound such as YBCO or YIG. Some authors, like [Sanpo et al. \(2013\)](#), used the nitrates as the initial products to start sol-gel procedure to obtain fine particles. The agent initiating the gelation was citric acid. Such additives as acetic acid modify the chemistry of solution and influence the morphology of coatings. For example, the structure of TiO_2 was changing from cracked to crack-free after the introduction of acetic acid into the solution ([Perednis and Gauckler, 2005](#)). The salts are used as a solution in water or in ethanol.

Physical properties of such solutions have been seldom measured. An example of such measurements, made for aqueous salts containing yttrium and zirconium by [Chen et al. \(2008b\)](#), showed that the properties depend on the precursor concentration. For the low molar concentration (0.6 M), the viscosity of solution was measured to be $\eta = 1.4 \times 10^{-3}$ Pa s, density $\rho = 1.05$ g/cm³, and surface tension $\sigma = 5.93 \times 10^{-2}$ N/m. The increase in the molar concentration to 2.4 M resulted in the modification of these parameters to reach the values of 7.0×10^{-3} Pa s, 1.21 g/cm³, and 4.82×10^{-2} N/m, respectively.

5.4 Phenomena occurring at spraying

The phenomena occurring during spray pyrolysis can be summarized by taking an example of spraying of metal salt solution onto a heated substrate. The most important of them is the deformation of the liquid into droplet and its thermal decomposition leading to the formation of the desired compound on the substrate ([Perednis and Gauckler, 2005](#)). The phenomena in-flight include mainly aerodynamic breakdown accompanied by the chemical reaction that occurs on the substrate.

The solution precursor thermal spraying includes more phenomena occurring in-flight before the impact with the substrate (see [Figure 5.3](#)):

- aerodynamic breakup;
- heating, vaporization, and internal precipitation;
- internal pressurization and droplet breaking-up;
- solid particle sintering, heating, and melting;
- evaporation from the melt.

The solid particles heating, melting, and evaporating during thermal spraying have been studied since more than 30 years ([Pawłowski, 1980](#)). That is why, the following sections will focus rather on the phenomena occurring in-flight before the formation of solid particles.

Table 5.2 Typical chemical composition of solution precursors used to spray

Final coating	Spray process	Coatings application	Precursor preparation	Additive	Solvent	Reference
La ₂ Zr ₂ O ₇	Spray pyrolysis	Thermal barrier	Zirconyl(IV) oxynitrate hydrate and lanthanum(III) nitrate hexahydrate, ratio 1:1, concentration 0.5 mol/L		Deionized water	Weber et al. (2013)
TiO ₂		Photocatalysis	Titanium(IV) isopropoxide and acetylacetone, ratio 1:2, concentration 6 vol. %		Ethanol	Oja et al. (2006)
YBa ₂ Cu ₃ O _{7-x}		High-temperature superconductor	Nitrates prepared from yttria+barium carbonate+copper(II) oxide mixing with nitric acid, ratio Y:Ba:Cu = 1:2:0.5, concentration 0.005 M	Nitric acid 0.1 M		Shields et al. (2002)
Yttrium iron garnet, Y ₃ Fe ₅ O ₁₂ , YIG	SPPS	Magneto-optics	Synthesis of yttrium(III) nitrate hexahydrate+iron(III) nitrate nonahydrate+citric acid monohydrate, ratio Y:Fe = 3:5, mixture 1:1 with solvents	Citric acid monohydrate	Ethanol and deionized water	Guo et al. (2005)
Cobalt ferrite, CoO·Fe ₂ O ₃		Magnetic recording and biomagnetic	Synthesis by sol-gel of cobalt(II) nitrate hexahydrate+iron(III) nitrate hexahydrate+citric acid, ratio Co:Fe = 1:2,	Citric acid as chelating agent	Water	Sanpo et al. (2013)
Alumina, Al ₂ O ₃	SPFS	Dielectric and diffusion barrier	Aluminum acetate, 1 M solution in demineralized water	Acetic acid	Demineralized water	Sivakumar et al. (2013)
Yttria-stabilized zirconia, ZrO ₂ +7 wt.% Y ₂ O ₃ , 7 YSZ		Thermal barrier	Zirconium oxynitrate+yttrium nitrate		Water	Ozturk and Cetegen (2005) and Saremi and Valefi (2013)
8 YSZ			Zirconium acetate and yttrium nitrate	Acetic acid		Govindarajan et al. (2011)

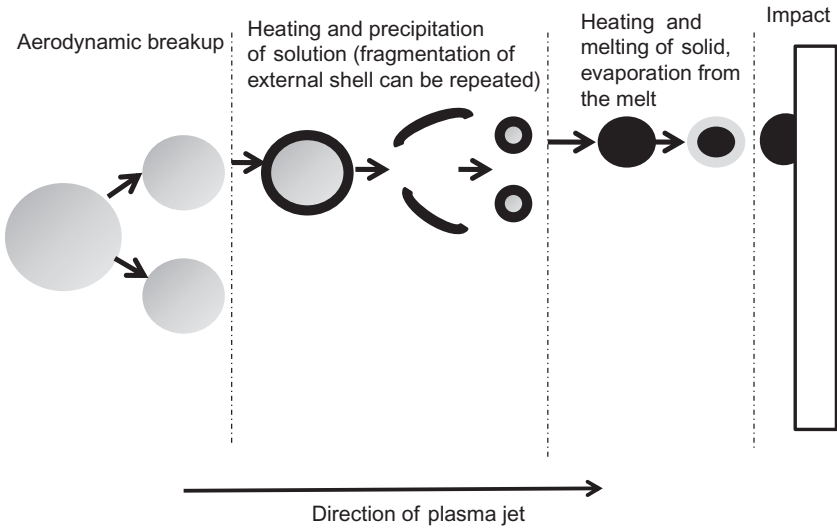


Figure 5.3 Phenomena that occur during a flight of a solution droplet in a high-temperature gas jet (inspired by [Saha et al., 2009](#)).

5.4.1 Injection

The solution may be transported to the injector with the use of a peristaltic pump or by a pneumatic transport. Its flow rate is controlled by the rotation of motor rollers or by the pressure acting on the fluid, respectively. The solution may be atomized as in spray pyrolysis process or injected as a liquid stream to the jet or flame (see [Figure 5.2b](#)). The atomization is a process of which the external energy phase is needed to break up the liquid bulk. The breakup can occur by action of (i) rotary atomizers, (ii) acoustic energy, or (iii) second phase in two-phase atomizers (see [Figure 5.2a](#)). The size of the solution droplets and their velocities in two-phase atomizers, called also effervescent ones, depend on gas-to-liquid ratio (GLR), nozzle design, and liquid properties (surface tension, density, and viscosity) ([Killinger et al., 2011](#); [Fauchais et al., 2013](#)). The size of the droplet can be calculated by an analytic formula presented by, for example, [Pawłowski \(2009\)](#) or calculated numerically from the Navier–Stokes equation ([Qian et al., 2010](#)). The sizes of the droplets obtained by atomization are in the range between 2 and 100 μm following [Fauchais et al. \(2013\)](#). On the other hand, the calculation of [Shan et al. \(2013\)](#) enabled to find the size of liquid droplet focused around 5 μm at the spray distance of 60 mm from the plasma torch. The injection as a liquid stream to a jet or a flame is possible if its dynamic pressure is greater than that of plasma:

$$\rho v_s^2 > \rho v_{pl}^2 \quad (5.2)$$

The liquid stream undergoes an aerodynamic breakup and the ligaments and large droplets are formed ([Figure 5.4](#)). Then, depending on the drag force acting on the droplet and their surface tension, the large droplet may disintegrate into smaller ones.

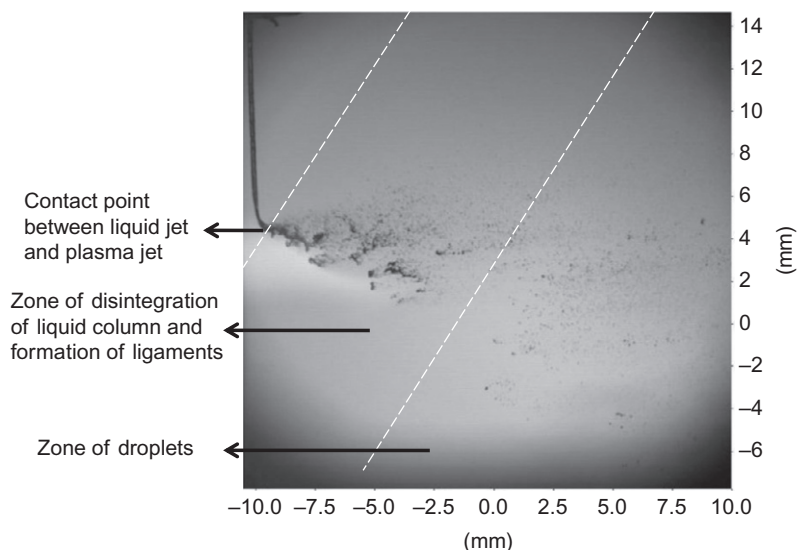


Figure 5.4 Aerodynamic interactions between liquid stream and high-temperature jet. Reproduced with permission from [Marchand et al. \(2008\)](#).

The process is called *secondary breakup* ([Basu et al., 2008](#)). This process leads to the formation of finer microstructure at the coating's buildup.

5.4.2 Thermophysical phenomena

The droplets formed by successive breakups undergo rapid vaporization of solvent in hot temperature flame or jet. Consequently, the concentration of solute at the droplets surface increases, which may lead to precipitation in this region (because the concentration of solute reaches the supersaturation limit). The process is known as homogeneous precipitation ([Saha et al., 2009](#)) and was investigated for different thermal spray processes by, for example, [Ozturk and Cetegen \(2005\)](#), [Basu and Cetegen \(2007\)](#), or [Saha et al. \(2009\)](#). The formation of shell was confirmed by experimental results as shown in [Figure 5.5](#). The formation of solid crust outside of heated liquid leads to an increase in internal pressure inside a shell. Under the action of the pressure, the shell may get fractured and smaller droplets of liquid get free and the process of precipitation and shell formation may be repeated. The processes may lead finally to the formation of solid particle as shown in [Figure 5.3](#). Small particles may undergo volumetric precipitation and transform entirely into solids. Moreover, the increase of precursor concentration may lead to volumetric precipitation ([Chen et al., 2008a,b](#)).

5.4.3 Chemical phenomena

The chemical phenomena occurring in-flight of liquid droplet depend on the used metal salt precursor and on temperature. Generally, the sequence of chemical reactions includes evaporation of solvent, precursor pyrolysis, and crystallization ([Chen et al., 2008b](#)).

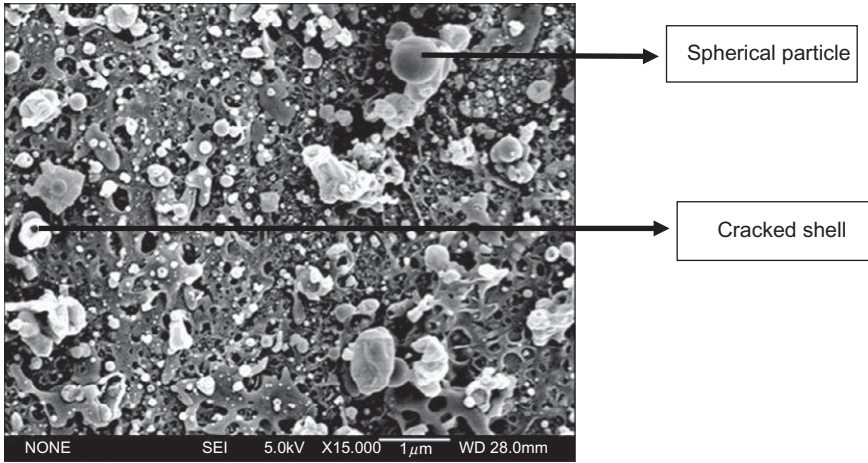
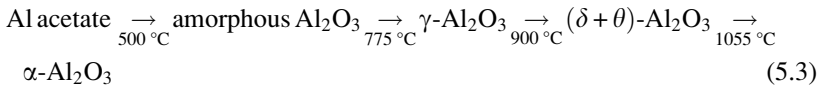


Figure 5.5 SEM of the deposition in a single pass of plasma torch spraying aqueous solution of salts including zirconium and yttrium and showing the presence of cracked shells and molten spherical particles.

Reproduced with permission from [Saha et al. \(2009\)](#).

The reactions may be followed experimentally by the, for example, use of TG/DTA techniques. These techniques were applied to find the reactions' sequence leading to the formation of 8YSZ from such precursors as zirconium acetate and yttrium nitrate. The sequence is as follows ([Govindarajan et al., 2011](#)): (i) evaporation of water at 100–220 °C, (ii) decomposition of acetate at 220–350 °C, (iii) decomposition of nitrate at 350–540 °C and formation of amorphous zirconia and yttria, (iv) formation of black tetragonal zirconia at 540–740 °C, and (v) formation of white tetragonal zirconia at 740–940 °C. Similarly, the synthesis of aluminum oxide from aluminum acetate precursor dissolved in demineralized water goes through the following steps ([Sivakumar et al., 2013](#)):



Finally, [Guo et al. \(2005\)](#) showed the sequence of reactions showing the formation of YIG from yttrium and iron nitrates and citric acid, water, and ethanol. The sequence of reactions of liquid gel tested with DTA and TGA depended of the ratio of citric acid to nitrate in the initial precursor. For the ratio equal to 0.75, the phenomena were as follows: (i) the removal of absorbed organics and moisture between 100 and 180 °C, (ii) burning of organic residues at 200–460 °C and also oxidation of residual carbon formed at combustion of organics and the rupture of citrate molecules at 300 °C, (iii) decomposition of carbonates above 700 °C, and (iv) crystallization of YIG at 755 °C. The reactions taking place at coating deposition occur in the plasma jet of flame, which has strong radial gradient of temperature. Consequently, the sequence

of chemical reactions would depend on the droplet trajectory and the particles impacting substrate.

The result of all these chemical reactions is that the synthesized coating may contain final and intermediate phases. The content of intermediate phases is influenced strongly by the above-mentioned inhomogeneity of plasma jets and flames and is difficult to predict. A design of experiments may help in reaching control of the content of these phases.

5.5 Microstructure of films and coatings synthesized by solution spray techniques

The coatings obtained using spray pyrolysis are built up from the liquid droplets that impact the heated substrate. The processes of solvent evaporation and reaction of pyrolysis take place on the heated substrate. The coatings' microstructure contains often vertical cracks, which result from the relaxation of thermal stresses generated at coating deposition. The coatings are formed on the substrates at the temperatures of 200–500 °C and are cooled down after deposition. The example of such cracking in mono- and multilayered lanthanum zirconate coatings deposited onto substrate heated to 280 °C and postspray-treated at 575 °C was presented by [Weber et al. \(2013\)](#) and is shown in [Figure 5.6](#). Such vertical cracking is useful to produce TBC because it acts in a beneficial way in enhancing the thermomechanical compliance of coatings.

The suspension precursor thermally sprayed coatings are built up from molten or heated small solid particles impacting the substrate. Such coating buildup is similar to that of conventional thermally sprayed coatings described by, for example, [Pawłowski \(2008b\)](#). The impacting particles are generally submicrometric or micrometric in size. However, the heat flux coming from plasma or flame spray torch is important, and coatings may reach temperatures as high as 770 °C reported by [Chen et al. \(2008b\)](#). Such temperatures may cause some chemical effects such as decomposition or physical effects such as sintering. The sintering of fine HA, TiO₂, and YSZ particles subjected to the heat flux at SPS process was discussed by, for example, [Łatka et al. \(2010, 2011\)](#). The results of calculation showed that sintering may be an important mechanism in coating deposition only for the particles being submicrometric in size.

The operational spray parameters influence the coatings' microstructure. A systematic study of the influence of spray parameters on the spray pattern of solution precursor plasma-sprayed 7YSZ coatings' microstructure was performed by [Xie et al. \(2004\)](#). It was shown that a low concentration of solutions may result in the formation of a columnar microstructure as shown in [Figure 5.7a](#). The mechanism of the formation of such microstructure in similar process of SPS is discussed in detail by [Sokołowski et al \(2014\)](#). The coatings having porous microstructure can be obtained by an increase of the spraying distance in SPPS process as shown by [Wang et al. \(2012\)](#) for La_{0.8}Sr_{0.2}MnO₃ deposits. The authors did also show that the use of ethanol solvent to form the solution results in coatings including better agglomerated solids than those obtained using water as solvent. This results from the additional heating of the formed solids due to the burning of alcohol in the plasma. The content of anatase

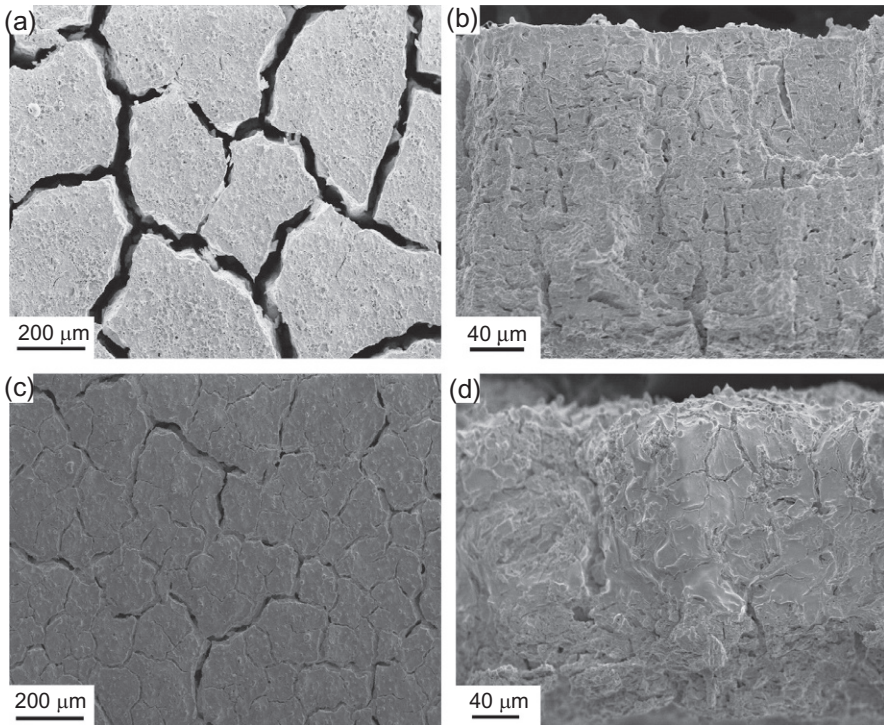


Figure 5.6 SEM microstructure of lanthanum zirconate coatings obtained by [Weber et al. \(2013\)](#) using spray pyrolysis as (a) and (b) monolayer and (c) and (d) multilayer. Reproduced with permission from [Weber et al. \(2013\)](#).

and rutile TiO_2 coatings sprayed by SPPS was tested by [Chen et al. \(2008c\)](#). The authors found that the content of rutile increases with the electric power input to the plasma torch.

5.6 Properties of films and coatings

The coatings obtained using liquid precursors are generally in the research and development stage. There are a couple of industrial applications, discussed in [Section 5.7](#), in which the coatings may be useful in a perspective. Consequently, their control is carefully done by using many techniques and the tested properties of films and coatings are closely related to their possible applications ([Pawłowski, 2008b](#)).

Thermophysical properties of 7YSZ obtained by SPPS were tested by [Jadhav et al. \(2006\)](#) for two different microstructures: (i) coating with homogeneously distributed porosity (noted as “SPPS” in [Figure 5.8](#)) and (ii) coatings with the layers of small and great porosity (noted as “layered SPPS” in [Figure 5.8](#)). The thermal conductivity

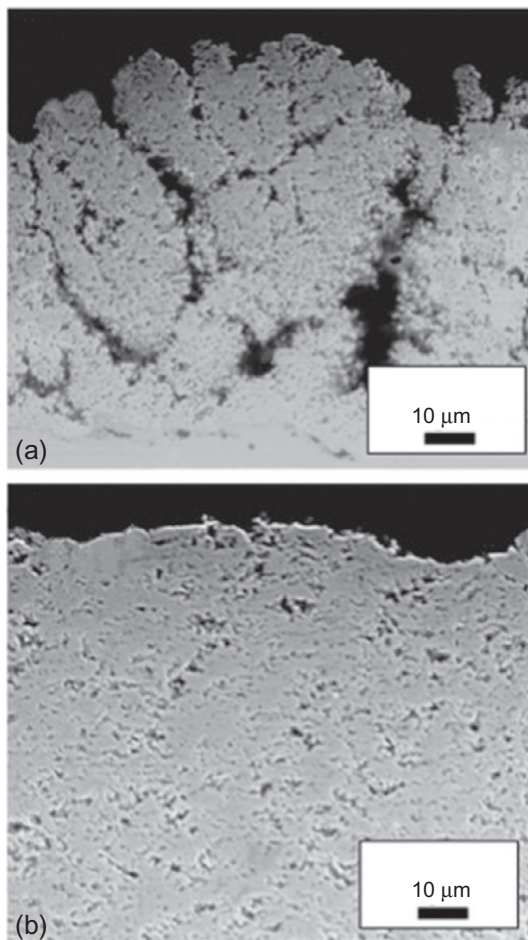


Figure 5.7 SEM microstructure of polished cross section of 7YSZ coating obtained by [Chen et al. \(2008b\)](#) using SPPS process: (a) low concentration of solution and (b) high concentration of solution. Reproduced with permission from [Chen et al. \(2008b\)](#).

was about 1 W/(mK) that is comparable for 7YSZ coatings obtained by APS shown by [Pawłowski \(2008b\)](#) but considerably lower than 2–3 W/(mK) shown for APS coatings by [Jadhav et al. \(2006\)](#). Thermal conductivity of $\text{ZrO}_2\cdot\text{La}_2\text{O}_5$ coatings obtained by spray pyrolysis was tested by [Weber et al. \(2013\)](#) and is also shown in [Figure 5.8](#). The coatings have columnar microstructure ([Figure 5.7a](#)) and their thermal conductivity is considerably lower than that of YSZ deposits ([Figure 5.8](#)). However, these coatings experience an increase of thermal conductivity with temperature, which might indicate the modification of microstructure with temperature, that is, grain sintering, and further research seems to be necessary to clarify the usefulness of this material for TBCs.

The dielectric properties of TiO_2 coatings obtained by spray pyrolysis were tested by [Oja et al. \(2006\)](#). The authors obtained coatings crystallized as anatase or rutile in function of postdeposition annealing temperature. The effective dielectric constant at

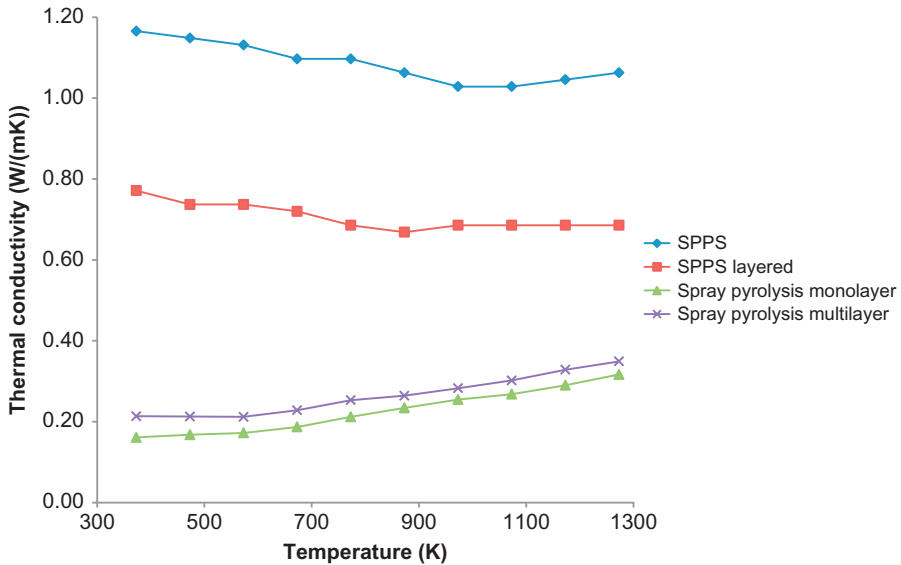


Figure 5.8 Thermal conductivity versus temperature of coatings obtained by spray pyrolysis by Weber et al. (2013) and by SPPS by Jadhav et al. (2006).

10 kHz was 36–46 for anatase and 53–70 for rutile crystallized coating. These values are well in the range of dielectric constants from 10 to 90, as found by Yang and Wolden (2006) for the titania films synthesized using such methods as CVD, PECVD, and PVD sputtering. The electrical conductivity activation energy was found to be equal to 101 meV for anatase and 63 meV for rutile structure of coatings.

High-temperature superconducting YBCO films were obtained by SPPS by Shields et al. (2002). The onset of critical temperature was found at 91 K, and critical current density at 77 K was found to be 1.2×10^5 A/cm². The values are comparable to that obtained for bulk YBCO (Desgardin et al., 2000).

All elements of an SOFC, that is, anode, electrolyte, and cathode, have been manufactured using suspension precursor spraying. The coatings produced by thermal spray methods have been reviewed by Killinger et al. (2011). The electrochemical properties of the cathode made of LSM obtained by SPPS were tested by Wang et al. (2012). In particular, the cathode polarization was found, using impedance measurements, to be equal to 1.04 Ω cm² at 850 °C and 0.15 Ω cm² at 1000 °C. The discharge capacity of the cathodes of composite powder 0.6Li₂MnO₃ · 0.4LiNi_{0.5}Mn_{0.5}O₂ prepared by spray pyrolysis was found to be from 213 to 225 mAh/g after 50 discharge cycles in a battery (Kim et al., 2013). Similar parameter for V₂O₅ cathode manufactured using SPPS was 200–250 mAh/g when cycled in the voltage window of 2–4 V (Varadaraajan et al., 2011). The anodes of SOFC on cermet coatings Ni–YSZ produced by SPPS were tested by Metcalfe et al. (2014). The performance of an entire SOFC with electrolyte produced by SPS and cathode by APS was tested in temperatures from 650 to 800 °C, and some parameters of the cell are shown in Figure 5.9.

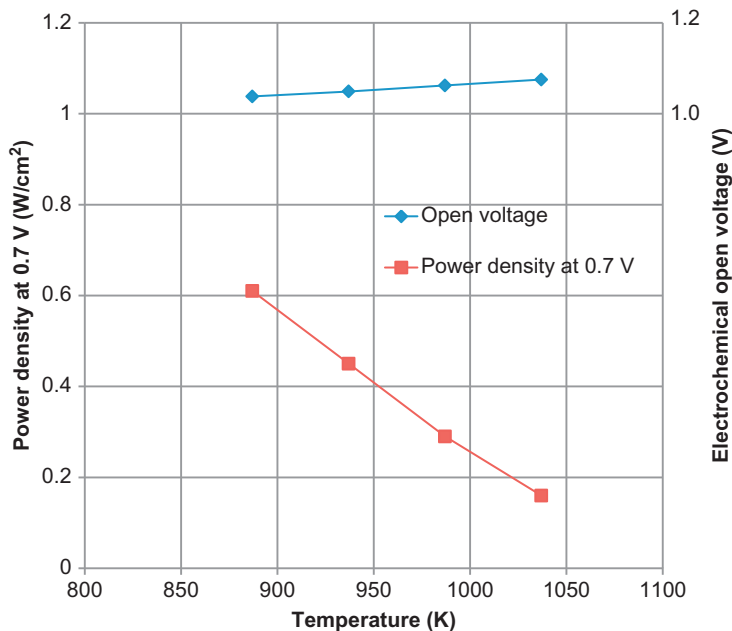


Figure 5.9 Electrochemical open-circuit voltage and power density at 0.7 V of SOF having Ni-YSZ anode manufactured using SPPS by [Metcalf et al. \(2014\)](#).

The authors found the performance of such SOFC being among the best obtained using thermal spray technology and similar design of materials. The same research group compared the performance of SOFC with YSZ electrolyte made using the technologies of SPPS and of SPS ([Marr et al., 2014](#)). Most of the parameters of electrolytes were comparable with an exception of leak rates through the electrolyte. The rates for SPPS-made electrolyte were higher than that of the one made using SPS.

The optoelectronic properties of $\text{Cu}_2\text{ZnSnS}_4$ (CZTS) films obtained by spray pyrolysis on soda lime glass were tested. The coatings of this material have been produced by such techniques as sputtering, pulsed laser deposition, and evaporation and are interesting candidates for thin films for solar cells ([Rajeshmon et al., 2011](#)). The band gap of the films was found to be 1.5 eV, their resistivity was ranging from 0.005 to 0.14 Ω cm depending on used precursor, and the mobility of the charge carriers (holes) was about 2 $\text{cm}^2/(\text{V s})$. These properties are comparable to that obtained for the coatings obtained using other film and coating methods. Finally, the optical properties of $\text{Eu:Y}_2\text{O}_3$ coatings obtained by SPPS were tested by [Chen et al. \(2012\)](#). This type of coatings, being useful in cathode ray tubes, has been deposited using sputtering, sol-gel, and PLD. The as-sprayed coatings of the chemical composition $(\text{Y}_{0.99}\text{Eu}_{0.01})_2\text{O}_3$ had desired photoluminescent properties with the strongest emission at the wavelength of about 612 nm.

5.7 Possible applications of the coatings

The solution precursor spray techniques including spray pyrolysis and thermal spray techniques are at present intensively explored. The potential advantage of these technologies can be related to the purity of the initial liquid precursors, which enable chemically pure coatings to be synthesized. The particularity of the processing of small nanoparticles renders it possible to obtain such phases as α -Al₂O₃, obtained by, for example, Sivakumar et al. (2013) or TiO₂ crystallized as anatase obtained by, for example, Chen et al. (2008c), which are difficult to obtain using conventional thermal spray technique. Finely grained microstructure has another advantage: useful small thermal conductivity while synthesizing thermally insulating coating for TBCs.

The spraying techniques seem to be easier to develop than CVD because there are no needs of thermodynamic calculations and the processes are much simpler. The capacity to coat large surfaces must be also underlined. Last but not the least, the possibility of obtaining columnar microstructure, as shown in Figure 5.7, is useful for enhancing the thermal shock resistance of coatings.

The properties of solution precursor-sprayed coatings have been tested by now for the following applications (see also Section 5.6):

- SOFC as electrodes, that is, Ni-YSZ as anode, V₂O₅ as cathode, and YSZ as solid electrolyte;
- TBC made of YSZ and of ZrO₂·La₂O₅;
- optoelectronic applications of Eu:Y₂O₃ or CZST coatings;
- dielectric coatings in electronics made of α -Al₂O₃;
- photocatalysis of TiO₂ coatings;
- magnetic applications of YIG coatings;
- biomedical coating of rutile TiO₂ coatings obtained by SPPS and postspray treated.

The further perspectives of application these coatings in industry are related to the better control of the deposition process.

References

- Basu, S., Cetegen, B.M., 2007. Modeling of thermophysical processes in liquid ceramic precursor droplets injected into a plasma jet. *Int. J. Heat Mass Transf.* 50, 3278–3290.
- Basu, S., Jordan, E.H., Cetegen, B.M., 2008. Fluid mechanics and heat transfer of liquid precursor droplets injected into high temperature plasma. *J. Therm. Spray Technol.* 17 (1), 60–72.
- Campbell, D.S., 1974. The basic principles of anodization. In: Chapman, B.N., Anderson, J.C. (Eds.), *Science and Technology of Surface Coating*. Academic Press, London, UK, pp. 87–99.
- Chen, D., Jordan, E.H., Gell, M., Wei, M., 2008a. Apatite formation on alkaline-treated dense TiO₂ coatings deposited using solution precursor plasma spray process. *Acta Biomater.* 4, 553–559.
- Chen, D., Jordan, E.H., Gell, M., 2008b. Effect of solution concentration on splat formation and coating microstructure using the solution precursor plasma spray process. *Surf. Coat. Technol.* 202, 2132–2138.

- Chen, D., Jordan, E.H., Gell, M., 2008c. Porous TiO₂ coating using the solution precursor plasma spray process. *Surf. Coat. Technol.* 202, 6113–6119.
- Chen, D., Gell, M., Jordan, E.H., Renfro, M.W., 2012. Solution precursor plasma spray Eu: Y₂O₃ phosphor coating. *Int. J. Appl. Ceram. Technol.* 9 (3), 636–641.
- Coudert, J.F., Rat, V., 2010. The role of torch instabilities in the suspension plasma spraying process. *Surf. Coat. Technol.* 205 (4), 949–953.
- Desgardin, G., Delamare, M.P., Delorme, F., Garnier, V., Giovannelli, F., Leblond-Harnois, C., Marinell, C., Monot-Laffez, I., Rouessac, V., Wang, J., 2000. Routes to obtain high performance, high T_c superconducting bulk materials. *Int. J. Inorg. Mater.* 2, 609–622.
- Fauchais, P., Joulia, A., Goutier, S., Chazelas, C., Vardelle, S., Vardelle, A., Rossignol, S., 2013. Suspension and solution plasma spraying. *J. Phys. D: Appl. Phys.* 46, 1–14.
- Govindarajan, S., Dusan, R.O., Joshi, S.V., 2011. In situ particle generation and splat formation during solution precursor plasma spraying of yttria-stabilized zirconia coatings. *J. Am. Ceram. Soc.* 94 (12), 4191–4199.
- Guo, X.Z., Ravi, B.G., Devi, P.S., Hanson, J.C., Margolies, J., Gambino, R.J., Parise, J.B., Sampath, S., 2005. Synthesis of yttrium iron garnet (YIG) by citrate-nitrate gel combustion and precursor plasma spray process. *J. Magn. Magn. Mater.* 295, 145–154.
- Jadhav, A.D., Pature, N.P., Jordan, E.H., Gell, M., Miranzo, P., Fuller Jr., E.R., 2006. Low-thermal-conductivity plasma-sprayed thermal barrier coatings with engineered microstructures. *Acta Mater.* 54, 3343–3349.
- Karthikeyan, J., Berndt, C.C., Tikkanen, J., Wang, J.Y., King, A.H., Herman, H., 1997. Preparation of nanophase materials by thermal spray processing of liquid precursors. *Nanostruct. Mater.* 9, 137–140.
- Killinger, A., Gadow, R., Mauer, G., Guignard, A., Vassen, R., Stöver, D., 2011. Review of new developments in suspension and solution precursor thermal spray processes. *J. Therm. Spray Technol.* 20 (4), 677–695.
- Kim, H.J., Choi, S.H., Son, M.Y., Kim, M.H., Lee, J.K., Kang, Y.C., 2013. Electrochemical properties of nano-meter sized 0.6Li₂MnO₃·0.4LiNi_{0.5}Mn_{0.5}O₂ composite powder prepared by flame spray pyrolysis. *Ceram. Int.* 39, 331–336.
- Klein, L.C., 1991. Sol gel methods. In: Vossen, J.L., Kern, W. (Eds.), *Thin Films Processes II*. Academic Press, Boston, pp. 501–520.
- Łatka, L., Goryachev, S.B., Kozerski, S., Pawłowski, L., 2010. Sintering of fine particles in suspension plasma sprayed coatings. *Materials (Open Access Journal)* 3 (7), 3845–3866.
- Łatka, L., Goryachev, S.B., Kozerski, S., Pawłowski, L., Łatka, L., Goryachev, S.B., Kozerski, S., Pawłowski, L., 2011. Sintering process occurring at suspension plasma sprayed of some oxides. In: *ITSC 2011, Hamburg, Allemagne, 27–29 September 2011*. ISBN 978-3-87155-268-7.
- Marchand, C., Vardelle, M., Mariaux, G., Vardelle, A., 2008. Injection and aerodynamic fragmentation of liquid precursors under plasma spray conditions. In: *Presentations of 2nd Int. Workshop on Suspension and Solution Thermal Sprayings, 14–15 June 2008, Tours, France*.
- Marr, M., Kuhn, J., Metcalfe, C., Harris, J., Kesler, O., 2014. Electrochemical performance of SOFCs having electrolytes made by suspension and solution precursor plasma spraying. *J. Power Sources* 245, 398–405.
- Metcalfe, C., Lay-Grindler, E., Kesler, O., 2014. Characterization of Ni-YSZ anodes for SOFC fabricated by SPPS with axial feedstock injection. *J. Power Sources* 247, 831–839.
- Oja, I., Mere, A., Krunk, M., Nisumaa, R., Solterbeck, C.H., Es-Souni, M., 2006. Structural and electrical characterization of TiO₂ films grown by spray pyrolysis. *Thin Solid Films* 515, 674–677.

- Ozturk, A., Cetegen, B.M., 2005. Experiments on ceramic formation from liquid precursor spray axially injected into an oxy-acetylene flame. *Acta Mater.* 53 (19), 5203–5211.
- Pawłowski, L., 1980. Optimization of arc plasma spraying parameters. *Surf. J.* 11, 8–16.
- Pawłowski, L., 2003. *Dépôts Physiques*. Presses Polytechniques et Universitaires Romandes, Lausanne, Switzerland.
- Pawłowski, L., 2008a. Finely grained nanometric and submicrometric coatings by thermal spraying: a review. *Surf. Coat. Technol.* 202, 4318–4328.
- Pawłowski, L., 2008b. *The Science and Engineering of Thermal Spray Coatings*. Wiley, Chichester, UK pp. 67–89.
- Pawłowski, L., 2009. Suspension and solution thermal spray coatings. *Surf. Coat. Technol.* 203, 2807–2829.
- Pawłowski, L., Blanchart, P., 2015. *Industrial Chemistry of Oxides for Emerging Applications*. Presses Polytechniques et Universitaires Romandes, Lausanne, Switzerland.
- Perednis, D., Gauckler, L.J., 2005. Thin film deposition using spray pyrolysis. *J. Electroceram.* 14, 103–111.
- Pierson, H.O., 1999. *Handbook of Chemical Vapor Deposition*, second ed. Noyes Publications, Norwich, NY, USA.
- Qian, L., Lin, J., Xiong, H., 2010. A fitting formula for predicting droplet mean diameter in various liquid in effervescent atomization spray. *J. Thermal Spray Technol.* 19 (3), 586–601.
- Rajeshmon, V.G., Sudha, K.C., Vijayakumar, K.P., Sanjeeviraja, C., Abe, T., Kashiwaba, Y., 2011. Role of precursor in controlling the opto-electronic properties of spray pyrolysed $\text{Cu}_2\text{ZnSnS}_4$ thin films. *Sol. Energy* 85, 249–255.
- Reif, R., Kern, W., 1991. Plasma-enhanced chemical vapor deposition. In: Vossen, J.L., Kern, W. (Eds.), *Thin Films Processes II*. Academic Press, Boston, pp. 526–559.
- Saha, A., Seal, S., Cetegen, B., Jordan, E., Ozturk, A., Basu, S., 2009. Thermo-physical processes in cerium nitrate precursor droplets injected into high temperature plasma. *Surf. Coat. Technol.* 203, 2081–2091.
- Sanpo, N., Berndt, C.C., Ang, A.S.M., Wang, J., 2013. Effect of the chelating agent contents on the topography, composition and phase of SPPS-deposited cobalt ferrite splats. *Surf. Coat. Technol.* 232, 247–253.
- Saremi, M., Valefi, Z., 2013. The effects of spray parameters on the microstructure and thermal stability of thermal barrier coatings formed by solution precursor flame spray (SFPS). *Surf. Coat. Technol.* 220, 44–51.
- Shan, Y.G., Wang, Y.L., Coyle, T., 2013. Analysis of deposits formation in plasma spraying with liquid precursors. *Appl. Therm. Eng.* 51, 690–697.
- Shields, T.C., Abell, J.S., Button, T.W., Chakalov, R.A., Chakalova, R.I., Cai, C., Haessler, W., Eickemeyer, J., de Boer, B., 2002. Deposition of YBCO films by high temperature spray pyrolysis. *Physica C* 372–376, 747–750.
- Sivakumar, G., Dusane, R.O., Joshi, S.V., 2013. A novel approach to process phase pure $\alpha\text{-Al}_2\text{O}_3$ coatings by solution precursor plasma spraying. *J. Eur. Ceram. Soc.* 33, 2823–2829.
- Sokołowski, P., Kozerski, S., Pawłowski, L., Ambroziak, A., 2014. The key process parameters influencing formation of columnar microstructure in suspension plasma sprayed zirconia coatings. *Surf. Coat. Technol.* 260, 97–106.
- Suntola, T., 1989. Atomic layer epitaxy. *Mater. Sci. Rep.* 4 (5), 261–312.
- Tomar, M.S., Garcia, F.J., 1981. Spray pyrolysis in solar cells and gas sensors. *Prog. Cryst. Growth Charact.* 4 (3), 221–248.

- Varadaraajan, V., Satishkumar, B.C., Nanda, J., Mohanty, P., 2011. Direct synthesis of nano-structured V_2O_5 films using solution plasma spray approach for lithium battery applications. *J. Power Sources* 196, 10704–10711.
- Vassen, R., Kassner, H., Mauer, G., Stöver, D., 2010. Suspension plasma spraying: process characteristics and applications. *J. Therm. Spray Technol.* 19 (1–2), 219–225.
- Wang, X.-M., Li, C.X., Li, C.J., Yang, G.J., 2012. Microstructure and polarization of $La_{0.8}Sr_{0.2}MnO_3$ cathode deposited by alcohol solution precursor plasma spraying. *Int. J. Hydrog. Energy* 37, 12879–12885.
- Weber, S.B., Lein, H.L., Grande, T., Einarsrud, M.A., 2013. Influence of the precursor solution chemistry on the deposition of thick coatings by spray pyrolysis. *Surf. Coat. Technol.* 221, 53–58.
- Xie, L., Ma, X., Ozturk, A., Jordan, E.H., Pature, N.P., Cetegen, B.M., Xiao, D.T., Gell, M., 2004. Processing parameter effects on solution precursor plasma spray process spray patterns. *Surf. Coat. Technol.* 183, 51–61.
- Yang, W., Wolden, C.A., 2006. Plasma-enhanced chemical vapor deposition of TiO_2 thin films for dielectric applications. *Thin Solid Films* 515, 1708–1713.

This page intentionally left blank

Future trends in cold spray techniques

6

R. Huang, H. Fukanuma

6.1 Introduction

Cold spray is an emerging spray coating technology that was first developed in the mid-1980s at the Institute of Theoretical and Applied Mechanics in the former Soviet Union (Alkhimov et al., 1990). This technology was discovered by accident when scientists were trying to put copper particles in a wind tunnel to study two-phase supersonic flows. Because those particles were flying so fast (exceeding critical velocity of cold spray), they started depositing on the surface of the part instead of going around it. It was this fortunate accident that they realized they could potentially use this technique to prepare coatings. In cold spraying process, spray particles are injected into a supersonic jet by compressed gas and accelerated to a high velocity (300–1500 m/s), and then, deposition will take place through intensive plastic deformation upon the impact of particles to the substrate in solid state at a temperature well below the melting point of the spray materials feedstock. Compared to traditional thermal spray processing, the most distinct characteristic of cold spray processing is its lower processing temperature, which consequently has lower thermal effects to the feedstock materials. Cold spray heats up compressed gas to accelerate the feedstock material towards the substrate with lower processing gas temperature due to the lack of combustion and plasma jets. Therefore, cold spraying is particularly suitable to prepare coatings that are sensitive to oxidation (i.e. metals) or to be applied in the fields in which oxidation and thermal influences during the coating process have to be avoided (i.e. intermetallics) (Voyer et al., 2003).

So far, cold spray technology has experienced a rapid development in about 30 years. Some mass production applications have appeared in some industrial fields. The process has been used to spray not only ductile materials such as copper (Calla et al., 2004; Xiong et al., 2005), aluminium (Morgan et al., 2004), nickel (Decker et al., 2001), nickel-based alloys (Raletz et al., 2004) and zinc (Li et al., 2010) but also metal matrix composites (Morelli et al., 2003; Wang et al., 2009), ceramic–metallic composites (cermets) (Karthikeyan et al., 2001; Lima et al., 2002) and ceramic materials (Yang et al., 2008). The characteristics and applications of this emerging technique will be presented below.

6.2 Cold spray technique

6.2.1 Characteristics of cold spray

In cold spray, feedstock particles are accelerated and heated by preheated supersonic gas. The supersonic gas is generated inside a de Laval (convergence–divergence) nozzle as shown in Figure 6.1. Gas velocity drastically increases after passing through the nozzle throat. After passing out of the nozzle, gas velocity starts to drop down since a high volume of air surrounds the high-speed jet. In contrast, preheated gas temperature intensely decreases after passing through the throat owing to the gas expansion.

Cold-sprayed particles are heated and accelerated by the working gas after being axially fed from the back of the spray gun. Figure 6.2 shows the particle velocity and temperature along the symmetrical centreline of nozzle accelerated and heated

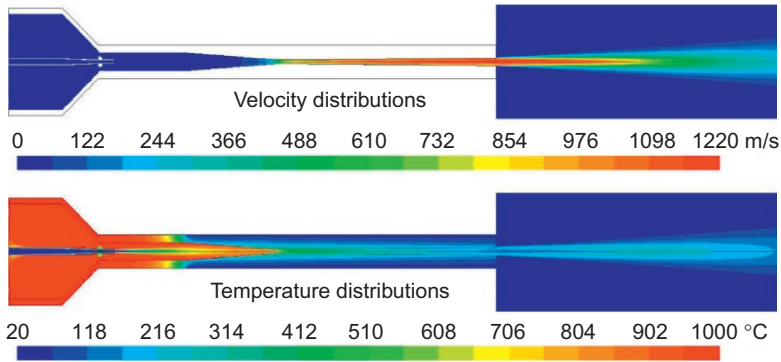


Figure 6.1 Gas velocity and temperature distributions at typical cold spray conditions.

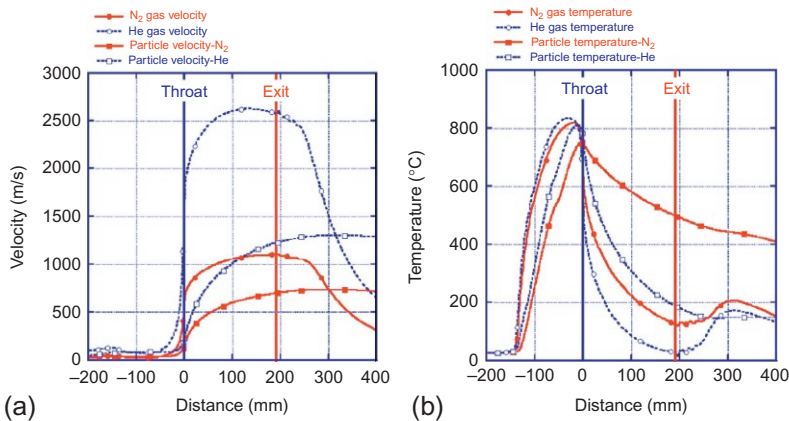


Figure 6.2 Particle velocity and temperature along the symmetrical centreline of nozzle. (a) Velocity. (b) Temperature.

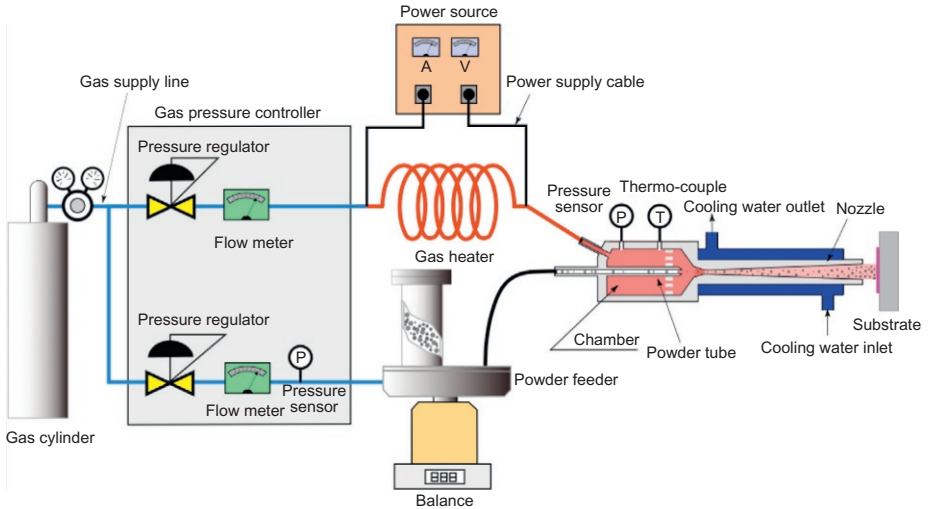


Figure 6.3 Schematic diagram of typical cold spray system.

by N_2 and He gas. Gas velocity increases to sonic speed at the nozzle throat and further increases passing through the divergence nozzle. Due to its higher sonic speed, He gas gets an extremely higher velocity than N_2 gas as shown in Figure 6.2a. As a result, the particle velocity accelerated by He gas is much higher than with N_2 gas. In contrast, the particle temperature heated by He gas is lower than the one with N_2 gas as shown in Figure 6.2b since He gas expands much more than N_2 gas in the convergence–divergence nozzle.

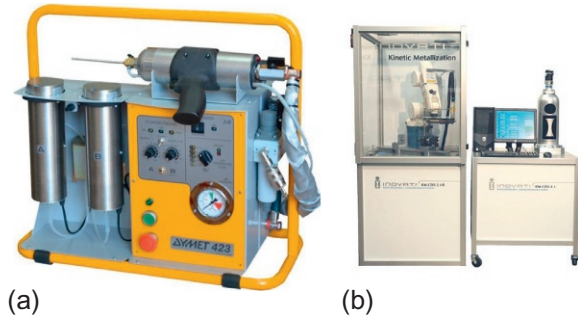
Figure 6.3 shows the schematic diagram of a typical cold spray system. The system is mainly composed of four units. The first unit is gas supply unit including the gas source and gas pressure controller. This unit provides and adjusts the working gas to a preset pressure value (up to 5 MPa for the current commercial cold spray system). The second unit is gas-preheating unit including heater and its power source. This unit is to heat working gas to a preset temperature value (up to 1100 °C for the current commercial cold spray system). The third unit is the powder supply unit, which feeds the cold spray powder to the gun at a specific rate. The last unit is the cold spray gun, which heats and accelerates the particles to a high speed with a de Laval nozzle.

6.2.2 Cold spray systems

Based on the range of working gas pressure, cold spray systems can be classified into two categories: low-pressure and high-pressure cold spray systems. It is usually considered that the boundary between low and high pressures is 1 MPa.

Typical commercial low-pressure cold spray systems are DYMET (Obninsk Center for Powder Spraying, Russia) and Kinetic Metallization (Inovati, the United States). Figure 6.4 shows the two low-pressure cold spray systems. For DYMET

Figure 6.4 Low-pressure cold spray system. (a) DYMET. (b) Inovati Kinetic Metallization.



system, compressed air is often utilized as working gas at the pressure of 0.2–0.6 MPa and temperature of 200–600 °C. Due its low gas pressure, the system is mainly used to spray low-melting-point metals such as Al, Cu and Zn. The Kinetic Metallization system employs helium or nitrogen as working gas with pressure of 0.4–0.9 MPa and temperature up to 760 °C. With nitrogen gas, Kinetic Metallization system works similarly to the DYMET system. With helium gas, higher particle velocities can be obtained and some high-melting-point metals can be deposited such as Ni. Generally, low-pressure cold spray systems have a lower deposition efficiency compared to high-pressure cold spray systems due to their lower particle velocity; consequently, they are more suited for repair or restoration.

In order to deposit high-melting-point metals at high-efficiency, high-pressure cold spray systems are required in order to cope with the high strength of the materials. The high-pressure cold spray systems can generate higher deposition efficiency owing to its higher particle velocity. Commercial high-pressure cold spray systems are mainly from four makers: Impact Innovations GmbH, Germany; Oerlikon Metco, Switzerland; CenterLine Supersonic Spray Technology, Canada and Plasma Giken Co. Ltd., Japan. The cold spray systems from Impact Innovations GmbH and Oerlikon Metco are based on the prototype of CGT Cold Gas Technology GmbH Germany. The highest capacity of cold spray system with nitrogen gas is 5 MPa of gas pressure and 1000 °C of gas temperature for Oerlikon Metco's cold spray system and 5 MPa of gas pressure and 1100 °C of gas temperature for Impact Innovations GmbH's. The cold spray system from CenterLine Supersonic Spray Technology has a lower capacity of 3.5 MPa gas pressure and 550 °C gas temperature. Radial direction powder injection is adopted for these three cold spray systems, which restrain the powder-feeding rate and increases the clogging risk. The cold spray system of Plasma Giken Co. Ltd. employs axial direction powder injection. It's capacity is 5 MPa gas pressure and 1000 °C gas temperature. The four high-pressure cold spray systems are shown in [Figure 6.5](#). With the high-pressure cold spray system, many types of metals and alloys can be deposited. [Figure 6.6](#) shows an example of deposition efficiency measured by PCS-1000 system from Plasma Giken Co. Ltd. It can be seen that the deposition efficiency of most metals and alloys exceeds 90%.



Figure 6.5 High-pressure cold spray system. (a) Impact Innovations GmbH. (b) Oerlikon Metco. (c) CenterLine Supersonic Spray Technology. (d) Plasma Giken Co. Ltd.

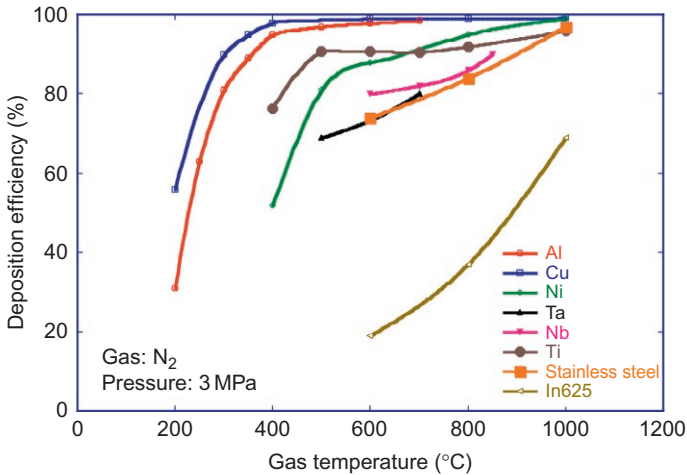


Figure 6.6 Deposition efficiency measured by Plasma Giken’s PCS-1000 cold spray system.

6.2.3 Properties of cold-sprayed coatings

As a low-temperature coating processing technology, the most outstanding advantage for the cold-sprayed coatings is the little oxidation or degradation to the feedstock material during the process. Therefore, the feedstock can be selected according to the requirements of the application. Figure 6.7 shows a Cu coating deposited by plasma spray and cold spray. Compared with plasma-sprayed coating, almost no oxides and denser microstructure can be observed in cold-sprayed coating.

In cold spray process, particle velocity is the main factor to determine the coating densification because higher particle velocity generates more intensive plastic deformation in both the impacting particles and the previously formed coating layers. Particle velocity increases with the increase of working gas temperature and pressure or using finer powder feedstock. The increased particle velocity is an advantage for the densification of cold-sprayed coatings. On the other hand, increased particle temperature contributes to the ductility of feedstock materials, consequently producing dense coatings. Particle temperature increases with working gas temperature because the particles are heated by the working gas. As shown in Figure 6.2, cold spray can accelerate particles to an extremely high velocity. Consequently, dense coatings can be obtained with few pores or cavities due to the intensive plastic deformation. Figure 6.8 shows some cross sections of typical cold-sprayed coatings. Not only soft metals such as Al but also hard metals such as Ti6Al4V can be sprayed by cold spray to produce dense coating.

Due to the intensive plastic deformation of feedstock particles and substrate, cold-sprayed coatings have extremely high bonding with the substrate if particle velocity is sufficiently high. Figure 6.9 shows the bonding strength of cold-sprayed Cu coatings on Al alloys and stainless steel substrates as a function of particle velocity (Huang et al., 2014). Even though the bonding mechanism of cold spray is still not fully understood, many researchers considered that bonding between cold-sprayed coating and substrate is mainly affected by mechanical interlock and metallurgical bonding caused by impact molten or diffusion bonding based on the shear instability. Therefore, the type of substrate significantly affects the bonding strength of cold-sprayed coatings as shown in Figure 6.9. For higher strength substrates, higher particle velocity is needed to obtain a high bonding strength. For Cu coating, more than 200 MPa of bonding

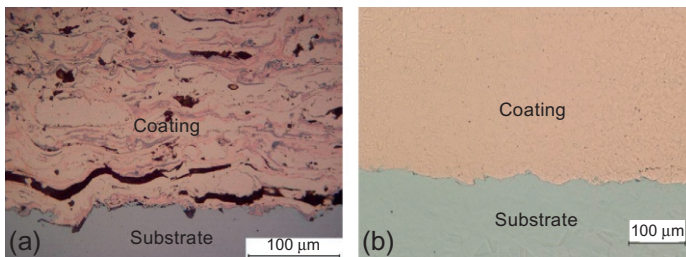


Figure 6.7 Comparison of Cu coatings deposited with plasma spray and cold spray. (a) Plasma-sprayed Cu coating. (b) Cold-sprayed Cu coating.

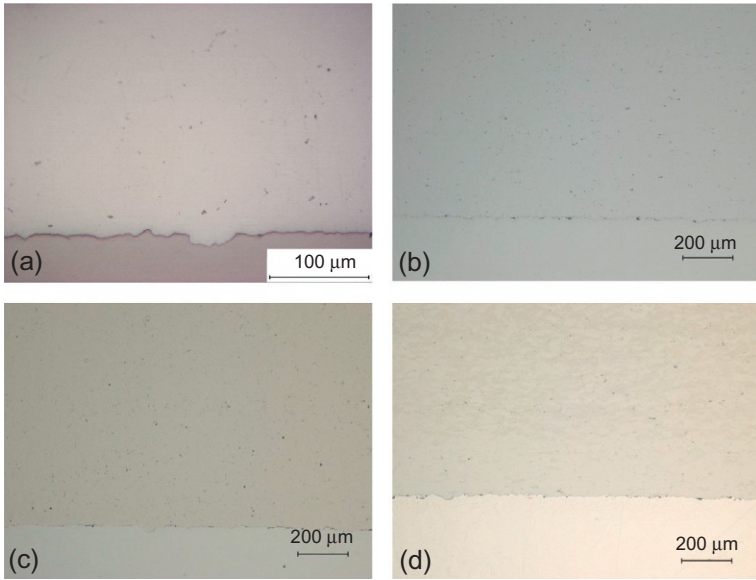


Figure 6.8 Typical cold-sprayed coatings. (a) Al. (b) Inconel 625. (c) Ni. (d) Ti6Al4V.

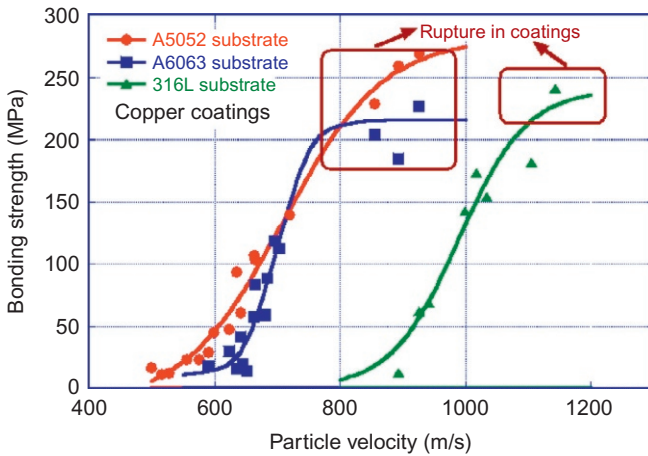


Figure 6.9 Bonding strength of cold-sprayed coatings on different substrates as function of particle velocity (Huang et al., 2014).

strength can be obtained at higher particle velocities even on stainless steel substrate as shown in Figure 6.9.

Dense cold-sprayed coatings with low oxidation also mean that they have excellent mechanical, thermal and electrical properties. Figure 6.10 shows the mechanical properties of cold-sprayed Cu coatings (Huang et al., 2015). It can be seen that the

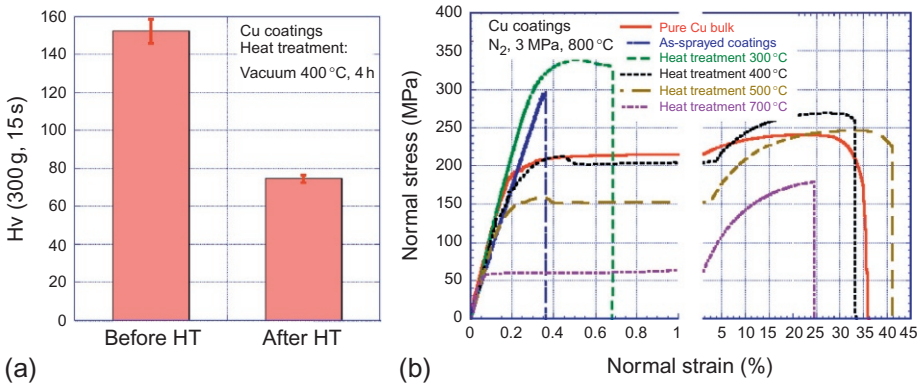


Figure 6.10 Mechanical properties of cold-sprayed coatings (Huang et al., 2015). (a). Microhardness. (b). Tensile properties.

as-sprayed coating has a higher hardness and tensile strength owing to the work hardening during particle impact process. Heat treatment can release the work hardening and amend some defects in the coating. Consequently, good elongation for cold-sprayed coatings could be expected. After suitable heat treatment, the mechanical properties of cold-sprayed coatings are more prominent than its corresponding bulk material. Therefore, it is possible that cold spray process with the subsequent heat treatment can be applied to restore some defective parts.

Figure 6.11 shows the electrical conductivity of as-sprayed Cu coating at different working gas temperatures. A high electrical conductivity can be obtained at higher working gas temperature, which results in higher particle velocity. An electrical conductivity of almost 100% IACS can be obtained even for the as-sprayed Cu coating at the spray condition of 5 MPa of gas pressure and 800 °C of gas temperature with

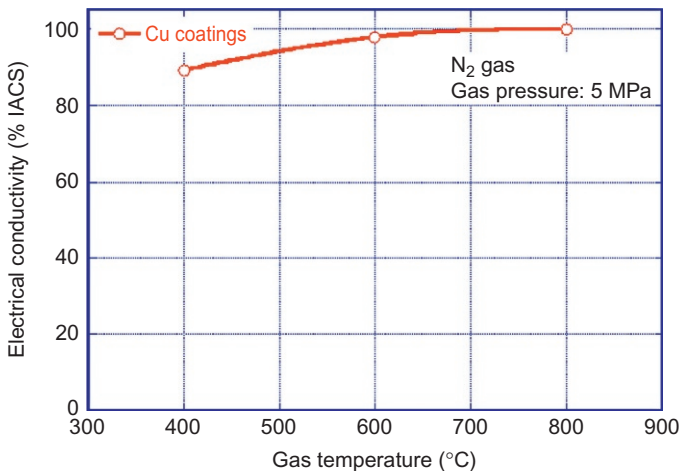


Figure 6.11 Electrical conductivity of as-sprayed Cu coating at different gas temperatures.

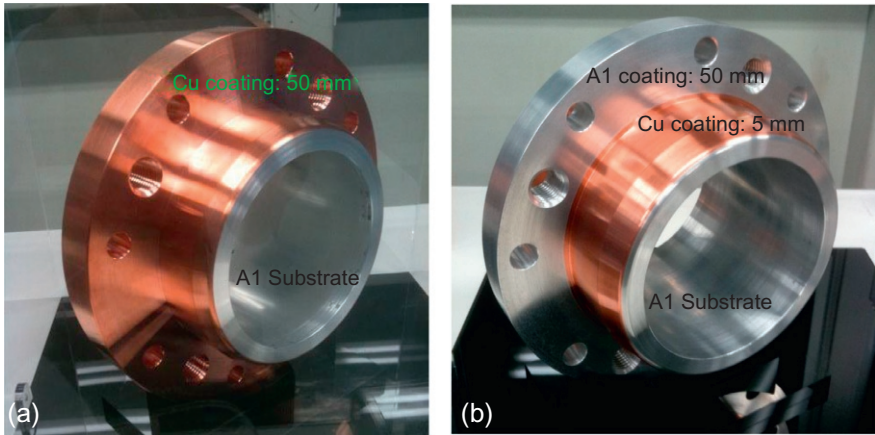


Figure 6.12 Thick coatings deposited by cold spray. (a) Thick Cu coating. (b) Thick Al coating.

nitrogen gas. The electrical conductivity of cold-sprayed Cu coating is significantly higher than that of plasma-sprayed coatings (about 20% IACS) due to the oxide and defects in the coating microstructure as shown in Figure 6.7.

For conventional thermal spray processes, the coatings are usually less than 2 mm in thickness due to the risk of delamination because of low bonding strength (generally less than 70 MPa, much lower compared to cold spray) and thermal residual stress accumulating during coating buildup. However, cold spray process can deposit not only thin films (about 40 μm) but also thick coatings (more than 50 mm) thanks to its high bonding strength. Figure 6.12 shows cold-sprayed thick Cu and Al coatings. The coatings can be deposited more than 50 mm of thickness. This can enlarge the application of cold spray to generate a dissimilar material bonding like welding or manufacture parts directly like spray forming.

6.3 Types of coatings and materials

6.3.1 Feedstock for cold spray: types and production methods

The feedstock used in cold spray process is principally metal and alloy powder because plastic deformation is necessary to form the coating during the coating building up process. Some special cermet powder can also be used in cold spray process. However, ceramic powder can hardly be sprayed by cold spray due to its poor ductility.

The metal and alloy powders used in cold spray process are mainly manufactured by atomization. Depending on the atomization medium, the atomization production methods can be classified into gas and water atomization. Figure 6.13a shows a gas-atomized Al powder. It can be seen that the gas-atomized particles show perfectly spherical shapes. Figure 6.13b shows a water-atomized Cu powder. The water-atomized particles show nearly spherical shapes. Compared with the gas-atomized

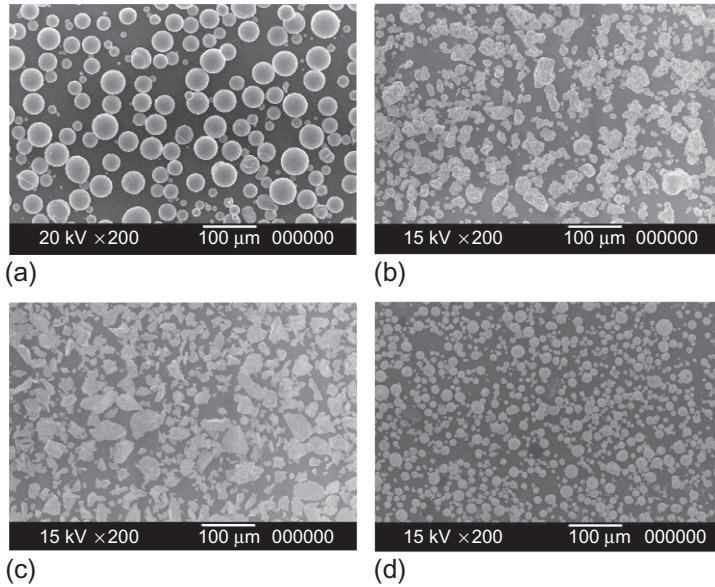


Figure 6.13 Typical cold spray powders. (a) Gas-atomized Al powder. (b) Water-atomized Cu powder. (c) Fused and crushed Ta powder. (d) Sintered WC–17%Co powder.

powder, the water-atomized powder has poorer flowability due to its morphology and lower purity.

For some high-melting-point metals such as Ta and Nb, production is difficult with atomization method because of the difficulty of melting them. Therefore, crushing is employed to manufacture the high-melting-point metal powders. [Figure 6.13c](#) shows a crushed Ta powder. Before crushing, the raw materials are made by fusion. It can be seen that the crushed particles are blocky and irregular; consequently, poorer flowability compared with the atomized powder is expected. For the cermet powder, sintering and agglomeration are employed as the same with the production method for conventional thermal spray techniques such as HVOF. [Figure 6.13d](#) shows the sintered WC–17%Co powder. It can be seen that the sintered particles have internal porosity due to the agglomeration process.

Generally, for cold spray powder, if the particle is too fine, it is difficult to feed with powder feeder due to its poor flowability. If the powder is too coarse, it is difficult to get a high particle velocity higher than the critical velocity to produce a coating and consequently difficult to form coating. Therefore, the powder diameter for cold spray process manufactured by different methods has to usually be controlled ranging from 5 to 45 μm .

6.3.2 Low-melting-point metals and alloys

Low-melting-point metals and alloys can be deposited by both low- and high-pressure cold spray systems for their high ductility. In the sections below, some typical materials for cold spray will be introduced and their properties will be discussed.

6.3.2.1 Tin (Sn)

Tin coatings and its alloys are mainly used for soldering films or as bearing materials. With a low melting point of 232 °C, Sn can only be sprayed at low gas temperature to avoid powder nozzle clogging. The deposition efficiency of tin and its alloys are more than 70% at suitable spraying conditions. Figure 6.14 shows the cross sections of different types of cold-sprayed tin alloy coatings. It can be seen that dense and uniform Sn alloy coatings can be obtained with cold spray method.

6.3.2.2 Zinc (Zn)

Zinc and its alloys are mainly used as rotational sputtering target materials and corrosion resistance. The current manufacture methods of rotational sputtering target are casting and thermal spray. All the methods have the problem of poor bonding between target materials and its base tube. High bonding strength of cold-sprayed coating made this process suitable to manufacture rotational sputtering target. In order to lower the cost, high deposition efficiency is demanded to reduce the waste of raw material. Figure 6.15 shows the cross sections of cold-sprayed Zn and its alloy coatings. It can be seen that dense and uniform Zn alloy coatings have been obtained. The deposition efficiency is 50–90% depending on its powder composition.

6.3.2.3 Aluminium (Al)

Al and Al alloy coatings are typically used for corrosion protection and repair. Al is easy to deposit by cold spray and their deposition efficiencies are often higher than 80%. Figure 6.16 shows the cross sections of cold-sprayed Al alloys. For the cold-sprayed pure Al coatings, the as-sprayed coating has a similar tensile strength as the bulk, which is more than 70 MPa. However, the elongation of cold-sprayed Al coating only can be generated via heat treatment like the Cu coating as shown in Figure 6.10b (Huang et al., 2015).

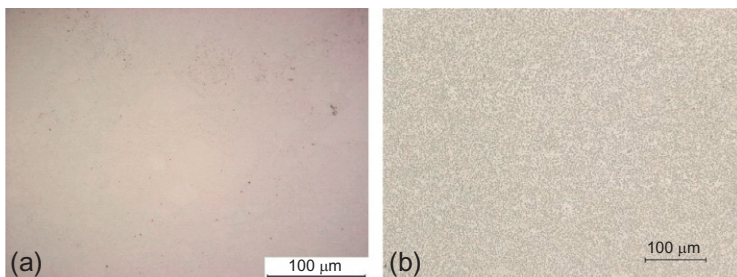


Figure 6.14 Cold-sprayed Sn alloy coatings. (a) Sn (99.7%). (b) Babbitt (Sn–¹²Sb–¹⁸Cu).

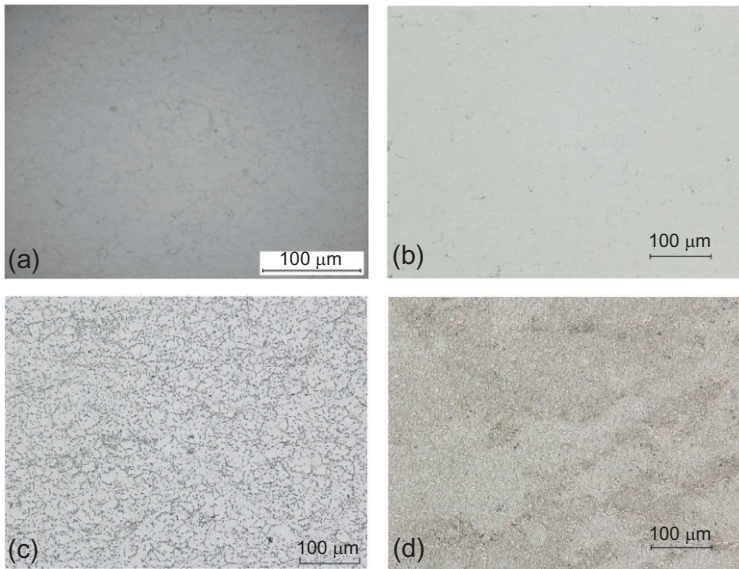


Figure 6.15 Cold-sprayed Zn alloy coatings. (a) Zn (99.7%). (b) Zn-2%Al. (c) Zn-12%Sn. (d) Zn-50%Sn.

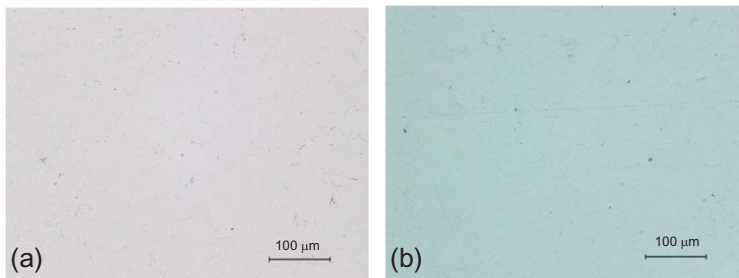


Figure 6.16 Cold-sprayed Al alloy coatings. (a) Al (99.7%). (b) A7075.

6.3.2.4 Copper (Cu)

Cu and its alloys are extremely suitable for cold spray owing to their excellent ductility. To spray pure Cu, there is almost no clogging of the nozzle and the deposition efficiency is close to 100% (see [Figure 6.6](#)). The coating has excellent mechanical and electrical properties almost the same to its bulk material as shown in [Figures 6.10](#) and [6.11](#). Moreover, the ultra adhesive strength (see [Figure 6.9](#)) with substrate extends its application in industrial field, for example, to replace explosion welding manufacturing Cu cladding in ITER Vacuum Vessel. This application will be given in the following section in detail. The cross sections of cold-sprayed Cu alloy coatings are shown in [Figure 6.17](#).

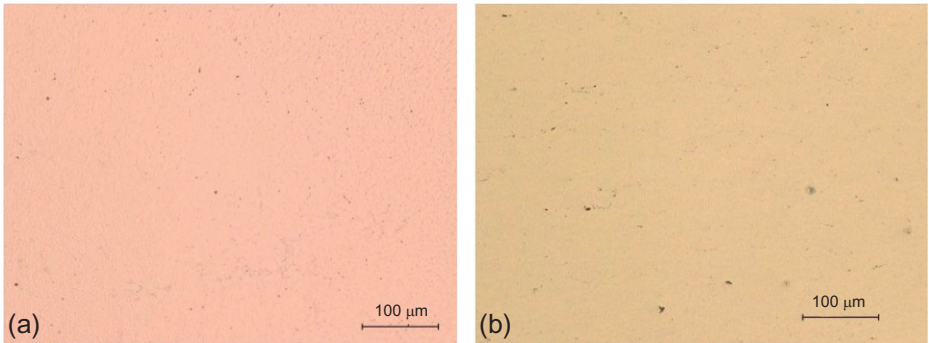


Figure 6.17 Cold-sprayed Cu alloy coatings. (a) Cu (99.7%). (b) Cu–10%Sn.

6.3.3 High-melting-point metals and alloys

High-melting-point metals and alloys can only be deposited by high-pressure cold spray systems since a higher particle velocity is needed in order to generate sufficient plastic deformation of the material due to the lower temperature of the jet compared to other thermal spray techniques. Below, some typical high-melting-point materials are shown and their properties are presented.

6.3.3.1 Iron (Fe) and stainless steel

Cold spray method can deposit pure iron and austenitic stainless steel with high deposition efficiency more than 90%. Figure 6.18 shows the cross sections of pure Fe and stainless steel 316. Compared with other thermal spray techniques, cold-sprayed coatings are denser and more uniform, that is, no oxide and defects can be observed in the cross-sectional microstructures. However, with the increase of carbon content or some non-metal elements in the steel, it becomes difficult to deposit with cold spray method due to the poor ductility. For example, the deposition efficiency of Fe–3.8%Si powder is about 50% with nitrogen gas. This is far lower than that of pure Fe.

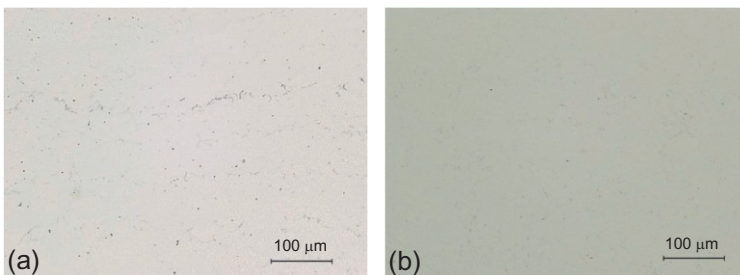


Figure 6.18 Cold-sprayed steel coatings. (a) Fe (99.9%). (b) Stainless steel 316.

6.3.3.2 Nickel (Ni)

To deposit pure Ni, high-efficiency deposition of more than 90% can be obtained with cold spray method. The coating is extremely dense as shown in [Figure 6.19a](#) even at the vicinity of coating surface. However, Ni alloy such as Inconel 718 becomes a little difficult to deposit with cold spray method because of its high strength. To make the deposition possible, a higher particle temperature is necessary to increase the ductility of the material. The capacity of working gas temperature for the current high-pressure cold spray equipment is limited to about 1100 °C. Even with the working gas of 1000 °C, the deposit efficiency of In718 is about 70%, and some porosity about 1–2% can be observed in the coating as shown in [Figure 6.19b](#).

6.3.3.3 MCrAlY alloys

MCrAlY coatings (where $M = \text{Co, Ni or Co/Ni}$) are widely applied to first- and second-stage turbine blades and nozzle guide vanes, where they may be used as corrosion-resistant overlays or as bond coats for thermal barrier coatings. Low oxide and dense coatings are necessary for the application. Cold-sprayed CoNiCrAlY and NiCoCrAlY coatings are shown in [Figure 6.20](#). It can be seen that some pores can be observed in the coatings due to the high strength of the materials. The deposition

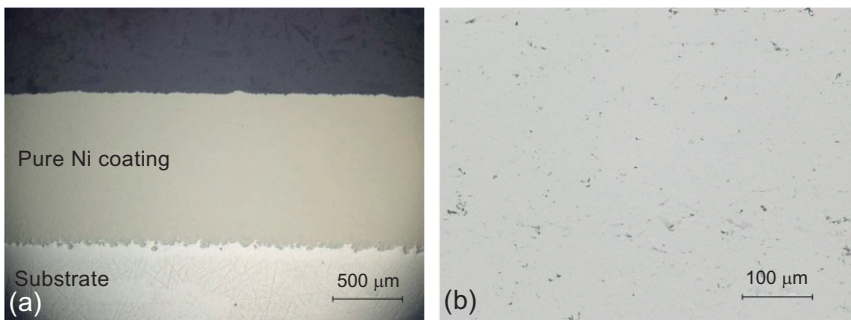


Figure 6.19 Cold-sprayed Ni alloy coatings. (a) Ni (99.9%). (b) Inconel 718.

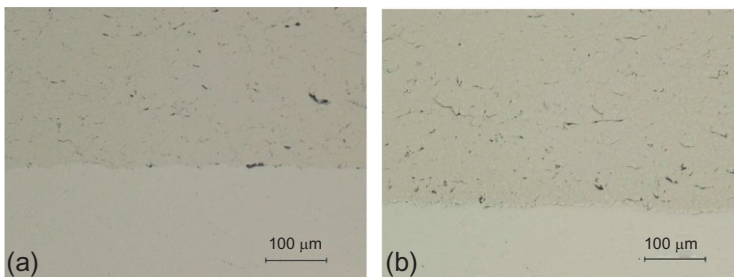


Figure 6.20 Cold-sprayed MCrAlY coatings. (a) CoNiCrAlY. (b) NiCoCrAlY.

efficiency of CoNiCrAlY can reach 50% and only about 20% for NiCoCrAlY with nitrogen gas in spite of only some difference of the elements ratio between the two materials. Compared with traditional HVOF MCrAlY coatings, the lower oxidation and receivable porosity of cold-sprayed coatings make it promising to be applied as corrosion-resistant overlays or bond coats for thermal barrier coatings.

6.3.3.4 Titanium (Ti)

It is difficult to deposit dense Ti alloy coatings especially Ti6Al4V with nitrogen gas even though its deposition efficiency is high to more than 90% owing to its high mechanical strength. However, Ti alloy coatings can be deposited extremely dense with helium gas because the higher particle velocity accelerated by He gas resulting in more intensive plastic deformation of the particle and the previous deposited coating layer. Porous Ti coatings can be used for bioapplications and dense Ti6Al4V coating can be used to repair aerospace parts. [Figure 6.21](#) shows the cross sections of cold-sprayed Ti alloy coatings. Both Ti and Ti6Al4V can be deposited significantly dense with cold spray method.

6.3.3.5 Other metals

Cold spray process is promising to deposit some refractory metal such as Ta and Nb to overcome the difficulty of traditional casting processes. Even though the melting points of Ta and Nb are extremely high, 3017 and 2477 °C, respectively, they are still suitable for cold spray process owing to their excellent ductility. The deposition efficiencies of the two materials are more than 70% and dense coatings can be obtained as shown in [Figure 6.22](#).

6.3.4 Cermets

Not only metal but also some cermets (ceramic–metallic materials) can be deposited by cold spray. [Figure 6.23](#) shows the cross sections of two cold-sprayed cermet coatings. Compared with the coatings prepared by HVOF method, the oxide and degradation are almost prevented by lower process temperature of cold spray. Therefore, the coatings are dense and uniform as shown in [Figure 6.23](#). However, compared

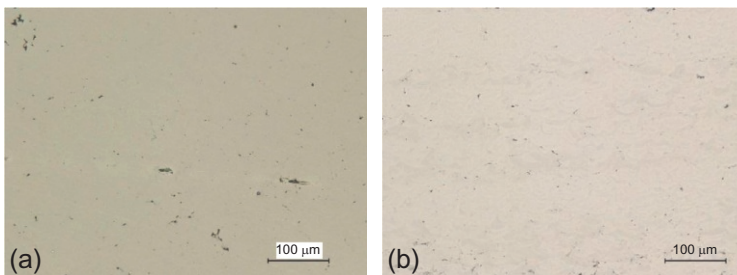


Figure 6.21 Cold-sprayed Ti alloy coatings. (a) Ti (99.7%). (b) Ti6Al4V.

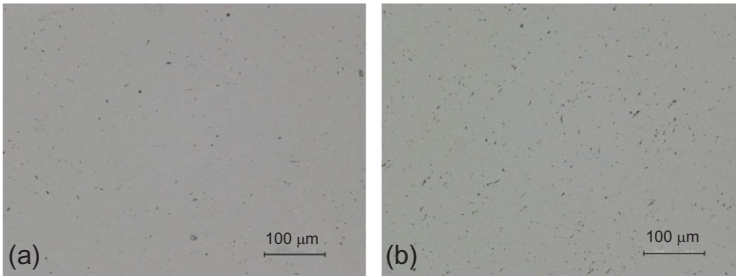


Figure 6.22 Cold-sprayed other metal coatings. (a) Ta (99.9%). (b) Nb (99.9%).

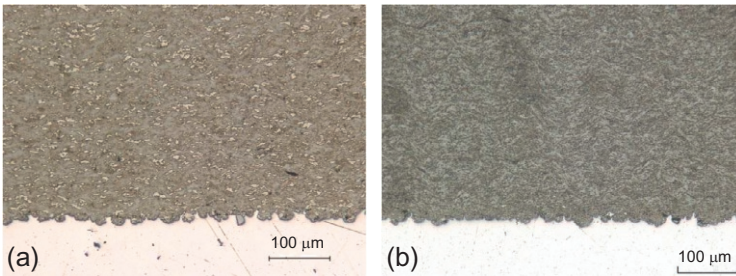


Figure 6.23 Cold-sprayed cermet coatings. (a) WC-25% stainless steel. (b) WC-17%Co.

to pure metals and alloys, the deposition efficiency of cermets is lower and commonly less than 30%. The reason of lower deposition efficiency of cermets is still unexplainable; however, it may lie in the brittle ceramic phase, which increases the rebound ratio during the impact process.

6.4 Applications

After about 30 years' development, cold spray is being increasingly used in a variety of industries. Furthermore, mass production with cold spray has appeared in Japan, the United States and Germany. Some applications of cold spray technology are given as follows.

6.4.1 Sputtering target

Sputtering target is one of the cold spray applications for mass production. Cold-sprayed rotational sputtering target has been widely used to manufacture low-emissivity glass in construction industry. Cold-sprayed sputtering target has some significant advantages compared to the target made by traditional processes such as casting. Firstly, almost no arcing (abnormal discharge) happens during sputtering

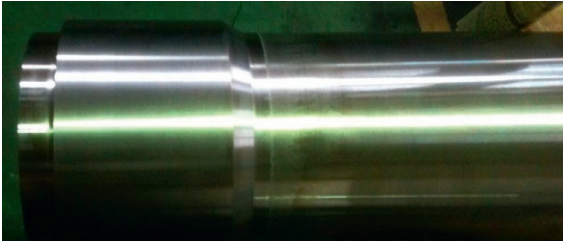


Figure 6.24 Cold-sprayed Ti target.

process because the cold-sprayed coating is dense and low oxidized. Secondly, the extreme strong bonding strength of the coating materials with the substrate (base tube, [Figure 6.24](#)) increases its water-cooling effect and prevents from the local melting during sputtering process. Thirdly, cold spray can repair the used targets consequently lowering the process costs. Up to now, cold spray can prepare the target materials of Zn, ZnAl, ZnSn, Al, Ag, Cu, Ti, Nb, Ta, etc. [Figure 6.24](#) shows a cold-sprayed Ti target.

6.4.2 Electromagnetic applications

With the advantage of its excellent electrical and magnetic properties, cold-sprayed coatings can be applied to manufacture electric conductive parts and cookware for mass production. [Figure 6.25](#) shows the cold-sprayed electric conductive part (a) of large electric current switchgear and cookware (b). The electric conductive part is made by cold spray Cu coating because almost 100% electric conductivity can be obtained with cold spray process. The cookware induction heater (IH) layer is prepared by cold-sprayed coating of iron or stainless steel at the bottom of the Al frying pan to generate the induction heat.

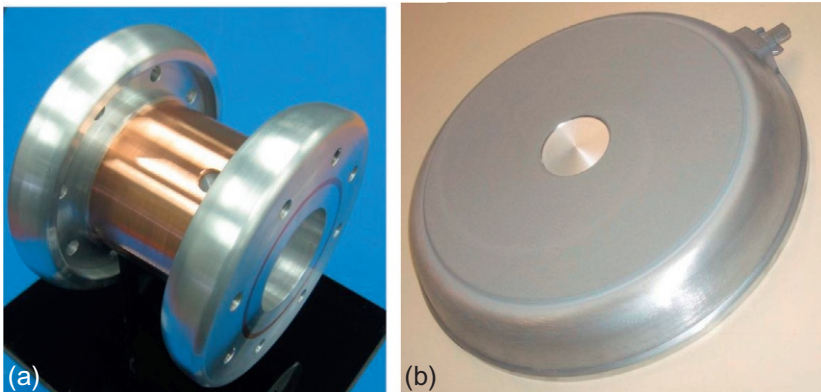


Figure 6.25 Electromagnetic applications of cold-sprayed coatings. (a) Electric conductive part. (b) Cookware.

6.4.3 Repair and restore

Repair and restore are the ideal applications of cold spray process. The application is typically used in the aircraft industry to repair Al alloys, Ni-based super alloys and Ti alloys parts. [Figure 6.26](#) shows the repaired sputtering target with cold spray at both ends.

6.4.4 Three-dimensional printer and spray forming

Since the mechanical properties of cold-sprayed coatings are excellent, this technique is perfect to be used for producing structural components ([Huang et al., 2015](#)). Therefore, cold spray can prepare thick coating as shown in [Figure 6.9](#) like spray forming or 3D printer technology to produce complex dimension parts directly.

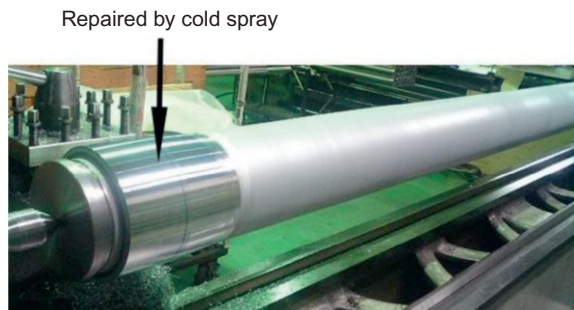
6.4.5 Other applications

Based on the excellent properties of cold-sprayed coating, some other applications are appearing. [Figure 6.27](#) shows the cold-sprayed triangular support used in ITER Vacuum Vessel. The Cu coating on the triangular support is to control plasma stability. The cold-sprayed mock-up of triangular support is shown in [Figure 6.27b](#). Superior to the cladding manufactured by overlay welding and explosion bonding, the cold-sprayed Cu coating meets all the requirements needed such as bonding strength and mechanical and electric properties under the harsh service conditions of the vacuum vessel.

6.5 Conclusions

In this chapter, cold spray technology has been briefly introduced. After three decades of development, cold spray process can deposit many metals and alloys, even ceramic-metallic composites, to form dense coatings. As a low-temperature process, almost no oxidation happens and the coatings have nearly the same microstructure as the feedstock material. Therefore, cold-sprayed coatings have excellent mechanical,

Figure 6.26 The end of sputtering target repaired by cold spray.



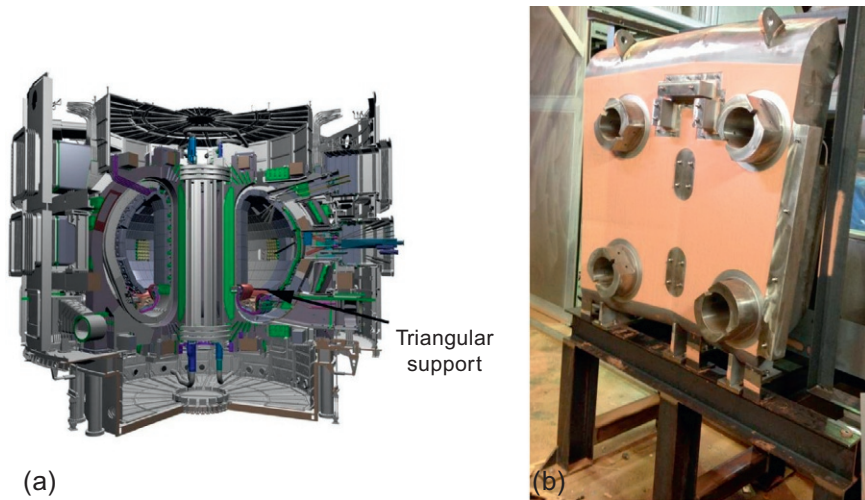


Figure 6.27 Manufacturing triangular support of ITER Vacuum Vessel with cold-sprayed technology. (a) ITER Vacuum Vessel. (b) Cold-sprayed triangular support.

thermal and electrical properties that are equivalent to the corresponding bulk materials. Moreover, cold spray can deposit thick coating with high deposition efficiency. Taking advantage of these characteristics, cold spray has been applied in some industrial fields such as electricity and aircraft industry even for mass production.

References

- Alkhimov, A.P., Kosarev, V.F., Papyrin, A.N., 1990. A method of cold gas-dynamic deposition. *Dokl. Akad. Nauk SSSR* 315, 1062–1065.
- Calla, E., McCartney, D.G., Shipway, P.H., 2004. Deposition of copper by cold gas dynamic spraying: an investigation of dependence of microstructure and properties of the deposits on the spraying conditions. In: von Hofe, D. (Ed.), *Thermal Spray 2004: Advances in Technology and Applications*, May 10–12, 2004. ASM International, Osaka, Japan, pp. 382–387.
- Decker, M.K., Neiser, R.A., Gilmore, D., Tran, H.D., 2001. Microstructure and properties of cold spray nickel. In: Berndt, C.C., Khor, K.A., Lugscheider, E.F. (Eds.), *Thermal Spray 2001: New Surfaces for a New Millennium*, May 28–30, 2001. ASM International, Singapore, pp. 433–439.
- Huang, R., Ma, W., Fukunuma, H., 2014. Development of ultra-strong adhesive strength coatings using cold spray. *Surf. Coat. Technol.* 258, 832–841.
- Huang, R., Sone, M., Ma, W., Fukunuma, H., 2015. The effects of heat treatment on the mechanical properties of cold-sprayed coatings. *Surf. Coat. Technol.* 261, 278–288.
- Karthikeyan, J., Kay, C.M., Lindemann, J., 2001. Cold sprayed nanostructured, WC–Co. In: Berndt, C.C., Khor, K.A., Lugscheider, E.F. (Eds.), *Thermal Spray 2001: New Surfaces for a New Millennium*, May 28–30, 2001. ASM International, Singapore, pp. 383–387.

- Li, W.-Y., Li, C.-J., Yang, G.-J., 2010. Effect of impact-induced melting on interface microstructure and bonding of cold-sprayed zinc coating. *Appl. Surf. Sci.* 257 (5), 1516–1523.
- Lima, R.S., Karthikeyan, J., Kay, C.M., Lindemann, J., Berndt, C.C., 2002. Microstructural characteristics of cold-sprayed nanostructured WC–Co coatings. *Thin Solid Films* 416, 129–135.
- Morelli, D., Elmoursi, A., Vansteenksite, T., Gorkiewicz, D., Gillispie, B., 2003. Kinetic spray of aluminum metal matrix composites for thermal management applications. In: Marple, B.R., Moreau, C. (Eds.), *Thermal Spray 2003: Advancing the Science and Applying the Technology*, vol. 1, May 5–8, 2003. ASM International, Orlando, FL, pp. 85–90.
- Morgan, R., Fox, P., Pattison, J., Sutcliffe, C., O'Neill, W., 2004. Analysis of cold gas dynamically sprayed aluminum deposits. *Mater. Lett.* 58 (7–8), 1317–1320.
- Raletz, F., Ezo'o, G., Vardelle, M., Ducos, M., 2004. Characterization of cold-sprayed nickel-base coatings. In: von Hofe, D. (Ed.), *Thermal Spray 2004: Advances in Technology and Applications*, May 10–12, 2004. ASM International, Osaka, Japan, pp. 344–349.
- Voyer, J., Stoltenhoff, T., Kreye, H., 2003. Development of cold gas sprayed coatings. In: Marple, B.R., Moreau, C. (Eds.), *Thermal Spray 2003: Advancing the Science and Applying the Technology*. ASM International, Materials Park, OH, pp. 71–78.
- Wang, H.-T., Li, C.-J., Yang, G.-J., Li, C.-X., 2009. Effect of heat treatment on the microstructure and property of cold-sprayed nano-structured FeAl/Al₂O₃ inter-metallic composite coating. *Vacuum* 83, 146–152.
- Xiong, T., Bao, Z., Li, T., Li, Z., 2005. Study on cold-sprayed copper coating's properties and optimizing parameters for the spraying process. In: Lugscheider, E. (Ed.), *Thermal Spray 2005: Explore Its Surfacing Potential*, May 2–4, 2005 (Basel, Switzerland). DVS-Verlag, Düsseldorf, Germany, pp. 178–184.
- Yang, G.-J., Li, C.-J., Han, F., Li, W.-Y., Ohmori, A., 2008. Low temperature deposition and characterization of TiO₂ photocatalytic film through cold spray. *Appl. Surf. Sci.* 54 (13), 3979–3982.

Current status and future prospects of warm spray technology[☆]

7

S. Kuroda, J. Kawakita, M. Watanabe, K.H. Kim, R. Molak, H. Katanoda

7.1 Introduction

Since the first papers on warm spraying (WS) were published in 2006 (Kawakita et al., 2006a,b), significant efforts have been made to understand its process fundamentals (Yokoyama et al., 2006; Watanabe et al., 2007a; Kuroda et al., 2008; Kim et al., 2008, 2009a,b,c, 2010a,b; Katanoda et al., 2009, 2011; Kim and Kuroda, 2010) and to explore potential advantages of coatings made by the process for industrial applications (Watanabe et al., 2007b; Kawakita et al., 2008a,b,c; Chivavibul et al., 2008, 2010), out of which a couple review articles have been published (Kuroda et al., 2008, 2011). Various thermal spray processes are classified schematically in terms of particles' temperature and velocity on a so-called process map (Sampath et al., 2003; Vaidya et al., 2005; Valarezo et al., 2010) as shown in Figure 7.1. In classical processes such as wire arc and flame spray, powder particles are almost completely melted and the impacting velocity onto the substrate is usually below 200 m/s. Plasma spray expanded the capability of thermal spray to a significantly high temperature range to include refractory materials such as oxides and high melting point metals into the sprayable feedstock materials. The particles' velocity increased remarkably by the advent of high-velocity oxy-fuel (HVOF) process in the 1980s, and the process includes a certain proportion of unmolten particles, of which amount depends on both the feedstock material and the process conditions. In the 1990s, cold spray (CS) was invented, by which completely solid particles are projected onto the substrate to form coatings (Papyrin et al., 2007; Tabbara et al., 2011; Stoltenhoff et al., 2002). The minimum velocity required to induce bonding of particles by adiabatic shear instability is defined as critical velocity, which depends on each metal's physical properties (Assadi et al., 2003). The WS process is based on high-velocity impact bonding of powder particles, which is similar to cold spraying, but the temperature of the particles at impact is significantly higher and often very close to the melting point of the material. Therefore, WS may be regarded as a process to fill the gap between HVOF and CS.

[☆] Much of the material in this chapter was originally published in "Current Status and Future Prospects of Warm Spray Technology" by Seiji Kuroda, Makoto Watanabe, KeeHyun Kim, and Hiroshi Katanoda, *Journal of Thermal Spray Technology*, Vol. 20, Issue 4, pp. 653–676, copyright 2011 ASM International.

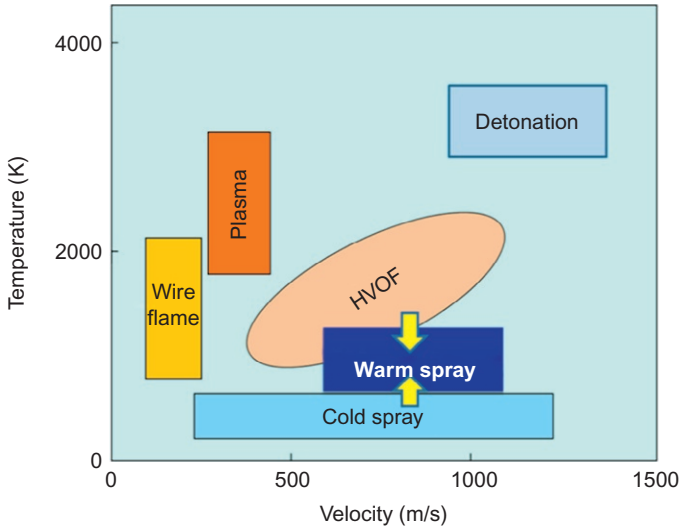


Figure 7.1 Schematic classification of various thermal spray processes by the temperature and velocity of sprayed particles.

In this chapter, the history of WS development is introduced firstly, and then, the characteristics of the process are discussed by making comparison with CS, HVOF, and high-velocity air-fuel (HVAF) spray. Microstructure and mechanical properties of WS coatings are discussed for titanium and other metals, and application-oriented results related to WC-based cermet coatings are introduced. At the end, conclusions with some future perspectives of the WS process are given.

7.2 Historical review of process development based on HVOF

7.2.1 Corrosion barrier coatings in Ultra-Steel Project

A Japanese national project called “Ultra-Steel Project” was conducted at the National Institute for Materials Science (NIMS) from 1997 to 2006. It was aimed to develop a family of new structural steels with remarkably upgraded properties such as strength, corrosion resistance, and creep resistance. The developed steels include high-strength (1800 MPa class) low-alloy steels with submicron grains, new weathering steels with Al and Si addition, high-nitrogen-bearing stainless steels, and heat-resistant steels with increased creep life by new alloy designs. As an approach to develop corrosion-resistant steels for marine environments, dense corrosion-resistant metallic coatings, which can be applied to large structures, were investigated. As an example of targeted applications, large pillars of the Tokyo Bay Aqua-Line Highway Bridge are

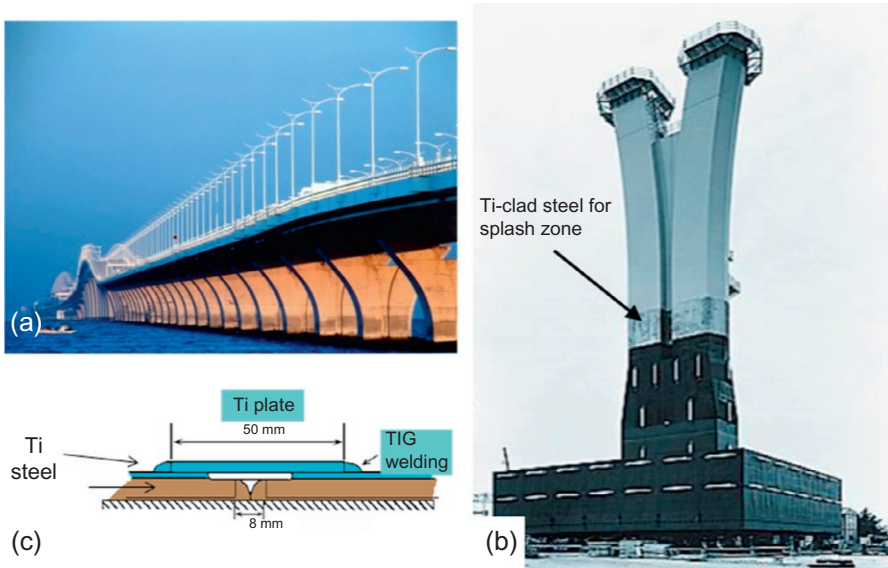


Figure 7.2 Ti-clad steel used for pillars of Tokyo Bay Aqua-Line Highway Bridge. (a) Overview, (b) pillar on the ground before installation onto the seabed, and (c) welding scheme adopted to connect the clad steel.

shown in [Figure 7.2a](#) after completion with its superstructure, and in [Figure 7.2b](#) is shown a pillar before it is sunk onto the seabed. While the immersed portion of the pillar is protected by a combination of heavy-duty painting (black) and cathodic protection by using aluminum anodes, the splash zone requires barrier-type protection. In this particular construction, titanium-clad steel was developed, and sophisticated welding procedure was adopted in order to fabricate a fully connected titanium surface layer in the zone as shown in [Figure 7.2c](#) ([Yamamoto et al., 1994](#)). If such layer of titanium or alloys such as stainless steels and Ni-base alloys can be produced by thermal spray, it should be more economical and widely applicable. With such an ambitious goal in mind, the process chosen by the authors' group was an HVOF process powered by combustion of kerosene and oxygen as it was known to produce very dense coatings with less degree of oxidation due to its high powder velocity and relatively low gas temperature as compared to other systems powdered by gaseous fuels. A schematic drawing of one commercially available apparatus (JP5000, Praxair TAFA, the United States) is shown in [Figure 7.3a](#). Kerosene and oxygen are injected into the combustion chamber, where the mixture is continuously combusted to generate a high-temperature gas at a relatively high pressure close to 1 MPa. The hot gas is allowed to emanate through a converging–diverging nozzle and becomes a supersonic jet by expansion ([Tabbara and Gu, 2009](#)). Feedstock powder is injected through a couple of powder feed ports and the powder particles are accelerated and heated in the straight barrel section. Substrate is usually placed at 200–400 mm downstream from the barrel exit, where the accelerated particles impinge onto the substrate

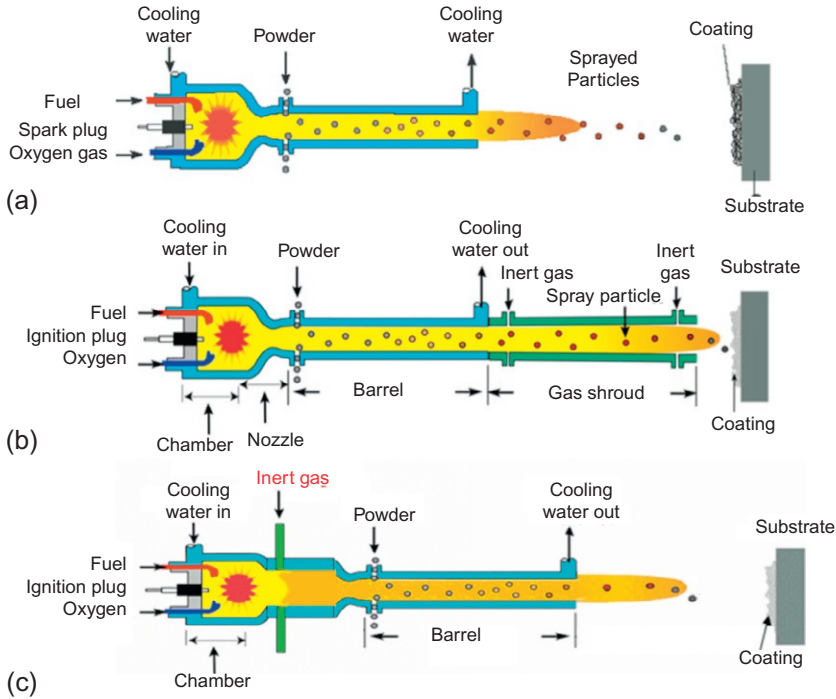


Figure 7.3 Schematic of a commercially available HVOF gun (a), improvement with a gas shroud (b), and two-stage HVOF with a mixing chamber named as warm spray (c).

at a velocity usually over 400 m/s. The temperature and velocity of powder particles are highly sensitive to the powder size and density as well as the HVOF operating conditions as described in many literatures (Swank et al., 1994; Hackett and Settles, 1995; Voggenreiter et al., 1995; Sobolev and Guilemany, 1998). Little information, however, was available about the corrosion performance of metal coatings by this process at the time (Sturgeon and Buxton, 2000).

7.2.2 Corrosion performance of HVOF coatings

At an early stage of the project, it became clear that titanium is too reactive for the process as the material reacts with the combustion gas and the surrounding air readily to become a mixture of oxides and nitrides through vigorous exothermic reaction. Therefore, more oxidation-resistant alloys such as stainless steel 316L and Hastelloy C 276 were chosen as the coating material. With these alloys, it was realized that there exist trade-off relationships between the porosity in the coatings and the oxygen contents in the coatings as shown in Figure 7.4 (Kawakita et al., 2002, 2003b; Kuroda et al., 2002). The curves in the figure indicate the limits of HVOF-sprayed deposits of 316L stainless steel and Hastelloy C. Porosity was measured by mercury intrusion porosimetry and oxygen was analyzed by the inert gas fusion technique. It was

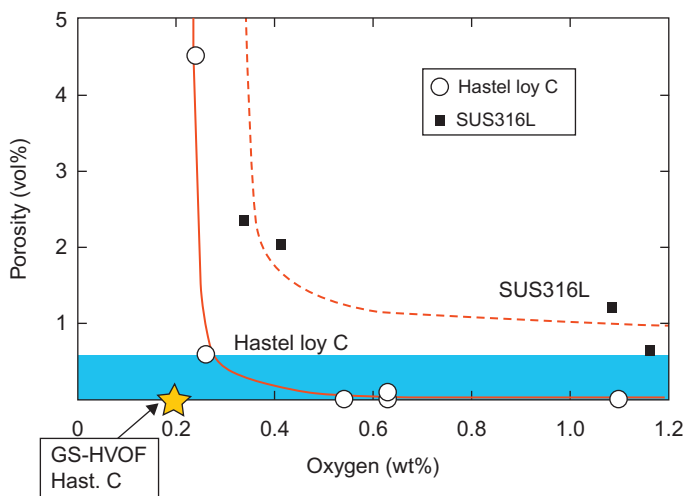


Figure 7.4 Porosity versus oxygen content of Hastelloy C and 316 stainless steel coatings fabricated by HVOF under various conditions. Two curves indicate trade-off relations between the two properties. The star plot indicates Hastelloy C coating made by the improved HVOF with a gas shroud.

indicated that one cannot achieve highly dense coatings without increasing oxidation of the feedstock materials. Another important point is that the trade-off curve is sensitive to the spray material. In the figure, one can see that with Hastelloy, it is relatively easy to eliminate pores that can be detected by MIP (porosity below 0.3 vol%), whereas it is more difficult to achieve high density with 316L SS.

When these coatings were formed on carbon steel substrates and immersed in artificial seawater in laboratory, 316L SS coatings with 600 μm were penetrated and exhibited significant amount of rusts on the coating surface after 3 days, which is the result of substrate corrosion through connected pores (Kuroda et al., 2011). Fe ions dissolved from the substrate surface traveled to the coating surface to form the rust where they meet with sufficient amount of oxygen. On the contrary, Hastelloy C coatings protected the steel substrate for periods longer than 3 months in laboratory even with the thickness of 200 μm . When the coatings were tested in the natural marine environments, however, Hastelloy C coatings with 400 μm thickness were penetrated after 3 months in the fully immersed zone (Kuroda et al., 2011).

7.2.3 Gas-shrouded HVOF and marine exposure tests

It was desired to improve the HVOF process to develop even denser and cleaner coatings and the shrouded HVOF was selected as an approach. There was already a report by Moskowitz about the effectiveness of a shrouded HVOF for corrosion problems in petrochemical plants, but the details of the process and the performance of such coatings in marine environments were not known (Moskowitz, 1993; Hacket and Settles, 1995; Pershin et al., 1998). A gas-shrouded attachment was developed at NIMS as

shown in [Figure 7.3b](#), where a tapered cylinder with two injection ports of nitrogen gas is attached to the barrel end in order to prevent the sprayed particles from contacting with the ambient air ([Kawakita et al., 2003a](#); [Kawakita and Kuroda, 2004](#)). In [Figure 7.5](#) are shown typical cross sections of Hastelloy coatings deposited by HVOF (a) and GS-HVOF (b), respectively. It is well known that the finely conjugated areas with darker contrast in the HVOF coatings compose of molten particles and oxygen concentration in these areas is high ([Yamada et al., 2001](#)). As compared to this cross section, that of GS-HVOF appears to be much more uniform and clean. Actually, the oxygen concentration of the coating on the left was 0.52 mass%, whereas that by GS-HVOF on the right was 0.20 mass%. It is not possible, however, to tell which coating is denser and contain less through pores from the cross sections. Since it was highly desirable to judge the barrier capability of these coatings in laboratory before testing them in the natural environments, a method with high sensitivity was developed ([Kawakita et al., 2003c](#)). As shown in [Figure 7.6](#), by using this technique, the specimen coated with HVOF showed a significant amount of Fe dissolution even with the coating thickness at 400 μm , whereas the GS-HVOF coating the detection limit was at 300 μm thickness. Based on these results, Hastelloy C coatings with 400 μm thickness were deposited on the two surfaces of steel plates and were tested in the marine exposure test sites. The coating protected the steel substrate in the immersed zone for 3 months, where the surface was covered with some seaweeds but the coating was intact. Summary of the test results for longer periods is shown in [Figure 7.7](#) in terms of the period until signs of corrosion were observed in the three test zones, that is, splash, tidal, and immersed zones. The specimens included coatings made by the standard HVOF in the as-sprayed condition, in the polished condition, and after heat treatment at 1273 K in vacuum for 1 h as well as these by GS-HVOF in the as-sprayed and polished conditions. The arrows in the figure indicate that the tests are still in progress after about 2 years. As a general observation, GS-HVOF coatings have longer life than the standard HVOF coatings. Life is shortest in the immersed zone, followed by the tidal zone and then the splash zone. For bulk steels and alloys, it is well established that the corrosion rate

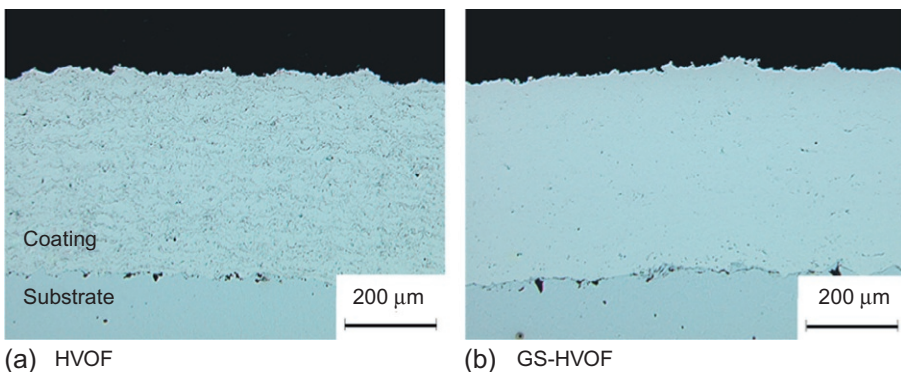


Figure 7.5 Cross sections of Hastelloy C coatings formed on steel substrate observed by optical microscopy: (a) standard HVOF and (b) HVOF with a gas-shrouded attachment.

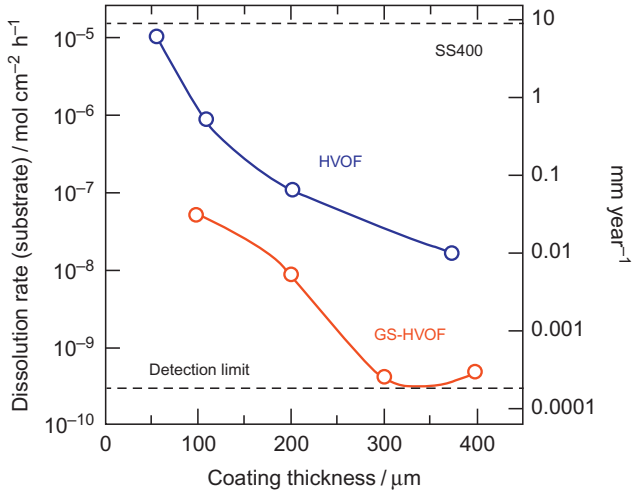


Figure 7.6 Dissolution rate of iron ions from coating specimens of Hastelloy C with different thicknesses formed on carbon steel substrate. Specimens were immersed in 0.5 M HCl solution and the solution was sampled and measured by ICP (Kawakita et al., 2003a).

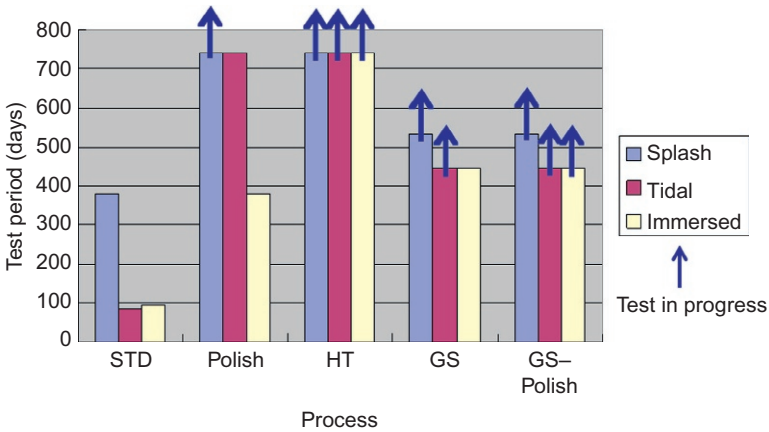


Figure 7.7 Summarized results of marine exposure tests showing the periods until appearance of corrosion damage of HVOF-sprayed Hastelloy C coatings. STD: standard HVOF, polish: polished standard HVOF, HT: heat-treated HVOF coating, GS: gas-shrouded HVOF, GS-polish: polished GS-HVOF coating. Test was conducted in the splash, tidal, and immersed zones.

in the splash zone is significantly higher than these in the other two zones because of the abundant supply of oxygen, water, and chlorides (LaQue, 1975). The situation is totally different for these sprayed coatings because the most damaging reaction of water invasion through the connected pores and substrate dissolution takes place during the wetted time. It should be noted that surface polishing has an effect to extend the life of these

coatings at least by a factor of two. Heat treatment was remarkably effective because it closes the connected pores and homogenizes the coating microstructure. Such heat treatment, however, is not applicable to large structures, and many substrate materials do not allow the treatment due to their lower melting points or destruction of the controlled microstructure.

Unfortunately, the efforts in this project did not result in successful fabrication of reliable pore-free barrier coatings. Serious criticism against this type of technology nested in the fact that if such coating should be penetrated by either poor quality control during fabrication or unpredicted mechanical damage, the coating–substrate interface will be preferentially corroded due to the galvanic coupling between the noble coating and the less noble steel substrate and will result in fatal debonding of the coating over the entire area in a relatively short time.

Nevertheless, several lessons were obtained:

- (1) The combustion gas jet in HVOF is too reactive to spray reactive metals such as titanium.
- (2) Even though one can find inferior coatings for corrosion protection rather easily by various testing methods, it is not easy to characterize coating that has a long service life in marine environment in the unit of years.
- (3) Classical metallographic preparation is not effective to find through pores detrimental to the service life of coatings made by high-velocity thermal spray processes such as HVOF.

In order to facilitate spraying of more reactive metals such as titanium, another modification of HVOF has been developed as shown in [Figure 7.3c](#). A mixing chamber was inserted in between the combustion chamber and the powder feed ports in order to mix the combustion gas with room-temperature nitrogen gas so that the gas temperature and composition at the powder injection position can be controlled in a wide range. This two-stage HVOF has been named as “warm spray” as its process characteristics occupy a position between HVOF and CS as discussed in more detail in the next chapter. It must be noted here that lowering of the gas temperature of HVOF spray by mixing the combustion gas jet in the expanded supersonic region with a room-temperature gas or water mist was patented by [Browning \(1994\)](#). He also patented the idea of spraying powder particles below the melting point but sufficiently higher temperature to soften the material substantially ([Browning, 1993](#)). The WS process by the present authors is essentially based on the same concept, but the gas mixing is achieved before the expansion into a supersonic jet, which is known to be much more effective ([Papamoschou and Roshko, 1988](#)).

7.3 Process characteristics of WS

7.3.1 *Numerical simulation of warm spraying and comparison with other processes*

There are several diagnostic devices for measuring the temperature and velocity of particles during thermal spraying. Another useful approach is numerical simulation because it can analyze flow fields and particle behavior inside the spraying apparatus, thereby saving much of the time and cost needed for experiments. In this chapter, the

method and results of the numerical simulation of the WS process, as well as that of the HVOF process for comparison, are described.

In the following calculations of combustion and mixing, nine gas species (CO , CO_2 , H_2O , H_2 , H , OH , O_2 , O , and N_2), which follow the equation of state, were included (Katanoda et al., 2009). The fuel (kerosene) was assumed to be fully burnt and no hydrocarbons were present in the mixture. In addition, the product gases were assumed to be fully mixed in the combustion chamber and the mixing chamber to reach chemical equilibrium state. The gas temperature and mole fractions of each species in the chemical equilibrium state were calculated by software called Chemical Equilibrium with Applications (Katanoda, 2006). In this chapter, the equivalence ratio ϕ was set at 1 for most of the cases.

Figure 7.8a shows a typical set of operating conditions, as well as the calculated pressure in the mixing chamber p_{03} , for the WS gun. The mixing ratio of kerosene to oxygen was set at the stoichiometric ratio for complete combustion. The flow rates of kerosene and oxygen had to be reduced as the nitrogen flow rate increased owing to the increase in the pressure within the combustion chamber. The pressure in the combustion chamber is slightly above the pressure in the mixing chamber p_{03} shown in Figure 7.8a. The gas temperature in the mixing chamber obtained by the chemical equilibrium calculation varied from 2740 (case 1) to 1780 K (case 4). Figure 7.8b shows a spray condition of an imaginary HVOF gun with the same geometry of the C–D nozzle and the barrel as the WS gun. The mixing ratio of kerosene to air was again set at the stoichiometric ratio, and their flow rates are adjusted so that the pressure in the combustion chamber p_{01} of the HVOF gun becomes the same values as p_{03} in Figure 7.8a. The gas temperature in the combustion chamber of the HVOF gun was calculated as 2250 K for cases 1–4. After obtaining the stagnant gas conditions just upstream of the C–D nozzle for both the WS and HVOF guns, a quasi-one-dimensional gas dynamics model (Katanoda, 2006) was used for the region inside the spray apparatus, which starts from the entrance of the C–D nozzle to the exit of the

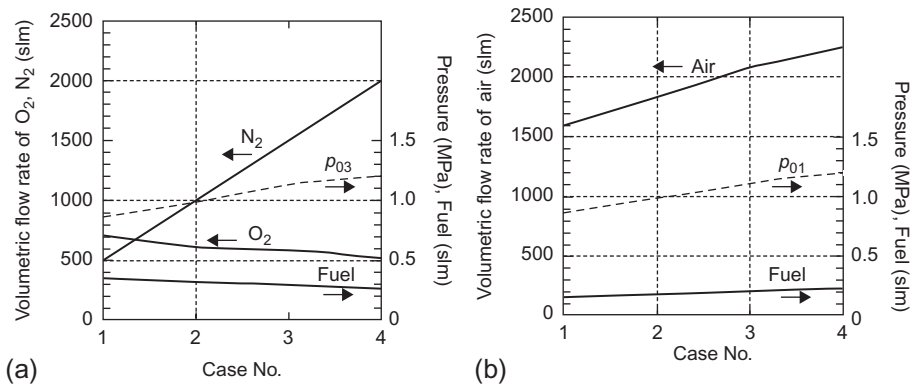


Figure 7.8 Operating conditions of warm spray (a) and HVOF (b) used for numerical simulation.

barrel. Outside the barrel, semiempirical equations (Kleinstejn, 1964) were used to calculate the gas velocity and temperature of the gas jet along the centerline.

7.3.2 Gas and particle flow field

For the WS gun, the gas velocity and temperature field from the nozzle to the barrel exit were calculated by integrating Equations (7.1)–(7.4), which take into account the change in the cross-sectional area of the gun, the pipe friction in the barrel, and the heat transfer (heat loss to the cooling water) through the inner wall of the barrel. The heat loss to the cooling water was determined experimentally by measuring the flow rate and the temperatures of the water at the inlet and outlet of the apparatus. The heat loss to the cooling water varied from 80 to 110 kW depending on the operating condition, while the total power generated by the combustion was approximately 200 kW. The cooling rates (Katanoda et al., 2009) of the combustion chamber and the mixing chamber were set constant at 0.20 and 0.14 (Katanoda et al., 2011), respectively, based on the measurement of the heat loss. The cooling rate of the barrel varies depending on the flow rate of the nitrogen gas and was calculated by an empirical equation derived from the experiment. As for the HVOF, the gun was assumed to be air-cooled with the cooling rate of 0.05 for the combustion chamber and that of 0.036 for the barrel:

$$\frac{du_g}{dx} = \frac{u_g}{(M_g^2 - 1)} \frac{dA}{A dx} - \frac{u_g}{(M_g^2 - 1)} \left(\frac{\gamma M_g^2 A f}{2 d} - \frac{\gamma - 1}{\gamma R T_g} \frac{\delta q}{dx} \right) \quad (7.1)$$

$$\frac{d\rho_g}{dx} = -\rho_g \left(\frac{1}{u_g} \frac{du_g}{dx} + \frac{1}{A} \frac{dA}{dx} \right) \quad (7.2)$$

$$\frac{dT_g}{dx} = \frac{\gamma - 1}{\gamma R} \left(-\frac{\delta q}{dx} - u_g \frac{du_g}{dx} \right) \quad (7.3)$$

$$p = \rho_g R T_g \quad (7.4)$$

where x is the axial direction, u_g the gas velocity, M_g the gas Mach number, A the cross-sectional area, γ the specific heat ratio, f the friction factor, d the barrel diameter, R the gas constant, q the heat loss per unit mass of gas, ρ_g the gas density, T_g the gas temperature, and p the static pressure.

Semiempirical equations (Kleinstejn, 1964) were used to calculate the gas velocity and temperature along the centerline outside the barrel. The underexpansion and overexpansion of the jet flow were also modeled as a stepwise change in the gas velocity and temperature at the barrel exit by introducing the fully expanded jet Mach number (Tam et al., 1985), as will be shown later in Figures 7.9 and 7.10. The gas velocity and temperature in the potential-core (Witze, 1974) region of the jet were set at constant values, which are calculated by the fully expanded jet Mach number. Once the gas flow field $u_g(x)$ and $T_g(x)$ is obtained, the acceleration and heating of a spherical particle injected at the powder feed ports can be expressed by the following two

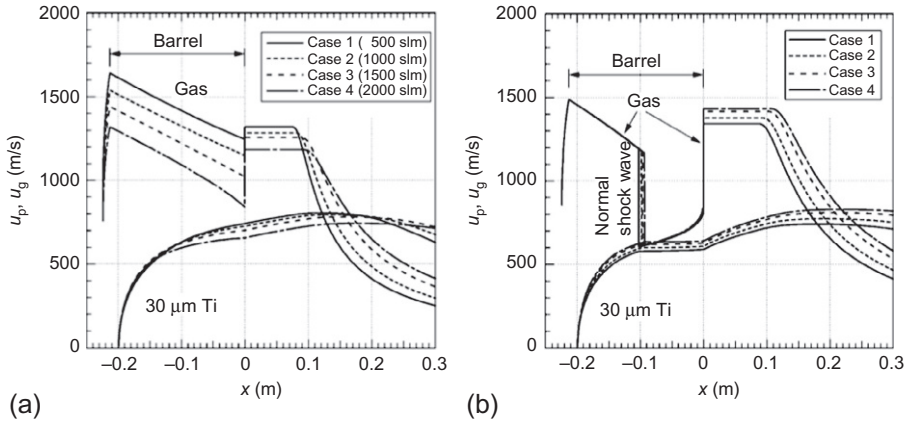


Figure 7.9 Gas/particle velocity of (a) WS gun and (b) HVAF gun.

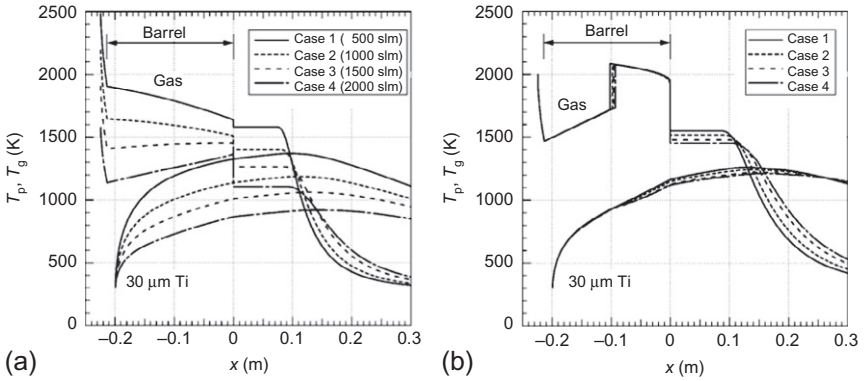


Figure 7.10 Gas/particle temperature of (a) WS gun and (b) HVAF gun.

Equations (7.5) and (7.6). The velocity and temperature of one particle along the centerline were obtained by integration of these equations:

$$m_p \frac{du_p}{dt} = \frac{1}{2} C_d \rho_g (u_g - u_p) \cdot |u_g - u_p| \frac{\pi}{4} d_p^2 \quad (7.5)$$

$$m_p C_p \frac{dT_p}{dt} = \alpha (T_g - T_p) \cdot \pi d_p^2 \quad (7.6)$$

$$\alpha = \frac{N_u k_g}{d_p} \quad (7.7)$$

$$Nu = 2 + 0.6 Re^{0.5} Pr^{0.33} \quad (7.8)$$

where t is the time, m_p the particle mass, u_p the particle velocity, C_d the drag coefficient, d_p the particle diameter, C_p the specific heat of particle, T_p the particle temperature, Nu the Nusselt number, k_g the gas thermal conductivity, Re the Reynolds number, and Pr the Prandtl number. In order to calculate the Re and Pr , the specific heat ratio at constant pressure, thermal conductivity, and viscosity of the combustion-mixed gas are required. These thermal properties for each gas species, as well as the averaged properties, were calculated by the equations proposed in McBride et al. (1993). The gas density, which is necessary to calculate the Re , was obtained by Equation (7.4). When numerically integrating Equations (7.5) and (7.6), the variable t was transformed to x . Then, the transformed equations (Katanoda, 2006) were numerically integrated in x -direction with the step size $\Delta x = 0.1$ mm, which was found to be sufficiently small to obtain solutions almost independent of the step size.

7.3.3 Model results

Figure 7.9a shows the calculated gas velocity and the velocity of a 30 μm diameter titanium powder injected at the powder feed port for the WS gun. Here, distance $x = 0$ corresponds to the barrel exit of the nozzle and the powder feed ports are situated about 0.2 m upstream. As the gas expands through the C–D nozzle, its velocity increases rapidly and then decreases gradually along the barrel length due to friction with the inner wall of the barrel. Outside the barrel, the gas velocity increases stepwise, which represents the underexpansion of the jet flow at the barrel exit, and it remains constant in the potential-core region outside the barrel and then decreases again due to mixing with the ambient air. It should be noted that the gas velocity is higher with less nitrogen flow rate through the gun and the potential-core region of the jet. This is mainly due to the higher gas temperature in the barrel and jet. This can be explained by the effect of nitrogen flow rate on the speed of sound and Mach number of the mixed gas; (1) less amount of mixing of nitrogen at room temperature means a higher gas temperature (larger speed of sound) in the mixing chamber, as well as in the barrel and (2) although the supersonic flow entering the barrel (around Mach 2.0 regardless of the nitrogen flow rate) is decelerated by the pipe friction in the barrel, a higher-temperature gas flow, from which more heat is transferred to the water-cooled barrel, results in less decrease in Mach number in the flow direction due to the effect of supersonic Rayleigh flow (Zucrow and Hoffman, 1976). Since the gas velocity is obtained by a multiplication of the speed of sound and the Mach number, the less nitrogen flow case shows a larger gas velocity in the barrel and barrel exit. It is very interesting to see that the velocity profiles of the Ti particle are almost unaffected by the nitrogen flow rate. This is attributed to the increase in the gas density by addition of nitrogen, which compensated the decreased gas velocity.

Figure 7.9b shows the calculated gas velocity and the velocity of a 30 μm diameter titanium powder for the HVAF gun. The gas velocity at the inlet of the barrel is 1500 m/s ($M_g = 2.0$), which is almost the same as that for case 2 of the WS gun. However, the gas speed decreases more rapidly after entering the barrel as compared to the WS gun, due to a larger decelerating effect by the pipe friction against the acceleration effect of cooling. Because of this, the gas flow cannot maintain a supersonic flow until the end of the barrel, causing a normal shock wave in the barrel at around $x = -0.1$ m

for all the four cases. As a result, subsonic flow region appears between the normal shock wave and the barrel exit, where the gas flow is “choked” ($M_g = 1$) generating underexpanded sonic jets. It is interesting to note though that the maximum particle velocity of the HVAF gun is roughly the same as that of the WS gun.

Figure 7.10a shows the significant effect of mixing nitrogen on the temperature of the mixed gas and particles. The gas temperature steeply decreases due to expansion C–D nozzle and then gradually decreases for cases 1–2 and increases for cases 3–4 in the barrel depending on the extent of the heat loss to the water-cooled through the barrel against the temperature recovery due to the deceleration of the gas flow by pipe friction. After exiting the barrel, the gas temperature remains constant in the potential-core region of the jet and finally decreases again due to mixing with the ambient air. In summary, the numerical simulation shows that the particle temperature at $x = 0.2$ m, where substrates are normally placed for the WS process, can be changed from 1250 to 900 K while keeping its velocity relatively unchanged.

Figure 7.8b shows the simulated gas/particle temperatures for the HVAF gun. As can be seen in the figure, hot gas region appears between the normal shock wave and the barrel exit. This is due to the result of the energy conversion from the decreased kinetic energy of the gas flow to the increased thermal energy. Since the distributions of the gas temperature are almost unaffected through cases 1–4, the profiles of the particle temperature also do not largely change.

Figure 7.11 shows the summary of the variation of the particle temperature against the particle velocity starting from the powder injection port ($u_p = 10$ m/s, $T_p = 300$ K) to the outside of the gun at $x = 0.3$ m for the WS and HVAF guns. Four solid circles plotted on the curves show the particle conditions at the barrel exit ($x = 0$). From Figure 7.11a, the overall trend of the particle condition for the WS gun is that the particle temperature and velocity increase at almost the same rate, showing rather linear increase from the powder injection port to the location where the maximum particle velocity is reached outside of the gun. The maximum particle temperature can be decreased from 1400 to 900 K by increasing the nitrogen flow rate from 500

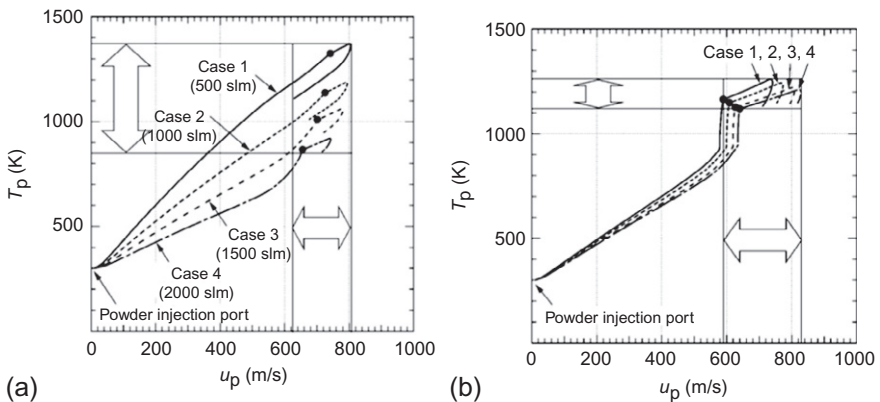


Figure 7.11 Temperature–velocity trajectories of $30\ \mu\text{m}$ Ti particles sprayed by (a) WS gun and (b) HVAF gun.

to 2000 slpm. The overall temperature range of the particle outside of the gun ($x=0-0.3$ m), where a substrate can be situated, for cases 1–4 is about 850–1400 K. The corresponding velocity range of the particle is about 620–800 m/s. As for the HVAF gun in Figure 7.11b, the particle temperature linearly increases in the range of the particle velocity of 0–600 m/s. Then, the particle temperature increases to about 1100 K, while the gas velocity remains constant at about 600 m/s. The overall ranges of the particle temperature and velocity outside the gun are 1100–1300 K and 600–840 m/s, respectively. Therefore, comparing the HVAF with the WS, it seems that the particle velocity of the WS is comparable to HVAF; however, the controllable range of the particle temperature is about three times wider for the WS compared to HVAF under the present numerical conditions, including the stoichiometric mixture of kerosene and air for complete combustion. The range of the particle temperature of the HVAF will be extended to a lower value if the gun is operated at fuel-lean/fuel-rich conditions within the limit of stable combustion.

Figure 7.11c shows the simulated gas/particle temperatures for the HVAF gun under fuel-lean equivalence ratio ($\phi=0.69$). This figure shows that if the HVAF gun is operated at $\phi=0.69$, the gun can provide as lower particle temperature as the WS gun operated at case 4 condition shown in Figure 7.11a while keeping the particle velocity almost unchanged from Figure 7.11b. Although the particle temperature sprayed by the HVAF gun can be lowered when the gun is operated at fuel-lean condition, the lower limit of the particle temperature directly depends on the lower limit of ϕ to generate stable combustion. In addition, the upper limit of the particle temperature of the HVAF gun can hardly be extended from Figure 7.11b. On the other hand, the WS gun is capable of extending the upper/lower limits of the particle temperature from Figure 7.11a by decreasing/increasing the flow rate of nitrogen gas.

7.4 Microstructure and mechanical properties of WS metallic coatings

Microstructure and mechanical properties of WS coatings have been investigated for materials such as titanium, copper, aluminum, metallic glass, WC–Co cermet, nanograin titanium oxide, UHMW-PE, and PEEK (Watanabe et al., 2007a,b; Chivavibul et al., 2008, 2010; Kawakita et al., 2008b; Kim et al., 2008, 2009a,b,c, 2010a). Among them, titanium and WC–Co have been most extensively studied due to their potential application importance and sensitivity to thermal degradation.

Figure 7.12 shows typical ranges of velocity and temperature of sprayed titanium particles (30 μm diameter) at the substrate position for both WS and CS as calculated by numerical simulation in the previous chapter. The plots indicate specific conditions at which coatings were prepared for characterization as shown in Figure 7.13. For warm-sprayed coatings, it can be seen that the coating at 500 slpm of nitrogen flow rate contains significant oxide at the particles' boundaries; the coatings formed at higher nitrogen flow rate become cleaner, but at 2000 slpm, it becomes highly porous. For CS coatings, the coatings are porous with the two nitrogen conditions, but it

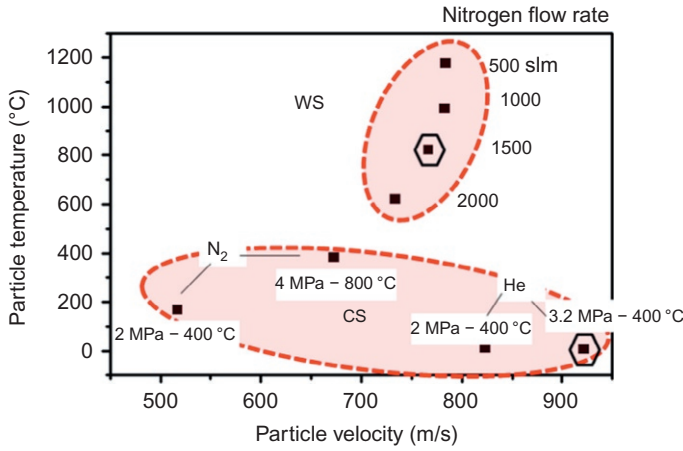


Figure 7.12 Process map showing the ranges of particle temperature and velocity achievable by warm spray and cold spray for titanium particles with 30 μm diameter. Plots represent the results of numerical simulation for the conditions used in the experiments. Two hexagonal marks indicate conditions under which splat specimens for TEM analysis were prepared.

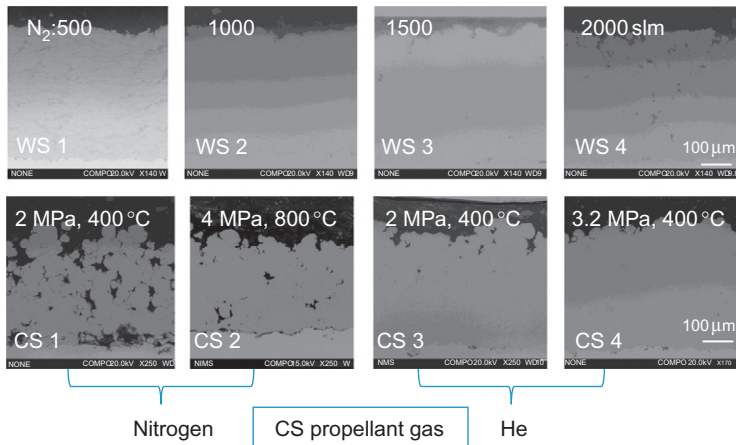


Figure 7.13 Cross sections of warm-sprayed and cold-sprayed titanium coatings deposited with conditions corresponding to the plots in Figure 7.12 observed by SEM.

becomes very dense with He as the propellant gas due to the higher impact velocity (Tabbara et al., 2011). Splats formed under the two conditions marked in Figure 7.12 were investigated in more detail later.

When one compares the cross sections obtained with WS3 and CS3, WS3 coating appears denser than CS3 even though the velocity should be lower as shown in

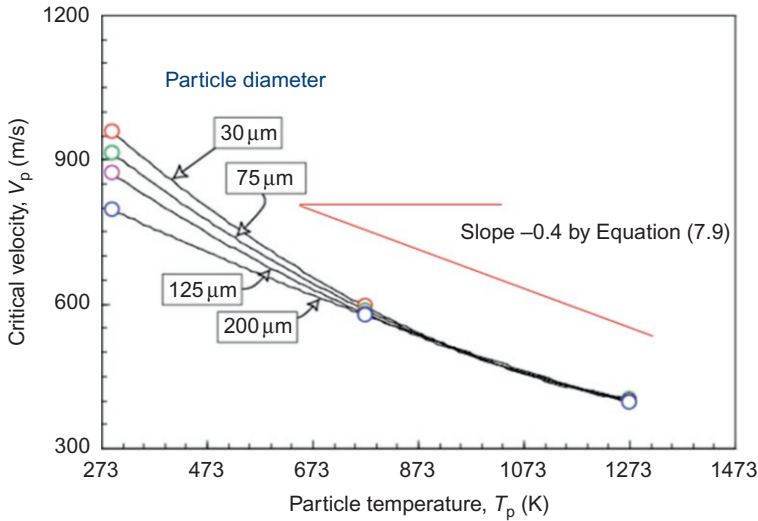


Figure 7.14 Temperature effect on the critical velocity of Ti particles by numerical impact simulation (Yokoyama et al., 2006). Slope -0.4 is given in Equation (7.9) by Assadi et al.

Figure 7.12. In order to consider the effects of particles temperature at impact, Figure 7.14 shows the dependence of the critical velocity (V_{cr}) necessary to cause adiabatic shear instability on the particle temperature, which was obtained by the FEM simulation of a spherical particle onto a substrate (Yokoyama et al., 2006). Since thermal conduction of heat generated by plastic deformation was taken into account in the simulation, some size dependence in the lower temperature regime appeared. As a rough measure of the temperature effect, a line with slope of -0.4 is drawn on the figure, which implies that a temperature rise by 400 K is equivalent to a reduction of critical velocity by 160 m/s. This coefficient is in agreement with Equation (7.9) proposed by Assadi et al. (2003):

$$V_{cr} = 667 - 14\rho + 0.08T_m + 0.1\sigma_u - 0.4T_i \quad (7.9)$$

where ρ is the density (g/cm^3), T_m is the melting point ($^{\circ}\text{C}$), σ_u is the yield stress (MPa), and T_i is the particle temperature ($^{\circ}\text{C}$).

The oxygen contents of the WS Ti coatings analyzed by the inert gas fusion method are shown in Figure 7.15 for various nitrogen flow rates and spray distances (Kawakita et al., 2006a; Kuroda et al., 2008). The oxygen level in the feedstock powder was 0.14 mass%, which increased significantly to 5.5 mass% when the nitrogen flow rate was 500 slpm. As the nitrogen flow rate increased from 500 to 1000 slpm, it decreased significantly and became less than 1 mass% at the distance of 180 mm. At shorter distances, it is believed that oxidation increased due to the overheating of the coating surface by the WS hot gas during spraying, whereas it increased due to a longer traveling distance in the air. The decrease in the oxygen content is caused by the lower

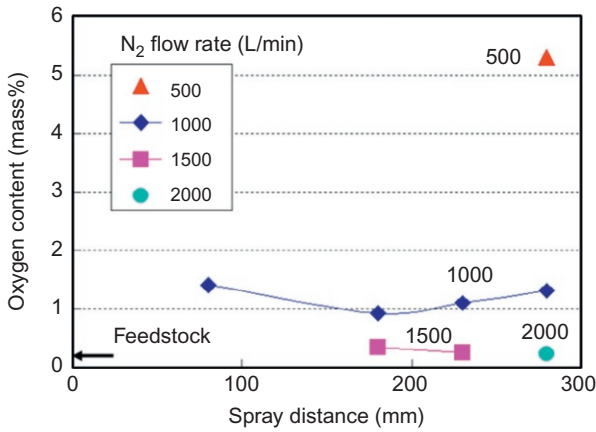


Figure 7.15 Oxygen contents in warm-sprayed titanium deposits formed under various nitrogen flow rates and spray distances (Kawakita et al., 2006a).

flame temperature. At a flow rate of 2000 slpm, the oxygen content decreased further to 0.22 mass% but the coating became highly porous as shown in Figure 7.13.

The analysis of titanium deposition by WS and CS is shown in Figure 7.16 in the form of process map. On the right-hand side of the map, oxygen levels acquired by each spray condition in WS and CS by nitrogen are shown. In CS, it is possible to achieve coatings with oxygen level as low as 0.15 mass%, whereas the minimum value achieved by WS is 0.22 mass%. If a coating with oxygen level below 0.2 mass% is required, it is not advisable to use WS and CS should be used. Since

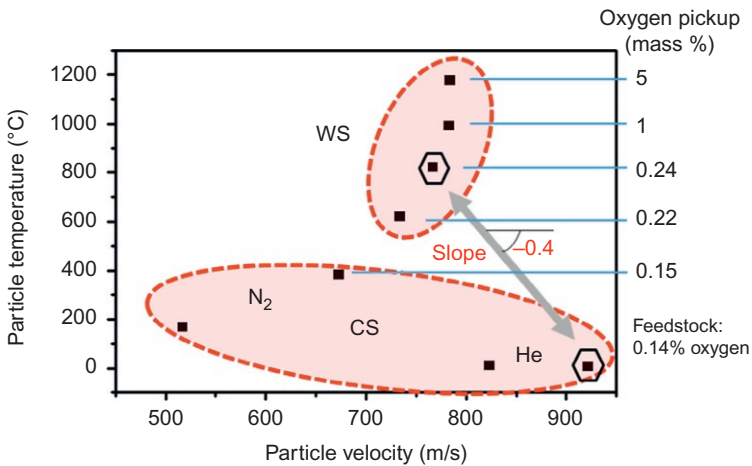


Figure 7.16 Modified process map based on Figure 7.12, onto which oxygen contents of titanium coatings and the slope of -0.4 relating temperature to velocity are superposed. Two hexagonal marks indicate conditions under which splat specimens for TEM analysis were prepared.

titanium is highly reactive with oxygen at the processing temperature of WS, it is readily expected that the amount of oxidation will be significantly less for more oxidation-resistant alloys based on other elements such as iron, nickel, copper, and cobalt. Another point to be noted is the gray arrow with a slope of -0.4 connecting the two marked spray conditions selected for WS and CS. When the cross sections of these coatings shown in Figure 7.13 are compared, their resemblance in terms of coating density is consistent with the discussion concerning critical velocity, although the barrier capability of such coatings in corrosive environments cannot be judged from such microstructures as discussed in Section 7.2.3.

7.4.1 Titanium splats

A typical WS titanium splat deposited on a medium carbon steel substrate is shown in Figure 7.17a top view and Figure 7.17b cross section, for which the operating condition of WS was case 3 in Figure 7.8a. Titanium splats were also prepared by cold spraying under various conditions as shown in Figure 7.12, and thin foil specimens for TEM observation have been cut out from the highest-velocity condition using He as shown in Figure 7.12. In Figure 7.18, comparison of the microstructure of the WS splat with CS splat is shown. Two characteristics are clearly seen from the figure, that is, the degree of substrate deformation by the impact is more pronounced for the CS splat than WS due to the higher impact velocity and lower temperature of the titanium particle and grain refinement due to dynamic recrystallization took place in a much larger volume in the WS splat as compared to CS. The original grain size of the feedstock powder is about a few micrometers, whereas the grain size was reduced to a few tens of nanometers after impact. For the rotational grain refinement to happen, the material needs to be at a high enough temperature for dislocations to move and needs to undergo severe plastic deformation (Kim et al., 2008). Schematic of grain refinement is shown in Figure 7.19. WS particle satisfies these conditions largely in the lower portion of a particle.

Another important aspect of splat characterization is bonding. Already a number of literatures have suggested that the splat–substrate interface consists of a poorly bonded or often unbonded region around the south pole of an impacted particle and a well-bonded region surrounding the south pole. It is believed that severe shear deformation due to the adiabatic shear instability ejects surface oxide film to mate the

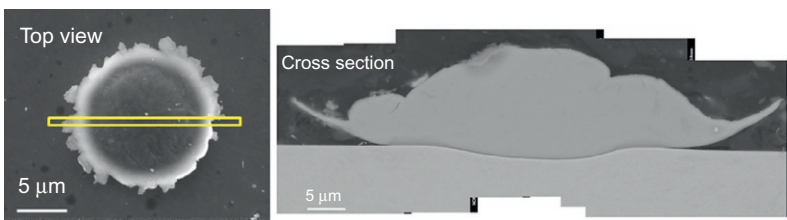


Figure 7.17 Top view and cross section of a titanium particle (splat) deposited onto steel substrate under the WS condition with 1500 slm.

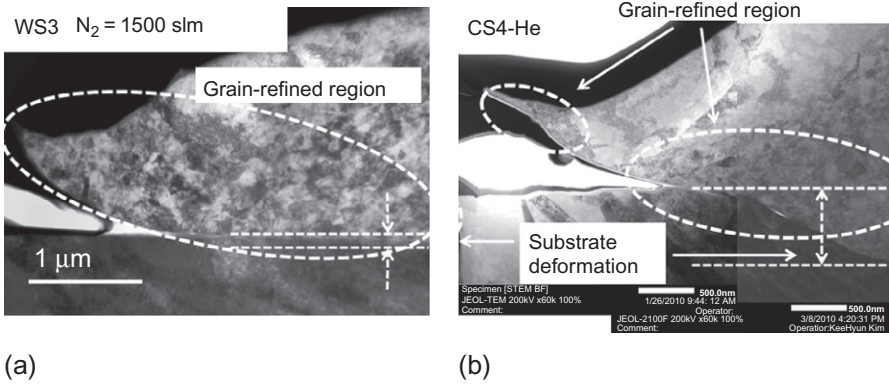


Figure 7.18 TEM images of cross section of titanium splats (a) by warm spraying and (b) by cold spraying, showing regions of grain refinement and substrate deformation.

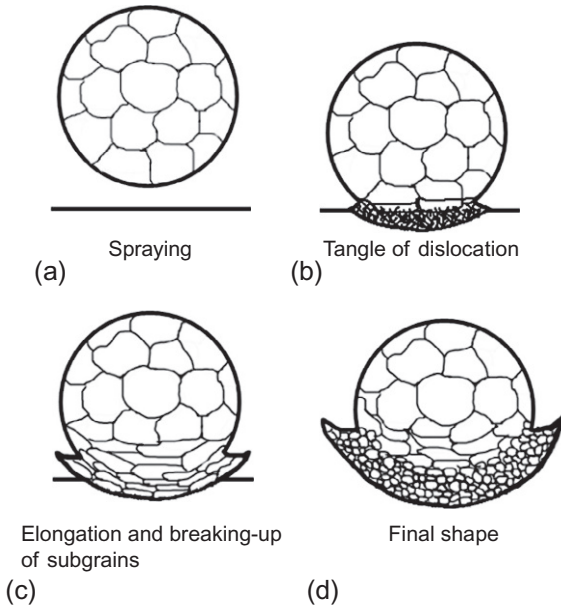


Figure 7.19 Schematic evolution of grain refinement by dynamic recrystallization: (a) spraying titanium particle onto the substrate, (b) entanglement of dislocations, (c) formation of dislocation cells (and subgrains) and re-elongation, and (d) breaking-up, rotation and recrystallization of subgrains by thermal softening effects enough to trigger the viscous flow (Kim et al. 2008).

fresh surfaces of the particle with the substrate to form bonding in the well-bonded region (Kim et al., 2009a,b, 2010b). Figure 7.20 shows an elemental mapping image of the south-pole region of a titanium splat obtained by the energy-filtered TEM technique (Kim et al., 2009a,b,c,d). A thin void was left at the bottom of the splat, but very interestingly, a thin layer of iron was attached to the bottom surface of the titanium particle. A possible interpretation of this is that a bond between the titanium particle and steel was formed temporarily by the compression during the impact, but in the

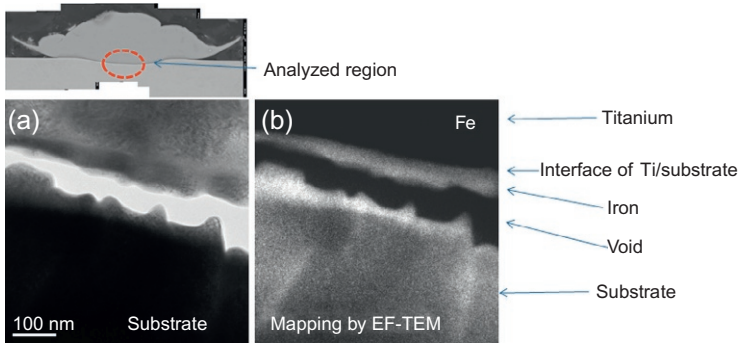


Figure 7.20 TEM (a) and EFTEM images (b) of iron taken near the bottom of a titanium splat.

later stage, when the interface was exposed to a high tensile stress due to the rebounding by the elastic energy accumulated during impacting, the bond was destroyed and a thin layer of the steel was exfoliated.

Highly magnified TEM images of the well-bonded interface region are shown in [Figure 7.21a and b](#), indicating the existence of a layer of a few nm thickness with nano-size crystalline structure ([Kim et al., 2009b,d, 2010a](#)). Line profile by electron energy loss spectroscopy (EELS) in [Figure 7.21c](#) shows that the thin layer contains significant concentration of oxygen and both Ti and Fe. The peak positions in the energy spectra obtained from this region are shown in [Figure 7.23d](#), which indicates that Fe is in metallic state, whereas Ti is in the oxidized state in the interface region corresponding to the distance from 2 to 6 nm and becomes metallic toward the inside as the oxygen concentration decreases gradually. This is reasonable considering the large solubility of Ti up to about 15 mass%. Therefore, the results indicate that it exists as a thin interlayer in the well-bonded interface, which it is composed of mixture of nanocrystals of titanium oxide and metallic iron.

Since a coating is formed by numerous number of particles, effects of successive deposition of particles were examined ([Kim et al., 2010a](#)). The first example shown in [Figure 7.22](#) represents a case of normal impact by the next particle, which impacted almost concentrically to the first particle. It can be seen from the TEM image that (1) the upper region of the first particle was grain refined by the second impact and (2) the gap under the first particle at the south-pole region is significantly closed. The four diffraction patterns from the regions marked as A, B, C, and D indicate that the first three regions have undergone severe plastic deformation accompanied with dynamic recrystallization, while the region D retains the microstructure of the feed-stock powder. This is because the diffraction pattern D is a diffraction from a single crystal, whereas the patterns A to C contain diffractions from multiple crystals, which means that the crystal sizes in region D are much larger as compared with the size of the selected area aperture of about 0.5 μm diameter, whereas the crystals are smaller than the aperture size in regions A to C.

An example of side impact is shown in [Figure 7.23](#) ([Kim et al., 2010a](#)), where particle A on the left arrived after particle B and collided with it from the side. It can be seen that

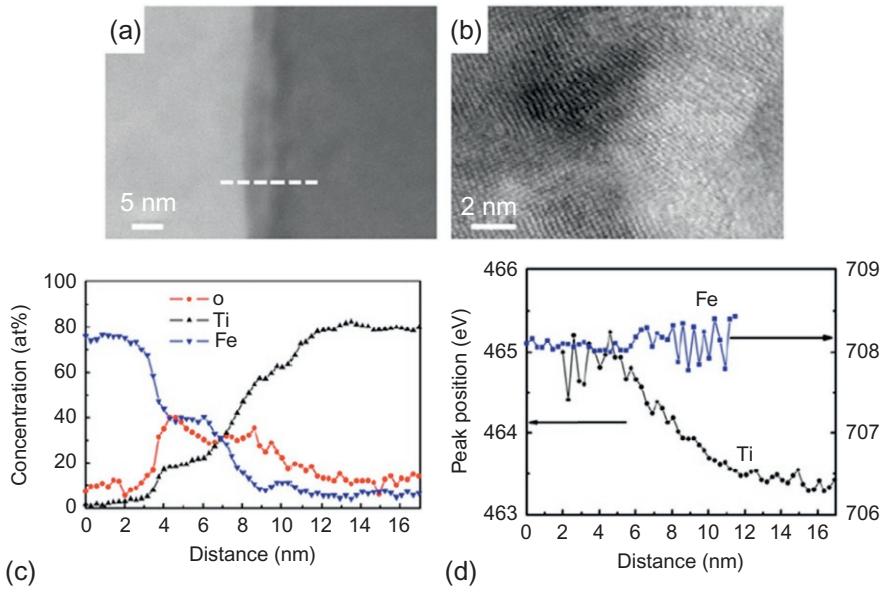


Figure 7.21 STEM images and EELS analysis near the steel/titanium interface: (a) image of the boxed area of Figure 7.4(a); (b) magnified view of panel (a) suggesting the presence of (1 0 0) oriented bcc steel in the left part and a partly disordered interface (right part); (c) and (d) analyses of an EELS line profile along the dotted line in (a) summarized (Kim et al. 2009d).

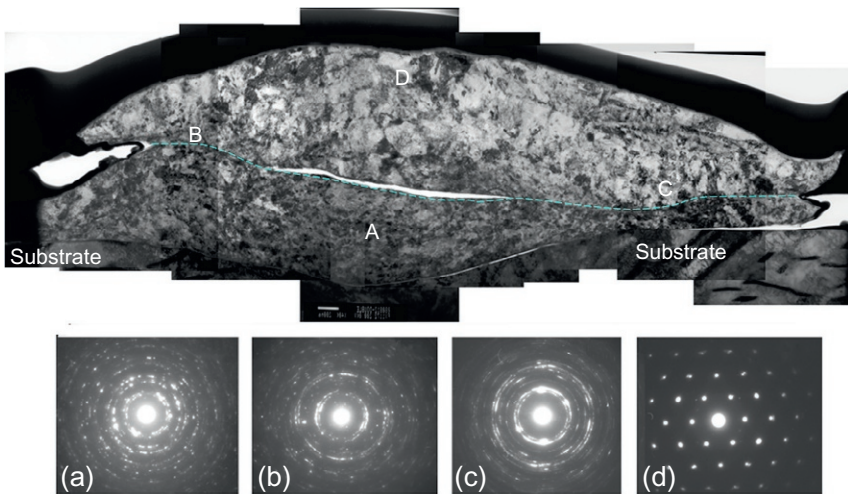


Figure 7.22 TEM cross-sectional observation of two titanium particles impacted in a concentric configuration on a steel substrate (upper) and diffraction patterns obtained from selected regions (lower) (Kim et al., 2010a).

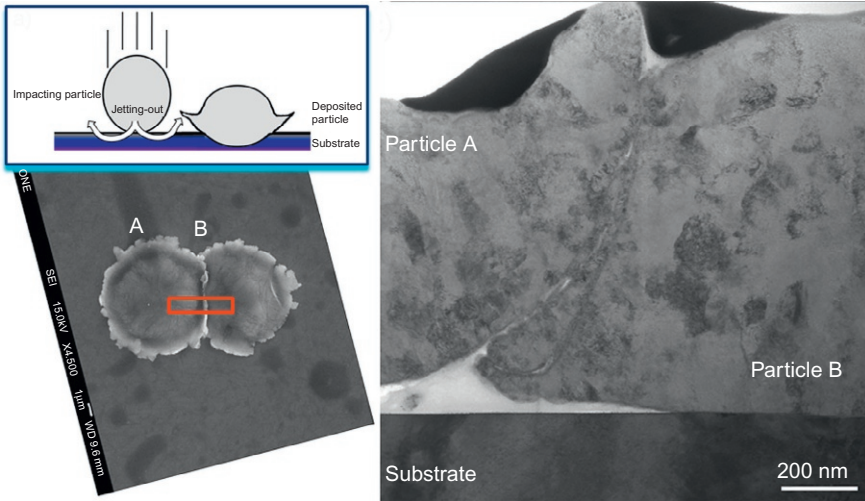


Figure 7.23 SEM top view and TEM cross-sectional observation of two titanium particles impacted side by side on a steel substrate (Kim et al., 2010a).

some kind of weak bonding is formed but it is expected that such bonding is not very strong. In a real coating, interfaces with different natures are interwoven: strong interface made by high-velocity impact (shear instability), south-pole region bonded by successive impacts, and interface made by side impacts. How these interfaces behave under various loading modes and affect transfer properties need to be studied.

7.4.2 Metal coatings

Figure 7.24 exhibits the stress–strain curves of titanium coatings deposited by warm spraying with various nitrogen flow rates of 0.5, 1.0, 1.5, and 2.0 m³/min. Those data were obtained by tubular coating tensile (TCT) tests. The details of the test method can be found in the references (Schmidt et al., 2006; Binder et al., 2010). The highest tensile strength of 250 MPa and the largest elongation to failure 2% were obtained for the coatings deposited with the nitrogen flow rate of 1.0 m³/min, which also had the lowest porosity as shown in Figure 7.13. For either the lower or higher nitrogen flow rate, both tensile strength and elongation to failure were decreased significantly. In Figure 7.25, SEM images of fracture surfaces after TCT tests were presented (Watanabe et al., 2010a). For the cases of nitrogen flow rate of 1.5 and 2.0 m³/min, the spherical morphologies of original feedstock powder were still maintained after impact due to high deformation resistance. Failure mainly occurred at the interfaces among the particles implying lower bonding strengths. For the nitrogen flow rate of 1.0 m³/min, particles were flattened more and the coating became denser because of higher temperatures and thermal softening of impacting particles. On the fracture surface, dimple formation from ductile fracture can be observed (Figure 7.25d). But the area is about 30% in the picture and the rest of it still shows the brittle failure. Thus,

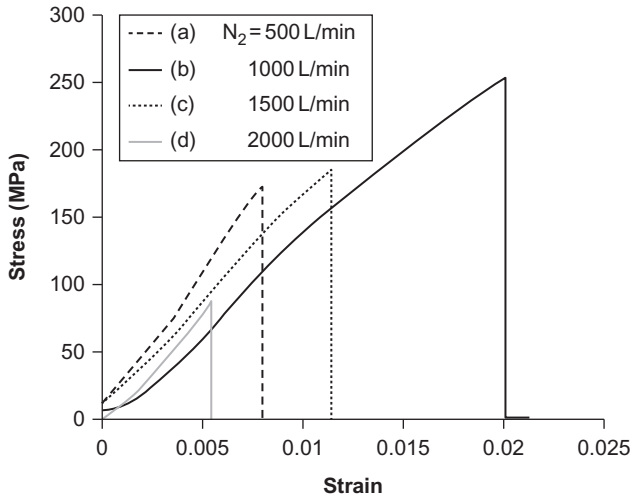


Figure 7.24 Stress–strain curves in TCT tests of freestanding titanium coatings (Watanabe et al., 2013).

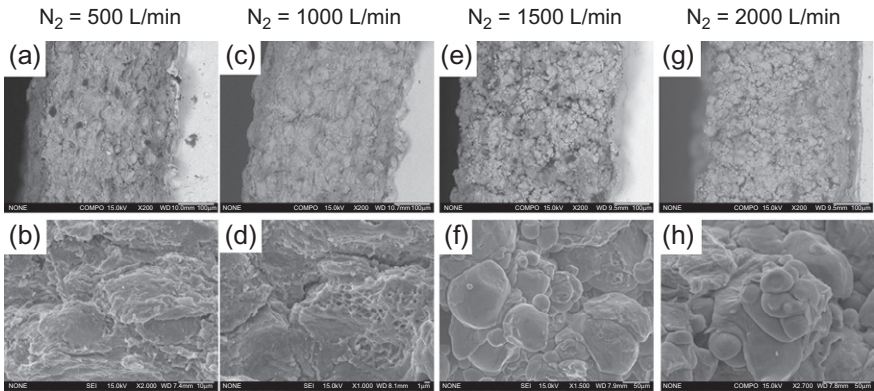


Figure 7.25 Fracture surface of titanium coatings after TCT tests (Watanabe et al., 2013).

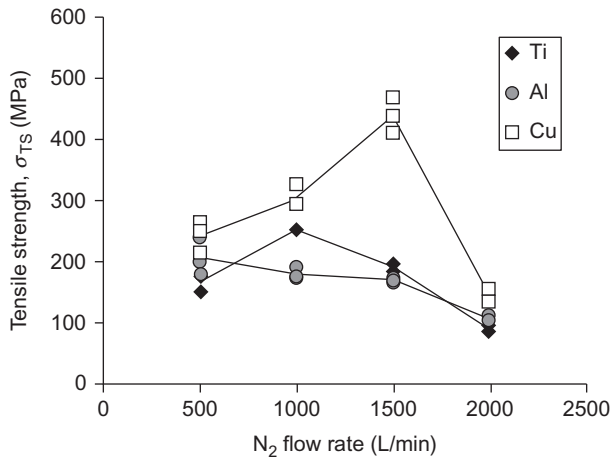
there is still room to improve the mechanical properties of the coating. For further reduction of nitrogen flow rate to $0.5 \text{ m}^3/\text{min}$, again, the fracture surface became that of brittle nature. The detailed analysis revealed the formation of oxides on the surface. Although larger deformation of particles could be induced upon impacts, as the thickness of the oxide layers on particles become thicker, it becomes more difficult to remove those oxides during impact and to form metal–metal bonding as elaborated in the previous sections, and the bonding occurs between amorphous titanium oxides (Kim and Kuroda, 2010). The results of the TCT tests clearly indicated that the existence of such interfacial oxides significantly decreases the strength of the coatings. The spray conditions used to fabricate the TCT samples were exactly the same as

the ones in Figure 7.16. In fact, the differences in the estimated velocities for the different nitrogen flow rates are within about 50 m/s, and the ones in the temperatures are only about 200 K. Nevertheless, it is evident that the mechanical strength of WS titanium coatings is significantly affected by such small differences, especially by particle temperature.

The ultimate tensile strength of a bulk titanium alloy for industrial use ($O < 0.2$ wt%, $N < 0.05$ wt%) is 350~530 MPa and the elongation to failure is more than 23%. If these results are compared to the TCT results for the WS coatings, there is a significant difference. One reason for the difference is the effect of the testing method. In TCT test, two cylindrical substrates are contacted but are not adhered to each other, and thus, these unbonded faces act like a crack and cause stress concentration near the tip area (Binder et al., 2010). Thus, the values obtained by TCT are usually 0.4~0.7 times smaller than the ones of tensile test of freestanding coatings (Gartner et al., 2006). By taking into account this notch effect, the titanium coatings for $N_2 = 1.0$ m³/min appear to have similar strength with bulk alloys; however, the elongation to failure is still one-tenth smaller. Probably, this poor plastic deformation is attributed to the existence of unbonded regions at the interfaces between particles as shown in Figure 7.22. In addition, nonuniform nano-/micrograin structures induced by local work hardening and grain refinements (Figures 7.18 and 7.22) can be other possible factors for such poor plastic deformation ability.

In Figure 7.26, the tensile strength of Ti, Al, and Cu coatings obtained from TCT tests is shown as a function of the nitrogen flow rate (Watanabe et al., 2010a). The tests were performed three times at least in all conditions. The copper coatings show the highest strengths of about 450 MPa for 1.5 m³/min for all nitrogen flow rates. The ultimate strength values increase constantly with the increase of N_2 flow rate until 1.5 m³/min due to lower oxidation of copper particles. But after the peak, it drastically drops to the lowest values at the 2.0 m³/min condition due to limited deformation of particles with lower particle temperature. Just like the titanium case, the nitrogen flow rate and thus particle temperature have a severe influence on the coating

Figure 7.26 Ultimate tensile strength in TCT tests of WS coatings as a function of N_2 flow rate (Watanabe et al., 2010a, 2013).



properties. In [Figure 7.26](#), the tensile strength of WS aluminum coatings is also plotted. Aluminum coatings exhibited the highest value at 500 slpm nitrogen flow rate, which monotonically decreased as the increase of N_2 flow rate. Perhaps aluminum oxide is very stable and thus the variation of oxidation degree was very small. In such case, higher particle temperature can provide better bonding because of larger deformation upon impact and thermally activated particle surfaces. In all three metals, the worst strength values were observed at the coldest condition (nitrogen flow rate of 2000 slpm). These results ensure that the mechanical strengths of WS coatings strongly depend on particle deformability and oxidation.

[Figure 7.27](#) is the comparison of the TCT test results with tensile strength of various copper coatings obtained by micro flat tensile tests ([Gaertner et al., 2006](#)). The highest tensile strength and elongation to failure obtained by WS coatings are comparable to cold rolled bulk and cold-sprayed coatings with helium gas. Since the titanium coating by cold spraying with helium gas is as dense as WS ([Figure 7.13](#)) and copper is softer than titanium, cold-sprayed copper coatings with helium gas could be as dense as WS coatings. In addition, the bonding between particles could be similar or better with less oxidation in CS. [Gaertner et al. \(2006\)](#) reported brittleness of as-sprayed CS copper coatings and the significant effects of heat treatments on them. The elongation to failure was significantly improved with the proper heating conditions due to enhanced interfacial bondings and recovering of work hardening. As already mentioned above, severe work hardening due to high-speed impact makes a coating harder and more brittle. In WS, the predeposited coating layers can be heated up by combustion flame, and thus, it can be moderately annealed during deposition simultaneously. It could be one possible explanation of better properties

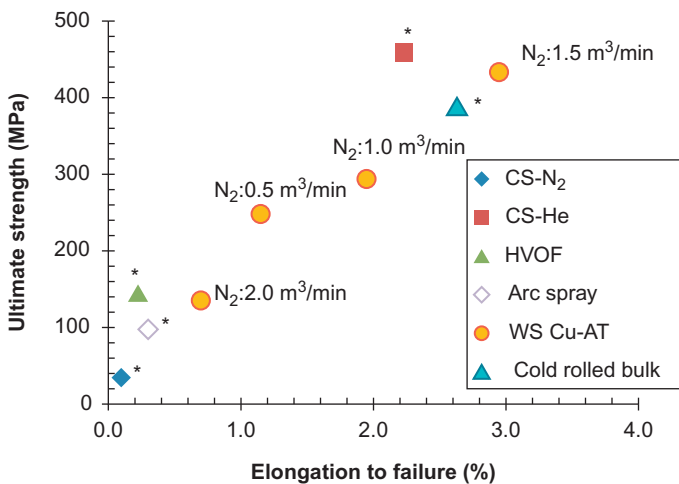


Figure 7.27 Comparison of the tensile strength and elongation to failure in TCT test with the reference data of various copper coatings obtained by micro flat tensile test ([Gaertner et al., 2006](#); [Watanabe et al., 2013](#)).

*[Gaertner et al., 2006](#).

of WS copper coatings. More detailed research would lead to further improvements of metallic WS coatings.

7.5 WC–Co cermet coatings

7.5.1 Coating microstructure

WC–Co cermet coatings have been used to enhance wear resistance of various engineering components due to their high hardness and moderate toughness compared with other coating materials. HVOF spraying is known as the most suitable technique to fabricate WC–Co coatings so far; however, when compared to sintered WC–Co, which has been fabricated in carefully controlled sintering conditions, HVOF-sprayed WC–Co coatings still suffer from lower performance due to decomposition and decarburization during spraying process, leading to a formation of undesirable phases such as W_2C , W, and amorphous or nanocrystalline Co–W–C phase (Chivavibul et al., 2007). Using WS to deposit WC–Co, it is expected to suppress such detrimental reactions and thus produce WC-based coatings consisting of similar microstructure and mechanical properties of sintered bulk materials.

Figure 7.28 shows the splat microstructures of WC–12 wt% Co on carbon steel substrates and the examples of the splat cross sections of HVOF (Figure 7.28a and c) and WS (Figure 7.28b and d), respectively (Watanabe et al., 2006, 2007b). While the splat deposited by HVOF indicates melting and solidification upon impacts, the one by WS kept the spherical shape of original feedstock powder indicating solid

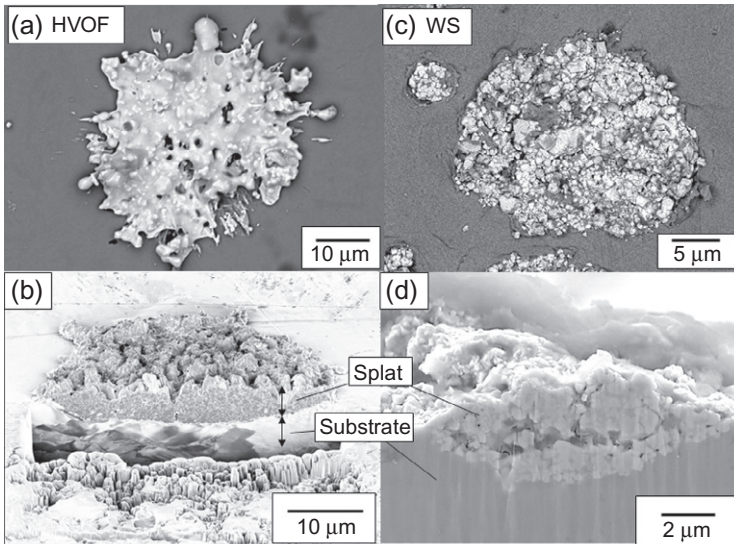


Figure 7.28 Comparison of splat microstructures of WC–12Co in (a) HVOF and (c) WS (Watanabe et al., 2006a). (b) and (d) are the cross-sectional images made by focused ion beam and cross-sectional polisher, respectively.

particle impact due to lower particle temperature. In the cross-sectional image of WS splat, the deeper impingement into the substrate and spherical morphology of the upper periphery of it can be understood. Since carbides are dissolved into Co binder in HVOF, the size of carbides in HVOF becomes smaller than the WS case.

The effect of nitrogen flow rate in WS on splat microstructures is shown in Figure 7.29 (Watanabe et al., 2007b; Kuroda et al., 2008). Both splats kept spherical shape, but the carbide morphologies are different. When the particle temperature is relatively lower for the nitrogen flow rate of 1500 L/min, the carbides kept blocky shape; however, they were covered with locally melted binder phases for higher particle temperature in the nitrogen flow rate of 500 L/min. Example of the cross-sectional image of a WC–12 wt% Co coating deposited by WS is presented in Figure 7.30 (Watanabe et al., 2007b; Kuroda et al., 2008). Dense and thick coatings suitable for different applications can be obtained.

Figure 7.31 contains higher magnification images of HVOF and WS coatings (Chivavibul et al., 2008). Both revealed a dispersion of fine carbide particles in binder phases. Pores were observed in both coatings. In some area of the HVOF WC–12Co coatings, the lack of splat–splat bonding was also observed as shown in Figure 7.31a.

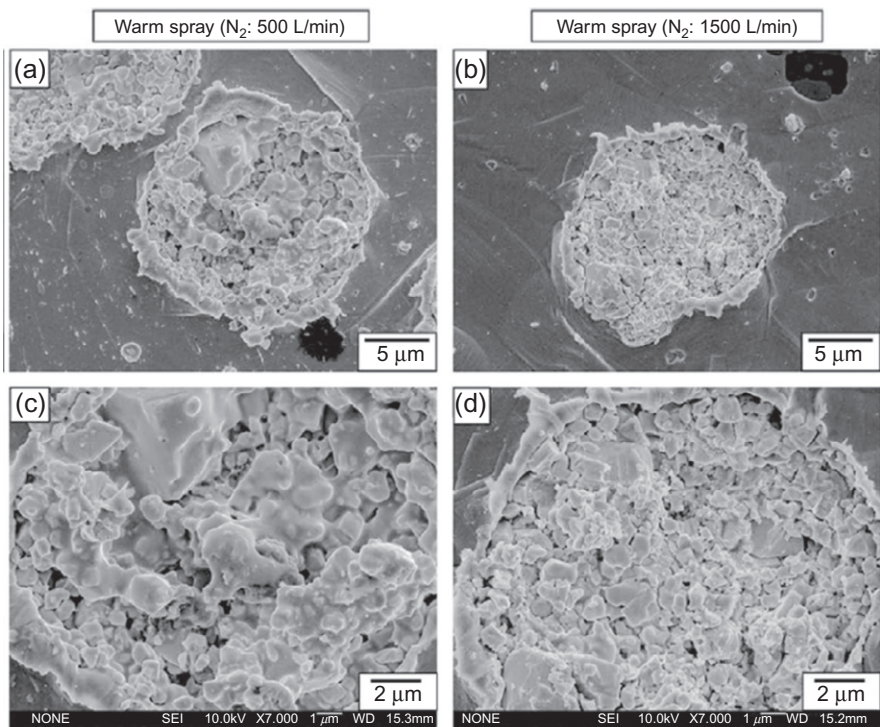


Figure 7.29 Splat microstructures deposited by (a) warm spray with nitrogen flow rate of 500 L/min, (b) warm spray with nitrogen 1500 L/min, (c and d) are higher magnification images of (a and b), respectively (Watanabe et al., 2007b).

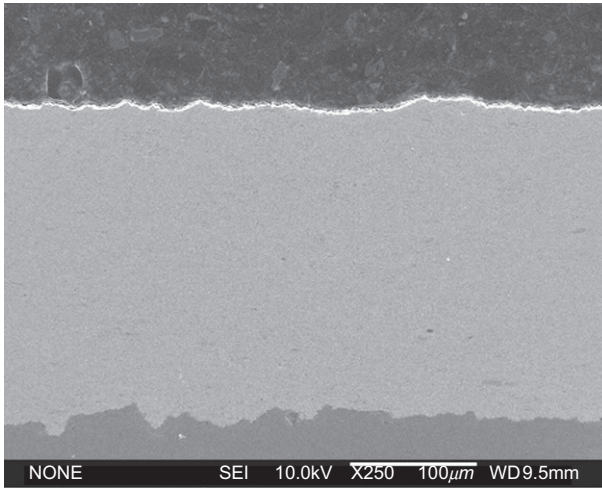


Figure 7.30 Cross-sectional image of a coating deposited by warm spray deposition (Watanabe et al., 2007b).

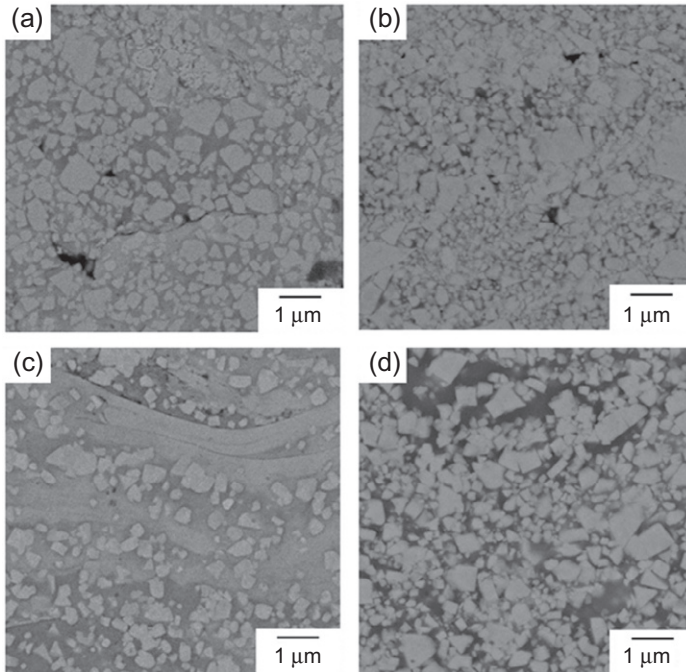


Figure 7.31 SEM observations of (a) HVOF WC-12Co, (b) WS WC-12Co, (c) HVOF WC-25Co, and (d) WS WC-25Co coatings (Chivavibul et al., 2010).

A clear difference can be recognized in the coatings with higher Co content. In the HVOF coating of WC–25Co (Figure 7.31c), the carbides are distributed in binder layers with different contrasts. These bright and dark binder layers were W-rich and Co-rich regions, respectively. The bright binder layer was not observed in the WS WC–25Co coating (Figure 7.31d). Moreover, the carbide fractions in HVOF coatings were much lower than those in WS coatings. The shape of carbides in HVOF coating became rounder than that of WS coatings. The loss of carbide and change of carbide morphology in HVOF coatings could be attributed to the dissolution of WC into the Co binder, while such reaction can be suppressed by WS process. This process provides a deposition of feedstock powder in solid state; therefore, the microstructure of the coating results from the stacking of particles under impact.

Examples of XRD patterns of HVOF and WS coatings are shown in Figure 7.32a and b, respectively (Chivavibul et al., 2008). The XRD plot of the WC–12Co feedstock powder is also given for a comparison. While the original powder contained only the peaks of Co and WC, HVOF coatings showed the crystalline peaks of WC, W₂C,

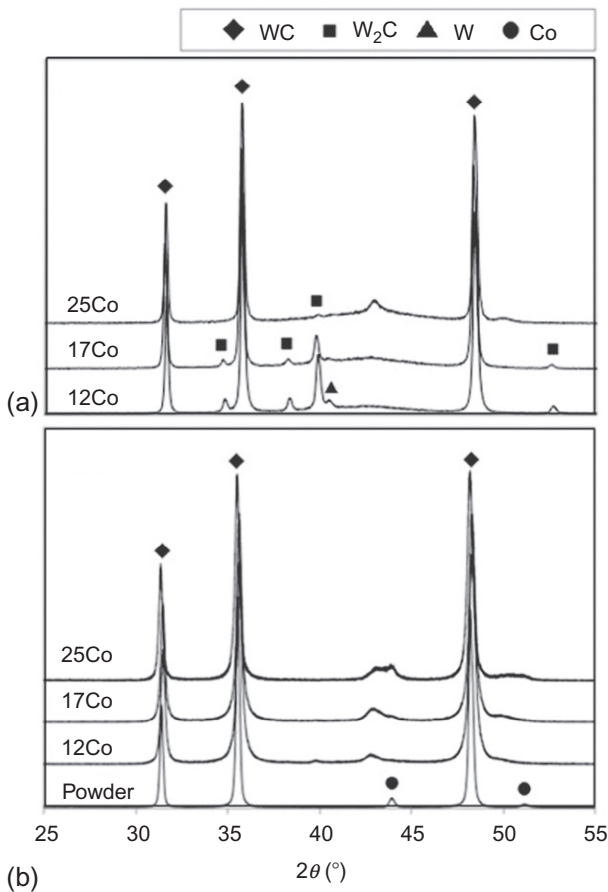


Figure 7.32 XRD results of (a) HVOF and (b) WS coatings. The result of WC–12Co powder coatings is given for a comparison (Chivavibul et al., 2010).

and W and a broad shoulder at the angle of the Co peak, indicating that the binder has become amorphous or nanocrystalline. There is a tendency for amorphous peak to increase as the Co content increases, while W_2C tended to decrease. In the case of WS coatings, only the peaks of WC and Co phase can be recognized for the 17 and 25% Co contents, while a very small peak of W_2C is observed in the 12% Co content. This meant that WS process can significantly suppress the decomposition and oxidation during deposition. The Co peaks of WS coatings were broadened and shifted to lower angles (Figure 7.34b). One possible explanation of this substantial peak shift can be high residual compressive stress in the binder due to large deformation of soft Co binder and constraining by the surrounding carbides. Another explanation could be the formation of high-pressure phase of Co due to high-speed impact, but this remains as a subject of further investigation. The broadening of the Co peak can be due to the formation of a nanocrystalline microstructure. As already observed in titanium splat (Figure 7.18), the high-speed impact of solid particle induces the dynamic recrystallization and leads to the formation of nano-order polycrystalline structure.

7.5.2 Mechanical properties of the coating

7.5.2.1 Hardness and fracture resistance

The Vickers hardness (load 0.3 kgf) and fracture resistance of the HVOF and WS coatings as a function of Co content are shown in Figure 7.33 (Chivavibul et al., 2008, 2010). Two types of feedstock powder F-series and C-series with different powder size were used for WS sample preparations in order to investigate the effect of particle size. For HVOF, only C-series powder was used because of the spitting problem of F-series powder. The powder F contained finer particles of 5–20 μm and the powder C had coarser particles of 15–45 μm (Figure 7.34; Chivavibul et al., 2010). The fracture resistance was evaluated by indentation fracture (IF) method (Chivavibul et al., 2008). It should be noted that the precision of the fracture toughness obtained by the IF method for such thin coatings is arguable, but it is still a very useful parameter for the quantitative comparison. Due to this, it is called as fracture resistance K_c in this paper. The values of the sintered materials are also given for a comparison. The WS coatings had lower hardness values than those of the sintered ones for all the Co contents; however, a trend of hardness reduction with Co content was the same. In contrast, the hardness of HVOF coatings only slightly changed with Co content. This can be attributed to the different phase distribution between WS and HVOF coatings as discussed above (Chivavibul et al., 2008). F-series coatings showed higher hardness values than C-series coating by about 100 HV for all the Co contents. SEM observations and mercury porosimetry of the coatings revealed the lower porosity in F-series than C-series coatings, which implies the better splat–splat bonding by using finer feedstock powder in WS (Chivavibul et al., 2010).

The fracture resistance of WS coatings showed a tendency to increase with increasing Co contents; however, the increment was not as large as that of sintered WC–Co. The fracture resistance of both C- and F-series coatings ranged from 4 to 6 MPam^{1/2}. In HVOF, the fracture resistance reduced as Co content increases probably due to

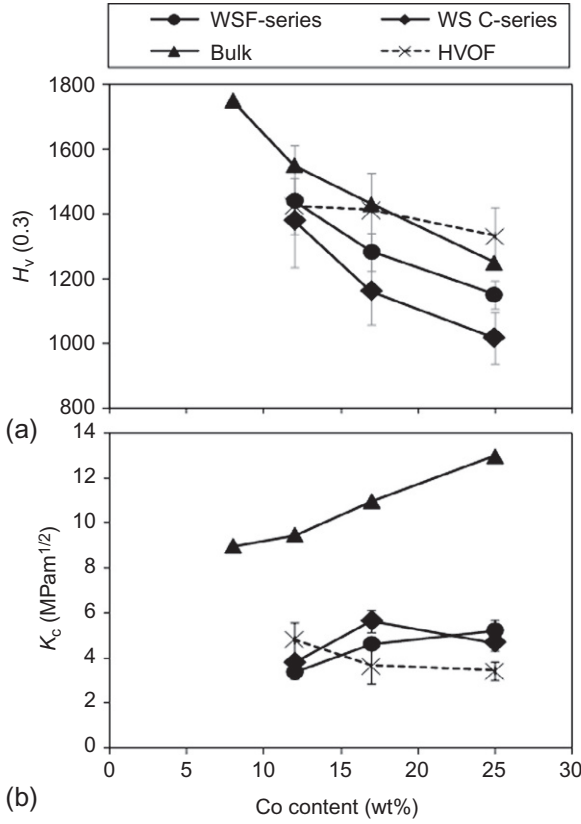


Figure 7.33 (a) Hardness and (b) fracture resistance as a function of cobalt content. Values of the sintered materials were given for a comparison (Chivavibul et al., 2008, 2010).

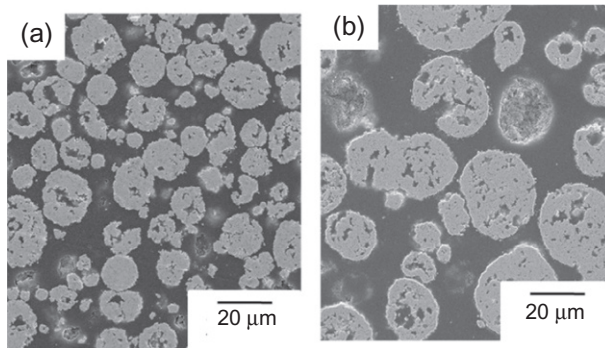


Figure 7.34 SEM observation of cross section of WC-12Co powder: (a) -20+5 μm and (b) -45+15 μm (Chivavibul et al., 2010).

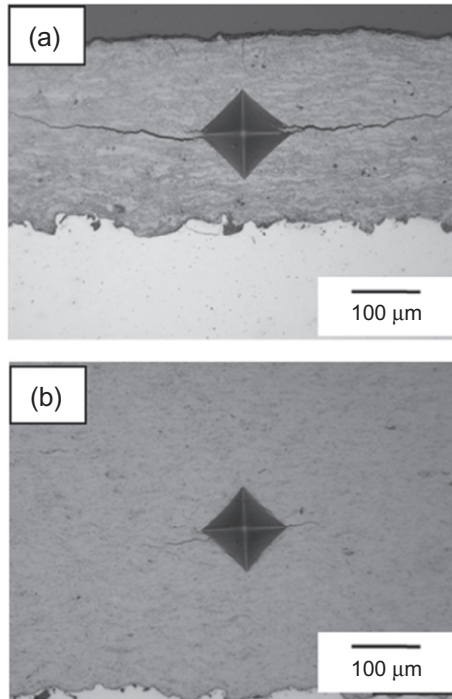


Figure 7.35 Cracks generated by the indentation fracture toughness test (load: 10 kgf) in WC–12Co coatings by (a) HVOF and (b) WS deposition. Drastic reduction of crack length can be recognized in the WS coating (Chivavibul et al., 2010).

embrittlement of binder phases. As mentioned above, reducing powder size lowered defects and enhanced splat–splat bonding in the WS coating leading to the increase of hardness; however, no improvement was recognized in terms of fracture resistance. Figure 7.35 shows the cross-sectional images of the crack configurations in WC–17Co coatings deposited by (a) HVOF and (b) WS, respectively. The drastic reduction in crack length can be recognized in WS sample indicating the effectiveness of suppression of the formation of brittle phases such as W_2C and amorphous binder phases. These values, however, are still lower than those of bulk WC–Co (9–14 MPam^{1/2}). The reason for the large gap may be caused by the existence of the microstructural defects such as pores, which can be recognized in Figure 7.36 (Kuroda and Watanabe, 2010). Although the bonding mechanism of a WC–Co particle in WS deposition is not yet understood, it is hypothesized that Co binder would work as a kind of glue with significant deformation upon impact. Thus, if there were not enough amounts of Co on the surface of a WC particle, for example, due to nonuniform distribution of Co in one particle, those regions could be poorly bonded. More detailed experiments are required to minimize the mechanical properties gap between a bulk WC–Co material and a WS WC–Co coating.

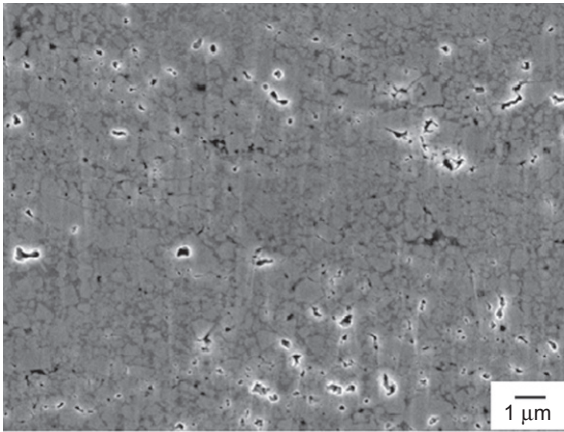


Figure 7.36 Cross-sectional image of a warm-sprayed WC–12Co coating (WC size: 0.2 μm) prepared by cross-sectional polisher (Kuroda et al., 2010).

7.5.2.2 Surface roughness

One very promising feature of WS WC–Co coating is the smoother coating surface in as-sprayed state, because it is possible to spray very fine powder. Fine powders cannot be sprayed by conventional HVOF due to spitting problem, in which a deposit of excessively molten sprayed particles adheres and grows on the inside wall of the nozzle of the spray gun and is ejected as large and irregular droplets. In Figure 7.37, the cross-sectional images around the surfaces of three WC–12Co coatings are presented, which were fabricated from the different feedstock powder consisting of different particle sizes (D_{50} = 28.5, 15.9, 7.5 μm) (Watanabe et al., 2010b). As the powder size becomes finer, the surface roughness becomes smaller. The surface roughness of those three coatings (average roughness, R_a , values) was evaluated by contact profilometry (Figure 7.38; Watanabe et al., 2010b). The surface roughness of WS WC–12Co was 1.22, 1.44, and 5.56 μm for the three powders, respectively. For coatings produced by conventional HVOF process, the reported values of R_a are typically reported in the range of 3–6 μm (Kuroda and Watanabe, 2010; Watanabe et al., 2010b; Kuroda et al., 2010). The smoother surface just after coating deposition can reduce costs and time for final polishing of commercial products. In addition, the achievable minimum surface roughness could be much smaller in WS than HVOF due to suppression of degradation of binder phase and due to the possibility to avoid the spallation of carbides during polishing.

The distribution of Vickers hardness and surface roughness of WS and HVOF WC–12Co coatings from F- and C-series powder has been plotted for various spray conditions (Figure 7.39) (Kuroda and Watanabe, 2010; Kuroda et al., 2010). It should be noted that only one data point is plotted for HVOF WC–12Co from F-series powder because it is very difficult to obtain coatings due to spitting in this combination. Such condition cannot be used in the practical applications. Interestingly, the conventional HVOF WC–12Co coatings show hardness of 1100–1300 HV (for 0.3 kgf load) and

Figure 7.37 Cross-sectional images around the surfaces of WS WC–12Co coatings from the different feedstock powder in terms of particle size distributions (Watanabe et al., 2010b; Kuroda et al. 2010).

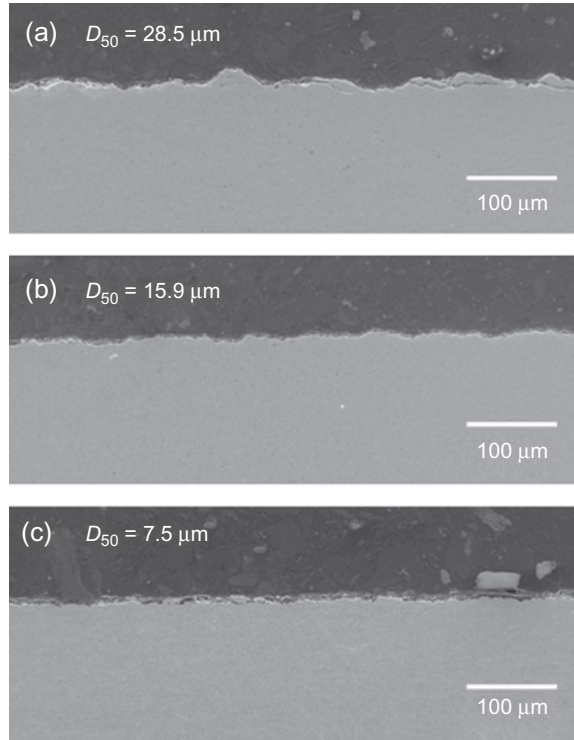
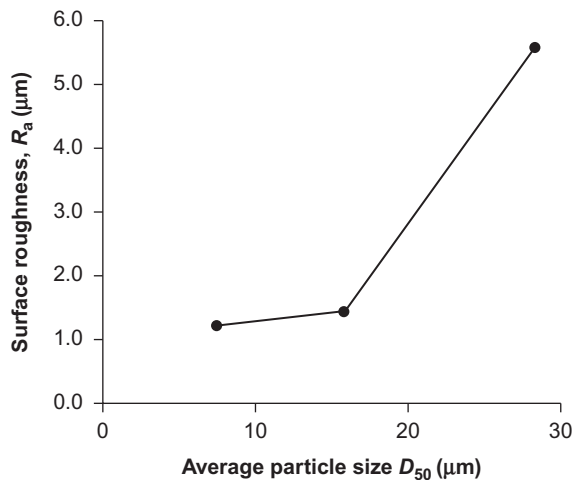


Figure 7.38 Variation of surface roughness of WS WC–12Co coatings as a function of average particle sizes in feedstock powder (Watanabe et al., 2010b; Kuroda et al. 2010).



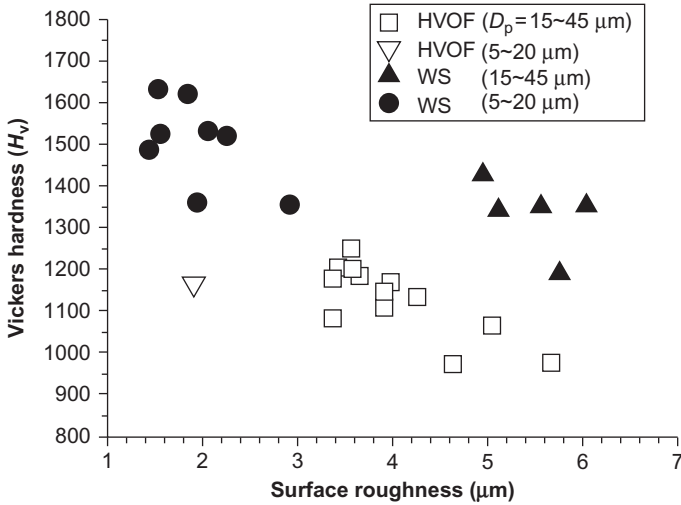


Figure 7.39 Map of surface roughness and Vickers hardness of HVOF and WS WC–12Co coatings for different feedstock powder size (Watanabe et al., 2010b; Kuroda et al. 2010).

surface roughness (R_a) of 3–4, but WS WC–12Co can achieve much higher hardness (1600 HV) and much smoother surface roughness ($R_a = 1-2 \mu\text{m}$).

7.5.2.3 Erosion behavior

Erosion wear property of C- and F-series coatings as a function of Co contents is shown in Figure 7.40 (Chivavibul et al., 2010). The data are presented in terms of the volume wear ratio, which is the volume loss of a coating normalized by that of

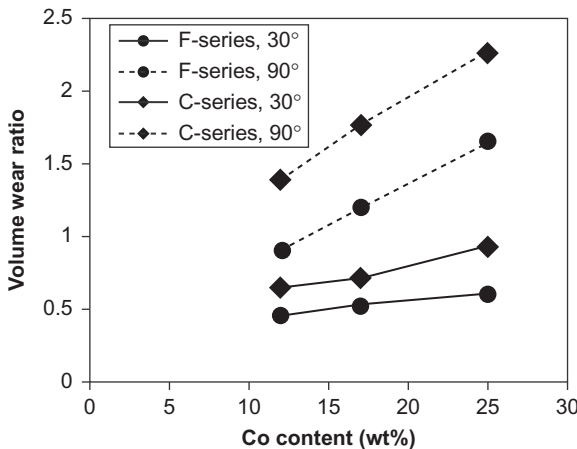


Figure 7.40 Erosion wear rate as a function of cobalt content (Chivavibul et al., 2010).

a low carbon steel (JIS-SS400). Solid and dashed lines represent the results obtained from impact angles of 30° and 90°, respectively. The figure clearly shows that the volume losses at 90° impact angle were higher than those at 30° for all Co contents, which is a typical erosion characteristic of brittle materials. The coatings' performance was actually inferior to the carbon steel at 90°. The volume wear ratio tended to linearly increase with increasing Co content for both 30° and 90° impact angles and F-series coatings showed less volume loss than C-series coatings. Previous studies about erosion of thermal sprayed cermet coatings described the erosion mechanism as follows: The first stage of erosion is caused by microcutting and microplowing of the soft binder by hard erodent particles. With progress of erosion, the carbide particles are exposed and then gouged by the impact of erodent particles and cause further cutting. The second is the spalling of the coating due to crack propagation. According to the observation of erosion wear morphology, the main erosion mechanism of the WS WC–Co coatings is also the latter one similar to conventional thermal spray coatings. The degree of spalling in the F-series coatings was considered to be lower than those in C-series coatings. The improvement in wear properties in F-series coating was attributed to the improvement of splat–splat bonding and reduction in porosity.

7.6 Recent development of high-pressure warm spray (HP-WS)

Recently, through collaboration among NIMS, Kagoshima University, and Plasma Giken Co. Ltd., the combustion pressure of WS has been increased from approximately 1 (low-pressure warm spray) to 4 MPa (high-pressure warm spray) with some internal design modifications (fuel injector and expansion nozzle; [Katanoda and Sun, 2013](#)), which was intended to increase particles' velocity up to 1000 m/s.

In order to increase the combustion pressure and thus the particles' velocity, the following two points were considered: fuel injector and convergent–divergent nozzle. Since it becomes more difficult to inject and atomize the liquid fuel in the combustion chamber with high pressure, optimization of the geometry of the coaxial type injector was carried out by a model experiment. In addition, gas dynamics simulation was carried out to optimize the geometry of the convergent–divergent nozzle to achieve high particle velocity ([Katanoda and Sun, 2013](#)). [Figure 7.41a](#) shows the geometry of the fuel injector and [Figure 7.41b](#) shows observed images of atomized liquid in the model chamber. [Figure 7.42a and b](#) shows the simulated gas and particle velocity along the central axis of the spray gun and the simulated gas and particle velocity, respectively, for different flow rates of nitrogen gas. [Figure 7.42c](#) shows a comparison of the low-pressure WS, high-pressure WS, CS with nitrogen, and helium as the propellant gas. It indicates that the developed high-pressure WS can achieve high particle velocity comparable to the He-driven CS but with significantly higher temperature range.

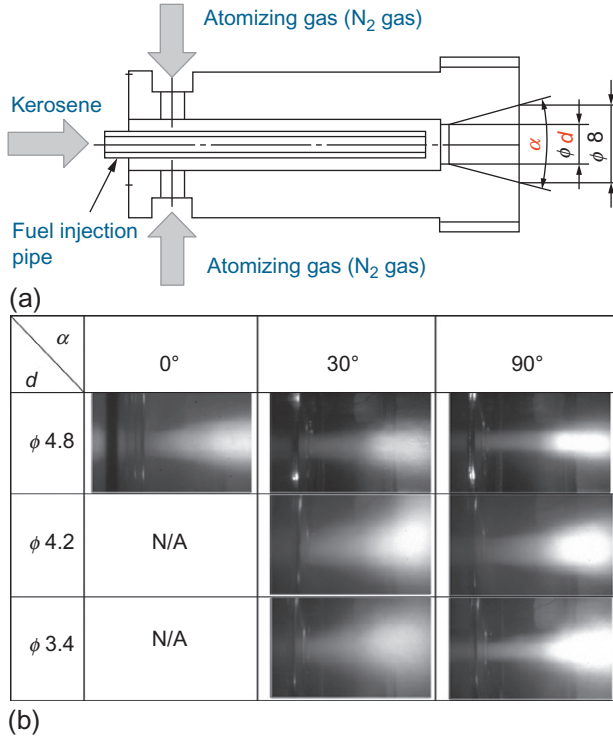


Figure 7.41 Geometry of the fuel injector (a) and observed images of atomized liquid into a chamber pressurized to 4 MPa with different injector geometries (b).

7.6.1 Ti-6Al-4V coatings by HP-WS

Ti-6Al-4V is an alloy that has been widely used in the aerospace industry in compressor blades and casings due to its high specific strength to weight ratio. There is a great interest in adequate processing technology to form parts made of this alloy because of difficulty in forging the alloy and the resultant high buy-to-fly ratio. Also, proper repair technology for damaged components is strongly desired. CS is apparently suited for this purpose, but obtaining dense deposits of this alloy requires very high impact velocity and He as the propellant gas, which is much more expensive than the gases used in WS.

Since WS, especially HP-WS, is capable of reaching high particle velocity with He-driven CS but with higher temperature range, this alloy is an ideal material to test the process. Figure 7.43 shows two series of cross sections of warm-sprayed coatings of Ti-6Al-V using 1 MPa as the combustion pressure (a)–(c) and 4 MPa (d)–(g), respectively. Both the values of porosity and oxygen content in these coatings were evaluated by the image analysis and the inert gas fusion technique and compared in

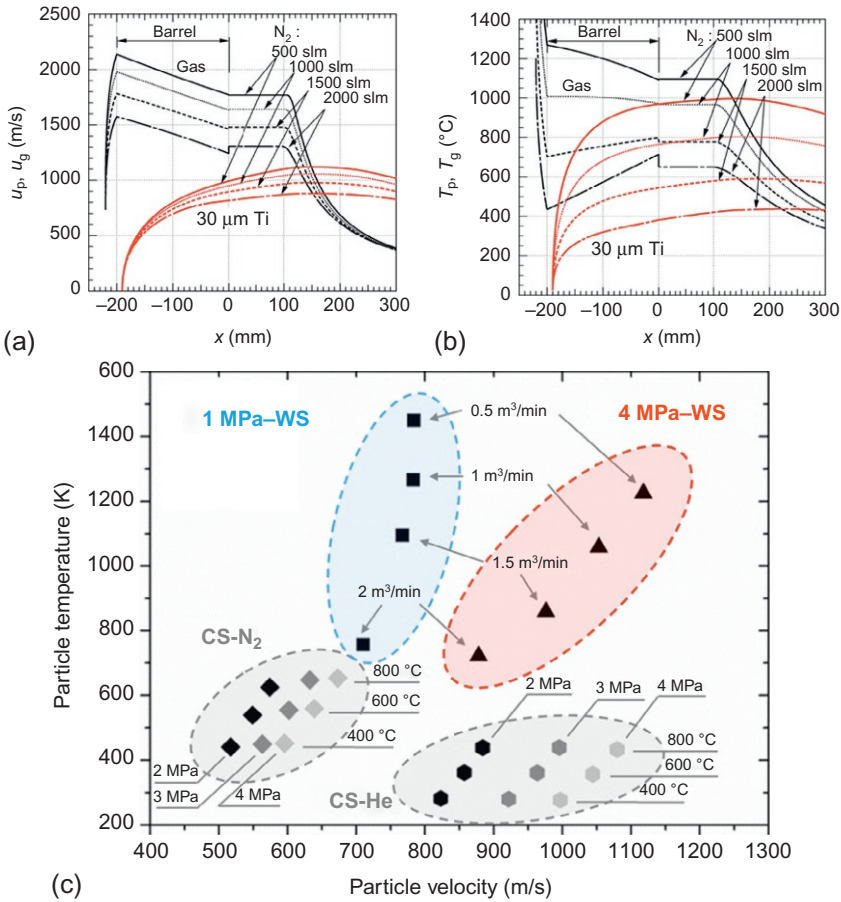


Figure 7.42 Numerical simulation profiles for high-pressure warm spraying of 30 μm titanium particles based on various process gas flow rates, starting from the combustion chamber to a spray distance of about 200 mm. (a) Gas and particle velocity profiles; (b) gas and particle temperature profiles; (c) process map showing the ranges of particle temperatures and velocities achievable by low- and high-pressure warm spray and CS (with the use of nitrogen or helium as a powder carrier gas).

Figure 7.44, where the benefit of the increased pressure is clearly shown for the reduction of porosity and oxygen content simultaneously (Molak et al., 2014). Mechanical properties of these deposits in the as-sprayed and heat-treated states were carried out by cutting out miniature tensile specimens. The results indicated that the as-sprayed deposits can be strong due to work hardening but essentially brittle. After proper heat treatment, however, significant failure strain up to 3% could be recovered with a strength level of 800 MPa (Molak et al., 2015).

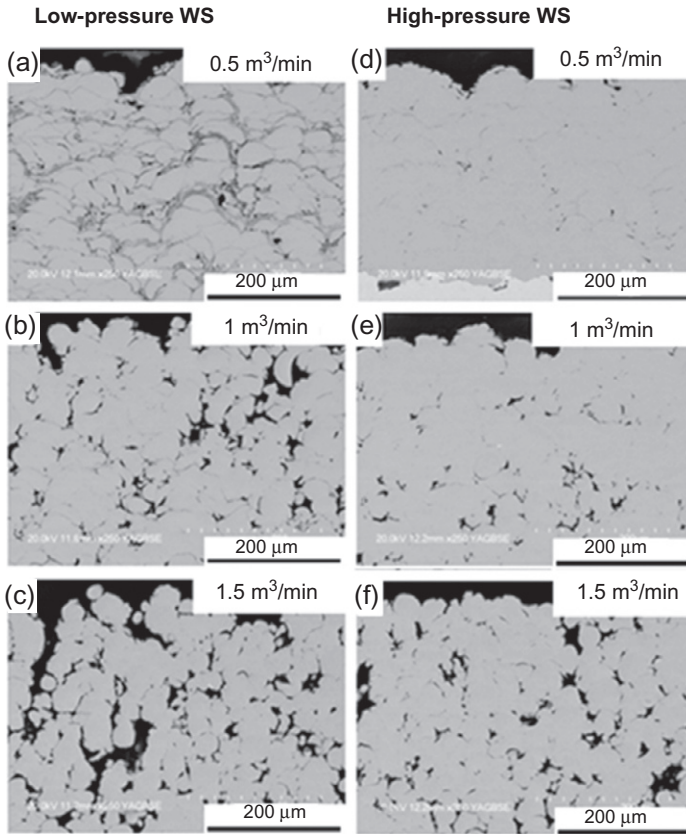


Figure 7.43 Two series of cross sections of warm-sprayed coatings of Ti-6Al-V using 1 MPa as the combustion pressure (a-c) and 4 MPa (d-f), respectively.

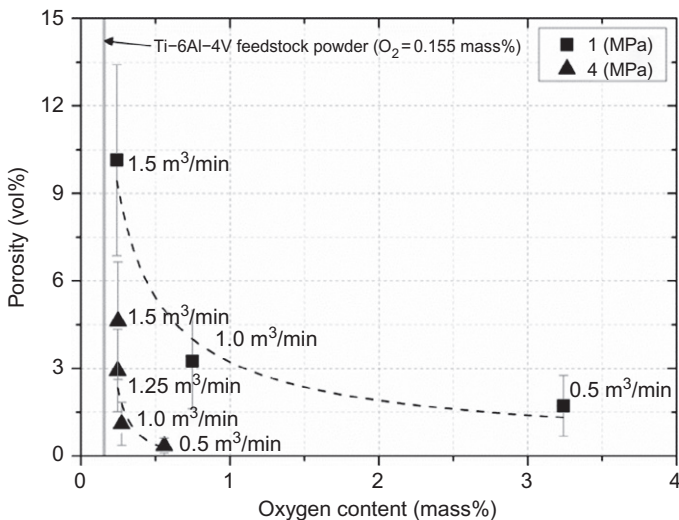


Figure 7.44 Porosity and oxygen content of Ti-6Al-4V coatings fabricated by low- and high-pressure warm spray system.

7.7 Conclusion

WS process has been developed on the basis of an HVOF apparatus using combustion gas. This, however, is just one route to achieve the concept of WS, that is, coating deposition by high-velocity impact of thermally softened solid powder particles. Process developments from different approaches are expected as the merits of warm spraying become better and more widely understood. In this chapter, the following points were presented to elucidate the characteristics of the WS process as well as some distinct characteristics of WS coatings to be explored for industrial applications in the near future:

- (1) WS was conceived in the efforts to improve the corrosion barrier capability of HVOF metallic coatings such as the density and degree of oxidation in the ultrasteel project conducted in NIMS from 1997 to 2006. Its main feature is the ability to control the temperature of the propellant gas while keeping the high velocity of HVOF.
- (2) Numerical simulation of the gas flow field and particle acceleration/heating of WS in comparison with HVAF revealed the higher degree of control over the powder temperature by the former process.
- (3) Titanium coatings with various degrees of porosity and oxidation could be fabricated by WS, where the nitrogen flow rate controlling the gas temperature was the dominant process parameter. Low porosity below 1 vol% with oxygen pickup below 0.25 mass% was possible for the feedstock powder with 0.14 mass% oxygen content.
- (4) Process map analysis of WS clarified the merits of thermal softening as an effective means to lower the critical velocity to achieve bonding and produce dense coating structures by high deformability in the thermally softened state of the powder.
- (5) High-resolution study of titanium splats by using TEM revealed the microstructure of various bonding interfaces created by warm spraying. They ranged from intimate metal–metal bonding, bonding via nm-scale oxide film, which can be crystalline or amorphous, to bonding formed by closure of the initially debonded south-pole regions by successive impacts of subsequent particles.
- (6) Tensile mechanical properties of several metallic coatings revealed the characteristics of warm-sprayed coatings and how they are sensitive to the impacting state of powder particles, which determine the degree of interparticle bonding and the thickness of oxides at the interfaces.
- (7) Warm-sprayed cermet coatings such as WC–Co exhibit certain advantages such as higher hardness, more homogeneous and fine microstructure, and fine surface quality, which should be encouraged for some advanced industrial applications.
- (8) Recently a high-pressure version of WS has been designed to increase the combustion pressure from 1 to 4 MPa. This new technique shows significant improvement of coating quality of Ti–6Al–4V in terms of porosity and oxygen content and can be a good alternative to CS.

Acknowledgments

We express our appreciation to Messrs. M. Komatsu and Hiraoka for skillful operation of spray equipment at the National Institute for Material Science. Dr. Y. Ishikawa (currently at Asahi Glass Co. Ltd.), Dr. P. Chivavibul (currently at the University of Tokyo), and Dr. G. S. Raman

(currently at IIT Madras) are thanked for their sincere research concerning cermet coatings at NIMS. Dr. J. Kitamura and K. Sato of Fujimi Incorporated are thanked for their support and collaboration in conducting WS research on WC–Co cermet coatings. Dr. H. Fukunuma and Dr. R.Z. Huang of Plasma Giken Kogyo Co. Ltd. are thanked for providing us with cold-sprayed samples and the data of CS particle state at impact obtained by numerical simulation.

References

- Assadi, H., Gartner, F., Stoltenhoff, T., Kreye, H., 2003. Bonding mechanism in cold gas spraying. *Acta Mater.* 51, 4379–4394.
- Binder, K., Gottschalk, J., Kollenda, M., Gartner, F., Klassen, T., 2010. Influence of impact angle and gas temperature on mechanical properties of titanium cold spray deposits. *J. Therm. Spray Technol.* 20, 1–9.
- Browning, J.A., 1993. Thermal spray method utilizing in-transit powder particle temperatures below their melting point. U.S. Patent 5,271,965, 21 December.
- Browning, J.A., 1994. Thermal spray method and apparatus for optimizing flame jet temperature. U.S. Patent 5,330,798, 19 July.
- Chivavibul, P., Watanabe, M., Kuroda, S., Shinoda, K., 2007. Effects of carbide size and Co content on the microstructure and mechanical properties of HVOF-sprayed WC–Co coatings. *Surf. Coat. Technol.* 202, 509–521.
- Chivavibul, P., Watanabe, M., Kuroda, S., Kawakita, J., Komatsu, M., Sato, K., Kitamura, J., 2008. Development of WC–Co coatings deposited by warm spray process. *J. Therm. Spray Technol.* 17, 750–756.
- Chivavibul, P., Watanabe, M., Kuroda, S., Kawakita, J., Komatsu, M., Sato, K., Kitamura, J., 2010. Effect of powder characteristics on properties of warm-sprayed WC–Co coatings. *J. Therm. Spray Technol.* 19, 81–88.
- Gaertner, F., Stoltenhoff, T., Voyer, J., Kreye, H., Riekehr, S., Kocak, M., 2006. Mechanical properties of cold-sprayed and thermally sprayed copper coatings. *Surf. Coat. Technol.* 200 (24), 6770–6782.
- Hackett, C.M., Settles, G.S., 1995. Research on HVOF gas shrouding for coating oxidation control. In: 8th National Thermal Spray Conference, September 1995. ASM International, Houston, pp. 21–29.
- Katanoda, H., 2006. Quasi-one-dimensional analysis of the effects of pipe friction, cooling and nozzle geometry on gas/particle flows in HVOF thermal spray gun. *Mater. Trans.* 47, 2791–2797.
- Katanoda, H., Sun, B., 2013. Design and development of high-pressure warm spray gun. In: Lima, R.S., Agarwal, A., Hyland, M.M., Lau, Y.C., Mauer, G., McDonald, A., Toma, F.L. (Eds.), International Thermal Spray Conference, May 13–15, 2013. ASM International, Busan, Republic of Korea, pp. 196–199.
- Katanoda, H., Kiriaki, T., Tachibanaki, T., Kawakita, J., Kuroda, S., Fukuhara, M., 2009. Mathematical modeling and experimental validation of the warm spray (two-stage HVOF) process. *J. Therm. Spray Technol.* 18, 401–410.
- Katanoda, H., Morita, H., Komatsu, M., Kuroda, S., 2011. Experimental and numerical evaluation of the performance of supersonic two-stage high-velocity oxy-fuel thermal spray (warm spray) gun. *J. Therm. Sci.* 20, 88–92.
- Kawakita, J., Kuroda, S., 2004. Oxidation restriction of in-flight particles upon GS-HVOF spraying by nitrogen addition to combustion gas. *Mater. Trans.* 45, 346–349.

- Kawakita, J., Fukushima, T., Kuroda, S., Kodama, T., 2002. Corrosion behaviour of HVOF sprayed SUS316L stainless steel in seawater. *Corros. Sci.* 44, 2561–2581.
- Kawakita, J., Kuroda, S., Fukushima, T., Kodama, T., 2003a. Corrosion resistance of Hastelloy C coatings formed by an improved HVOF thermal spraying process. *Mater. Trans.* 44, 253–258.
- Kawakita, J., Kuroda, S., Fukushima, T., Kodama, T., 2003b. Corrosion resistance of HVOF sprayed Hastelloy C nickel base alloy in seawater. *Corros. Sci.* 45, 2819–2835.
- Kawakita, J., Kuroda, S., Kodama, T., 2003c. Evaluation of through-porosity of HVOF sprayed coating. *Surf. Coat. Technol.* 166, 17–23.
- Kawakita, J., Kuroda, S., Fukushima, T., Katanoda, H., Matsuo, K., Fukanuma, H., 2006a. Dense titanium coatings by modified HVOF spraying. *Surf. Coat. Technol.* 201, 1250–1255.
- Kawakita, J., Kuroda, S., Krebs, S., Katanoda, H., 2006b. In-situ densification of Ti coatings by the Warm Spray (two-stage HVOF) process. *Mater. Trans.* 47, 1631–1637.
- Kawakita, J., Katanoda, H., Watanabe, M., Yokoyama, K., Kuroda, S., 2008a. Warm spraying: an improved spray process to deposit novel coatings. *Surf. Coat. Technol.* 202, 4369–4373.
- Kawakita, J., Maruyama, N., Kuroda, S., Hiromoto, S., Yamamoto, A., 2008b. Fabrication and mechanical properties of composite structure by warm spraying of Zr-base metallic glass. *Mater. Trans.* 49, 317–323.
- Kawakita, J., Shinohara, T., Kuroda, S., Suzuki, M., Sodeoka, S., 2008c. Fabrication of nano-sized oxide composite coatings and photo-electric conversion/electron storage characteristics. *Surf. Coat. Technol.* 202, 4028–4035.
- Kim, K., Kuroda, S., 2010. Amorphous oxide film formed by dynamic oxidation during kinetic spraying of titanium at high temperature and its role in subsequent coating formation. *Scr. Mater.* 63, 215–218.
- Kim, K., Watanabe, M., Kawakita, J., Kuroda, S., 2008. Grain refinement in a single titanium powder particle impacted at high velocity. *Scr. Mater.* 59, 768–771.
- Kim, K., Watanabe, M., Kawakita, J., Kuroda, S., 2009a. Effects of temperature of in-flight particles on bonding and microstructure in warm-sprayed titanium deposits. *J. Therm. Spray Technol.* 18, 392–400.
- Kim, K., Watanabe, M., Kuroda, S., 2009b. Jetting-out phenomenon associated with bonding of warm-sprayed titanium particles onto steel substrate. *J. Therm. Spray Technol.* 18, 490–499.
- Kim, K., Watanabe, M., Kuroda, S., 2009c. Thermal softening effect on the deposition efficiency and microstructure of warm sprayed metallic powder. *Scr. Mater.* 60, 710–713.
- Kim, K., Watanabe, M., Mitsuishi, K., Iakoubovskii, K., Kuroda, S., 2009d. Impact bonding and rebounding between kinetically sprayed titanium particle and steel substrate revealed by high-resolution electron microscopy. *J. Phys. D.: Appl. Phys.* 42, 065304.
- Kim, K., Kuroda, S., Watanabe, M., 2010a. Microstructural development and deposition behavior of titanium powder particles in warm spraying process: from single splat to coating. *J. Therm. Spray Technol.* 19, 1244–1254.
- Kim, K., Watanabe, M., Kuroda, S., 2010b. Bonding mechanisms of thermally softened metallic powder particles and substrates impacted at high velocity. *Surf. Coat. Technol.* 204, 2175–2180.
- Kleinstejn, G., 1964. Mixing in turbulent axially symmetric free jets. *J. Spacecraft Rockets* 1, 403–408.
- Kuroda, S., Watanabe, M., 2010. Structure and properties of thermal sprayed cermet (WC-Co) coatings. *J. High Temp. Soc.* 36, 254–263 (in Japanese).

- Kuroda, S., Fukushima, T., Sasaki, M., Kodama, T., 2002. Microstructure and corrosion resistance of HVOF sprayed 316L stainless steel and Hastelloy C coatings. *Mater. Trans.* 43, 3177–3183.
- Kuroda, S., Kawakita, J., Watanabe, M., Katanoda, H., 2008. Warm spraying—a novel coating process based on high-velocity impact of solid particles. *Sci. Technol. Adv. Mater.* 9.
- Kuroda, S., Raman, G.S., Watanabe, M., Komatsu, M., Sato, K., Kitamura, J., 2010. In: *International Thermal Spray Conference, 2010 Singapore*.
- Kuroda, S., Watanabe, M., Kim, K., Katanoda, H., 2011. Current status and future prospects of warm spray technology. *J. Therm. Spray Technol.* 20, 653–676.
- Kuroda, S., Molak, R.M., Watanabe, M., Araki, H., Katanoda, H., Sun, B., Ohno, H., Fukanuma, H., 2013. Velocity measurement of sprayed particles and coatings fabrication of titanium alloys by high-pressure warm spray. In: Lima, R.S., Agarwal, A., Hyland, M. M., Lau, Y.C., Mauer, G., McDonald, A., Toma, F.L. (Eds.), *International Thermal Spray Conference, May 13–15, 2013. ASM International, Busan, Republic of Korea*, pp. 196–199.
- Laque, F.L., 1975. *Marine Corrosion: Causes and Prevention*. John Wiley & Sons, New York.
- McBride, B.J., Gordon, S., Reno, M.A., 1993. Coefficients for calculating thermodynamic and transport properties of individual species. NASA TM-4513, 89.
- Molak, R.M., Araki, H., Watanabe, M., Katanoda, H., Ohno, N., Kuroda, S., 2014. Warm Spray Forming of Ti-6Al-4V. *Journal of Thermal Spray Technology* 23, 197–212.
- Molak, R.M., Araki, H., Watanabe, M., Katanoda, H., Ohno, N., Kuroda, S., 2015. To be submitted to *Journal of Thermal Spray Technology*.
- Moskowitz, L.N., 1993. Application of HVOF thermal spraying to solve corrosion problems in the petroleum industry – an industrial note. *J. Therm. Spray Technol.* 2, 21–30.
- Papamoschou, D., Roshko, A., 1988. The compressible turbulent shear layer: an experimental study. *J. Fluid Mech.* 197, 453–477.
- Papyrin, A., Kosarev, V., Klinkov, S., Alkhimov, A., Fomin, V., 2007. *Cold Spray Technology*. Elsevier Ltd, Oxford.
- Pershin, V., Mostaghimi, J., Chandra, S., Coyle, T., 1998. A gas shroud nozzle for HVOF spray deposition. In: *15th International Thermal Spray Conference, May 1998. ASM International, Nice, France*, pp. 1305–1308.
- Sampath, S., Jiang, X., Kulkarni, A., Matejicek, J., Gilmore, D.L., Neiser, R.A., 2003. Development of process maps for plasma spray: case study for molybdenum. *Mater. Sci. Eng. Struct. Mater. Properties Microstruct. Process.* 348, 54–66.
- Schmidt, T., Gartner, F., Assadi, H., Kreye, H., 2006. Development of a generalized parameter window for cold spray deposition. *Acta Mater.* 54, 729–742.
- Sobolev, V.V., Guilemany, J.M., 1998. *HVOF Spraying: Theory and Applications*. Maney Publications, London.
- Standard Specification for Titanium and Titanium Alloy Strip, Sheet, and Plate. ASTM International, 100 Barr Harbor Drive, PO Box C700, West Conshohocken, PA 19428–2959, United States.
- Stoltenhoff, T., Kreye, H., Richter, H.J., 2002. An analysis of the cold spray process and its coatings. *J. Therm. Spray Technol.* 11, 542–550.
- Sturgeon, A.J., Buxton, D.C., 2000. The electrochemical corrosion behavior of HVOF sprayed coatings. In: Berndt, C.C. (Ed.), *International Thermal Spray Conference. ASM International, Materials Park, OH*, pp. 1011–1015.
- Swank, W.D., Fincke, J.R., Haggard, D.C., Irons, G., Bullock, R., 1994. HVOF particle flow field characteristics. In: Berndt, C.C., Sampath, S. (Eds.), *International Thermal Spray Conference. ASM International*.

- Tabbara, H., Gu, S., 2009. Computational simulation of liquid fuelled HVOF thermal spraying. *Surf. Coat. Technol.* 204, 676–684.
- Tabbara, H., Gu, S., McCartney, D.G., Price, T.S., Shipway, P.H., 2011. Study on process optimisation of cold gas spraying. *J. Therm. Spray Technol.* 20, 608–620.
- Tam, C.K.W., Jackson, J.A., Seiner, J.M., 1985. A multiple-scales model of the shock-cell structure of imperfectly expanded supersonic jets. *J. Fluid Mech.* 153, 123–149.
- Vaidya, A., Streibl, T., Li, L., Sampath, S., Kovarik, O., Greenlaw, R., 2005. An integrated study of thermal spray process–structure–property correlations: a case study for plasma sprayed molybdenum coatings. *Mater. Sci. Eng. Struct. Mater. Properties Microstruct. Process.* 403, 191–204.
- Valarezo, A., Choi, W.B., Chi, W.G., Gouldstone, A., Sampath, S., 2010. Process control and characterization of NiCr coatings by HVOF-DJ2700 system: a process map approach. *J. Therm. Spray Technol.* 19, 852–865.
- Voggenreiter, H., Huber, H., Beyer, S., Spies, H.J., 1995. Influence of particle velocity and molten phase on the chemical and mechanical properties of HVOF-sprayed structural coatings of alloy 316L. In: Berndt, C.C., Sampath, S. (Eds.), *International Thermal Spray Conference, 1995*. ASM International, pp. 303–308.
- Watanabe, M., Owada, A., Kuroda, S., Gotoh, Y., 2006. Effect of WC size on interface fracture toughness of WC–Co HVOF sprayed coatings. *Surf. Coat. Technol.* 201, 619–627.
- Watanabe, M., Kishimoto, S., Xing, Y., Shinoda, K., Kuroda, S., 2007a. Evaluation of strain field around impacted particles by applying electron Moire method. *J. Therm. Spray Technol.* 16, 940–946.
- Watanabe, M., Chivavibul, P., Kuroda, S., Kawakita, J., Kitamura, J., Sato, K., 2007b. Development of WC–Co coatings by warm spray deposition for resource savings of tungsten. *J. Jpn. Inst. Metals* 71, 853–859.
- Watanabe, M., Brauns, C., Komatsu, M., Kuroda, S., 2010a. In: *Japan Thermal Spray Society Fall Meeting*, pp. 1–2.
- Watanabe, M., Raman, G.S., Komatsu, M., Kuroda, S., Sato, K., Kitamura, J., 2010b. In: *Japan Thermal Spray Society Spring Meeting, Osaka*, pp. 39–40.
- Watanabe, M., Brauns, C., Komatsu, M., Kuroda, S., Gaertner, F., Klassen, T., Katanoda, H., 2013. Effect of nitrogen flow rate on microstructures and mechanical properties of metallic coatings by warm spray deposition. *Surface & Coatings Technology* 232, 587–599.
- Witze, P.O., 1974. Centerline velocity decay of compressible free jets. *AIAA J.* 12, 417–418.
- Yamada, H., Kuroda, S., Fukushima, T., Yumoto, H., 2001. Capture of HVOF thermal sprayed particles by a gel target for evaluation of their in-flight condition. *J. Jpn. Inst. Metals* 65, 317–322.
- Yamamoto, A., Nakamura H., Nishiyama, Y., Kurahashi, R., 1994. Development of hot-rolled titanium-clad steel coils by using liquid phase at titanium-steel interface for bonding. *Nippon Steel Technical Report*, No. 62, pp. 34–39.
- Yokoyama, K., Watanabe, M., Kuroda, S., Gotoh, Y., Schmidt, T., Gartner, F., 2006. Simulation of solid particle impact behavior for spray processes. *Mater. Trans.* 47, 1697–1702.
- Zucrow, M.J., Hoffman, J.D., 1976. *Gas Dynamics*, vol. 1. John Wiley & Sons, NY.

Functionalized thermal spray coatings

8

S. Armada, R. Schmid, H. Johnsen, N. Espallargas

8.1 Introduction and background

According to the Oxford Dictionary, functional means having a special activity, purpose or task or being designed to be practical and useful, rather than attractive. Any thermal spray coating can be considered functional since it has a special activity or purpose. However, the development of functional coatings in other areas has been associated with the development of smart coatings. A functional and smart coating is defined as a coating with unusual and innovative properties that is able to respond to external stimuli (<http://www.sfcconference.eu>; <http://www.european-coatings.com/Events/Functional-Coatings>). The term “functional coatings” describes systems that possess, besides the classical properties of a coating (i.e. decoration and protection), an additional functionality (Adler and Potje-Kamloth, 2002). This additional functionality may be diverse and depends upon the actual application of a coated substrate. Typical examples of functional coatings are self-cleaning, anti-static, anti-reflective and anti-bacterial, whereas typical expectations of functional coatings include durability, reproducibility, easy application and cost effectiveness, tailored surface morphology and environmental friendliness (<http://www.mbraun.com/solutions/functional-coatings/>). Functionalizing thermal spray coatings has been a very important topic in thermal spraying due to the versatility of the technique and the possibilities this opens for many applications. Nowadays and thanks to the emerging of nanotechnologies, many different types of functional coatings are available in the market (Montemor, 2014; Mathiazhagan and Joseph, 2011).

Functional coatings are already used in different markets, and they already comply with the most stringent specifications in industries such as the automotive. The existing functionalized coatings are mainly developed for the paint and biomedical industries (Sridhar, 2010; Perkins et al., 2014; Yousaf et al., 2015), while there is still little development in thermal spraying. Most of the new functionalized thermal spray coatings are still at the research level due to the difficulties in making them work in a real application. In thermal spraying, functional coatings have been classically devoted to functionally graded layers for thermal barrier coatings and solid self-lubricated coatings. The definition of functional in functionally graded thermal barrier is different from the definition used in this chapter. Functionally graded thermal barrier coatings are defined as those barriers that change the composition gradually; hence, these coatings will not be taken into account in this chapter. The latter types of coatings (solid self-lubricated coatings) have been a major topic of interest in

thermal spraying in the last decades. Until today, self-lubricated coatings obtained by thermal spraying are exclusively based on solid lubricants (PTFE, hBN, graphite, MoS₂, etc.) embedded in the matrix. The production of thermal spray coatings with other types of functionality or smart capability has not been fully developed yet. However, coatings able to host capsules containing a liquid inside have been produced recently and will be described in detail in this chapter. The primary functionality of these coatings is to act as self-lubricants (i.e. the liquid in the capsules is an oil). Being able to keep a liquid inside a solid matrix during the thermal spraying process opens the possibility for the first time to produce functional and smart thermal spray coatings with selected functionalized liquids that can be released on demand.

Materials that can release appropriate chemicals on demand have been a major topic of research due to the savings associated with maintenance costs that might arise. Based on this idea, the first autonomic self-healing material (a material able to heal itself without human intervention) was developed at the University of Illinois, the United States, in 2001 (White et al., 2001). The self-healing material consisted of a polymeric matrix reinforced with homogeneously distributed catalysts and microcapsules filled with healing agents. The healing concept was based on repairing the cracks formed in the material, that is, when the crack propagates inside the material and hits a particle, the particle breaks and releases the healing liquid that reacts with the catalyst agent, thus restoring the initial properties of the material. This concept has been further developed, and it is used in paints and other polymer-based materials (Kessler, 2007; Hughes et al., 2010; Koene et al., 2009; Kumar et al., 2006).

Further development of such a concept for the production of harder coatings would open new fields of application. As mentioned above, most self-healing coatings have been developed to be used as paints, which are not an optimal technology for mechanical components where high contact pressures are required. Therefore, other coating technologies producing coatings with a better mechanical stability are needed to develop the next generation of self-healing materials for components with high mechanical demands. These coatings should provide machine elements with a reservoir of liquid lubricant in the material that can be released when starving conditions occur in the system. This concept has been developed by electrodeposition (Patel, 2009a) and thermal spraying recently (Armada et al., 2013). In the first case, the main limitation is that only metals can be used as matrix. This is a disadvantage in many mechanical components, since metal–metal contact can lead to galling and severe failure of machines. In the second case, this limitation is overcome since thermal spraying can produce coatings of a variety of matrix materials (polymers, metals and ceramics); however, the lubricant needs to be protected during spraying, due to the high deposition speed and temperature achieved in the process.

The first liquid–solid self-lubricating thermally sprayed coatings consisted of a polymer matrix (Armada et al., 2013; Espallargas et al., 2013) containing liquid lubricant-filled capsules. The main challenge for producing liquid-containing self-healing coatings by thermal spraying is to avoid any damage of the capsules during the production process since the temperature of the flame can damage the capsule material and thus burn or degrade the liquid lubricant, which is normally an oil. The thermal effect on the capsules can be minimized with a modified flame spray system for

spraying lubricant-filled microcapsules together with the matrix material. This process for spraying self-lubricated coatings has been developed recently (Espallargas and Armada, 2012), and it widens the possibility of spraying multiple matrix-capsule combinations (Espallargas and Armada, 2015). The production of the first liquid lubricant-filled self-lubricated coating included lubricant-filled polyurea microcapsules. These were produced by a miniemulsion polymerization process (Johnsen and Schmid, 2007). The capsules were kept in a water-based solution in order to protect them during the thermal spraying process. As a result, a coating with homogeneously distributed capsules was obtained (Armada et al., 2013; Espallargas et al., 2013).

8.2 Capsules technology

Microencapsulation is a process in which individual particles or droplets of solid or liquid material are surrounded or coated with a continuous film of polymeric material to give capsules ranging from less than one micron to several hundred microns in size (Ghosh, 2006; Umer et al., 2011; Jyoti Sri et al., 2012). The material inside the microcapsule is referred to as the core, internal phase or fill, whereas the wall is sometimes called a shell, coating or membrane. In its simplest form, a microcapsule is a small sphere with a uniform wall around it. Other microcapsules may be asymmetrically and variably shaped, with a quantity of smaller droplets of core material embedded throughout the microcapsule.

The core material may be encapsulated with the intention that it should be confined within the capsule wall for a specific period of time. Alternatively, the core material may be released either gradually through the capsule wall due to diffusion or when external conditions trigger the capsule wall to rupture, melt or dissolve. The core materials are most often used in the form of a solution, dispersion or emulsion. The compatibility of the core material with the shell and the size of the core material are important factors for the diffusion, permeability and controlled release of the core material. In addition, the core material and shell compatibility and the deposition process of the shell decide the morphology of the microcapsules. Mononuclear capsules contain the shell around the core, whereas polynuclear capsules have many cores enclosed. Matrix encapsulation has the core material distributed homogeneously throughout the capsule material.

Microencapsulation offers a wide range of potential benefits, such as

- environmental protection of sensitive materials, preventing degradation reactions and separating reactive compounds;
- improved material handling properties, better processability and converting liquids to solids;
- safe and convenient handling of toxic materials.

A wide variety of core materials can be encapsulated, including pigments, dyes, monomers, catalysts, curing agents, lubricants, anti-corrosion additives, drugs, vitamins, flavours and pesticides. Microencapsulation provides the possibility of combining the properties of different types of materials (e.g. inorganic and organic). Given the microencapsulation benefits and the versatility of the method, there are almost limitless applications for microencapsulated materials.

8.2.1 Capsule applications

The development of microencapsulation began with the preparation of capsules containing dyes in the late 1930s, as a cleaner substitute for carbon paper and carbon ribbons. Tiny gelatine capsules containing dyes were incorporated into paper for copying purposes and replaced carbon paper in the 1950s; the dye in the paper was released after impact by a typewriter key or the pressure of a pen (Schleicher and Green, 1956). Since then, encapsulation technologies have been explored in many fields of research. Microencapsulated materials are utilized in agriculture, pharmaceuticals, foods, cosmetics and fragrances, textiles, paper, paints, coatings and adhesives, printing applications and many other industries (Xiao et al., 2014; Alagusundaram et al., 2009; <http://www.microtekklabs.com/technical-overview.html>; Andersson et al., 2009).

Drug delivery takes advantage of the possibility of prolonged release, whereas microencapsulated vitamins are protected against the environment before release. Ingredients in food are often encapsulated for protection against degradation, as is the case for flavours, or to mask the unpleasant taste of ingredients. Pesticides and fertilizers are encapsulated to be released over time, allowing for the use of lower amounts and a less demanding distribution scheme. Today's textile industry makes use of microencapsulated materials to enhance the properties of finished goods. One application increasingly utilized is the incorporation of microencapsulated phase change materials. Microencapsulation offers great potential in the coating industry, but limited development has been carried out in the last years. Protective coatings containing self-healing microcapsules have been widely studied in the last decade (Ghosh, 2006; Wang et al., 2014; Cho et al., 2008; Grigoriev et al., 2014).

8.2.2 Encapsulation techniques

The technique of microencapsulation depends on the physical and chemical properties of the material to be encapsulated. Numerous preparation technologies are available, and they are usually categorized into two groups: chemical processes and mechanical or physical processes. Chemical processes are conducted in a tank or a reactor containing liquid, whereas mechanical or physical processes are mainly conducted in commercially available devices and equipment using a gas phase as part of the encapsulation. Physicomechanical processes include spray drying, fluidized bed technology, pan coating, spinning disc and coextrusion, whereas physicochemical processes include coacervation, solvent evaporation, encapsulation by polyelectrolyte multilayers, phase inversion and hot melt. Chemical processes are mainly interfacial polymerization and in situ polymerization.

8.2.3 Lubricant-filled microcapsules

The lubricant-filled microcapsules presented in this chapter have been prepared by a miniemulsion process, based on a stable oil-in-water emulsion where all the ingredients in the dispersed phase (e.g. monomer and lubricant) are mixed before emulsification. Interfacial polymerization at the droplet interface is used for shell formation around the liquid core (i.e. lubricant) by adding a second monomer to the continuous

phase of the emulsion. In this way, the amount and type of lubricant can be modified and tuned to the desired application and properties aimed at.

Miniemulsion processes are based on using premade stable emulsions in the submicron or micron range as nano- and microreactors. The droplets are stabilized against both diffusional degradation (Ostwald ripening) and coagulation by the use of a costabilizer together with an efficient surfactant (El-Aasser and Sudol, 2004; Asua, 2002; Ugelstad et al., 1973). In the case of this work, the liquid lubricants (Table 8.1) themselves could be used as costabilizers due to their low water solubility. In the miniemulsion process, all ingredients in the dispersed phase (isophorone diisocyanate and lubricant) are mixed before the emulsification resulting in an emulsion with the same composition of lubricant and monomer in each droplet. These droplets function as microreactors and keep size and content almost equal to the droplet size and content of the initial emulsion, when polymerizing into microparticles (Figure 8.1) (Landfester, 2006). The work described in this chapter, interfacial polymerization at the droplet interface was used for shell formation around the liquid core (oil) by adding one of the monomers (diisocyanate) to the lubricant droplets and the other monomer (guanidine) to the continuous phase of the premade stable emulsion.

Table 8.1 Overview of polyurea microcapsule synthesis using various amounts and types of lubricants

Lubricant type	Lubricant amount (vol.%)	Capsule size (μm)
Polyalphaolefin ^a (PAO)	30	3.4
PAO ^a	50	2.7
PAO ^a	70	2.9
Silicone oil 100 cs ^b	70	2.4
Silicone oil 1000 cs ^c	70	7.1

^aMereta 46 (Statoil).

^bSilicone oil AP 100 (FLUKA).

^c200[®] Fluid 1000 cs (Dow Corning).

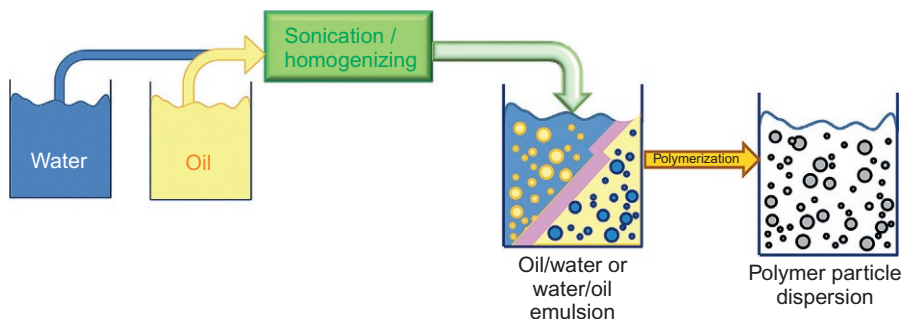


Figure 8.1 Principle of miniemulsion polymerization process.

The oil-in-water miniemulsions were prepared by emulsifying an oil phase (20%, v/v) in an aqueous phase by means of an ultrasonifier (Labsonic 2000) in small-scale experiments and a homogenizer (15MR-8TA, APV GAULIN Inc.) in large-scale experiments. The oil phase consisted of isophorone diisocyanate and lubricant (Table 8.1) in various ratios. The aqueous continuous phase consisted of a 10 g/l polyvinyl alcohol (Celvol 523) stabilizer solution. Guanidine carbonate (isocyanate/primary amine molar ratio of 1) was added to this premade miniemulsion, and interfacial polymerization performed at 70 °C during 16 h. The size and size distribution of the prepared microcapsules were determined by means of dynamic light scattering using a LS230 Coulter Counter (Beckman Coulter Inc.).

The amount and type of lubricant were varied; an overview of the capsule synthesis is shown in Table 8.1. In almost all cases, lubricant type or amount did not influence the capsule size and yield (>90%). The exception is for the silicone oil with the highest viscosity, where the encapsulation was incomplete (yield ~70%, substantial oil phase floating on top of the aqueous dispersion) and the capsule size remarkably larger, explained by a less effective homogenization in high-viscosity

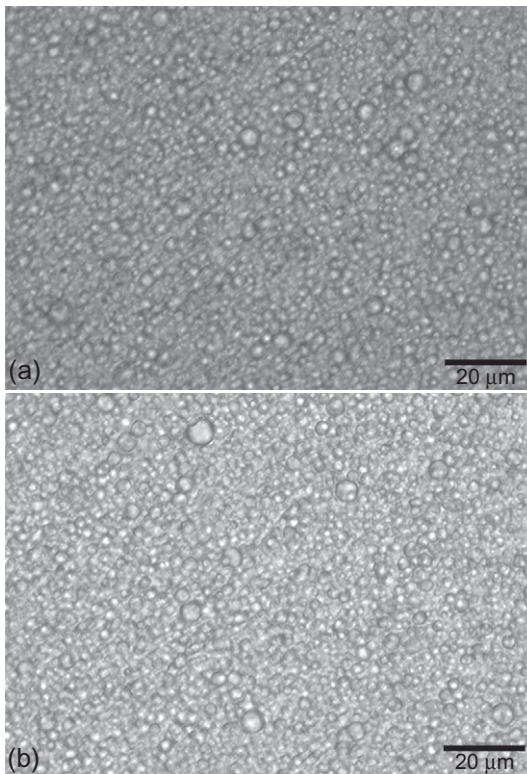


Figure 8.2 Optical micrograph of aqueous dispersions of liquid-filled polyurea capsules with various types and amounts of lubricant: (a) 30% polyalphaolefin (PAO), (b) 50% PAO, (Continued)

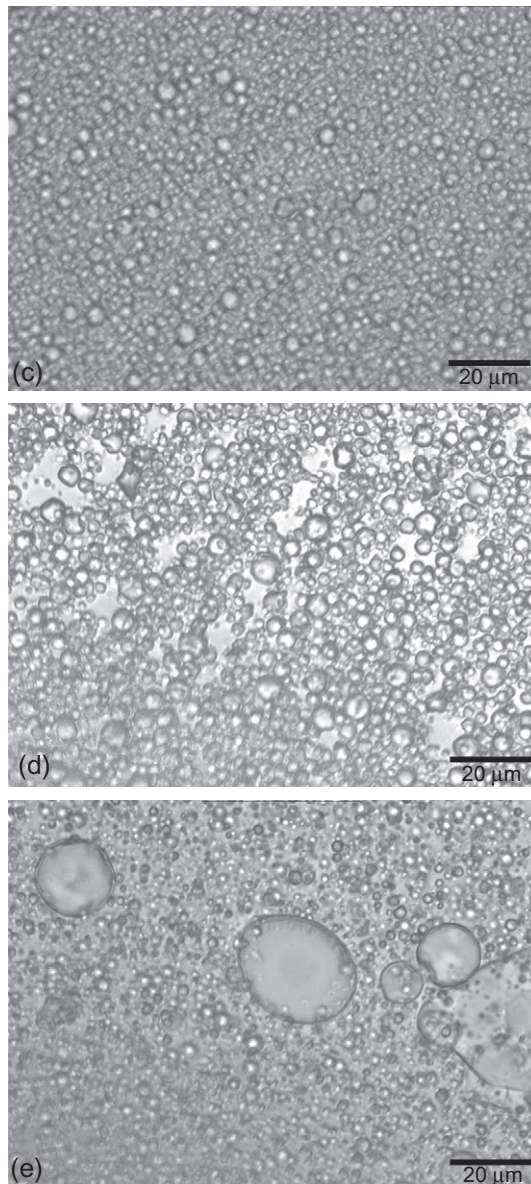


Figure 8.2, cont'd (c) 70% PAO, (d) 70% silicone oil 100 cs and (e) 70% silicone oil 1000 cs (bar in micrographs = 20 μm) (Armada et al., 2013).

systems. Polyurea capsules in the size range of 3 μm , containing 30–70 vol.% of polyalphaolefin (PAO) as liquid lubricant, were used in the coating experiments. An optical micrograph of aqueous dispersions of these capsules is shown in [Figure 8.2](#).

8.3 Functionalizing thermal spray coatings

Functionalized thermal spray coatings have been produced for a long time. The first US patent for a bonded material containing solid lubricants was issued in the mid-1940s; however, the use of solid lubricants (PTFE, hBN, graphite, MoS₂, etc.) has been driven by the aircraft industry (Miyoshi, 2001). The use of solid lubricants embedded in wear-resistant coatings has also become popular in thermal spraying, and many examples are found in the literature including polymers as solid lubricants such as MoS₂ (Marple and Voyer, 2001; Yamada et al., 2009), graphite and hBN (Tsunekawa et al., 2006) and BaF₂–30 wt.% CaF₂ (Stanford et al., 2004). These coatings can be considered as functionalized since they have an additional functionality besides the classical properties of the coating (i.e. protection against corrosion, wear and high temperature). The use of solid lubricants has been the only way to produce functionalized thermally sprayed self-lubricated coatings. The recently developed technology at SINTEF/NTNU for producing liquid-containing coatings has opened the possibility of producing a vast number of functionalized coatings that could not be produced with solid particles (Espallargas and Armada, 2012).

The novelty of the thermal spray liquid–solid self-lubricated coatings consists of the presence of a liquid element inside the coating. Introducing a liquid in thermal spray coatings is a challenging task due to the high temperatures and velocities reached during the spraying process. The high temperatures of the flame can degrade the walls of the capsules containing the liquid phase and the liquid. In addition, the high speeds reached in the process will produce high impacts on the capsule walls that may break them, thus making it impossible to keep and retain the liquid inside the coating.

The importance of developing functionalized thermal spray coatings relies on the possibility of producing a wide range of coating materials, from ceramic to metals and polymers. Since 2001, when White et al. produced the first autonomic self-healing polymeric material at the University of Illinois (the United States) (White et al., 2001), many different approaches have been used for developing new self-healing materials; however, most of the proposed coatings are only polymer based (Wool, 2008; Kessler, 2007). Some specific examples described in the literature are filled elastomers, hard elastic propylene, fibre-composites (for both polymer and concrete matrices), epoxy, low-density polyethylene, etc., but there are no specific examples of either metallic or ceramic self-healing materials. In addition, the polymer-based self-healing coatings found in the literature are developed for being used as paint coatings or bulk polymers (Montemor, 2014). The main drawback of paint coatings is their limited mechanical properties, thus limiting their use for high demanding mechanical components in machine elements. Therefore, producing coatings that can fulfil both a self-healing property and high mechanical demand would be a big achievement.

Recently, a metallic coating obtained by electrodeposition with homogeneously distributed capsules that may be able to repair itself after sustaining damage has been presented. Electrodeposition opens up new applications in different markets such as construction and car manufacturing. Metals or alloys including copper, zinc and nickel have been used, but theoretically, it would be possible to obtain coatings from any

metal that can be electroplated. However, at present, the self-healing property of these coatings has not been demonstrated yet (Metzner, 2009; Patel, 2009b).

The functionalized coatings can become very relevant and important in the market via different applications. The possibility of encapsulating almost any liquid, combined with the possibility of spraying almost any existing materials, opens the opportunity for tailor designing coatings for very specific applications. The encapsulated liquids can play different roles in different applications based on their properties. In theory, it is possible to encapsulate lubricants that can reduce the friction and wear between moving parts, corrosion inhibitors that can hinder metal degradation, pH modifiers that can act as buffers in different environments, catalysers that can promote chemical reactions in situ, etc. The potential application for such coatings is thus almost infinite.

8.3.1 Types of functionalization and potential applications

The new liquid–solid thermally sprayed coatings open a wide variety of applications. Most of them are based on existing concepts in different coatings obtained with other techniques. Some examples of existing research performed on encapsulated chemicals that might inspire the use of liquid–solid thermal spray coatings are the following:

- *Optical properties:* 3M has developed protective, microencapsulated components including anti-corrosive chemicals, film-forming components and marker dyes for visual identification of coating damage (Guilbert et al., 1998). The presence of dyes in the coating that can be released when the coating is damaged reveals visually those impacted areas and thus makes them accessible to repair processes leading to reduced maintenance costs and longer life span of the components.
- *Thermal-resistant coatings:* Giraud et al. (2002) have shown the flame-retardant effect of diammonium hydrogen phosphate by microencapsulating it with a polyurethane shell. The capsules were used for improving the flame retardancy of polyurethane coatings used as fabrics. The use of polyurethane wall capsules aims at optimizing the compatibility between the polyurethane fabric and the capsule. It was shown that microencapsulated diammonium hydrogen phosphate improves the flame retardancy of the polyurethane fabrics.
- *Corrosion protection coatings:* Damages in coatings applied to metallic substrates for corrosion protection promote that corrosive species reach the metal surface and corrode it. Self-healing materials have been largely investigated for restoring the initial barrier properties of the coating, hence protecting the metallic surface against corrosion (Jadhav et al., 2013). Jadhav et al. have encapsulated linseed oil along with drier and corrosion inhibitors in multicore phenol formaldehyde microcapsules, added to a polyurethane coating. The linseed oil due to its high content of unsaturated esters of oleic acid, linoleic acid and linolenic acid is susceptible to polymerization reactions upon exposure to oxygen in air. Whenever the coating is damaged, the capsules release the linseed oil, which, through the polymerization process, solidifies promoting the protection of the metal from corrosive species.

Cho et al. (2009) at the University of Illinois at Urbana-Champaign also developed a similar system based on the self-healing coating containing microencapsulated catalyst and phase-separated healing agent droplets (or encapsulated healing agent if it reacts with the matrix) in a matrix on a metallic substrate. Damage to the coating layer releases

the catalyst and healing agent, which are mixed together in the damaged region, producing a cross-linked reaction that protects the substrate from the environment.

- *Anti-fouling coatings:* New research at the University of Gothenburg and Chalmers University of Technology (Dahlback et al., 2010) includes the potential use of microcapsules that can carry biocides in paint for optimized anti-fouling properties. The microcapsules are capable of loading very large amounts of biocides and when the capsule containing the biocide is exposed to water at the coating surface, it opens up and the biocide is released.
- *Low-friction coatings:* Liqun (2006) has shown the possibility of improving the wear resistance and friction coefficient of copper composite electrodeposited coatings containing lube oil microcapsules. Liqun also proved the possibility of reducing the coefficient of friction (CoF) of composite coatings containing lubricant-filled capsules. The average CoF of copper coatings was ~ 0.5 , while the CoF for the composite coatings was reduced to 0.02.

Among all the above-mentioned examples, the one that would find a wide range of applications in thermal spraying is most likely the development of corrosion protection capsules. The corrosion resistance of thermal spray coatings is known to be one of the properties to be improved, even though the global market for thermal spraying in corrosion protection is around 10–20%. Producing coatings containing capsules that could release corrosion inhibitors or fill in/seal the pores in corrosion applications would be a big step forward in the current market of thermal spraying for corrosion protection. However, finding new markets for thermal spraying like, for example, in optical applications would benefit the thermal spraying community.

8.3.2 Functionalized coatings manufacturing techniques

It is well known that the most characteristic property of thermal spraying is the possibility of imparting high temperatures or high velocities (or both at the same time) to materials. The proper selection of the thermal spraying technique is based on the physical and chemical properties of the material that is being sprayed. For the different thermal spraying techniques available in the market, one could define some general trends:

- Flame spraying is typically used when low temperatures and low velocities are needed; thus, it can be used with low melting point materials such as polymers and metals (e.g. Al and Zn).
- Arc spraying (AS) is also known for its low temperature and particle velocity; however, they are higher than in flame spraying. This technique is also used for spraying low melting point and conductive metals. A broader range of metal alloys can be sprayed as compared with flame spraying.
- Plasma spraying generates extremely high temperatures and relatively high particle velocities. This technique is most used for spraying ceramic materials, which have high melting points, and metal alloys.
- High velocity oxy-fuel and high velocity air fuel (HVOF and HVAF) and detonation techniques are recognized as very high speed and low thermal input techniques. These techniques are normally used for spraying cermets (ceramic–metallic materials) and metals. In this chapter, a technique called high velocity oxy–air fuel, which is a variation of the HVAF, will be mentioned later.
- Cold spraying has more recently been introduced in the market and it is characterized by a very low temperature and high particle velocity.

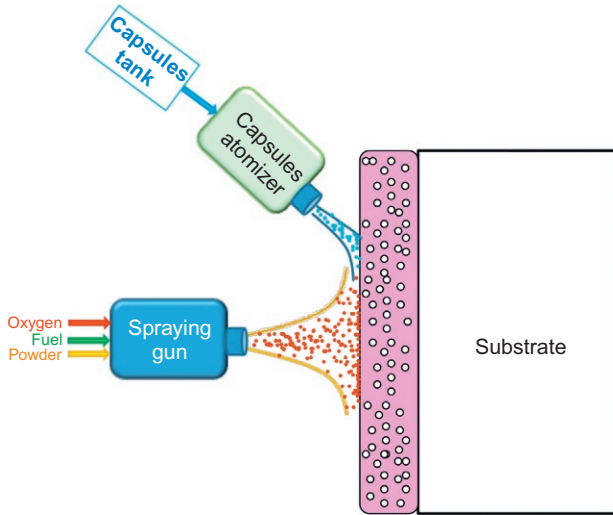


Figure 8.3 Sketch showing the injection of the capsules in the flame spraying process.

Based on the above-mentioned properties of thermal spraying techniques, flame spraying seems to be the most suitable technology for spraying liquid-filled capsules (the lowest temperatures and particle speeds). A sketch of the process for spraying the capsule-containing coatings to flame spraying is shown in [Figure 8.3](#). Another characteristic of flame spraying is related to the porosity in the coatings. Since the temperatures and the speeds are not very high, the particles reaching the substrate are not fully plastically deformed or adapted to the surface and thus, pores are formed during the coating build up. This might limit the application of capsule-filled coatings where high mechanical properties are necessary (e.g. high contact pressures are required).

AS can also be seen as a preferred technique for producing capsule-filled coatings. As in the case of flame spray coatings, the porosity might also hinder their use in demanding applications such as those where corrosion might be the main degradation mechanism. However, the porosity in the coatings can be beneficial in oil-lubricated systems since pores can act as lubricant reservoirs.

HVOF/HVAF and detonation techniques produce very dense coating structures due to the high speed achieved in the process. Due to the high speeds, the porosity in the coatings is minimized and is normally kept below 1% in cermets. This is of high importance for obtaining coatings with good mechanical properties, but it risks the possibility of spraying capsules. The high speeds reached promote big deformations upon impact on the substrate surface. Due to these impacts, the capsules might break and release the liquid during the spraying process. This effect has two main drawbacks: it limits the number of functionalized capsules inside the coating and damages the spraying process by polluting the sprayed surface with undesirable liquid chemical species. Thus, a good control on the spraying parameters (i.e. gas flow and powder feed) can allow obtaining an optimal microstructure of the coating to host the capsules.

Plasma spraying is a challenging technique for spraying liquid-filled capsules due to the high temperatures involved in the process (up to 10,000 °C in the core of the jet). However, by optimizing the capsule injection into the system, it is possible to minimize the damage and obtain a coating with liquid-filled capsules as shown by [Espallargas and Armada \(2015\)](#). In terms of porosity, plasma spraying produces coatings with porosity up to 10% in some cases due to the lower jet speeds; therefore, the capsules can find a place in the coating without suffering large deformations.

Based on the experience gained in our work ([Armada et al., 2013](#); [Espallargas et al., 2013](#); [Espallargas and Armada, 2012, 2015](#)), it can be concluded that the most critical parameter for spraying liquid-filled capsules is the spraying velocity. High impacts are associated with high velocities; hence, the capsules are more prone to breakages or deformations. In addition, the properties of the capsules (wall thickness, size, amount, etc.) need to be properly designed in order to minimize the breakage during the spraying process. As a general rule, it can be stated that capsules with thick walls will withstand higher impact velocities, while capsules with thin walls will not withstand high impacts, but they will be able to release bigger amounts of liquid to the system.

8.4 Low-friction functionalized thermal spray coatings

8.4.1 Polymer matrix coatings

8.4.1.1 Background

For the first liquid–solid self-lubricating thermal spray coating, a polymer material (polyurea) was used for encapsulating liquid lubricants; hence, spraying the capsules with polymeric matrix was the most favourable situation as a starting point. Both the capsule wall material and the polymeric matrix have similar melting points (which are relatively low compared with metals and ceramics) and thus, they will behave similarly during the spraying process. The main difference between the liquid-filled capsules and the polymeric feedstock material used for spraying was their particle size. This requires that both components (polymer feedstock material and capsules) are fed in different positions in the flame. By optimizing the injection of the capsules in the flame, it was confirmed that most of the liquid-filled capsules could withstand the spraying process.

8.4.1.2 Method

Flame spraying was selected for spraying the polymeric coatings containing liquid-filled capsules. The relatively low speed and low temperatures involved in flame spraying makes this technique the most suitable for spraying the capsules.

Since the capsule wall is made of polyurea, it was decided to use standard thermal spraying parameters normally used for spraying a polymer feedstock material. The first thermal spray coatings containing liquid-filled capsules were obtained with nylon matrix ([Armada et al., 2013](#); [Espallargas et al., 2013](#); [Espallargas and Armada,](#)

2012). The thermal spraying parameters corresponded to typical parameters used for nylon. The gases used for spraying the nylon together with the capsules were propylene and compressed air. The spraying distance was kept constant between 150 and 250 mm and air was used as carrier gas. The nylon powder was axially fed into the flame spraying gun, while the capsules were introduced radially inside the flame using an independent powder feeder as shown in Figure 8.3. The independent powder feeder can be controlled in order to adjust the amount of capsules injected into the flame and also the injection angle. As mentioned before, the capsules are made of a thin wall of polyurea, which can be burnt easily. In order to minimize the thermal input to the capsules, the capsules were injected as a water-based solution into the flame. The feeding rate of the water-based solution containing the capsules was adjusted to avoid any excess of liquid during the spraying process, which could enhance porosity formation in the coating. The water is evaporated during the spraying process and no adhesion or cohesion defects were found in the coatings. Thermal spraying parameters used for spraying the capsules together with the nylon were the same as the parameters used for spraying the nylon powder alone. The effect of co-spraying the nylon together with the slurry containing the capsules might have an effect on the porosity of the coating due to water evaporation during spraying. The capsules are fed into the system by an external feeder, which will minimize the influence of the capsules on the spraying parameters and will give flexibility for spraying the capsules. This broadens the potential for producing coatings with different matrices and materials.

The injection of the capsules was optimized by using different nozzles in the external feeding system. The nozzle plays a very important role in the spraying process since it determines how the capsules are introduced into the flame, which could have an adverse effect on the coating properties. By testing different nozzle shapes, it was found that a cone-shaped nozzle led to the best results. A stream-shaped cone produced more porous coatings because the water slurry is confined to a very narrow position on the coating. Since only two nozzles were tested, it is probable that the final properties of the coating can be further improved by other nozzle configurations. This is a further work to be done in order to optimize the coating microstructure and properties.

8.4.1.3 Results

An optical microscopy image of the surface of the self-lubricating coating shows a homogeneous dispersion of the capsules in the nylon matrix (Figure 8.4). The capsules have the same size and shape as before spraying; thus, it is confirmed that they can be sprayed without any damage.

The cross section of the coatings was analysed for confirming the presence of the liquid-filled capsules in the nylon coating. Figure 8.5 shows that the capsules inside the coating survived the thermal spray process. The cross section in Figure 8.5 was obtained by cutting the coating in a V-shape using a scalpel. The shape and size of the capsules were similar to the starting material and the capsules were well distributed in the matrix. This will allow controlling the mechanical and tribological

Figure 8.4 Surface of the capsules containing thermally sprayed nylon.

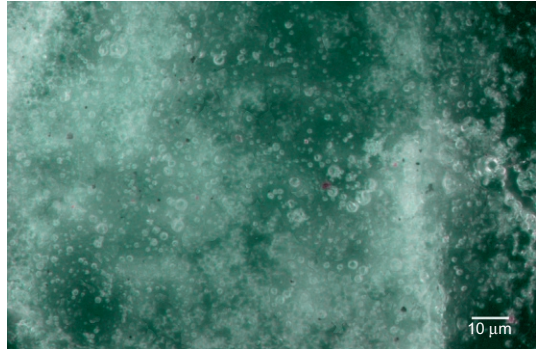
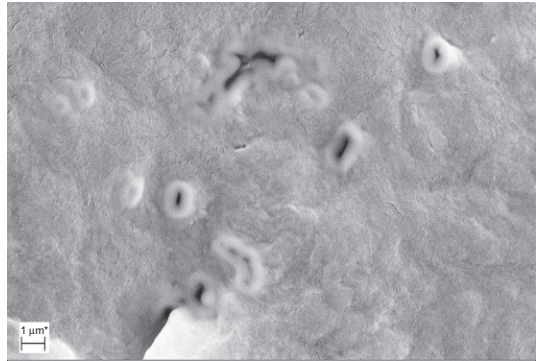


Figure 8.5 Cross section of the capsules containing thermally sprayed nylon.



properties of the coating. Some capsules were also deformed (i.e. flattened) during the spraying process due to the high impact.

Tribological tests consisting of rubbing the surface in a reciprocating way with a steel ball confirmed the presence of lubricant inside the capsules. The CoF was continuously measured during the test and compared with the CoF obtained with a nylon coating without capsules. Coatings composed only of nylon gave a CoF of 0.47, while the introduction of liquid-containing capsules in the nylon matrix reduced the CoF down to values between 0.12 and 0.19. This clearly revealed that the liquid is released when the capsules are broken during the rubbing test.

As mentioned in [Section 8.2.3](#), the amount of liquid inside the capsules can be tailored. This also has an effect on the amount of liquid released. Depending on the amount of encapsulated liquid, the final properties of the coating might change. The effect on the tribological properties by using three different capsules containing different amounts of lubricant (30, 50 and 70%) is clearly seen in the friction values shown in [Table 8.2](#). Coatings containing higher amounts of lubricant in the capsules (i.e. thinner capsule walls) resulted in a lower CoF. Hence, a clear correlation between the amount of liquid and the coating performance was observed.

Table 8.2 Average CoF for the different coatings tested at two different normal loads against a stainless steel ball

Coatings	Normal load (N)	Average CoF	Length of the test (min)
Nylon coating	5	0.47	30
	10	0.47	30
Capsule-containing coating (30% PAO capsules)	5	0.19	30
	10	0.17	30
Capsule-containing coating (50% PAO capsules)	5	0.14	30
	10	0.14	30
Capsule-containing coating (70% PAO capsules)	5	0.12	30
	10	0.14	30

8.4.2 Metal matrix coatings

8.4.2.1 Background

In the previous chapter, the production of polymer-based liquid–solid self-lubricated coatings was described, which in terms of compatibility between the polymer matrix and the capsules wall is the most favourable system due to the polymer origin of both. The main limitation of polymeric coatings is related to their mechanical properties and thus their application in more demanding components like machine elements. Therefore, it is of great interest obtaining metallic coatings with better mechanical properties containing liquid-filled capsules. This section will describe the production of metallic coatings containing liquid-filled capsules with different thermal spraying techniques and the advantages and disadvantages of each technique.

Metal matrix coatings with self-lubricating properties might be very interesting for the industry since most machine elements are made of metals or metal alloys that require lubrication for avoiding severe wear and galling. Therefore, the aim of the coatings presented in this section is to minimize the CoF in the mixed lubrication regime, that is, below 0.2 (Stachowiak and Batchelor, 2006). In this way, we assure a sufficient fluid film thickness to minimize the contact between the metal surfaces and thus reduce wear.

8.4.2.2 Methods

Three different thermal spraying techniques (AS; atmospheric plasma spraying, APS and high velocity oxy–air fuel, HVOAF) were used for obtaining the metal matrix coatings. The metal alloy chosen for these coatings was stainless steel. The selection of these techniques is based on their temperature and speed ranges of the flame and the in-flight particles for comparison. This gives an idea about the most important parameters (speed or temperature) in order to obtain a fully functional liquid–solid coating and how these may be optimized.

During the polymeric coating production, it was observed that axial injection of the capsules is required; therefore, for spraying the metal matrix, the capsules were injected almost axially and towards the substrate using an independent slurry feeder in all cases. It is also important to minimize the thermal input to the capsules; therefore, the capsules were also in this case injected in a water-based solution. The coatings were sprayed by alternating a layer of metal and a layer of capsules in order to avoid any decomposition of the wall capsule material.

Finally, the effect of the capsule wall thickness on the spraying process was studied by spraying two different types of capsules with the same size. The first ones consisted of capsules containing 70% volume of lubricant inside (i.e. thin wall thickness), while the second ones only contained 30% lubricant volume inside (i.e. thick wall thickness).

8.4.2.3 Results

The cross-sectional analysis confirmed the presence of the liquid-filled capsules in the coatings showing that the capsules survived all the spraying processes, including the APS process, which involved high flame temperatures ($>10,000$ °C) as shown in [Figure 8.6](#). The porosity of the coatings was directly proportional to the amount of capsules in the slurry injected into the flame. This is due to the presence of water, which evaporated during the thermal spraying process, hence increasing the porosity. An increase of porosity might have a beneficial effect indeed; if no porosity was generated in the coating, the capsules would most probably have been damaged due to the solidification process of the metal and to the high impact forces of the sprayed metal feedstock.

In all the three processes, the capsules were well distributed in the matrix, and in the case of the AS coating, they were specifically located in the pores of the matrix. Among the thermal spraying techniques used in this work, AS is the technique leading to the largest porosity due to the lower particle speed in the flame, and therefore, the presence of capsules in the pores is promoted. In the case of the APS and HVOAF processes, the speed of the particles in the flame is larger, and therefore, the porosity is lower.

In order to establish whether the coatings containing the liquid-filled capsules performed better, the CoF evolution with time for the coatings without capsules was used as a comparison. A summary of all CoF measurements is shown in [Table 8.3](#). Friction was the highest (above 0.5 in all cases) for the coatings without capsules, which is indicative of severe wear and bad performance. This is expected since the tests were run at atmospheric conditions of room temperatures and ambient relative humidities of 30%. When the coatings containing the lubricating capsules are tested in the same conditions, friction decreases drastically. For the tested AS samples, the CoF was below 0.2; therefore, lubrication of the contact was demonstrated.

Furthermore, the evolution of friction with time was very stable at all loads tested (5, 10 and 20 N) ([Espallargas and Armada, 2015](#)). For the APS and HVOAF samples, friction was below 0.2 when the tests were performed at the lowest load of 5 N, but when the load increased to 10 and 20 N, friction showed a tendency to increase after some sliding cycles resulting in a breakdown of the lubrication as shown in

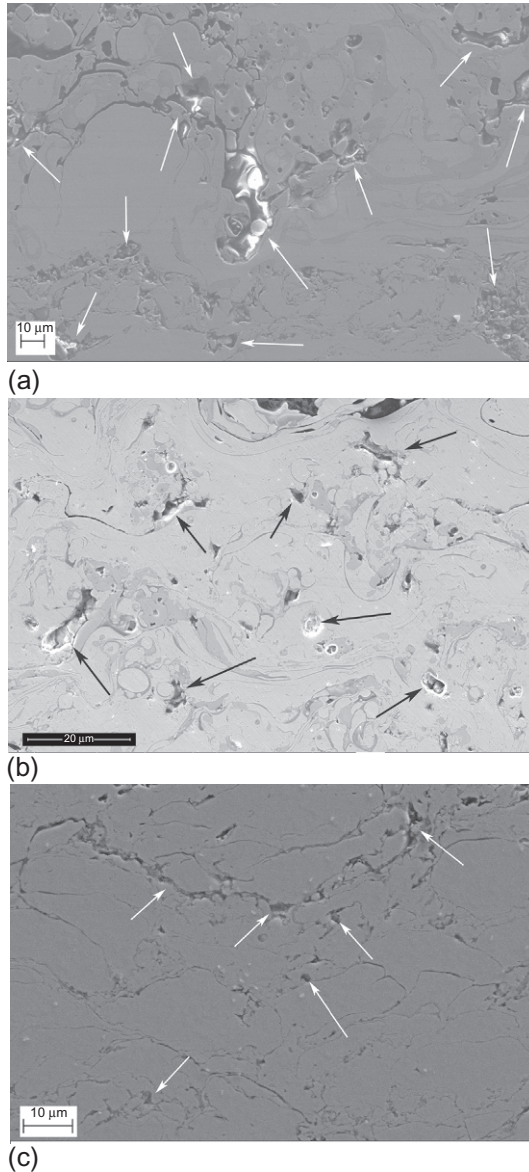


Figure 8.6 Scanning electron microscope images of the cross sections of the stainless steel coatings containing liquid-filled capsules obtained with (a) arc spraying, (b) atmospheric plasma spraying and (c) high velocity oxy-air fuel. The capsule sites are pointed with an arrow. Only in (a) a capsule that survived the polishing process and the electron beam can be observed.

Figure 8.7. This shows that the temperature and the speed of the flame during spraying play a role in the performance of the self-lubricating coatings.

For thermal spraying techniques with very high flame/jet temperature (APS), it was observed that capsules with thicker walls are needed in order to withstand the higher

Table 8.3 Average CoF for the different coatings tested at three different normal loads against a stainless steel ball

Coatings	Normal load (N)	Thermal spraying technique	Average CoF
Metal coating	5	AS	0.97
		APS	0.89
		HVOAF	0.55
	10	AS	0.88
		APS	0.70
		HVOAF	0.54
	20	AS	0.85
		APS	0.68
		HVOAF	0.54
Capsule-containing coating (30% PAO lubricant capsules)	5	AS	0.16
		APS	0.19
		HVOAF	0.16
	10	AS	0.14
		APS	0.54
		HVOAF	0.16
	20	AS	0.12
		APS	0.64
		HVOAF	0.19
Capsule-containing coating (70% PAO lubricant capsules)	5	AS	0.15
		APS	0.11
		HVOAF	0.15
	10	AS	0.15
		APS	0.12
		HVOAF	0.23
	20	AS	0.17
		APS	0.21
		HVOAF	0.41

temperatures in the process. On the other hand, when the speed of the thermal spraying process is high (HVOAF), the wear mechanisms seem to depend very much on the microstructure of the metal matrix (the presence or absence of porosity). The lowest porosity is found for the HVOAF coatings due to the higher spraying speed; therefore, the available amount of lubricant inside the coating is greatly influenced by the wall thickness of the capsules (e.g. the lowest friction for HVOAF of 70% PAO lubricant capsules). These conditions are needed in order to compensate for the lack of porosity and sites for storing the lubricant once released from the capsule. The APS coatings have an intermediate porosity, and the capsule wall thickness seems to have the

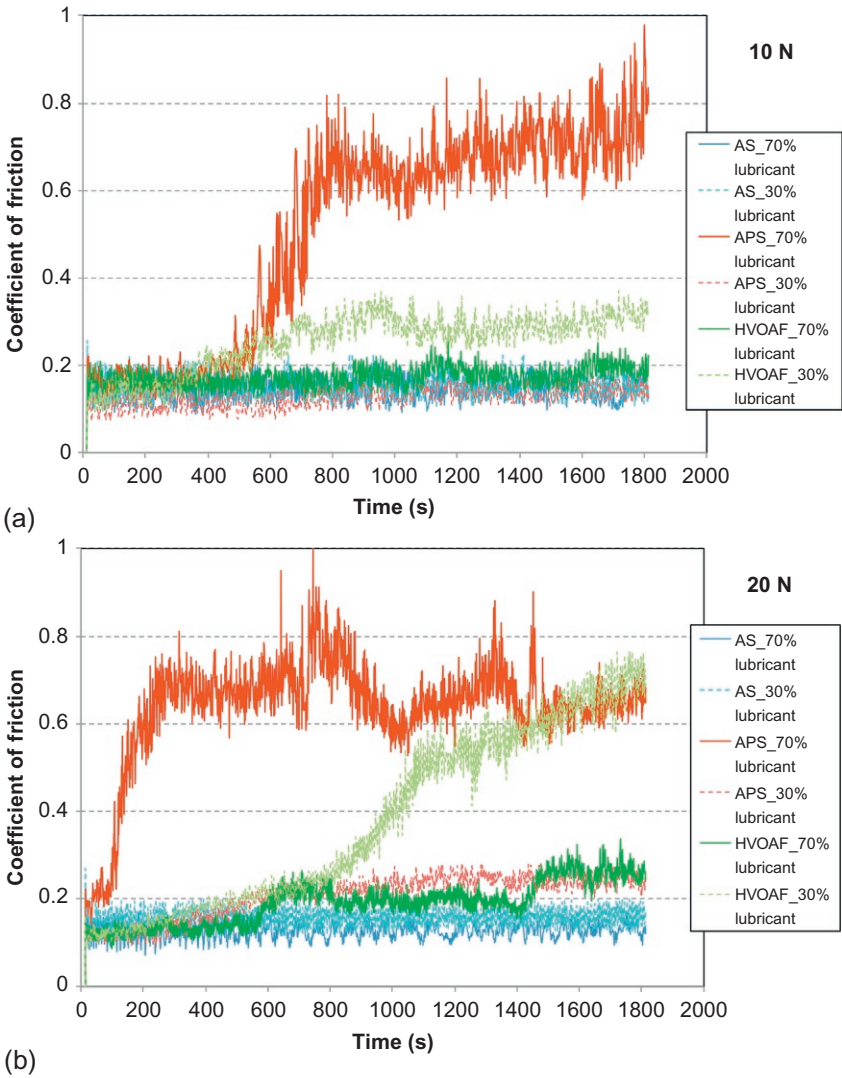


Figure 8.7 Coefficient of friction evolution with time for stainless steel coatings containing liquid-filled microcapsules tested against stainless steel at (a) 10 N and (b) 20 N normal forces.

greatest impact on friction (e.g. the lowest friction for APS of 30% PAO lubricant capsules). This can be attributed to the temperature of the flame since it could be expected that the capsules with the thinnest walls will experience the most degradation. Therefore, a low-temperature and low-speed technique like AS is best suited for spraying the capsules since more of them will survive the thermal spraying process and more porosity hosting the capsules will be introduced in the coating. This is confirmed by the fact that the AS coatings performed best at high loads (10 and 20 N).

8.5 Conclusions

A new process for obtaining functionalized liquid-containing coatings has been developed based on thermally spraying a solid matrix together with liquid-filled capsules. The liquid-containing capsules can be tailored depending on the requested functionalized properties of the coatings, hence broadening the potential use of thermal spraying.

Spraying low melting temperature liquid-filled capsules together with high-temperature melting materials (e.g. metals, ceramics and cermets) is a challenge; however, its feasibility has been demonstrated with both polymeric and metallic matrices.

Low-friction coatings have been successfully obtained and tested. In addition, the potential for the liquid–solid coatings may include also corrosion protection, anti-fouling or self-healing properties. These functionalized thermal spray coatings have not yet been produced, but the results obtained with the self-lubricating function demonstrate the feasibility.

Efforts should also be put in commercializing the functionalized low-friction thermal spray coatings since there is always a gap between new developments and market introduction. In addition, more focus could be directed towards the development of harder and wear-resistant coatings (i.e. WC–CoCr) containing lubricant-filled capsules.

Further research and development is still needed for developing new kinds of functionalized thermal spray coatings before they can be launched into the market. However, merging two fields of research such as liquid encapsulation and thermal spraying has shown promising and good advancements in the field.

References

- Adler, H.-J.P., Potje-Kamloth, K. (Eds.), 2002. Special Issue: Quo Vadis – coatings? *Macromol. Symp.* 187 (1), 1–958.
- Alagusundaram, M., Madhu Sudana Chetty, C., Umashankari, K., Attuluri, V.B., Lavayana, C., Ramkanth, S., 2009. Microspheres as a novel drug delivery system – a review. *Int. J. ChemTech Res.* 1, 526–534.
- Andersson, C., Järnström, L., Fogden, A., Mira, I., Voit, W., Zywicki, S., Bartkowiak, A., 2009. Preparation and incorporation of microcapsules in functional coatings for self-healing of packaging board. *Packag. Technol. Sci.* 22, 275–291.
- Armada, S., Schmid, R., Equey, S., Fagoaga, I., Espallargas, N., 2013. Liquid–solid self lubricated coatings. *J. Therm. Spray Technol.* 22 (1), 10–17.
- Asua, J.M., 2002. Miniemulsion polymerization. *Prog. Polym. Sci.* 27, 1283–1346.
- Cho, S.H., White, S.R., Braun, P.V., 2008. Self-healing polymer coatings. *Adv. Mater.* 20, 1–5.
- Cho, S.H., White, S.R., Braun, P.V., 2009. Self-healing polymer coatings. *Adv. Mater.* 21, 645–649.
- Dahlback, B., Blanck, H., Nyden, M., 2010. The challenges to find new sustainable antifouling approaches for shipping. *Coast. Mar. Sci.* 34 (1), 212–215.
- El-Aasser, M., Sudol, D., 2004. Miniemulsions: overview of research and applications. *JCT Res.* 1, 21–31.

- Espallargas, N., Armada, S., 2012. Self-lubricated coatings obtained by thermal spray methods. Patent Number WO 2013/058660.
- Espallargas, N., Armada, S., 2015. A new type of self-lubricated thermal spray coatings: liquid lubricants embedded in a metal matrix. *J. Therm. Spray Technol.* 24 (1–2), 222–234. <http://dx.doi.org/10.1007/s11666-014-0152-8>, online (September 2014).
- Espallargas, N., Vitoux, L., Armada, S., 2013. The wear and lubrication performance of liquid–solid self-lubricated coatings. *Surf. Coat. Technol.* 235, 342–353.
- Ghosh, S.K., 2006. Functional coatings and microencapsulation: a general perspective. In: *Functional Coatings*. WILEY-VCH Verlag GmbH & Co. KGaA, Weinheim, <http://onlinelibrary.wiley.com/doi/10.1002/3527608478.ch1/summary>. ISBN 3-527-31296-X.
- Giraud, S., Bourbigot, S., Rochery, M., Vroman, I., Tighzert, L., Delobel, R., 2002. Microencapsulation of phosphate: application to flame retarded coated cotton. *Polym. Degrad. Stab.* 77, 285–297.
- Grigoriev, D., Akcakayiran, D., Schenderlein, M., Shchukin, D., 2014. Protective organic coatings with anticorrosive and other feedback-active features: micro- and nanocontainers-based approach. *Corrosion* 70 (5), 446–463.
- Guilbert, C.R., Enos, D.G., Boyer III, C.E., 1998. Latent coating for metal surface repair. US Patent 6075072 A.
- Hughes, A.E., Cole, I.S., Muster, T.H., Varley, R.J., 2010. Designing green, self-healing coatings for metal protection. *NPG Asia Mater.* 2, 143–151.
- Jadhav, R.S., Mane, V., Bagle, A.V., Hundiwale, D.G., Mahulikar, P.P., Waghoo, G., 2013. Synthesis of multicore phenol formaldehyde microcapsules and their application in polyurethane paint formulation for self-healing anticorrosive coating. *Int. J. Ind. Chem.* 4, 31.
- Johnsen, H., Schmid, R.B., 2007. Preparation of polyurethane nanocapsules by miniemulsion polyaddition. *J. Microencapsul.* 24 (8), 731–742.
- Jyoti Sri, S., Seethadevi, A., Prabha, K.S., Muthyprasanna, P., Pavitra, P., 2012. Microencapsulation: a review. *Int. J. Pharma BioSci.* 3 (1), 509–531.
- Kessler, M.R., 2007. Self-healing: a new paradigm in materials design. *Proc. Inst. Mech. Eng. G-J. Aerosp. Eng.* 221 (4), 479–495.
- Koene, B.E., Own, S., Taushanoff, R.S., 2009. Self healing superhydrophobic coatings for corrosion protection. In: *Corrosion Conference*, Department of Defense, August 10–14.
- Kumar, A., Stephenson, L.D., Murray, J.N., 2006. Self healing coatings for steel. *Prog. Org. Coat.* 55, 244–253.
- Landfester, K., 2006. Synthesis of colloidal particles in miniemulsions. *Annu. Rev. Mater. Res.* 36, 231–279.
- Liquin, Z., 2006. Electrolytic co-deposition of polymer-encapsulated (microencapsulated) particles. In: Ghosh, S.K. (Ed.), *Functional Coatings*. Wiley Online Library.
- Marple, B.R., Voyer, J., 2001. Improved wear performance by the incorporation of solid lubricants during thermal spraying. *J. Therm. Spray Technol.* 10 (4), 626–636.
- Mathiazhagan, A., Joseph, R., 2011. Nanotechnology – a new prospective in organic coating – review. *Int. J. Chem. Eng. Appl.* 2, 225–237.
- Metzner, M., 2009. Self-healing surfaces. In: *Research News*, vol. 8. Fraunhofer Press, Germany.
- Miyoshi, K. (Ed.), 2001. *Solid Lubrication Fundamentals and Applications*. Marcel Dekker AG, Switzerland, ISBN 0824789059.
- Montemor, M.F., 2014. Functional and smart coatings for corrosion protection: a review of recent advances. *Surf. Coat. Technol.* 258, 17–37.
- Patel, P., 2009a. A metal coating that repairs itself. *MIT Technology Review*, News and Analysis (10 August).
- Patel, P., 2009b. A metal coating that repairs itself. *Technol. Rev.* (August).

- Perkins, J., Hong, Y., Ye, S.H., Wagner, W.R., Desai, S., 2014. Direct writing of bio-functional coatings for cardiovascular applications. *J. Biomed. Mater. Res. A* 102, 4290–4300.
- Schleicher, L., Green, B.K., 1956. Manifold record material. US Patent 2730456.
- Sridhar, T.M., 2010. Nanobioceramic coatings for biomedical applications. *Mater. Technol.* 25, 184–195.
- Stachowiak, G.W., Batchelor, A.W., 2006. *Engineering Tribology*, third ed. Butterworth-Heinemann, Dordrecht, ISBN 978-0-7506-7836-0.
- Stanford, M.K., DellaCorte, C., Eylon, D., 2004. Effect of particle morphology on flow characteristics of a composite plasma spray powder. *J. Therm. Spray Technol.* 13 (4), 586–592.
- Tsunekawa, Y., Ozdemir, I., Okumiya, M., 2006. Plasma sprayed cast iron coatings containing solid lubricant graphite and h-BN structure. *J. Therm. Spray Technol.* 15 (2), 239–245.
- Ugelstad, J., El-Aasser, M.S., Vanderhoff, J.W., 1973. Emulsion polymerization: initiation of polymerization in monomer droplets. *J. Polym. Sci. C: Polym. Lett.* 11 (8), 503–513.
- Umer, H., Nigam, H., Tamboli, A.M., Nainar, M.S.M., 2011. Microencapsulation: process, techniques and applications. *Int. J. Res. Pharm. Biomed. Sci.* 2 (2), 474–481.
- Wang, W., Xu, L., Li, X., Yang, Y., An, E., 2014. Self-healing properties on protective coatings containing isophorone diisocyanate microcapsules on carbon steel surfaces. *Corr. Sci.* 80, 528–535.
- White, S.R., Sottos, N.R., Geubelle, P.H., Moore, J.S., Kessler, M.R., Sriram, S.R., Brown, E.N., Viswanathan, S., 2001. Autonomic healing of polymer composites. *Nature* 409, 794–797.
- Wool, R.P., 2008. Self healing materials: a review. *Soft Matter* 4, 400–418.
- Xiao, Z., Liu, W., Zhu, G., Zhou, R., Niu, Y., 2014. A review of the preparation and application of flavour and essential oils microcapsules based on complex coacervation technology. *J. Sci. Food Agric.* 94, 1482–1494.
- Yamada, M., Wakabayashi, J., Fukumoto, M., Kitamura, J., 2009. Fabrication of Cu–MoS₂ composite coating by cold spraying and evaluation of its property. In: *Thermal Spray 2009: Expanding Thermal Spray Performance to New Markets and Applications*, May 1. ASM International, pp. 326–330.
- Yousaf, S., Albed Alhnan, M., Abdallah, A., Abdallah, B., Khan, I., Ahmed, W., 2015. Chapter 16 – Nanocoatings in medicine: antiquity and modern times. In: Ahmed, W., Mark Jackson, J. (Eds.), *Emerging Nanotechnologies for Manufacturing*, A Volume in Micro and Nanotechnologies. Elsevier, Oxford, UK/Burlington, MA, USA.

Part Two

New applications of thermal spray coatings

This page intentionally left blank

Thermal spray coatings in environmental barrier coatings

9

N.M. Melendez, A.G. McDonald

9.1 Introduction

Environmental barrier coatings (EBCs) have been developed and designed to protect machine components from harsh environmental conditions. These coatings are usually deposited by using high-temperature thermal spraying processes such as air plasma spraying (APS), high velocity oxy-fuel (HVOF) spraying, and direct current–radio frequency plasma spraying, to name a few. The EBCs may be a single layer of coating or they may consist of multiple layers of different coating materials, with each layer having a specific function or meeting a prescribed requirement. The topmost layer will usually provide direct protection against the harsh environmental conditions, while the innermost layers will complement the properties of the substrate to increase coating properties such as adhesion strength. The choice of coating structure and materials will depend on the area of application, the surface degradation process, and coating integrity issues such as cohesion and adhesion to the substrate. EBCs may be considered similar in their design to thermal barrier coatings (TBCs). However, unlike EBCs, TBCs serve primarily to reduce the adverse effects of high temperature on component parts, thereby extending the longevity of the component part.

Oxidation and corrosion are usually the two main degradation processes that characterize harsh environments for which EBCs provide protection. Without the EBCs, significant chemical degradation of the substrate components would occur. This chapter will detail EBCs that provide protection from such chemical degradation that is caused by solutions of gases or solid materials dissolved in water, molten salts, or other reactive species. Based on the nature of the degradation process and its source, the appropriate material and coating deposition process will be selected. [Table 9.1](#) shows a listing of examples of degradation mechanisms and typical coating materials that have been used to combat them. The table also shows the thermal spray deposition process that was used to fabricate the coating.

The objectives of this chapter will be to describe the various types of coating materials that are used as EBCs and the areas in which these coatings are applied to provide protection against harsh environmental conditions. The typical thermal spraying processes that are used to fabricate the EBCs will also be presented. Given that research and development occurs constantly to improve the quality and longevity of EBCs, examples of future trends in this application area will be explored.

Table 9.1 Examples of degradation mechanisms, typical EBC materials, and thermal spray deposition processes

Degradation mechanism	EBC material	Deposition process
Oxidation	Alumina (Al_2O_3)	Direct current–radio frequency (DC-RF) plasma spraying
Calcium–magnesium–aluminosilicate (CMAS) melts	$\text{Ba}_{1-x}\text{Sr}_x\text{Al}_2\text{Si}_2\text{O}_8$ (BSAS)	Atmospheric plasma spraying
Corrosion	Functionally graded material (FGM) coatings of Al_2O_3 and Ni–20Cr	High velocity oxy-fuel (HVOF) spraying
Hot corrosion	Mullite ($3\text{Al}_2\text{O}_3-2\text{SiO}_2$) and BSAS	Atmospheric plasma spraying
Molten salt corrosion	Ni–20Cr	Cold spraying
Molten salt corrosion	Yttria-stabilized zirconia (YSZ)/Ni–Cr–Al–Co– Y_2O_3	Atmospheric plasma spraying
Hot corrosion in molten salt	YSZ/LaMgAl ₁₁ O ₁₉ or lanthanum zirconate ($\text{La}_2\text{Zr}_2\text{O}_7$)	Atmospheric plasma spraying
Hot corrosion and oxidation	Zircon (ZrSiO_4)	Low-pressure plasma spraying (LPPS)

9.2 Types of coatings, materials, and application areas

EBCs are developed specifically to mitigate surface degradation by corrosive species, such as water vapor in a combustive environment or high-temperature corrosion that involves molten salts. The type of coating and material that are used depend on the application. For example, due to stringent requirements in the energy sector, it is required to reduce a component's weight (such as in turbines) and to improve the component's thermal degradation resistance. Silicon-based ceramics, such as SiC fiber-reinforced SiC ceramic matrix composites (SiC/SiC CMCs) and Si_3N_4 , have been proposed as an alternative to the conventional nickel-based superalloys due to their lower weight and superior high-temperature strength and durability (Lee et al., 2003; Murthy et al., 2007). Although these silicon-based ceramics form protective, dense silica scales in dry air (Jacobson, 1993), the silica scale easily degrades when water vapor is present (Opila and Hann, 1997), which requires an EBC to protect the silicon-based substrate. There are four main criteria to consider when considering an effective EBC: (i) resistance to reaction in aggressive environments and low oxygen permeability limit, (ii) similar coefficient of thermal expansion (CTE) to the substrate to prevent cracking and possible spallation, (iii) no phase transformations while in service, and (iv) chemical compatibility.

A popular material that is used as an EBC for the protection of silicon-based ceramics used in gas turbines is $\text{Ba}_x\text{Sr}_{1-x}\text{Al}_2\text{Si}_2\text{O}_8$ (BSAS). BSAS is often a suitable EBC because it has a CTE ($\sim 4 \times 10^{-6} \text{ }^\circ\text{C}^{-1}$) that is similar to that of silicon-based ceramics

($\sim 5 \times 10^{-6} \text{ }^\circ\text{C}^{-1}$) (Harder et al., 2009a), a low silica activity, and a low Young's modulus, which is thought to yield excellent crack propagation resistance during thermal cycling (Lee et al., 2003). However, BSAS is not a suitable EBC on its own because postdeposition cracks can be present in the coating, which will allow water vapor to attack the substrate. Furthermore, BSAS can react with silica to form glassy products that have low melting points ($\sim 1300 \text{ }^\circ\text{C}$), which can be easily removed in turbine engines, thus exposing the underlying BSAS layer (Lee et al., 2005). Interfacial porosity can also be created in the layer, ultimately decreasing its effectiveness as an EBC (Lee et al., 2003). Therefore, it is necessary to deposit the intermediate layer(s) to form coating systems that are similar to those used in TBCs (ceramic topcoat/metallic bond coat/substrate). Mullite is used as an intermediate layer because of its similar CTE; however, it does not adhere well to SiC during thermal exposure (Lee, 2000). In order to use mullite effectively as an intermediate layer, silicon must be deposited onto the silicon-based ceramic to promote the adhesion of mullite (Lee, 2000). This yields a layered system that contains a silicon-based ceramic substrate, with a silicon intermediate layer, followed by a mullite intermediate layer or a mullite+BSAS composite layer, and a BSAS topcoat. More et al. (2002) mixed BSAS with mullite to form a mullite+BSAS composite layer. This was used in an attempt to improve the corrosion resistance of the mullite intermediate layer in a water vapor environment. The presence of BSAS in the mullite+BSAS composite layer did reduce the rate of silica formation; however, the mullite did decompose preferentially and ultimately led to failure of the coating system (More et al., 2002). Harder et al. (2009a,b) added strontium aluminosilicate (SAS) to the mullite intermediate layer in an attempt to reduce the difference in the CTE between the intermediate layer and the topcoat. The addition of SAS did not lower the stress in the other layers; however, it did increase the compressive stress, which may increase the resistance to surface cracking, thus improving the durability of the BSAS topcoat (Harder et al., 2009b). Furthermore, the presence of SAS did not stop the crack propagation in the mullite+SAS composite layer, as expected (Harder et al., 2009a).

Ytria-stabilized zirconia (YSZ) has been explored as an EBC to protect silicon-based ceramics due to its proved ability to resist corrosion in water vapor environments in TBC systems (Lee et al., 1994). However, the higher CTE of YSZ ($\sim 11 \times 10^{-6} \text{ }^\circ\text{C}^{-1}$) with respect to that of silicon-based ceramics, along with the sintering effects of the YSZ topcoat at high temperatures, induces stresses that cause the coating to crack and spall off of the substrate (Cojocaru et al., 2011a). Functionally graded mullite/YSZ coatings have been examined in an attempt to change the CTE between the layers gradually, but it did not improve the performance of the coatings when subjected to thermal cycling. Although YSZ may not be suitable as an EBC for silicon-based ceramics, YSZ along with a MCrAlY bond coat deposited onto nickel superalloy substrates is an excellent EBC candidate in gas turbines when sulfate salts are present (Marple et al., 2006); however, YSZ corrodes easily in the presence of V_2O_5 , which is a species that can be formed when combusting lower-grade fuels. Other materials such as LaZr_2O_7 can be used as an EBC in gas turbines to protect against V_2O_5 corrosion (Marple et al., 2006). Other studies (Chen et al., 2011) have found that the addition of $\text{LaMgAl}_{11}\text{O}_{19}$ to YSZ or applying a $\text{LaMgAl}_{11}\text{O}_{19}$ overlay, with a Ni–23.7Co–20Cr–8.7Al–0.6Y–3.5Ta (wt.%) bond coat, improved the hot

corrosion resistance (50 wt.% Na_2SO_4 + 50 wt.% V_2O_5 molten salt at 950 °C for 60 h) of the coating system because the presence of $\text{LaMgAl}_{11}\text{O}_{19}$ reduced leaching of yttrium. The leaching of yttrium from YSZ is undesirable because it can cause the metastable tetragonal phase (t') of YSZ to transform into the monoclinic or cubic phase. These transformations lead to volume changes within the coating and eventually cause the coating to crack (Mohan et al., 2007). Cracking could permit the transportation of corrosive media toward the substrate or it could eventually cause the coating to spall off the substrate. YSZ coatings along with a MCrAlY bond coat have been used to protect other components, such as Kraft recovery boilers and superheater tubes used in the pulp and paper industry, where superheater tubes and boilers are severely corroded in the presence of molten salts and sulfidic gases. It was found that bimodal coatings fabricated using nanoagglomerated YSZ powder feedstock outperformed their conventional powder counterparts because the “nanozones” in the coating acted as collection sites for the corrosive salts, which prevented the salts from penetrating through the coating and corroding the substrate (Rao et al., 2012).

Rare earth silicates (RE_2SiO_5 or $\text{RE}_2\text{Si}_2\text{O}_7$, where RE refers to rare earth elements such as Yb or Er) have been proposed as EBCs to protect silicon-based ceramics since they are less volatile than BSAS topcoats at higher temperatures (BSAS topcoat becomes less effective when operating temperatures exceed 1300–1350 °C) (Lee et al., 2005). Rare earth silicates have similar CTE values as those of silicon-based ceramics and can be deposited without any cracks, preventing water vapor from penetrating toward the substrate (Xu and Yan, 2010). However, some rare earth silicates are known to have multiple polymorphs that can lower the coating performance at higher temperatures because of the volume change that is associated with the phase transformation (Lee et al., 2005). Lee et al. (2005) fabricated a variety of rare earth silicates or a BSAS topcoat onto either SiC or SiC/SiC composite substrates or Si_3N_4 substrates. It was determined that although the rare earth silicates were less volatile than the conventional BSAS topcoats at 1380 °C, the rare earth silicates often had through-thickness cracks. This may not be an issue when deposited onto SiC/SiC composite substrates because the cracks cease to propagate within the intermediate layer or intermediate/bond coat interface (Lee et al., 2005). Khan et al. (2012) determined that after 10 thermal cycles, where the coated substrate was heated to 1500 °C for 6 min and cooled down to ~400 °C within 3 min, the Yb_2SiO_5 coating did not spall off of the C/C–SiC substrate. However, after deposition, some of the Yb_2SiO_5 decomposed to Yb_2O_3 , which would reduce the overall corrosion resistance of the coating and introduce stresses. Furthermore, after thermal cycling, more Yb_2O_3 formed in the coating. This is of concern because Yb_2SiO_5 is supposed to be the nonvolatile phase protecting the substrate. Rare earth silicate coatings should not be deposited onto Si_3N_4 substrates because through cracking can propagate to the bond coat/substrate interface, which would allow for the transportation of water vapor to the substrate (Lee et al., 2005). It has been suggested that the additives commonly present in Si_3N_4 substrates (AS800™, Honeywell Engines) can react with rare earth silicates to promote the formation of undesirable glassy products. In addition, rare earth silicates should not be applied to gas turbine environments where the operating temperature is equal to or exceeds 1400 °C because the rare earth silicates react aggressively with mullite, mullite + SAS, or mullite + BSAS to

form glassy products at those temperatures, which would ultimately lead to rapid recession of the EBC (Lee et al., 2005).

Other ceramics have been explored as possible candidates for EBCs. Plasma-sprayed AlNbO_4 (5 mol.%) + mullite exhibited improved water vapor corrosion resistance at 1400 °C in comparison with mullite because AlNbO_4 formed a stable glassy surface layer that ultimately protected the rest of the EBC and the Si_3N_4 substrate. However, after being subjected to that temperature for 100 h, the AlNbO_4 (5 mol.%) + mullite layer began to spall off the substrate because of the large difference in CTE ($7.5 \times 10^{-6} \text{ K}^{-1}$ for AlNbO_4 (5 mol.%) + mullite vs. $4 \times 10^{-6} \text{ K}^{-1}$ for Si_3N_4) (Wu et al., 2010). Thermal-sprayed tantalum oxide (Ta_2O_5) coatings have been proposed as a potential EBC because it has a CTE ($\sim 3\text{--}4 \times 10^{-6} \text{ K}^{-1}$) that is very close to that of Si_3N_4 , and it has phase stability up to ~ 1200 °C (Moldovan et al., 2004). Ta_2O_5 coatings typically contain both the alpha (α) and beta (β) phases of Ta_2O_5 after deposition via plasma spraying, where the α -phase is undesirable because of the volume change that accompanies that phase transformation (Moldovan et al., 2004; Weyant et al., 2005). Heat treatment at 1200 °C for 72 h is required after plasma spraying to convert any α - Ta_2O_5 back to β - Ta_2O_5 (Moldovan et al., 2004) and to heal any macrocracking that may be present in the coating (Weyant et al., 2005).

Ceramic and metal mixtures have been used as functionally graded material (FGM) coatings. However, the metallic components can be easily corroded by corrosive media, and the difference in the CTE between the ceramic layer and the metallic substrate is usually large and causes the coating to spall off, becoming ineffective. Malinina et al. (2005) fabricated a variety of coatings to protect steel substrates that were subjected to sodium and potassium chlorides, carbonates, polysulfides, and sulfates at temperatures ranging between 400 and 750 °C. A HVOF-sprayed pure alumina coating spalled from the steel substrate due to the high difference of the CTEs, and the Ni–20 wt.% Cr coating corroded easily. In order to reduce the difference in the CTE of the coating and substrate, a Ni–20 wt.% Cr powder was sprayed simultaneously with the alumina powder to fabricate metal matrix composite (MMC) coatings with various compositions (25 wt.% alumina + 75 wt.% Ni–20 wt.% Cr, 50 wt.% alumina + 50 wt.% Ni–20 wt.% Cr, and 75 wt.% alumina + 25 wt.% Ni–20 wt.% Cr). However, the chlorides preferentially attacked the Ni–20 wt.% Cr matrix until the substrate was exposed. The most successful coating for this application was an FGM coating that varied the composition of alumina for each layer (0 wt.% alumina (closest to the substrate), 25 wt.% alumina, 50 wt.% alumina, 75 wt.% alumina, and 100 wt.% alumina (topcoat)) to produce a coating system with five layers. This coating effectively protected the substrate because the corrosion-resistant alumina layer adhered well to the intermediate layers due to the lower stress generated by the gradual change in the CTE from layer to layer.

Corrosion-resistant metals have been proposed as EBCs. Careful selection of the spray parameters and the thermal spray process is necessary to ensure that the desired mechanical/chemical properties of the metals are retained. The corrosion of boiler tubes is of great concern because corrosive gases or the accumulation of molten salts will corrode most stainless steels. Detonation-sprayed 50 wt.% Ni–50 wt.% Cr coating improved the service life of the boiler surfaces when exposed to a waste incinerator environment (ash: 4.66% Na, 5.11% K, 15.4% Ca, 1.8% Mg, 5.4% Fe, 0.11% Pb,

0.66% Zn, 8.04% S, and 11.3% Cl; gas: 8% CO₂ + 8% O₂ + 18% H₂O + 0.1% HCl + bal. N₂ at either 773 or 873 K for 72 h (Yamada et al., 2002). When uncoated substrates were subjected to the waste incinerator environment, there was a reduction in thickness of approximately 0.2–0.4 mm/year; however, the detonation-sprayed 50 wt.% Cr–50 wt.% Ni coatings did not exhibit any reduction in coating thickness after 7 years (Yamada et al., 2002). The detonation-sprayed 50 wt.% Cr–50 wt.% Ni coatings can be used as an effective EBC because of its minimal coating porosity. In addition, when the chromium and nickel oxidize, they form stable adhering oxides that prevented further attack of the coating (Yamada et al., 2002).

Other coatings have been used to improve the corrosion resistance of the metal substrate. For example, cold-sprayed Ni–20 wt.% Cr coatings effectively protected the substrate and outperformed the uncoated SA516 boiler steel in terms of corrosion resistance (Bala et al., 2010). The molten salts that accumulated on the surface allowed oxygen to diffuse easily into the bulk of the material; however, the Ni–20 wt.% Cr reduced the weight gain (which was mostly due to oxides) by 87%, maintaining the integrity of the coating and substrate (Bala et al., 2010).

Cu–Cr coatings have been explored as potential EBCs for combustion liners of reusable space launch vehicles. Although copper is not typically known for its corrosion resistance, the presence of chromium should develop an adherent Cr₂O₃ layer. Furthermore, Cu–Cr has similar mechanical properties to the alloy substrate that was used, that is, Cu–8Cr–4Nb, which should reduce the mechanical stresses and improve the adhesion between the coating and substrate (Ogbuji, 2005). The static and cyclic oxidations of the coatings were examined at a temperature range of 550 and 750 °C. Depending on the environment to which the coated substrate was subjected, a variety of coating compositions would be deemed acceptable. Coatings with a Cr composition of 8.5 wt.% or higher can offer sufficient protection for up to 20 h at 750 °C under static oxidation. However, coatings with a Cr composition of 21 wt.% or higher for protection for 10 h at 750 °C or a Cr composition of at least 17 wt.% to protect the substrate for 10 h at 650 °C or 3 h at 750 °C are required. The increased presence of Cr in the Cu–Cr coating forms a Cr₂O₃ layer, which can act as a diffusion barrier, provided that it is a continuous layer (Ogbuji, 2005).

Although many different coatings were presented in this section, there is no coating that can be used for every application. Each coating must follow the four criteria mentioned previously. They must (i) resist reaction with aggressive environments and have a low oxygen permeability limit, (ii) have a similar CTE to the substrate to prevent cracking and possible spallation, (iii) undergo no phase transformations, and (iv) be chemically compatible.

9.3 Thermal spraying fabrication techniques

A variety of thermal spraying techniques, such as APS, HVOF, and cold gas dynamic spraying (“cold spraying”), can be used to fabricate EBCs. However, material properties, desired coating quality and microstructures, application, and substrate material types may dictate which process is used to fabricate the coatings.

APS uses a high-temperature ionized gas (plasma) jet to melt and accelerate powdered particles toward the substrate, making it an excellent option for materials that have high melting points (Pawlowski, 2008). It is possible to achieve low porosity in plasma-sprayed coatings, if the parameters are optimized (Moldovan et al., 2004). However, the large difference in temperature between the particles and the substrate causes the particle to solidify quickly, which can form amorphous phases (Lee, 2000), generate undesirable phases (Harder et al., 2009b; Moldovan et al., 2004; Weyant et al., 2005), or generate residual stresses due to resolidification (Weyant et al., 2005). Heating the substrate to an appropriate temperature during plasma spraying will reduce the quenching rate of the deposited particles, which can eliminate the formation of amorphous phases, such as that observed in mullite coatings (Lee et al., 1995). Mullite should not be amorphous because when it is subjected to thermal cycling, the heat causes the amorphous phase to recrystallize and generate cracks, which facilitate penetration of corrosive species to attack the substrate (Lee, 2000).

BSAS is deposited as a metastable hexacelsian crystal structure when parameters are not carefully monitored during plasma spraying (Harder et al., 2009a,b). The hexacelsian crystal structure is not desired because it has a higher CTE mismatch to the intermediate mullite and silicon layers, in comparison with the equilibrium phase, monoclinic celsian (Harder et al., 2009b). Furthermore, if the coating system is subjected to temperatures greater than 1200 °C, the hexacelsian phase transforms to the monoclinic phase, which has a volume reduction of 0.5%. Therefore, if the coating system is subjected to fluctuating temperatures, cracks can form and propagate (Harder et al., 2009a,b). In order to counteract these issues, a relatively new process known as “spray manufacturing and annealing in real time (SMART)” has successfully been used to deposit fully crystalline BSAS coatings (Cojocaru et al., 2011b). Although some cracks were present in the coating, there were no through-thickness cracks present, suggesting great potential for the SMART process to fabricate effective EBCs.

Issues such as phase transformations (Harder et al., 2009b; Moldovan et al., 2004) and stresses from resolidification (Moldovan et al., 2004) are prominent in plasma-sprayed coatings; however, these issues can be reduced by heat treatment. Weyant et al. (2005) had shown that it is possible to heal macrocracking via heat treatment at 1200 °C, but the length of heat treatment must be controlled because microcracks can form due to grain growth.

HVOF spraying uses a flame generated during the combustion of a fuel in oxygen to melt or partially melt particles that are accelerated to high speeds (Pawlowski, 2008). The high speed of the impacting particles generates coatings with a low porosity, when compared with other high-temperature thermal spraying processes. Due to the combination of high-temperature and high particle velocities, HVOF spraying is typically used for some ceramics, metals, and cermets. HVOF spraying has been used to fabricate dense FGM coatings that contained softer materials, such as nickel and chromium, and hard materials, such as alumina (Yamada et al., 2002).

Cold spraying is an excellent alternative for spraying metals because they deform plastically. The spray temperatures are much lower than the melting point of the particles, which minimizes or eliminates phase transformations and the generation of residual stresses (Papyrin, 2001). The particles are accelerated to high velocities to fabricate thick, dense, and adherent coatings. Furthermore, if specific mechanical

properties are required, cold spraying can produce coatings with similar properties to those of the bulk material (Karthikeyan, 2005). Coatings fabricated by cold spraying or kinetic metallization exhibit the same chemical composition as their feedstock powder and have low coating porosities (Bala et al., 2010; Ogbuji, 2005).

9.4 Future trends

Future trends in the development and application of EBCs have focused primarily on new spraying techniques and materials. For example, cold gas dynamic spraying has been used recently to fabricate metal-based coatings to act as environmental barriers (Bala et al., 2010). Suspension plasma spraying of small nanostructured powders (Mesquita-Guimarães et al., 2012) and small particle plasma spraying (Otsuka and Yamamoto, 2003) have also been explored to fabricate dense EBCs. The use of smaller particles has been shown to produce denser coatings since they are easier to melt and accelerate in the plasma jet (Otsuka and Yamamoto, 2003; Mawdsley et al., 2001).

In terms of materials development, zircon (ZrSiO_4) is an example of a promising candidate for use as an EBC because of its excellent high-temperature properties (Garvie, 1979). However, it is very difficult to fabricate ZrSiO_4 because it has a dissociation line at 1676 °C (1949 K), as seen in the phase diagram of Figure 9.1

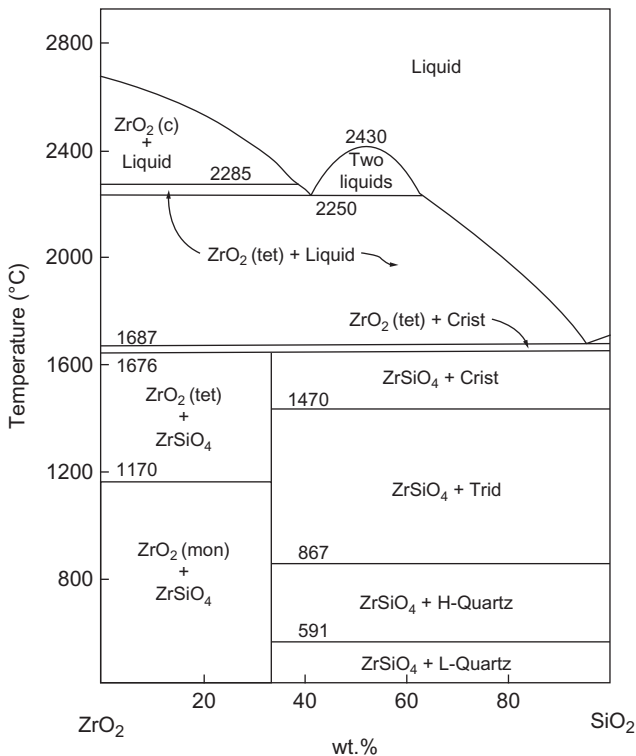


Figure 9.1 Phase diagram of ZrSiO_4 (Butterman and Foster, 1953; Suzuki et al., 2005).

(Butterman and Foster, 1953). Suzuki et al. (2005) deposited a dense coating by plasma spray deposition of a $\text{ZrO}_2 + \text{SiO}_2$ powder blend and heating the substrates; however, no ZrSiO_4 was present in the coating. The coatings that were subjected to heat treatment at 1673 K for approximately 24 h had a significant amount of ZrSiO_4 , and the coating porosity was high. The porosity was formed due to the volume shrinkage when ZrSiO_4 was formed. Although the desired material, ZrSiO_4 , was present in the coating, it led to a coating with an increased porosity. Therefore, further work will be necessary to optimize this coating to be a suitable EBC.

References

- Bala, N., Singh, H., Prakash, S., 2010. High temperature corrosion behavior of cold spray Ni–20Cr coating on boiler steel in molten salt environment at 900 °C. *J. Therm. Spray Technol.* 19, 110–118.
- Butterman, W.C., Foster, W.R., 1953. Zircon stability and ZrO_2 – SiO_2 phase diagram. *Am. Mineral.* 52, 880–888.
- Chen, X., Zhao, Y., Gu, L., Zou, B., Wang, Y., Cao, X., 2011. Hot corrosion behaviour of plasma sprayed YSZ/LaMgAl₁₁O₁₉ composite coatings in molten sulfate–vanadate salt. *Corros. Sci.* 53, 2335–2343.
- Cojocaru, C.V., Wang, Y., Moreau, C., Lima, R.S., Mesquita-Guimarães, J., García, E., Miranzo, P., Osendi, M.I., 2011a. Mechanical behavior of air plasma-sprayed YSZ functionally graded mullite coatings investigated via instrumented indentation. *J. Therm. Spray Technol.* 20, 92–99.
- Cojocaru, C.V., Lévesque, D., Moreau, C., Lima, R.S., 2011b. Performance of thermally sprayed Si/mullite/BSAS environmental barrier coatings exposed to thermal cycling in water vapor environment. *Surf. Coat. Technol.* 216, 215–223.
- Garvie, R.C., 1979. Improved thermal shock resistant refractories from plasma-dissociated zircon. *J. Mater. Sci.* 14, 817–822.
- Harder, B.J., Almer, J.D., Weyant, C.M., Lee, K.N., Faber, K.T., 2009a. Residual stress analysis of multilayer environmental barrier coatings. *J. Am. Ceram. Soc.* 92, 452–459.
- Harder, B.J., Almer, J., Lee, K.N., Faber, K.T., 2009b. In situ stress analysis of multilayer environmental barrier coatings. *Powder Diffract.* 24, 94–98.
- Jacobson, N.S., 1993. Corrosion of silicon-based ceramics in combustion environments. *J. Am. Ceram. Soc.* 76, 3–28.
- Karthikeyan, J., 2005. Cold spray technology. *Adv. Mater. Process.* 163, 33–35.
- Khan, Z.S., Zou, B., Huang, W., Fan, X., Gu, L., Chen, X., Zeng, S., Wang, C., Cao, X., 2012. Synthesis and characterization of Yb and Er based monosilicate powders and durability of plasma sprayed Yb_2SiO_5 coatings on C/C–SiC composites. *Mater. Sci. Eng. B* 177, 184–189.
- Lee, K.N., 2000. Current status of environmental barrier coatings for Si-based ceramics. *Surf. Coat. Technol.* 133–134, 1–7.
- Lee, K.N., Jacobson, N.S., Miller, R.A., 1994. Refractory oxide coatings on SiC ceramics. *MRS Bull.* 14, 35–38.
- Lee, K.N., Miller, R.A., Jacobson, N.S., 1995. New generation of plasma-sprayed mullite coatings on silicon carbide. *J. Am. Ceram. Soc.* 78, 705–710.
- Lee, K.N., Fox, D.S., Eldridge, J.I., Zhu, D., Robinson, R.C., Bansal, N.P., Miller, R.A., 2003. Upper temperature limit of environmental barrier coatings based on mullite and BSAS. *J. Am. Ceram. Soc.* 86, 1299–1306.

- Lee, K.N., Fox, D.S., Bansal, N.P., 2005. Rare earth silicate environmental barrier coatings for SiC/SiC composites and Si₃N₄ ceramics. *J. Eur. Ceram. Soc.* 25, 1705–1715.
- Malinina, M., Sammi, T., Gasik, M., 2005. Corrosion resistance of homogeneous and FGM coatings. *Mater. Sci. Forum* 492–493, 305–310.
- Marple, B.R., Voyer, J., Thibodeau, M., Nagy, D.R., Vassen, R., 2006. Hot corrosion of lanthanum zirconate and partially stabilized zirconia thermal barrier coatings. *J. Eng. Gas Turbines Power* 128, 144–152.
- Mawdsley, J., Su, Y., Faber, K., Bernecki, T., 2001. Optimization of small-particle plasma-sprayed alumina coatings using designed experiments. *Mater. Sci. Eng. A* 308, 189–199.
- Mesquita-Guimarães, J., García, E., Miranzo, P., Osendi, M., Cojocar, C., Lima, R., 2012. Mullite–YSZ multilayered environmental barrier coatings tested in cycling conditions under water vapor atmosphere. *Surf. Coat. Technol.* 209, 103–109.
- Mohan, P., Yuan, B., Patterson, T., Desai, V.H., Sohn, Y.H., 2007. Degradation of yttria-stabilized zirconia thermal barrier coatings by vanadium pentoxide, phosphorous pentoxide, and sodium sulfate. *J. Am. Ceram. Soc.* 90, 3601–3607.
- Moldovan, M., Weyant, C.M., Johnson, D.L., Faber, K.T., 2004. Tantalum oxide coatings as candidate environmental barriers. *J. Therm. Spray Technol.* 13, 51–56.
- More, K.L., Tortorelli, P.F., Walker, L.R., Kimmel, J.B., Miriyala, N., Price, J.R., Eaton, H.E., Sun, E.Y., Linsey, G.D., 2002. Evaluating environmental barrier coatings on ceramic matrix composites after engine and laboratory exposures. In: *Proceedings of ASME TURBO EXPO*, June 3–6, 2002, ASME. Amsterdam, The Netherlands, 8 pages.
- Murthy, P.L., Nemeth, N.N., Brewer, D.N., Mital, S., 2007. Probabilistic analysis of a SiC/SiC ceramic matrix composite turbine vane. *Compos. B* 39, 694–703.
- Ogbuji, L.U., 2005. Oxidation behavior of Cu–Cr environmental barrier coatings on Cu–8Cr–4Nb. *Surf. Coat. Technol.* 197, 327–335.
- Opila, E.J., Hann, R., 1997. Paralineer oxidation of CVD SiC in water vapor. *J. Am. Ceram. Soc.* 80, 197–205.
- Otsuka, A., Yamamoto, M., 2003. Formation of an environmental barrier coating using DC-RF hybrid plasma. *J. Am. Ceram. Soc.* 86, 1068–1075.
- Papyrin, A., 2001. Cold spray technology. *Adv. Mater. Process.* 159, 49–51.
- Pawlowski, L., 2008. *The Science and Engineering of Thermal Spray Coatings*. John Wiley and Sons, Chichester.
- Rao, S., Frederick, L., McDonald, A., 2012. Resistance of nanostructured environmental barrier coatings to the movement of molten salts. *J. Therm. Spray Technol.* 21, 887–899.
- Suzuki, M., Sodeoka, S., Inoue, T., 2005. Structure control of plasma sprayed zircon coating by substrate preheating and post heat treatment. *Mater. Trans.* 46, 669–674.
- Weyant, C.M., Faber, K.T., Almer, J.D., Guiheen, J.V., 2005. Residual stress and microstructural evolution in tantalum oxide coatings on silicon nitride. *J. Am. Ceram. Soc.* 88, 2169–2176.
- Wu, J., Lin, H., Li, J.-B., Li, J.-F., 2010. Corrosion behavior of AlNbO₄/mullite composite as environmental barrier coating in water vapor environment. *J. Inorg. Mater.* 25, 445–448.
- Xu, Y., Yan, Z., 2010. Investigation of the preparation of Si/mullite/Yb₂Si₂O₇ environmental barrier coatings onto silicon carbide. *J. Rare Earths* 28, 399–402.
- Yamada, K., Tomono, Y., Morimoto, J., Sasaki, Y., Ohmori, A., 2002. Hot corrosion behavior of boiler tube materials in refuse incineration environment. *Vacuum* 65, 533–540.

Thermal spray coatings in renewable energy applications

10

S. Wijewardane

List of chemicals

H₂S	hydrogen sulfide
SO₂	sulfur dioxide
HNO₃	nitric acid
H₂SO₄	sulfuric acid
HCl	hydrochloric acid
NH₃	ammonia
FeS	iron sulfide
TiO₂	titanium dioxide
SiC	silicon carbide
CdS	cadmium sulfide
NiO	nickel (II) oxide
Mg₂Si	magnesium silicide
Er₂O₃	erbium oxide
Sm₂O₃	samarium oxide
Ne₂O₃	neodymium oxide
Yb₂O₃	ytterbium oxide

10.1 Introduction

Renewable energy sources have gained a lot of attention in last few decades mainly due to the environmental concerns and the depletion of fossil fuels. Extensive research has been carried out to extract energy from renewable energy sources at a competitive price. Coating technologies are playing a major role in renewable energy conversions, and therefore, cost-effectiveness of these technologies is of prime importance. Sophisticated coating techniques such as physical vapor deposition (PVD) (Selvakumar and Barshilia, 2012), chemical vapor deposition (CVD) (Wang et al., 2002), and simple paint and spray methods (Wijewardane and Goswami, 2012) are used in renewable energy for achieving various functions from conventional device protection to more advanced spectral selectivity and self-cleaning.

Thermal spraying can be used as an effective low-cost method to alter the surface properties of a component and to fabricate multilayer stacks with desired properties. These coatings are used in wide range of well-commercialized applications including automotive systems, aircraft engines, and marine turbines. Although thermal spray

coatings have been used in oil and gas industries (Tucker, 2002) for a significant amount of time, its usage in other forms of energy conversions, especially in renewable energy, is limited only for few applications. Currently, there is an enormous interest on the thermal spray techniques that can be utilized in renewable energy applications, mainly due to the flexibility, the impressive cost–benefit relationship, and the track record as a potential industry-scalable coating technique. In this chapter, a review of current and emerging applications of thermal spray coatings in the renewable energy sector will be presented. We start with the coatings that have been utilized as erosion–corrosion protection, followed by illustration of emerging and more advanced applications of thermal spray. Corrosion and erosion have always been a significant problem for the energy industry, regardless of whether its in the renewable energy sector or the traditional oil and gas industries. The ability to alter coating properties by employing different types of thermal spray techniques such as plasma spraying and detonation spraying makes thermal spray usable in a variety of applications including thermoelectric power generation, photocatalytic hydrogen production, and thermophotovoltaic (TPV) applications. However, producing these coatings with all the desired properties in an industrial scale and in an economic and reliable manner is a challenge.

10.2 Biomass incineration boilers

Biomass is one of the most important renewable energy sources that cover approximately 10% of the world's energy supply. Utilization of biomass extracted from waste as a fuel to produce power has two major advantages. It reduces the land requirement for the waste disposal, and also, the power production is “carbon-neutral.” Incineration of biomass using industrial boilers to produce steam and run steam turbines is a standard way of producing electric power. Generally, water tube boilers are used, and the tubes are heated by the flames of burning biomass to produce steam inside the tubes (Figure 10.1). Formation of iron and copper slats; acids such as HNO_3 , nitric, sulfuric, and HCl , hydrochloric; and gases such as chlorine, H_2S , and SO_2 in the combustion process together with high temperature drastically corrodes the vital parts of the boiler, which reduces the viability of biomass-based thermal plants (Adamiec, 2009).

Materials that have adequate corrosion resistance in boiler combustion environments are highly alloyed and thus expensive. The lack of processability and the inability to justify the extra cost against the improved corrosion resistance in most cases exclude the use of bulk corrosion-resistant materials. Under such circumstances, solutions based on low-cost substrate materials in combination with tailored coatings become technically and economically attractive (Paul and Harvey, 2013). There are several methods for producing coatings for boiler applications. Coated tubes are produced by means of diffusion coating (Naji et al., 2012), thermal spraying (Kaushal et al., 2011), and laser cladding (Verdi et al., 2014). The most notable drawbacks of diffusion coatings are (i) inability to create thick coatings, (ii) difficulty to

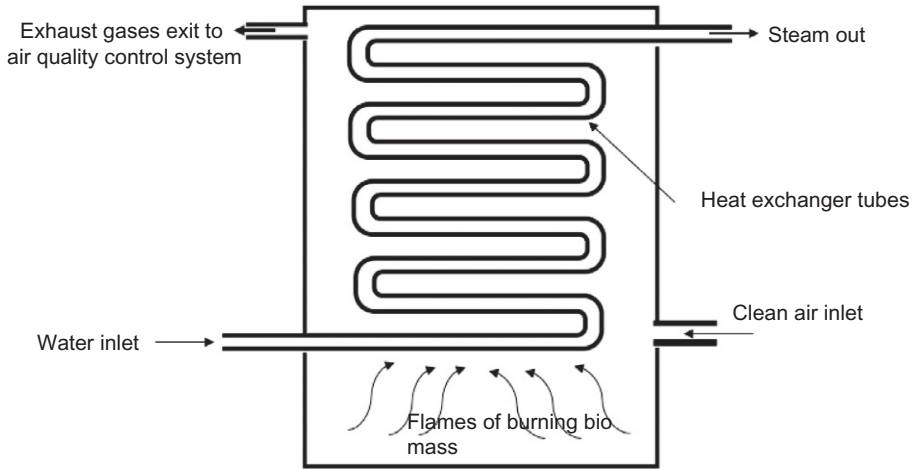


Figure 10.1 A sketch of a biomass boiler.

produce and repair onsite, and (iii) the requirement of high substrate temperatures. In comparison, thermal sprayed coatings do not require such a high temperature of the base metal that would weaken the mechanical or microstructural properties of the tubes and can be used onsite. The laser cladding process is complex, and also, the equipment and running costs are relatively high. Because of aforementioned shortcomings in diffusion and laser cladding techniques, attention is increasingly being focused on thermal sprayed coatings. Ideal thermal sprayed coatings in these conditions must be dense and sufficiently thick and should have a thermal expansion coefficient similar to that of the base material to withstand thermal cycle-induced cracks and to tightly adhere and protect the base material for a long time. They must also be resistant to chemical environments with high temperatures and must have low internal stresses and low oxide content (Rogers et al., 1995).

In reducing atmosphere inside the boilers, sulfur in fuels is released as H_2S , which is very corrosive compared to SO_2 released in oxidizing atmosphere. Chromium is considered as the most effective alloying element to resist sulfidation in steels (Lai, 1990), and therefore, homogeneous and dense thermal sprayed coatings with high-chromium content are used to protect the substrate in these conditions. The thermal sprayed coatings such as 50/50 nickel–chromium alloy (Gainger and Blunt, 1998) and NiCrBSi alloy deposited by high-velocity oxygen fuel (HVOF) (Orita et al., 2000) are usually recommended as an erosion–corrosion protection for boiler tubes in power generation applications. For long-term protection, however, the porosity of the coating is a key factor. Although HVOF coatings are homogeneous and dense compared with most of the other thermal sprayed coatings, the HVOF coatings always contain some oxides and porosity at splat boundaries. Because of this interconnected porosity appearing at the splat boundaries, these coatings are permeable to corrosive gases to some extent, and therefore, the long-term corrosion resistance of HVOF coatings has been doubted (Moskowitz, 1993).

The detonation thermal spray process has the highest particle velocity realizable for thermal spraying processes, and the high particle velocity will lead to the production of dense coatings with low porosity (Li and Ohmori, 1996). The Ni-50Cr alloy coating produced by the detonation spray method exhibited the most corrosion resistance in a laboratory test (Yamada et al., 2002). Therefore, the detonation thermal spray process could be a solution to improve the durability of biomass incineration plants.

Tendency to extract biomass from various waste sources increases the overall chlorine content of the entire feed. Even high-chromium materials corrode rapidly in presence of chlorine (Bakker, 1997). Steam temperatures of boilers are limited by corrosion and creep resistance of boiler components. For boilers burning high-chlorine fuels, corrosion effects limit the steam temperature to 400–460 °C (Kawahara, 1997). Demands to improve the efficiency of these thermal plants require higher steam temperatures, and therefore, corrosion-resistant coatings that can survive in higher temperatures in highly corrosive environments are required.

10.3 Geothermal piping systems

Although geothermal is one of the most reliable renewable energy sources, metal corrosion in geothermal plants (Figure 10.2) has become a serious problem, which reduces its viability. Geothermal brine contains huge amounts of chemicals including dissolved CO₂, H₂S, NH₃, FeS, sulfuric acid, and chloride ions, which are highly corrosive (Kaya and Hoşhan, 2005). Substantial differences in chemical composition, temperature, etc., can be found within the wells of the same geothermal field. All sorts of corrosion types such as pitting corrosion or stress corrosion cracking are possible in the metal pipes used in geothermal power plants. As material cost is a significant contributor to the overall cost in geothermal systems, low-carbon metals and other low-alloyed metals are preferred mainly to reduce the cost. Thermal spray coatings have been used to protect these metal surfaces from aggressive geothermal environments. The experience gained from using the thermal spray coatings in similar aggressive environments in petrochemical industry can be well utilized in geothermal applications as well. As in biomass applications, the coating should have a low porosity and be free from cracks in order to protect the substrate from corrosive gases. A NiCrMo alloy applied by thermal spraying (high-velocity arc spraying) is a preferred coating for these systems (Amend and Yee, 2013).

The ability to apply thermal spray coatings on the interior surface of piping is highly advantageous compared with other coating processes. Idaho National Engineering and Environmental Laboratory (INEEL) is developing a system that can be used to coat the interior of the piping (Moore et al., 2002). They have utilized a “coupon tree” for inserting test coupons into operating systems as shown in Figure 10.3. The formation of a scale on the coupons and high porosity of the deposited coatings are the major drawbacks. Once developed with the anticipated reliability, this technique has the potential to be used in the field for repair as well.

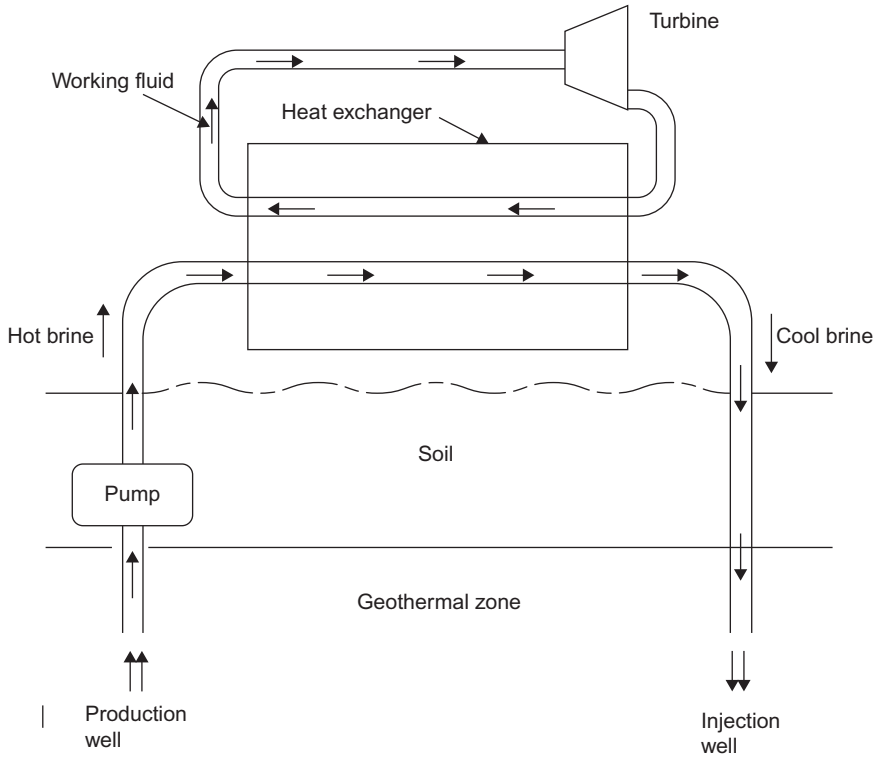


Figure 10.2 Binary cycle geothermal power plant.



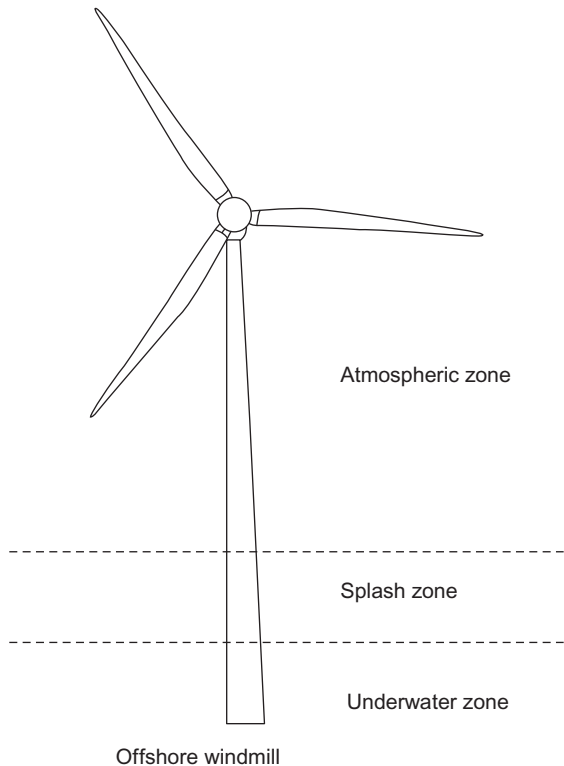
Figure 10.3 Insertion of the “coupon tree” into the pipeline (Moore et al., 2002).

10.4 Offshore wind turbine towers

The utilization of wind energy to produce electricity is expanding rapidly with annual global market growth of 10% and capacity growth of about 19% ([Annual Market Update, 2013](#)). The recent trend is to install wind turbines in remote environments, such as far offshore, to avoid noise and visual pollution. Offshore wind towers are exposed to three different environments ([Figure 10.4](#))—underwater zone, splash zone, and atmospheric zone—and corrosion mechanisms are very different in these three zones. Underwater zone is the area permanently exposed to water; splash zone, which has the highest corrosion rate, is the area wetted by wave and spray action; and atmospheric zone is the region exposed to humid air with high salinity. Also, in the atmospheric zone, offshore turbine towers are exposed to UV radiation, acid rain, extreme temperatures, vibrations, etc. Compared to oil and gas platforms, the accessibility for maintenance is very limited for wind towers. Therefore, advance anticorrosive coating technologies are important for wind towers for attaining the desired level of performance and operating efficiency.

The requirements for corrosion protective coatings for offshore windmills are determined by the exposure conditions; such formal coating systems are selected by considering corrosive categories as described in references ([ISO, 20340, 2005](#);

Figure 10.4 Different corrosion zones of an offshore windmill tower.



Ault, 2006). Corrosion protection of offshore structures is regulated mainly by the following standards:

- DIN EN ISO 12944: Corrosion protection of steel structures by protective paint systems.
- ISO 20340: Paints and varnishes—performance requirements for protective paint systems for offshore and related structures.

Tables 10.1 and 10.2 summarize the coating systems that can be used to protect the areas exposed to atmospheric zone and underwater/splash zone, respectively.

Various coating systems are applied to offshore wind turbine towers (Mühlberg, 2004), and thermal sprayed coatings top the list of preferences as they offer a very resilient finish, which is less susceptible to damage than many paint coatings. Most of the manufacturers of wind turbine towers specify thermally sprayed (flame sprayed) metallization (zinc or zinc/aluminum alloys) followed by an epoxy-based paint as a method of corrosion protection (Mühlberg, 2010; Challener, 2010), and an excellent performance and an impressive cost–benefit relationship were reported

Table 10.1 Coating system(s) to protect from atmospheric exposure (Mühlberg, 2010)

Norm/standard	Prime coat	Number of layers	Total dry film thickness (μm)
DIN EN ISO 12944 C5-Marine, high	EP, PUR	3–5	320
	EP, PUR	2	500
	EP, PUR (zinc rich)	4–5	320
ISO 20340, C5-Marine, high	EP (zinc rich)	Minimum 3	>280
	EP	Minimum 3	>350

EP is epoxy resin, PUR is polyurethane resin, and C5-Marine, high, and Im^2 are corrosivity categories according to ISO 12944.

Table 10.2 Coating system(s) for underwater and splash zone areas (Mühlberg, 2010)

Norm/standard	Prime coat	Number of layers	Total dry film thickness (μm)
DIN EN ISO 12944 Im^2 , high (splash zone not described)	EP, PUR (zinc rich)	3–5	540
	EP, PUR	1–3	600
	EP	1	800
ISO 20340, Im^2 , high, splash zone	EP (zinc rich)	Minimum 3	>450
	EP, PUR	Minimum 3	>450
	EP	Minimum 2	>600

EP is epoxy resin, PUR is polyurethane resin, and high and Im^2 are corrosivity categories according to ISO 12944.

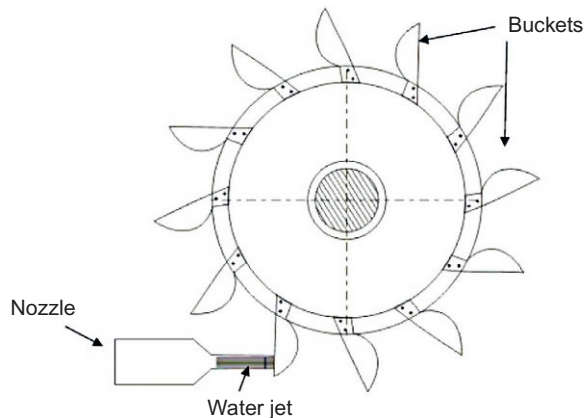
for the above coating system. Typically, a thickness of around 100 μm of zinc-/aluminum-metalized layer is well sufficient for the atmospheric and splash zones.

10.5 Hydroturbines

Hydropower plants are located in 150 countries throughout the world making hydropower one of the most widely used forms of renewable energy. In hydropower industry, silt erosion and corrosion of turbine parts are a major engineering problem. Erosion and corrosion cause changes in surface texture and blade profile, which in turn decrease the efficiency of hydroturbines significantly (Padhy and Saini, 2008). The severity of erosion largely depends on the size, type, and concentration of particles and also on the impact velocity and impact angle of particles relative to turbine parts (Duan and Karelin, 2002), while corrosion depends mainly on the chemical constituents of the water. Studies have revealed that the silt mainly consists of quartz (70–98%), which is extremely hard and causes significant damage to all the common types of turbines such as Pelton (Figure 10.5), Francis, and Kaplan. In general, the size of the particles is restricted to 250 μm and velocity below 75 ms^{-1} , but in the systems where extensive filtration process is not feasible, maintaining these limits is not possible especially in monsoon seasons.

CA6NM also known as hydroturbine steel (Fe–Cr–Ni–Mo alloy; composition: 13% Cr, 4% Ni, and 0.7% Mo) is the material that is extensively used for hydroturbines because of its good corrosion and cavitation resistance and high impact toughness (Iwabuchi and Sawada, 1982). Therefore, lot of research is done on the coating systems on CA6NM to further increase its performance and concluded that thermally sprayed coatings can improve the slurry erosion resistance of the components made by this material and also concluded that the process is cost effective (Sugiyama et al., 2005; Kulu et al., 2005). For this purpose, HVOF is the preferred thermal spray process, and tungsten carbide-based coatings such as WC–Co are the preferred coating materials. For water with high corrosive substances, a coating with chromium such as WC–CoCr can be well utilized as well.

Figure 10.5 Pelton wheel turbine.



When particle size is increased (generally up to 127 μm), the mode of erosion changed from ductile to brittle. Therefore, for the water with high particles sizes, nickel-based tungsten carbide coating is preferred to increase the ductility of the turbine components. It has been documented that thermally sprayed coatings with thickness 200–400 μm can effectively protect the components with economic viability (Chauhan et al., 2010). For the other steel structures necessary in the hydropower industry, Zn- and aluminum-based coating can be applied to prevent atmospheric corrosion.

10.6 Photocatalytic hydrogen production

Hydrogen has gained much attention as the most promising energy resource to overcome future energy crises. With the shift toward a hydrogen economy, which has been already forecast, there will be a huge demand for hydrogen. Water is the ideal source for hydrogen. Therefore, water splitting using renewable energy sources such as solar energy is one of the most sustainable ways of producing hydrogen gas without the evolution of the greenhouse gases. Although water splitting is not economically competitive with current energy costs, when developed with economic viability in the future, this could be the eventual technology that could solve the energy problem and save the environment (Wijewardane, 2013).

Photocatalytic water splitting using sunlight has been studied for a long time (Fujishima and Honda, 1972), and good progress has been recorded in the recent past (Maeda and Domen, 2010; Jing et al., 2010). Water splitting into H_2 and O_2 is highly endothermic (Figure 10.6). Therefore, a light-responsive photocatalyst should have a suitable thermodynamic potential for water splitting. Hundreds of materials and derivatives including semiconductor photocatalytics, such as TiO_2 , SiC , and CdS , have been developed so far. Basic requirements for a potential photocatalytic material other than the thermodynamic potential are the following: (1) it should absorb efficiently the photons with required energy, (2) it should facilitate the separation of photo-generated electron–hole charges, and (3) it should transport these generated charges quickly to

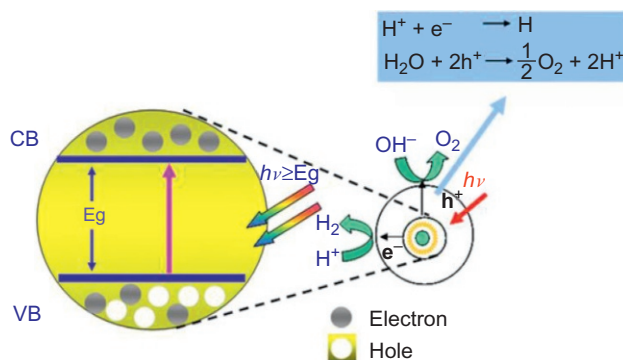


Figure 10.6 Basic principle of water splitting (Jing et al., 2010).

avoid electron–hole recombination. These requirements are strongly affected by bulk properties of the material such as crystallinity. Also, larger surface area and active reaction sites are important for a better production rate. Cocatalysts such as Pt and NiO are often loaded on the surface in order to introduce active sites for H₂ evolution. Although the theoretical efficiency of photocatalytic H₂ generation is about 30% (Walter et al., 2010) in practice, the achieved efficiencies are well below this theoretical limit. The reason is lack of a semiconductor material that fulfills all the thermodynamic, electronic, optical, and microstructural requirements. In addition, the potential material should be cost-effective and environmentally friendly.

In this scenario, thermal spray coatings have a critical role to play. Thermal spraying technology allows forming porous and nanostructured coatings of various metals (Kim et al., 2006). Not only have these coatings replaced expensive bulk materials but also by forming porous and nanostructured surfaces, they increase the surface area of the anode. Recently, a nickel-based electrode coating has been fabricated with larger electrochemical active surface areas consisting of small cauliflower-like aggregates (Figure 10.7), using suspension plasma spray process (Aghasibeig et al., 2014). Also, a novel approach “solution precursor plasma spraying” is used to fabricate ferrite nanocomposite (ZnFe₂O₄:Fe) photoelectrodes, which exhibit photoactivity six times higher than pure ZnFe₂O₄ (Dom et al., 2013).

Although small-size electrodes are already being produced with the desired quality by thermal spraying, producing electrodes in technical and industrial levels (larger than 1 m²) in an economical and reliable way is still a significant challenge for the thermal spray technique. For this purpose, several issues have to be addressed: (i) optimization of spray material with respect to composition and powder particle size; (ii) preparation/

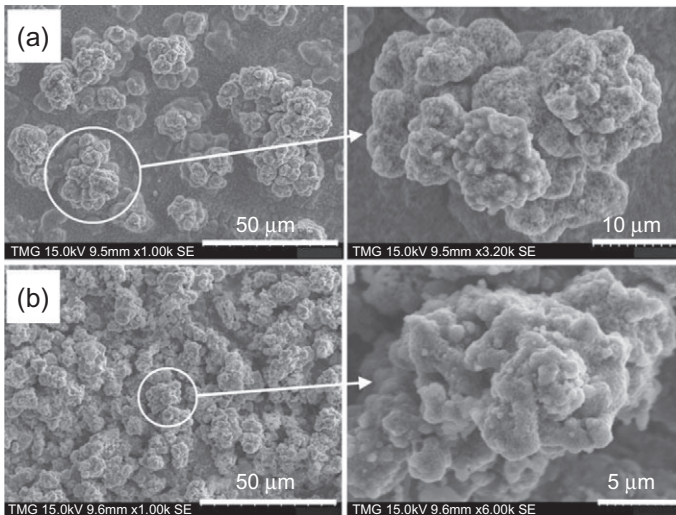


Figure 10.7 SEM images of suspension plasma spray samples (Aghasibeig et al., 2014).

activation of substrate surface for stable bonding of coating; and (iii) industrialization of the production process, with the improvement of spray equipment.

10.7 Thermoelectric power generation

Thermoelectric devices (Figure 10.8) can convert a temperature gradient produced by either a renewable energy source or any other heat source into electrical power and possess several key advantages. They have comparatively long operating lifetime, little or no maintenance, and no moving parts, and they are quiet as well. However, these devices have low converting efficacy, and that is the major hindrance toward their commercialization. Therefore, huge effort is currently being made to produce efficient thermoelectric materials.

The basic material property governing the efficiency of thermoelectric energy converters is the thermoelectric figure of merit (Goldsmid, 1960):

$$Z = S^2 \sigma / \kappa$$

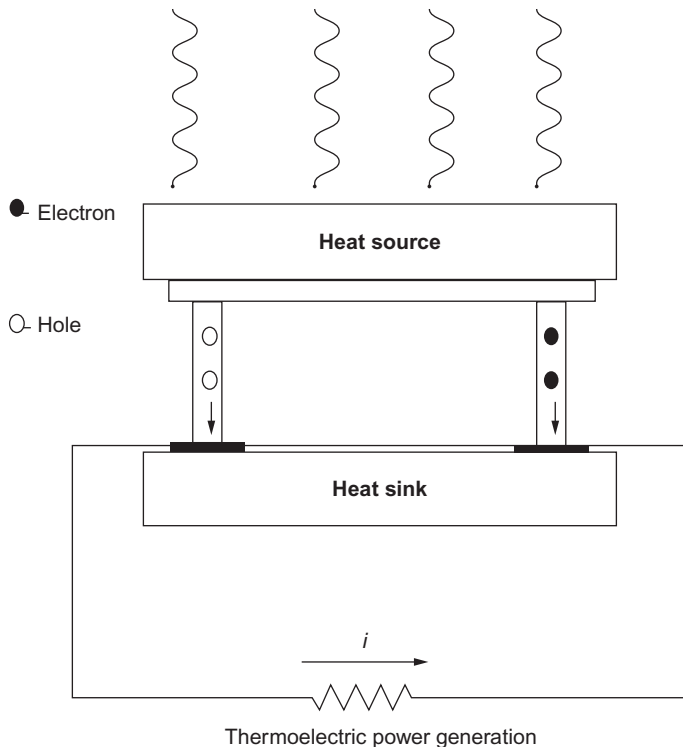


Figure 10.8 Working principle of a thermoelectric device.

where S is the Seebeck coefficient, σ is the electrical conductivity, and κ is the thermal conductivity. To improve the Z value, high S , high σ , and low κ are required. An increase in S normally results to a decrease in σ because of carrier density considerations, and an increase in σ suggests an increase in the electronic contribution to κ as given by the Wiedemann–Franz law; it is very difficult to increase Z value in conventional thermoelectric materials beyond some level (Wood, 1988).

Mainly, because thermal spraying is a flexible, industry-scalable, and cost-effective manufacturing process, researchers have paid their attention to thermal spraying to fabricate efficient and cost-effective thermoelectric material layers (Longtin et al., 2013). But the main drawback with this is the oxidation of particles during the spraying process, which lowers the electrical conductivity of deposited layers (Fu et al., 2012). On the other hand, thermal spray has been considered as an effective way to reduce thermal conductivity, which may be attributed to the coating microstructure with pores and cracks. It has shown that the thermal conductivity of Mg_2Si layers deposited by atmospheric plasma spray is considerably lower than the bulk value (Fu et al., 2014). Even though there is hardly an improvement in Z values of the layers deposited by thermal spraying so far, researchers will keep their attention intact just because the cost-effectiveness of the thermal spraying processes.

10.8 Thin films for photovoltaic power generation

Photovoltaic conversion is the most renowned and conventional way of converting solar power to electricity. It utilizes the “photovoltaic effect” of semiconducting materials, and silicon is the most popular material so far for solar cells. Although silicon is the second most abundant element in Earth’s crust, to be used in solar cells (solar-grade silicon), silicon must be refined to a purity of 99.9999%, which makes material cost one of the major cost contributor to the overall PV manufacturing. Apart from purity, the crystalline structure, microstructure, porosity, etc., affect the performance of the solar cell. Therefore, producing silicon films for photovoltaic cells is sophisticated, and the rate of production is low. CVDs, PVD, and slicing techniques are the common methods of producing silicon films, but either these processes are slow (1 cm²/min) or material wastage is high. Therefore, thermal plasma spraying (RF plasma method or ultrafast thermal plasma) processes are being researched to develop a deposition technique that can produce quality silicon films at a higher production rate (Chae et al., 2001).

An innovative ultrafast plasma surface melting technique is being developed (Figure 10.9), which has the potential of fabricating solid silicon films at a rate of 150 cm²/min (Goortani et al., 2009). Here, a suspension of silicon particles in a volatile solvent is spread on a refractory substrate first. Then, the solvent is evaporated and the dried porous silicon layer is exposed to the flame of inductively coupled RF plasma to get a solid film of silicon by sintering and melting the particles together. They have shown that the flow dynamics, heat transfer around the substrate, exposure time, substrate transport speed, and reaction kinetics are all important parameters to

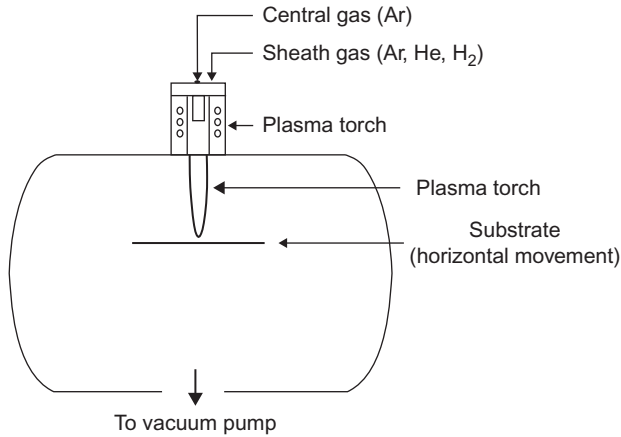


Figure 10.9 Schematic of the experimental setup for the fabrication of Si films (Goortani et al., 2009).

produce quality crystalline Si films suitable for photovoltaic applications. Therefore, these parameters have to be further optimized, and the produced silicon films have to be tested to find out the feasibility of this technique.

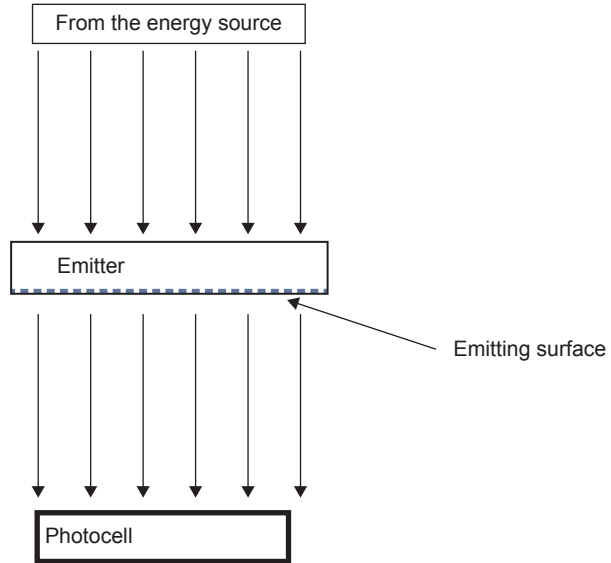
10.9 TPV power generation

TPV is a system that combines a photocell and an appropriate thermal emitter (Figure 10.10), which can emit most of its radiation at frequencies just above the cut-off frequency of the photocell. TPV systems have been researched for decades. However, the lack of a photocell that can convert thermal radiation efficiently to justify the cost of a thermal emitter delayed the progress of this field. With the availability of high-performance photocells based on semiconductor materials from the III–V family and with the development of spectrally selective thermal emitters that can emit radiation within a narrow frequency band, there has been a renewal of interest on TPV systems (Wijewardane and Goswami, 2014).

The current trend in TPV is to produce electricity from the waste heat of industrial furnaces in which the temperatures could go up to 1500 °C, and the prospective frequencies are within the near-infrared region. Although at the moment, the unit price of the electricity produced by conventional thermal plants using the industrial waste heat is slightly lower than the unit price of TPV generated electricity, in general, TPV systems exhibit several key advantages over conventional thermal plants. TPV systems produce no noise and occupy a comparatively small space. Also, these systems are portable and have little or no routine maintenance.

Rare earth oxides such as erbium (Er₂O₃), samarium (Sm₂O₃), neodymium (Nd₂O₃), and ytterbium (Yb₂O₃) (Adair and Rose, 1994; Panitz et al., 2000; Good and Chubb, 2002) have the ability to emit radiation within narrow bands in contrast to most natural

Figure 10.10 Components of a possible thermophotovoltaic system.



substances that emit radiation in wider and continuous bands. These rare earth oxides therefore are suitable for TPV applications. However, the high thermal expansion coefficients, combined with low thermal conductivities and high cost, make the production in bulk of rare earth oxide emitters for TPV applications impractical. Therefore, plasma spray techniques have been used to coat rare earth oxides on cheaper metal substrates mainly due to its cost-effectiveness and the ability to apply them on complicated geometries. Also, the ideal thickness range of rare earth oxides coatings for TPV applications (100–1000 μm) can be achieved easily with thermal sprays. Commercially available Yb_2O_3 and Er_2O_3 powders have been used recently (Tobler and Durisch, 2008a,b) to prepare the samples for thermal spray coatings. These coatings have shown good selective emitting properties and can be used in temperatures as high as 1600 $^\circ\text{C}$.

10.10 Conclusion

The urge from various industries, such as aerospace, for novel, complex, and reliable coatings paves the way to industrialization of thermal spray techniques. This is quite a unique scenario compared with other advance coating and deposition techniques in which scientific innovation has played a major role for commercialization. There is a similar push from the renewable energy sector for novel, reliable, and cost-effective coatings to compete with other forms of power generation sources. However, these coatings should perform better than the existing coatings, and their fabricating costs should be lowered as much as possible to be competitive in the energy market. As thermal spraying has evolved, mainly due to the urge from industry, there is a significant amount of experience-based knowledge/information that has not been published but vital for the

development of the field. Sharing this knowledge/information may be important when exploring for novel coatings at lower prices. Therefore, collaboration among research groups may be the key to success by overcoming many potential drawbacks.

References

- Adair, P.L., Rose, M.F., 1994. Coutts, T.J., Benner, J.P. (Eds.), AIP Conference Proceedings – The First NREL Conference on Thermophotovoltaic Generation of Electricity, vol. 321. The American Institute of Physics, Copper Mountain, CO, p. 245.
- Adamiec, J., 2009. High temperature corrosion of power boiler components clad with nickel alloys. *Mater. Charact.* 60, 1093–1099.
- Aghasibeig, M., Mousavi, M., Ben Ettouill, F., Moreau, C., Wuthrich, R., Dolatabadi, A., 2014. Electrocatalytically active nickel-based electrode coatings formed by atmospheric and suspension plasma spraying. *J. Therm. Spray Technol.* 23, 220–226.
- Amend, B., Yee, J., 2013. Selective application of corrosion resistant alloys mitigates corrosion in pH-modified geothermal fluids. In: NACE – International Corrosion Conference Series 2013, Orlando, FL, United States.
- Annual Market Update, 2013. Global wind report. Global Wind Energy Council.
- Ault, P., 2006. The use of coatings for corrosion control on offshore oil structures. *Protect. Coatings Europe* 11 (4), 42–46.
- Bakker, W.T., 1997. The effect of chlorine on mixed oxidant corrosion of stainless-steels. *Mater. High Temp.* 14, 197.
- Chae, Y.K., Ohno, H., Eguchi, K., Yoshida, T., 2001. Ultrafast deposition of microcrystalline Si by thermal plasma chemical vapor deposition. *J. Appl. Phys.* 89 (12), 8311–8315.
- Challener, C., 2010. Coatings critical for wind energy efficiency. *J. Coating. Technol.* 7, 46–49.
- Chauhan, A.K., Goel, D.B., Prakash, S., 2010. Erosive wear of a surface coated hydro turbine steel. *Bull. Mater. Sci.* 33 (4), 483–489.
- Dom, R., Kumar, G.S., Hebalkar, N.Y., 2013. Eco-friendly ferrite nanocomposite photoelectrode for improved solar hydrogen generation. *RSC Adv.* 3, 15217–15224.
- Duan, C.G., Karelin, V.Y., 2002. Abrasive Erosion and Corrosion of Hydraulic Machinery. Imperial College Press, London.
- Fu, G., Zuo, L., Longtin, J., Chen, Y., Sampath, S., 2012. Progress on searching optimal thermal spray parameters for magnesium silicide. In: Materials Research Society Symposium Proceedings 2012 MRS Fall Meeting; Boston, MA, vol. 1490, pp. 173–177.
- Fu, G., Zuo, L., Longtin, J., Nie, C., Chen, Y., Tewolde, M., Sampath, S., 2014. Thermoelectric properties of magnesium silicide deposited by use of an atmospheric plasma thermal spray. *J. Electron. Mater.* 43, 2723–2730.
- Fujishima, A., Honda, K., 1972. Electrochemical photolysis of water at a semiconductor electrode. *Nature* 238, 37–38.
- Gainger, S., Blunt, J., 1998. Engineering Coatings: Design and Application. Abington Publishing, Cambridge, England.
- Goldsmid, H.J., 1960. Applications of Thermoelectricity. Methuen, London.
- Good, B.S., Chubb, D.L., 2002. Thermophotovoltaic generation of electricity. In: Coutts, T.J., Guazzoni, G., Luther, J. (Eds.), AIP Conference Proceedings, vol. 653. p. 142.
- Goortani, B.M., Gitzhofer, F., Bouyer, E., Mousavi, M., 2009. Ultrafast thermal plasma preparation of solid Si films with potential application in photovoltaic cells: a parametric study. *J. Therm. Spray Technol.* 18, 50–57.

- ISO 20340, 2005. Performance Requirements for Protective Paint Systems for Offshore and Related Structures. International Organization for Standardization, Genève.
- Iwabuchi, Y., Sawada, S., 1982. Metallurgical characteristics of a large hydraulic runner casting of type 13Cr-Ni stainless steel. In: *Stainless Steel Castings*. ASTM, pp. 332–354.
- Jing, D., Guo, L., Liang, Z., 2010. Efficient solar hydrogen production by photocatalytic water splitting: from fundamental study to pilot demonstration. *Int. J. Hydr. Energy* 35 (35), 7087–7097.
- Kaushal, G., Singh, H., Prakash, S., 2011. High-temperature erosion–corrosion performance of high-velocity oxy–fuel sprayed Ni-20 Cr coating in actual boiler environment. *Metall. Mater. Trans. A: Phys. Metall. Mater. Sci.* 42, 1836–1846.
- Kawahara, Y., 1997. Development and application of high-temperature corrosion-resistant materials and coatings for advanced waste-to-energy plants. In: Bakker, W.T., Norton, J.F., Wright, I.G. (Eds.), *Proceedings of the Second International Workshop on Corrosion in Advanced Power Plants, Materials at High Temperatures*, Tampa, FL, vol. 14 (3), pp. 261–268.
- Kaya, T., Hoşhan, P., 2005. Corrosion and material selection for geothermal systems. In: *Proceedings World Geothermal Congress 2005; Antalya, Turkey, 24–29 April*.
- Kim, J.-H., Yang, H.-S., Baik, K.-H., Geun Seong, B., Lee, C.-H., Young Hwang, S., 2006. Development and properties of nanostructured thermal spray coatings. *Curr. Appl. Phys.* 6, 1002–1006.
- Kulu, P., Hussainova, I., Veinthal, R., 2005. Solid particle erosion of thermal sprayed coatings. *Wear* 258, 488–496.
- Lai, G.Y., 1990. *High-Temperature Corrosion of Engineering Alloys*. ASM International, Materials Park, OH p. 230.
- Li, C.-J., Ohmori, A., 1996. The lamellar structure of a detonation gun sprayed Al₂O₃ coating. *Surf. Coat. Technol.* 82, 254–258.
- Longtin, J.P., Zuo, L., Hwang, D., Fu, G., Tewolde, M., Chen, Y., Sampath, S., 2013. Fabrication of thermoelectric devices using thermal spray: application to vehicle exhaust systems. *J. Therm. Spray Technol.* 22, 577–587.
- Maeda, K., Domen, K., 2010. Photocatalytic water splitting: recent progress and future challenges. *J. Phys. Chem. Lett.* 1, 2655–2661.
- Moore, K.A., Mizia, R.E., Zatorski, R.A., 2002. Internal metallic pipe coatings for the geothermal industry. In: *Transactions-Geothermal Resources Council: 2002 Annual Meeting; Reno, NV, United States*.
- Moskowitz, L.N., 1993. Application of HVOF thermal spraying to solve corrosion problems in the petroleum industry—an industrial note. *J. Therm. Spray Technol.* 2, 21–29.
- Mühlberg, K., 2004. Corrosion protection for windmills on-shore and off shore. *Protect. Coatings Europe* 9 (4), 30–35.
- Mühlberg, K., 2010. Corrosion protection of offshore wind turbines – a challenge for the steel builder and paint applicator. *J. Prot. Coat. Lin.* 27, 20–32.
- Naji, A., Galetz, M., Schütze, M., 2012. Development of diffusion coatings to optimize the high temperature corrosion resistance of reformer materials. In: *NACE – International Corrosion Conference Series, Corrosion 2012; Salt Lake City, UT, United States; vol. 7, pp. 5741–5754*.
- Orita, N., Kawahara, Y., Takahashi, K., Nakagawa, Y., 2000. Development of high-efficiency waste-to-energy plant. *Technical Review*, vol. 37. Mitsubishi Heavy Industries, Ltd., p. 1.
- Padhy, M.K., Saini, R.P., 2008. A review on silt erosion in hydro turbines. *Renew. Sustain. Energy Rev.* 12, 1974–1987.

- Panitz, J.C., Mayor, J.C., Grob, B., Durisch, W., 2000. A Raman spectroscopic study of rare earth mixed oxides. *J. Alloy. Compd.* 303–304, 340–344.
- Paul, S., Harvey, M.D.F., 2013. Corrosion testing of Ni alloy HVOF coatings in high temperature environments for biomass applications. *J. Therm. Spray Technol.* 22, 316–327.
- Rogers, P.M., Hutchings, I.M., Little, J.A., 1995. Coatings and surface treatments for protection against low-velocity erosion–corrosion in fluidized beds. *Wear* 186/187, 238–246.
- Selvakumar, N., Barshilia, H.C., 2012. Review of physical vapor deposited (PVD) spectrally selective coatings for mid- and high-temperature solar thermal applications. *Sol. Energ. Mater. Sol. Cells* 98, 1–23.
- Sugiyama, K., et al., 2005. Slurry wear and cavitation erosion of thermal-sprayed cermets. *Wear* 258, 768–775.
- Tobler, W.J., Durisch, W., 2008a. High-performance selective Er-doped YAG emitters for thermophotovoltaics. *Appl. Energ.* 85, 483–493.
- Tobler, W.J., Durisch, W., 2008b. Plasma-spray coated rare-earth oxides on molybdenum disulfide – high temperature stable emitters for thermophotovoltaics. *Appl. Energ.* 85, 371–383.
- Tucker Jr., R.C., 2002. Thermal spray coatings: broad and growing applications. *Int. J. Powder Metall.* 38, 45–53.
- Verdi, D., Garrido, M.A., Múñez, C.J., Poza, P., 2014. Mechanical properties of Inconel 625 laser cladded coatings: depth sensing indentation analysis. *Mater. Sci. Eng. A* 598, 15–21.
- Walter, M.G., Warren, E.L., McKone, J.R., Boettcher, S.W., Mi, Q., Santori, E.A., et al., 2010. Solar water splitting cells. *Chem. Rev.* 110, 6446e73.
- Wang, Q., Perkins, J., Branz, H.M., Alleman, J., Duncan, C., Ginley, D., 2002. Combinatorial synthesis of solid state electronic materials for renewable energy applications. *Appl. Surf. Sci.* 189, 271–276.
- Wijewardane, S., 2013. The role of CNT and CNT/composites for the development of clean energy. In: Kar, K.K., Rana, S., Pandey, J.K. (Eds.), *Technological Advancement in the Carbon Nanotube (CNT) Based Polymer Composites: Processing, Performance and Application*. Springer-Verlag GmbH, Berlin/Heidelberg.
- Wijewardane, S., Goswami, D.Y., 2012. A review on surface control of thermal radiation by paints and coatings for new energy applications. *Renew. Sustain. Energy Rev.* 16, 1863–1873.
- Wijewardane, S., Goswami, Y., 2014. Extended exergy concept to facilitate designing and optimization of frequency-dependent direct energy conversion systems. *Appl. Energy* 134, 204–214.
- Wood, C., 1988. Materials for thermoelectric energy conversion. *Rep. Prog. Phys.* 51, 459–539.
- Yamada, K., Tomono, Y., Morimoto, J., Sasaki, Y., Ohmori, A., 2002. Hot corrosion behavior of boiler tube materials in reduce incineration environment. *Vacuum* 65 (3–4), 533–540.

This page intentionally left blank

Manufacturing engineering in thermal spraying by advanced robot systems and process kinematics

11

R. Gadow, M. Floristán

Abbreviations

APS	atmospheric plasma spraying
CAD	computer-aided design
CFD	computational fluid dynamics
FEA	finite element analysis
FEM	finite element method
HVOF	high-velocity oxygen fuel
IFKB	Institut für Fertigungstechnologie keramischer Bauteile, Universitaet Stuttgart
IR	infrared
LERMPS	Laboratoire d'Etudes et de Recherches sur les Matériaux, les Procédés et les Surfaces, Université de Technologie Belfort-Montbéliard
SEM	scanning electron microscope
TCP	tool centre point
TST	Thermal Spray Toolkit

11.1 Introduction

Robots and handling systems are traditionally used in thermal spraying processes to control the movement of the spray torch relative to the substrate and to assure a safe working environment. Moreover, the use of automation systems enhances the flexibility and reproducibility of the processes, giving rise to the production of high-quality and cost-effective coatings (Deng et al., 2012a). The process kinematics has a significant impact on the deposition process and on the quality and properties of the resulting coating. Heat and mass transfer to the substrate or to an already deposited coating during spraying is strongly influenced by the robot trajectory (Li, 2003; Xia et al., 2009). The process deposition efficiency can be, to a given extent, controlled by the process kinematics, since these influences the state of the impacting particles regarding their momentum and viscosity and the material deposition rate per cycle

(Montavon et al., 2005). Further on, the relative movement between torch and component affects the heat transfer to the substrate. The heat flux of the high-energy jet or flame on the substrate depends, among other factors, on the spraying distance used. Similarly, spraying velocity and path can determine the residence time of the hot spot on the component and, therefore, the substrate and coating temperature, which affects the flattening and deposition of sprayed particles, and thus a great number of coating properties such as anisotropic elastic properties, porosity, development of residual stresses or coating crystallinity and phase composition.

Moreover, the development of thermal spray technologies has given rise in the last years to new application fields and to the use of more complex-shaped substrate geometries. In this regard, robot programming needs to be optimized for spraying complex-shaped components in order to fulfil coating quality standards and dimensional accuracy (Candel and Gadow, 2006). This can be achieved by an accurate control of the process kinematics in order to maintain adequate spray velocity, spray distance and spray angle during the deposition process, supporting a constant and controlled heat and mass transfer to the substrate. Although still nowadays, many processes in the area of robot programming are done by online methods (Deng et al., 2012a), offline programming supported by the use of virtual working cells, where the process kinematics can be simulated and optimized, is gaining importance in the field of thermal spraying, specially for the coating of complex-shaped parts.

Current research in robot trajectory generation for thermal spraying is directed to plan the spray torch path regarding the heat and mass transfer to the substrate or already deposited coating in order to obtain the required coating properties. With this aim, offline programming approaches have been combined with simulation tools, giving rise to a virtual design of the coating process and expected coating characteristics. This chapter will discuss the importance of the process kinematics in thermal spraying and will give an overview of the current trends and the newest results of research in the field.

11.2 Influence of the process kinematics on the coating properties

The so-called kinematic parameters define the relative movement between the spray torch and the substrate during deposition and are controlled by the handling systems, which bring the spray torch and/or the substrate in motion. The main kinematic parameters are the spray angle, spray distance, spray velocity and spray path, and they are schematically displayed in Figure 11.1.

11.2.1 Spray angle

The spray angle was defined by Ilavsky et al. (1997) as the “angle between the axis of the spray torch and the surface of the substrate”. In thermal spraying, the torch is normally arranged perpendicular to the substrate surface at each point of the trajectory. However, in some cases when coating substrates having complex-shaped geometries,

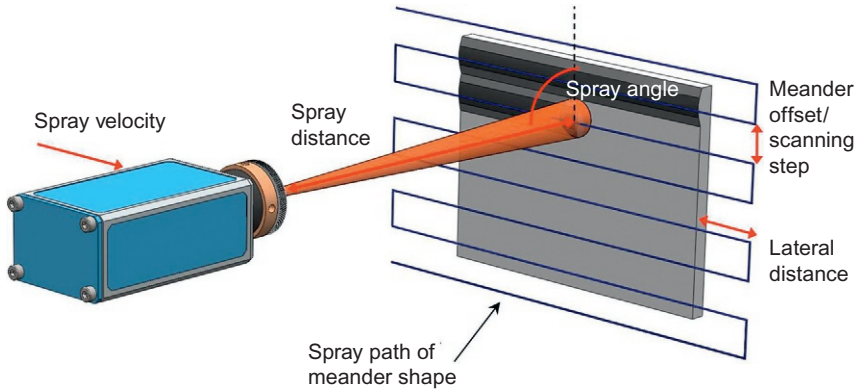


Figure 11.1 Main kinematic parameters (based on Cai et al., 2011; Floristán et al., 2012).

the spray angle needs to be reduced. Changes in the spray angle lead to a modified flattening and formation of the splats and therefore of their morphology (Smith et al., 1994; Montavon et al., 1997; Bussmann et al., 1999; Kang et al., 2006). If a spray angle of 90° is used, the in-flight particles can be considered to impact perpendicularly to the substrate with a normal momentum. With a reduction of the spray angle, the tangential component of the in-flight particle velocity with respect to the substrate surface is increased, while the normal component is reduced. This leads to a lower normal momentum at impact with the substrate than with a spray angle of 90° . The velocity tangential component promotes particles spreading over the substrate, giving rise to elongated splats. Such changes in the splat impact have a great influence on many coating properties. Several studies (Ilavsky et al., 1997; Leigh and Berndt, 1997; Friis et al., 2001; Krebs, 2011; Floristán, 2013) had described an increase in the coating porosity with low spray angles. The particles sprayed with off-normal angles present a lower-normal velocity component, which determines the effective bonding of the splat with the substrate or already deposited particles (Kang et al., 2006). Therefore, the particles do not have enough energy to effectively cover the substrate, producing more porous coatings (Leigh and Berndt, 1997). Furthermore, the lower impact momentum of such particles leads to a higher probability of rebounding and a decrease in the deposition efficiency. Friis et al. (2001) found that the particle velocity and the particle temperature control the porosity, while the substrate temperature and the spray angle control the cracks and delamination of the coating. Coatings sprayed with angles lower than 90° present a sawtooth-shaped profile (Smith et al., 1994). The “peaks” of such a sawtooth-shaped profile have a shadowing effect on neighbouring areas, which cannot be covered by particles impacting with off-normal angles. As a result, porous coatings are produced. Also, a reduction of coating microhardness with lower spray angles has been reported in the literature (Strock et al., 2001; Candel, 2009; Houdková et al., 2010) and can be related to the higher coating porosity. Coating roughness is expected to increase with low spray angles and can be attributed to the particles interlocking with surface inhomogeneities (Tillmann et al., 2008).

Figure 11.2 displays cross section micrographs and SEM images of the surfaces of $\text{Al}_2\text{O}_3/\text{TiO}_2$ atmospheric plasma spraying (APS) coatings deposited on copper substrates. The samples were sprayed at different spray angles and the number of spray cycles was adjusted in order to produce the same coating thicknesses for microstructure comparison. The dark areas of the micrographs are attributed to Al_2O_3 , while the lighter ones correspond to TiO_2 (Yilmaz et al., 2007). A change in the orientation of the white areas with reduced spray angles can be observed as a result of the change in the splat deposition. The orientation of other microstructure features, such as vertical cracks, can also change with the spray angle (Ilavsky et al., 1997; Smith et al., 1994). The sawtooth-shaped profile characteristic of coatings deposited with low angles can be clearly observed in the sample sprayed with 30° .

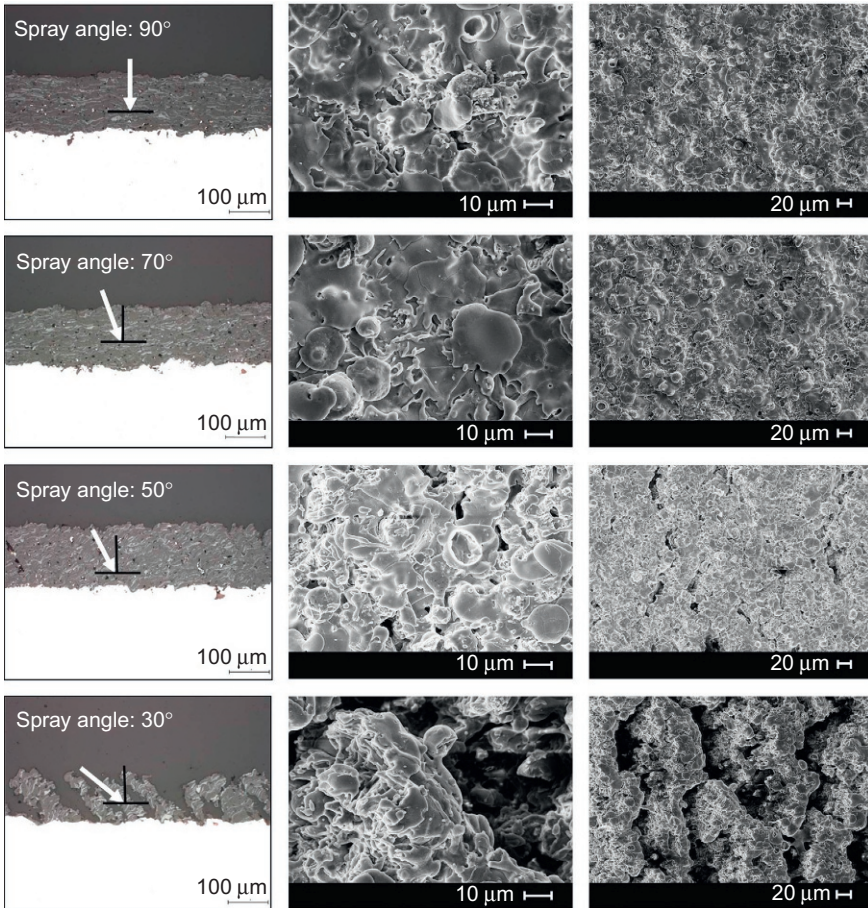


Figure 11.2 Micrograph cross-section (left) and surface SEM (middle and right) images of $\text{Al}_2\text{O}_3/\text{TiO}_2$ APS coatings on copper substrates sprayed with 90° , 70° , 50° and 30° spray angle and with adjusted parameters to obtain equal coating thickness (Floristán et al., 2011).

Changes in coating properties like roughness or porosity with a reduction of the spray angle, which can be considered significant for the coating quality, have been reported to appear at spray angles below 50° (Tillmann et al., 2008; Smith et al., 1994). The spray angle should be maintained perpendicular to the substrate surface during the spray process in order to produce coatings with homogeneous properties. This is nevertheless difficult for the coating of complex-shaped parts. In such cases, there might be points of the robot trajectory in which a slight reduction of the spray angle can be done in order to program a smoother trajectory, reachable by the robot, and thus to improve the spraying operation and overall coating quality.

11.2.2 Spray distance and velocity

Another important spray parameter that is determined by the handling systems is the spray or standoff distance, which is measured between the spray torch nozzle exit and the substrate surface. This parameter and its influence on the resulting coating have been extensively analysed in the literature for different spray materials and thermal spray processes. Since the spray distance controls the in-flight time of the particles in the high-energy jet or flame, it also determines the particle temperature and velocity at impact on the substrate. Therefore, the coating buildup process is significantly influenced by this parameter. The spray distance should be set to assure a dwell time of the spray particles in the jet or flame, which provides them with optimized thermal and kinetic energy for the required coating properties. Too short spray distance can result in insufficiently melted particles impacting the substrate, while too high distances can lead to the cooling of the already melted in-flight particles (Killinger, 2010). Several studies have reported a decrease in the mechanical properties of the coating if too large spraying distances are used (Hamatani et al., 2002; Vijay et al., 2009). The increase in spray distance can lead to too long in-flight times of the particles, which arrive to the substrate surface partially or totally solidified. Such particles have a higher probability of rebounding from the substrate, reducing the deposition efficiency, or they weakly adhere to the coating, giving often rise to low coating cohesion and further coating defects, like the formation of voids. Coating microhardness can also be reduced if spraying at too large distances (Vijay et al., 2009). The melting degree of the particles can be controlled by the spray distance and, with this, partially the phase changes of the spraying material.

The speed of the torch relative to the substrate conditions, the amount of matter deposited per coating cycle and the thermal history of the coating composite are also determined by the spraying velocity, since they define the residence time of the jet or flame on the substrate.

11.2.3 Spray path

The path described by the spray torch relative to the substrate has a distinct influence on the resulting coating properties, as the lateral or local resolution of heat and mass transfer during coating deposition affects the coating properties. In thermal spraying, a meander-shaped spray path is commonly used, as displayed in Figure 11.1. Such a path is composed by equidistant and parallel horizontal passes of the torch with respect to the

substrate. The distance between each two consecutive passes is known as scanning step, and it determines the overlapping of the coating material beads deposited in consecutive passes and, therefore, the coating thickness (Krebs, 2011). Other coating properties, such as porosity, can also be affected by the scanning step used (Floristán, 2013).

Some publications have pointed out the importance of the spray path regarding the heat transfer to the substrate and the absolute coating composite temperature and the related developed residual stresses. Friedrich et al. (2001) and Friedrich (2002) tested different spray paths and cooling configurations to optimize the residual stress state on borosilicate glass tubes coated with oxide ceramics for the production of ozonizer tubes for environmental engineering applications, such as water purification. The heat management during spraying operations on borosilicate glass and glass ceramic substrates is especially relevant due to the specific thermophysical properties of these materials, that is, low thermal expansion coefficient (Escribano et al., 2003). In the experiments, the high residual stresses lead to the breakage of the coated tubes during the cooling down after the deposition process (see Figure 11.3a). By adapting the spray torch path and the cooling system with compressed air nozzles, the thermal gradients in the substrate and coating during spraying, as well as the reached temperatures, could be reduced, leading to lower residual stresses and higher process security (Figure 11.3b).

Similarly, Li (2003) analysed the effect of the spray path for the deposition of thermally sprayed film heaters on glass ceramic substrates used for cooking plates. He deposited via APS an oxide ceramic bond coat on glass ceramic substrates and a metallic top coat with a defined geometry acting as the heater (Figure 11.4). Two of the analysed spray paths are displayed in Figure 11.4. The path type “A” represents a meander-shaped spray path, while type “B” is a modified meander-shaped spray path, which describes a top-down-top movement with respect to the substrate for each coating cycle, leading to a lower-temperature gradient within the component. The IR images in Figure 11.4 correspond to the coating temperatures in working conditions. It can be observed that the sample sprayed with the path type “B”, which gives rise to a more homogeneous heat distribution in the composite during spraying, presents a uniform heating of the operating film, while the sample sprayed with the typical meander-shaped spray path shows hot spots with overheating during its functioning.

Other studies have also analysed the influence of the spray path used for the coating process on the temperature gradients and temperature levels in the coating composite, relating these effects with the development of residual stresses in coating and substrate and with changes in coating properties like void content or bonding strength (Gadow et al., 2002;

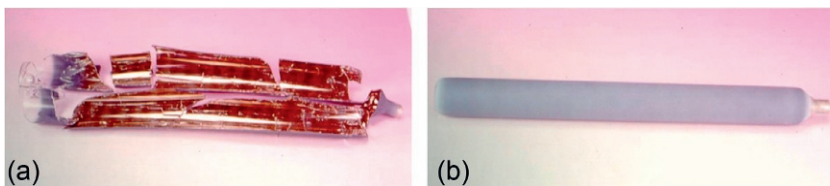


Figure 11.3 Broken (a) and non-broken (b) coated glass tube (Al/Si and Al₂O₃/TiO₂) due to different residual stress situations (Friedrich, 2002).

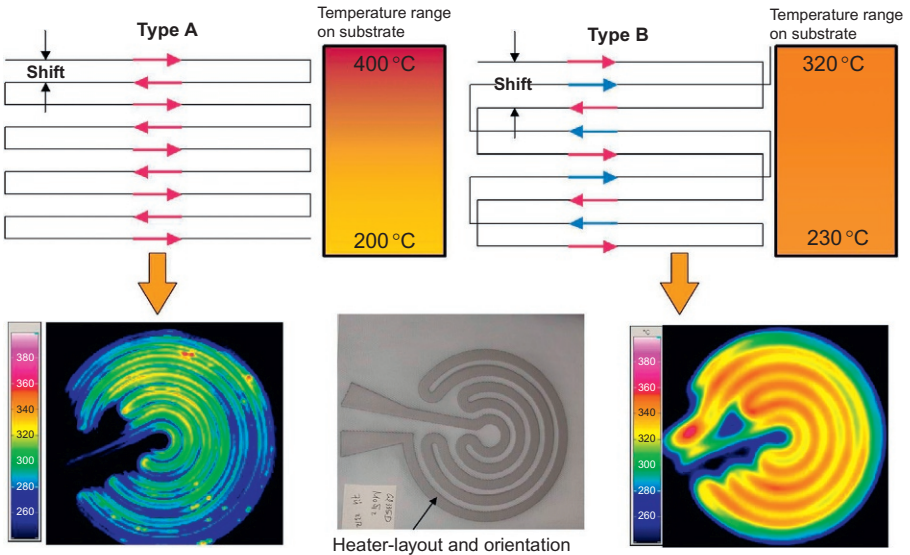


Figure 11.4 Analysed spray paths and their effect on the surface temperature distribution and IR images showing coating temperature distribution in working conditions for the case study of film heaters for cooking plates (Li, 2003).

Killinger, 2010). These experiments underline the importance of an adequate planning of the torch path in thermal spraying on the resulting product properties and quality.

11.3 Offline programming of robots for thermal spraying applications

If the robot is used during the programming phase, online and offline methods can be differentiated. Online processes refer to the robot programming carried out in the spray cell using the real robot or a miniaturized model of this one, while programming approaches, which are made in a separate working station without using the real robot, are denoted as offline methods. A combination of both programming procedures is also possible, and it is known as hybrid programming (Dai, 2000).

In thermal spraying, most operations related to robot programming are still carried out by online methods (Deng et al., 2012a). These are simple and effective for the generation of spray trajectories to coat non-complex-shaped geometries. Moreover, the initial investment for online methods is lower than for offline methods, and it requires little programming knowledge. Programming is often made by teach-in methods, in which the operator uses a handheld control box called teach pendant to move the tool centre point (TCP) of the robot through the required points in order to create a trajectory. The sequence of points is then recorded, and it describes the robot movement to coat the substrate surface (Kerama, 1999). Hybrid programming is also often applied in thermal spraying. In this case, some points of the trajectory are

taught-in manually with the help of the teach pendant and are used to offline-program the robot trajectory, for example, by alphanumeric methods using the robot programming language, in another working station.

However, online methods are inaccurate and time-consuming for the generation of robot trajectories to coat complex-shaped geometries. For this reason, the use of offline programming methods has increased in the field of thermal spraying, and research has focused on the improvement and adaptation of offline tools to the specific requirements of these coating processes.

11.3.1 Approaches to offline-program robots for thermal spraying processes

The robot trajectory can be defined by a number of positions of the TCP in the space, the orientation of the spray torch at each point and the velocity between each two consecutive points. The main steps carried out to offline-generate the robot trajectory for the coating of complex-shaped geometries and the different approaches discussed in the literature are presented below.

11.3.1.1 Substrate geometric model

A model of the substrate real geometry is required to generate the robot trajectory for the coating process. This is often provided by the manufacturer of the workpiece; otherwise, a geometric 3-D model can be generated using commercial CAD software. In case of complex-shaped substrate geometries, Zieris and Schmidt (2004) and Candell (2009) proposed the use of reverse engineering methods, with which the geometric description of the part can be acquired from the physical real object. Optical or tactile coordinate measurement systems can be used to acquire the workpiece geometry, which is given in the form of a group of discrete points. The geometry description by discrete points can be converted into a mathematical surface representation. Figure 11.5a displays a kneader blade, which is used in injection moulding machines that can be thermally sprayed to increase its surface wear resistance. The piece was measured with an optical device, and a cloud of points, which represents the object geometry, was obtained (Candell, 2009). In the case of free-form geometries, the surface is often divided into “patches” for a lighter processing of the data, as noted from “A” to “E” in Figure 11.5b. From the cloud of points and by means of a programmed routine in MATLAB® (the MathWorks™, Massachusetts, the United States), a meshed surface of the kneader blade was obtained (Figure 11.5c).

11.3.1.2 Trajectory generation

In order to program the robot trajectory, the kinematic parameters should be defined first. Normally, spray tests are carried out on planar substrates in order to optimize the coating for the specific application, and the selected spray parameters are used for the coating of the real complex-shaped geometry. Spray distance, velocity and angle should be kept constant during the spraying process. Meander-shaped spray paths are commonly used also to coat free-form geometries, and the scanning step is set according to the required coating thickness.

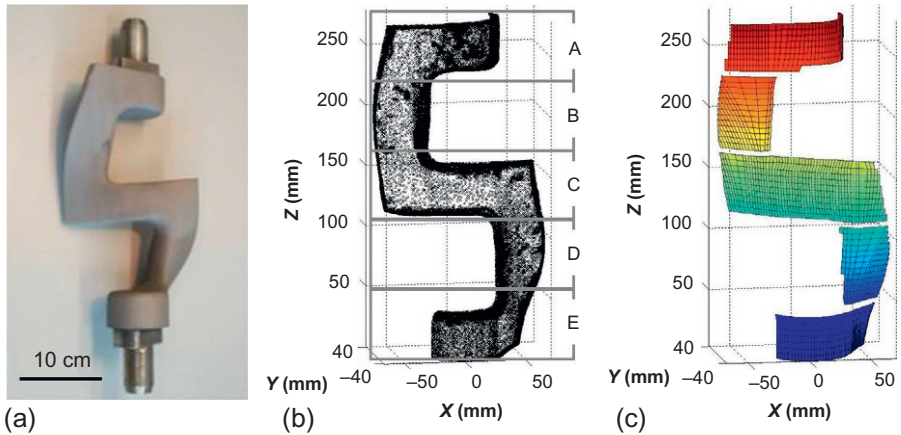


Figure 11.5 (a) Kneader blade, (b) cloud of points obtained by optical measuring device (Candel, 2009) and (c) meshed surface obtained from the cloud of points (Floristán et al., 2012).

Several tools are commercially available nowadays to offline-program robot trajectories and are used for thermal spray processes, such as IGRIP system (Deneb Robotics Inc., Auburn Hills, MI) used by Nylén and Edberg (1997), Hansbo and Nylén (2000) and Ahmaniemi et al. (2002); an adaptation of DCAM-nc (NC-Soft Wagner kG, Schwerin, Germany) used by Zieris and Schmidt (2004) and RoPaGen (Technischen Universität Dortmund, Germany) and RobotStudio™ (ABB AG) used by Krebs (2011). However, commercial software often needs to be adapted or coupled with other modules in order to meet the specific requirements of thermal spray processes.

The team at LERMPS has worked during the last years on the development of an extended program of ABB RobotStudio™ (ABB Ltd.) specifically designed for thermal spray processes, called Thermal Spray Toolkit (TST) (Deng et al., 2005, 2006; Fang et al., 2010b, 2011; Cai et al., 2012). The main module of TST is called PathKit, and it is employed to autogenerate the trajectory of the robot TCP from the CAD model of the part. The 3-D model of the substrate is loaded in TST and the surface to be sprayed is selected. The spray parameters such as spray velocity and scanning step can be given in a programmed interface. The spray path is meander-shaped, and it is generated by several intersections of a plane with the substrate surface, perpendicularly to the latter. The intersections are separated by a distance corresponding to the scanning step. Like this, intersection curves are generated, which contain the points of the robot TCP trajectory on the substrate. The normal vectors to the substrate surface at each point of the trajectory are calculated by the TST in order to define the torch orientation. Several modules have been created attending to the substrate geometry (planar, curved, etc.). With this add-in program of RobotStudio™, robot trajectories for coating real components have been generated, as it can be seen in Figure 11.6.

Another methodology was proposed by Candel (2009) to offline-generate robot trajectories for thermal spray processes using routines programmed in MATLAB®. The methodology has been further developed (Floristán et al., 2012) and an interface was programmed to load the 3-D model of the substrate, choose the surface that needs to be

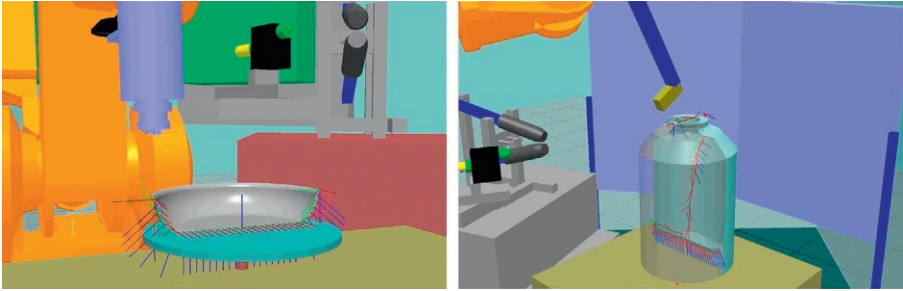


Figure 11.6 Off-line trajectory generation with Thermal Spray Toolkit for the coating of real components (courtesy of LERMPS).

coated and give the spray parameters, such as spray velocity and scanning step. Using the 3-D model of the part, the surface to be coated is meshed in MATLAB[®]. Figure 11.7 displays this method to generate the trajectory to coat a blade used in printing industry to guide paper. The points of the mesh are used as points of the robot TCP trajectory in the coating process. If a horizontal meander-shaped spray path is chosen (see Figure 11.7d), the spray process is driven top-down with respect to the piece.

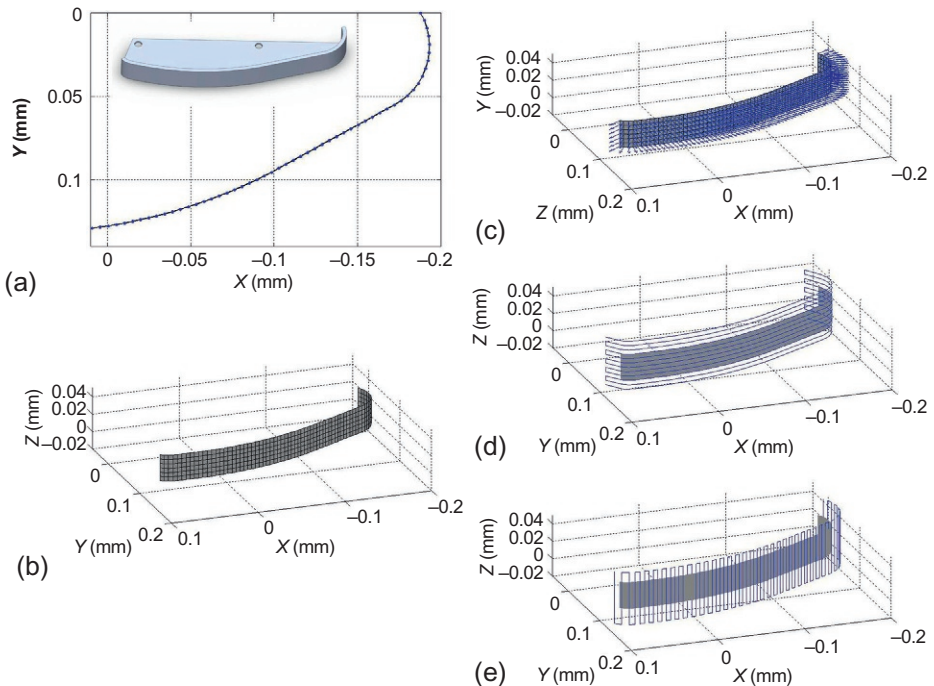


Figure 11.7 (a) Blade used as substrate, (b) meshing of the substrate surface which needs to be coated, (c) normal vectors to the surface at each point of the trajectory, generated trajectories for (d) a horizontal and for (e) a vertical spray strategy (Floristán, 2013).

In such case, the mesh size in that direction is equal to the scanning step. On the other hand, the mesh size along each horizontal pass of the spray path, which defines the amount of points considered in each horizontal pass, can be determined depending on the curvature of the substrate. The movement of the robot TCP between two consecutive points is linear, so that enough points need to be chosen in order to obtain an accurate trajectory to coat the substrate surface. The normal vectors to the substrate surface at each point of the trajectory are calculated and are used to define the spray torch orientation during coating (Figure 11.7c). More points are automatically added to the trajectory in order to define the lateral distance of the spray path and the first and last passes of the meander-shaped spray path, which do not take place directly on the substrate. The generated trajectories for a horizontal spray strategy and a vertical spray strategy are shown in Figure 11.7c and d, respectively. An important advantage of this method is that it can be applied independently of the robot brand used, since the generated trajectory can be translated to the programming language of the specific robot used. Moreover, the programmer gets control over all the trajectory parameters and points, which can be easily modified. Robot trajectories for complex-shaped geometries can be generated with this method, as it was shown by [Candel and Gadow \(2009\)](#) for the case of a ship propeller.

11.3.1.3 Virtual and real robot trajectory implementation

Once the robot trajectory has been offline-generated, implementation is carried out in a virtual environment. Most of the offline programming software provides an animation tool with a virtual robot control in order to test the robot trajectories in a virtual spray booth. This allows the programmer to optimize the robot movement in order to avoid collisions with elements in the working cell or robot axes singular positions and increases the process flexibility and adaptability to production changes, such as changes in substrate position. Figure 11.8 displays virtual models of two real spray booths designed with ROBOGUIDE (FANUC Robotics) and with RobotStudio™ (ABB Ltd.).

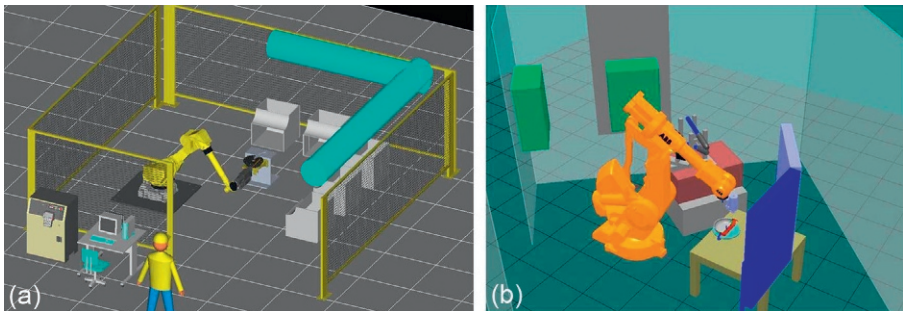


Figure 11.8 Virtual cell created (a) with Roboguide (FANUC Robotics) ([Floristán et al., 2012](#)) and (b) with RobotStudio™ (ABB Ltd.) (courtesy of LERMPS).

11.3.2 Integration of a coordinated external rotational axis

For the coating of some complex-shaped pieces, the integration of a coordinated external rotational axis can be considered. This extends the space that the robot can reach, and it is of special interest for cases in which also the rear face of the component needs to be coated, for example, turbine blades. In such cases, the six axes of an industrial robot might not allow performing the complete spray path in one operation, and the turbine blade would have to be coated on one side, moved and then sprayed on the other side. The use of an external axis, which positions the substrate during the spraying process in coordinated movement with the robot, can give solution to the problematic presented above.

Two spray strategies are considered in literature to coat a piece using a coordinated external axis – vertical and horizontal meander-shaped spray paths – as it can be seen in [Figure 11.9](#) for the case study of a piece with a geometry similar to a turbine blade. A vertical path results in easier kinematics, since the robot can follow each vertical pass with a TCP speed equal to the spray velocity, while the external axis remains with no motion. After each vertical pass, the external axis rotates while the spray torch is located at the outer area of the path, where it does not reach the substrate surface. Next, the axis stops and the robot drives the next pass. For the case of a horizontal spray strategy, the robot and external axis move simultaneously and coordinately between each two points of the trajectory with the aim at keeping spray velocity,

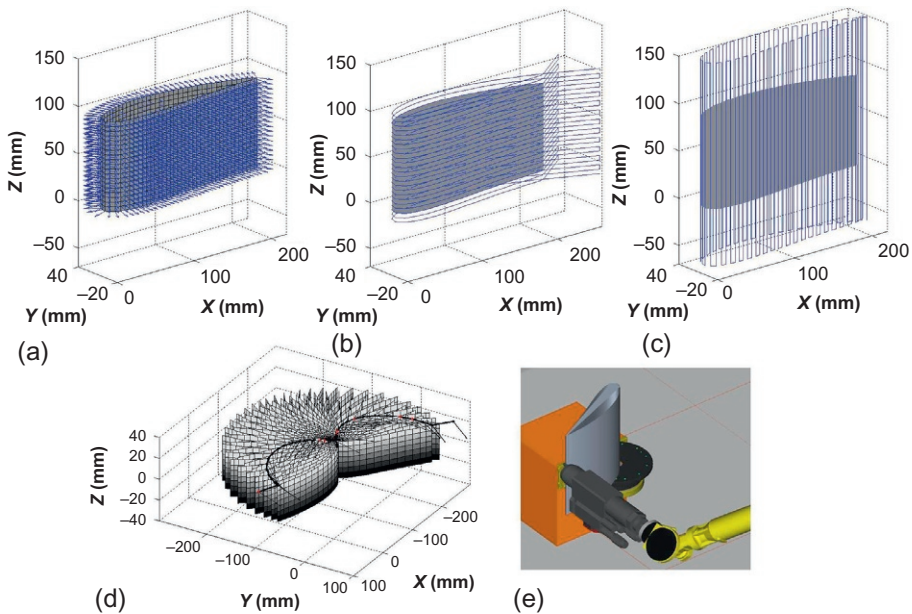


Figure 11.9 (a) Calculation of normal vectors to the substrate surface, meander-shaped trajectory for (b) horizontal and (c) vertical spray strategy. (d) Substrate positions due to the rotation of the external axis and robot trajectory for the first pass of a horizontal spray path and (e) visualisation of coating process with Roboguide (FANUC Robotics) ([Floristán et al., 2012](#)).

distance and angle constant. If the substrate surface presents strong curvature, the normal vector to the surface strongly changes between two consecutive points of the trajectory. This can lead, for example, in the case of a convex curvature, to a great angle between the normal vectors of the two points, which has to be covered by the robot movement. The external axis moves simultaneously with the robot in order to reduce this angle. However, the rotational speed of the external angle is limited, and if the angle to cover is too high, it can lead to a reduction in the spray velocity (Floristán, 2013). Experimental tests have revealed for a similar part geometry as the one shown in Figure 11.9 that a more constant coating thickness could be achieved by using a vertical meander strategy (Deng et al., 2012b). This was explained attending to reductions in the spray velocity from the programmed value when a horizontal path was used.

However, although the external axis speed limitations do not represent a problem when a vertical strategy is chosen and the area of movement of the robot is quite reduced, other aspects should also be taken into account. Depending on the substrate geometry, a vertical path can lead to higher losses of powder due to the time that the spray torch is out of reach of the substrate after each vertical pass (Deng et al., 2012b). Moreover, the thermal load and temperature distribution on the substrate or already deposited coating should be considered. For the case displayed in Figure 11.9, a vertical meander generates a more focused heating of the substrate than a horizontal spray path, which can have a negative effect on the development of residual stresses in the coating.

11.4 Process kinematics optimization

As underlined in Section 11.2, process kinematics has a strong influence on the heat and mass transfer on the substrate and already deposited coating. For this reason, robot trajectories should be planned considering their effect on the resulting coating characteristics. In this section, a review of some contributions dealing with the optimization of process kinematics in order to control the heat and mass transfer to the substrate, and therefore also the coating structural properties, is presented.

Like for spray painting and lacquering processes, many research works in thermal spraying have focused on the modelling of the mass transfer and optimization of the robot trajectory to obtain homogeneous coating thickness (Hansbo and Nylén, 2000; Djuric and Grant, 2003; Duncan et al., 2004; Kout and Müller, 2009). Fasching et al. (1993) optimized the spray angle and scanning step of the robot trajectory in order to compensate the changes of the deposited material droplets due to process instabilities and to produce uniform and even coating thickness. Trifa et al. (2005, 2007) analysed the relationships between the operating parameters and the spray droplets for $\text{Al}_2\text{O}_3/\text{TiO}_2$ APS coatings. Taking in account the interrelated dependencies, they created a model-based expert system for the offline generation of robot trajectories, integrating a spray deposition model, which considered not only coating thickness but also hardness and roughness. The robot trajectory was offline-generated in RobotStudio™ (ABB Ltd.). Afterwards, the expert system was used to predict the coating attributes depending on the selected processing parameters and programmed robot trajectory.

Spraying of curved surfaces can lead to a reduction of the TCP speed, if the normal angles to the substrate surface change strongly. That is the case of convex surfaces where the torch has to follow a large trajectory angle. For these processes, an optimization of the robot trajectory is required. Fang et al. (2010a) proposed a change of the torch orientation from the normal arrangement before and after the curve in order to distribute the angle in a larger trajectory. Krebs (2011) worked also on optimizing the kinematic parameters in convex and concave curvatures of complex-shaped substrates. By adapting the spray velocity or angle, it was possible to produce homogeneous coatings also on surfaces with strong curvature.

Fewer publications are found in literature, in which the heat transfer is also considered and integrated in the planning and optimization of the process kinematics. The heat transfer is a characteristic aspect of thermal spray processes, and it plays a key role in the development of residual stresses, which strongly affect a large number of other coating properties, like hardness, adhesion, coating lifetime and reliability, among others (Wenzelburger et al., 2006). The process kinematics can control to a given extent the thermal history of the coating composite during the spray process and should be therefore planned attending also to thermal aspects. One of the few publications considering the heat transfer for trajectory optimization is the work of Jones et al. (2007). Their studies considered spray forming processes for the production of press tools. A self-standing steel shell was deposited on a ceramic substrate by using several arc spray guns and afterwards separated from the substrate, obtaining, with this, the tool. The robot spray path used for the processes was “mirror box-shaped” (see Figure 11.10a). Jones et al. (2007) developed a method to optimize the “mirror box-shaped” trajectories in order to minimize thermal variations in the coating. Related contributions dealt with the implementation of a controller to adjust the sprayed metal rate during deposition in order to regulate the surface temperature profile (Jones et al., 2003) and the development of transient heat flow models (Rayment and Grant, 2006).

Although the “mirror box-shaped” spray path is adequate for the tool forming process, a meander-shaped spray path is commonly used for the production of functional coatings (Figure 11.10b). Work has been also carried out for trajectory optimization of meander-shaped spray paths in order to reduce thermal gradients in the coating

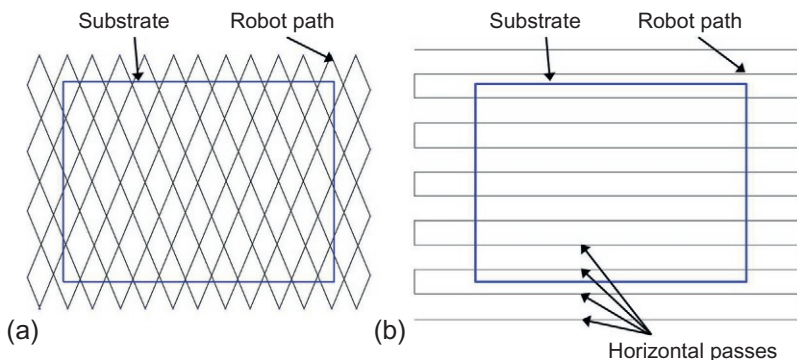


Figure 11.10 (a) “Mirrorbox”-shaped spray path proposed by Jones et al. (2007). (b) Meander-shaped spray path.

composite (Floristán, 2013). As case study for the optimization work, APS was used to deposit $\text{Al}_2\text{O}_3/\text{TiO}_2$ coatings on planar copper substrates. The objective was, for a given spray distance, velocity, angle and scanning step in order to obtain the required coating thickness, to plan the order of each single horizontal pass of the meander-shaped spray path (see Figure 11.10b) in order to minimize the temperature gradients in the substrate. A thermal balance was applied on an element of the substrate, and the transient heat transfer from the plasma jet and particles, considering also the heat losses, was mathematically modelled. By means of genetic algorithms, the meander-shaped spray path was optimized, so that the temperature gradient in the substrate was minimized. Experiments were carried out to verify the obtained results. The substrate temperature gradients and the temperature absolute values were significantly reduced when the robot followed the optimized meander-shaped spray path. If no compressed air cooling was used during the coating process, the reduction of temperature gradients was especially strong. Results of residual stress measurements carried out with the incremental milling and drilling method (Gadow et al., 2005) on a sample sprayed with a typical meander-shaped spray path and with the optimized one are displayed in Figure 11.11. The sample sprayed with a meander-shaped spray path presents compressive stresses in the coating up to approximately 70 MPa (measured by microhole drilling and milling method). This can be explained by the development of cooling stresses, which due to the higher thermal expansion coefficient of copper compared to the $\text{Al}_2\text{O}_3/\text{TiO}_2$ coating are compressive. Quenching stresses, which are tensile, are lower than the cooling stresses, and as a result of both stress mechanisms, the final state of residual stresses in the coating is compressive. On the other hand, the sample sprayed with optimized kinematics shows almost no residual stresses in the coating. Both samples present compressive stresses in the substrate due to grit blasting pretreatment. These results prove therefore the importance of adapting the process kinematics considering the heat transfer to the composite in order to control the coating process and tailor the coating characteristics.

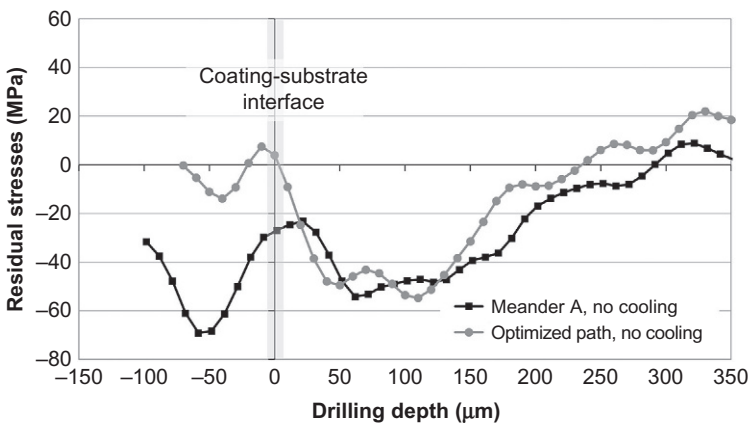


Figure 11.11 Residual stress measurements on $\text{Al}_2\text{O}_3/\text{TiO}_2$ coatings on copper substrates deposited with no forced air cooling sprayed with a meander-shaped and an optimised robot path regarding substrate temperature homogeneity (Floristán, 2013).

11.5 Coupled numerical simulation and offline trajectory generation

Many studies have dealt with the modelling of different aspects of thermal spray process, in the case of APS, for example, from the plasma formation and plasma jet to the coating buildup, including the impact of the melted particles on the substrate and the formation of splats, among other aspects. This section focuses, however, on how such simulations can be coupled with offline programming tools. Like this, the spray path can be adapted and modified depending on the substrate temperature and related phenomena, like the development of residual stresses in the coating composite. Such an approach was introduced for the case of APS by [Nylén and Edberg \(1997\)](#). They suggested a modelling concept combining robot offline programming and coating thickness prediction, CFD for the modelling of the impinging plasma jet and plasma-particle interactions and finite element method (FEM) for the modelling of heat transfer between plasma jet and workpiece. The objective was to enable a link between the torch trajectories and coating thickness and temperatures. In order to do that, the exact process kinematics needs to be considered in the numerical simulations. Some publications have dealt with the transfer of programmed robot trajectories to the simulation by FEMs and are described below.

The influence of the robot trajectory on the heat transfer to the substrate was analysed at IFKB by transferring planned robot trajectories from MATLAB[®] to ANSYS[®] (Ansys Inc., USA) ([Candel, 2009](#); [Floristán et al., 2012](#)). The 3-D model of the substrate is imported in ANSYS[®] and meshed with the adequate element type for the specific part geometry. The nodes of the mesh corresponding to the substrate surface, which has to be coated, are then exported to MATLAB[®] as ASCII data. A routine is programmed in MATLAB[®] in order to select and order a subgroup of the nodes imported from ANSYS[®], depending on the programmed robot trajectory, which will be thermally loaded in FEM to simulate the robot trajectory on the component. This group of nodes describes therefore the movement of the plasma jet or flame hot spot on the substrate surface ([Candel, 2009](#)). The time that each node has to be thermally loaded in ANSYS[®] is calculated in the program routine considering the spray velocity and the distance between two consecutive nodes. Moreover, also the time that the spray torch is not spraying on the substrate, like at reverse points of the path or when it moves between two cycles from the last spray path position to the first one, is also calculated. Although no deposition occurs in this time, cooling of the component takes place, and it should be considered. In order to apply the thermal loads at each node of the simulation model according to the torch orientation at each corresponding point of the robot trajectory, the rotations of a local coordinate system, which will define the thermal load in ANSYS[®], with respect to the global coordinate system are calculated as well ([Floristán et al., 2012](#)). The obtained data are transferred to ANSYS[®] for the numerical simulation.

Considering the case of APS, heat input from the plasma jet and spray particles, as well as heat losses by natural and forced convection with compressed air cooling nozzles and by radiation, are calculated. A local cylindrical coordinate system is used to define the loads at each node of the trajectory. [Figure 11.12](#) displays the surface

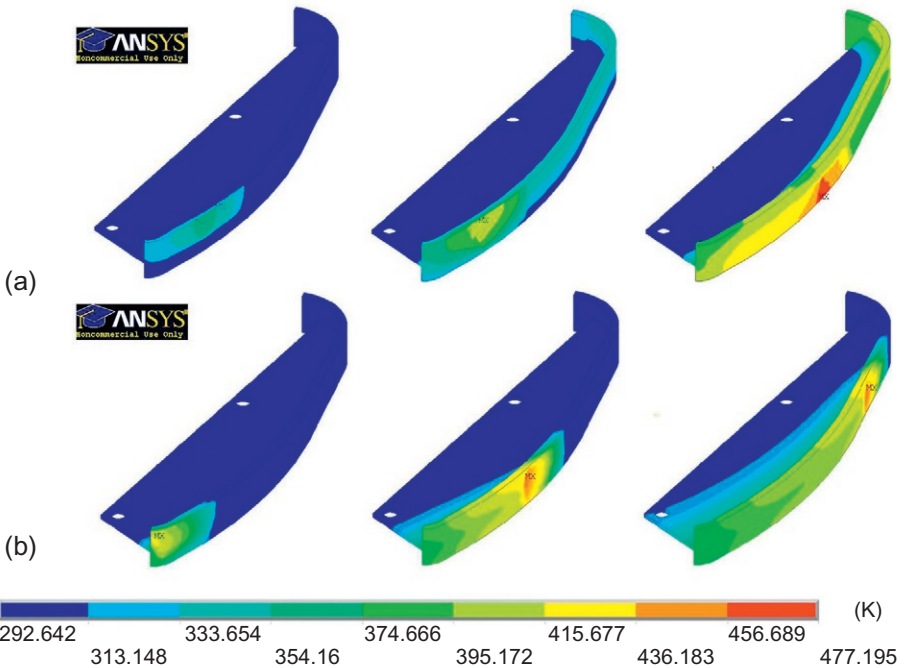


Figure 11.12 Results of temperature distribution obtained by numerical simulation for (a) a horizontal and (b) for a vertical meander-shaped spray path (refer to Figure 11.7d and e, respectively) (Floristán et al., 2012).

temperatures for a horizontal spray path and vertical spray path used for the coating of a blade and obtained from the numerical simulation applying the method exposed above. In order to analyse the effect of the different temperature distributions and temperature absolute values on the coating and substrate, coupled temperature stress field analysis should be carried out. Wenzelburger et al. (2004) used FEA to model the heat and mass transfer during the APS inner coating of an aluminium tube. The thermally induced strains were simulated, and from the obtained values, the thermal stresses could be calculated. Such approaches would allow the consideration of residual stress formation depending on the thermal history of the composite, which, as seen in Figure 11.12, is strongly influenced by the process kinematics.

Another approach to consider the program robot trajectory in the numerical simulation has been developed at LERMP. The TST was used to couple the planning of the robot trajectory with numerical simulation by FEM made with ANSYS® (Cai et al., 2011, 2012). With this aim, the CAD model of the substrate is loaded in ANSYS® and meshed with hexahedral elements with the size of the scanning step. The nodes defining the ANSYS® mesh are exported from to RobotStudio™ and filtered, and they are used to define the robot trajectory. This method enables the exchange of data between RobotStudio™ and ANSYS® and is used as a new tool

for trajectory generation. However, the meshing of the component in ANSYS® is restricted to the use of hexahedral elements with a size corresponding to the scanning step, which, depending on the substrate geometry or dimensions, might not be adequate to obtain accurate results.

11.6 Summary and conclusions

A large amount of processing parameters in thermal spraying influence the formation and final properties of the coating. In the case of APS, for example, it has been reported that the coating service or thermomechanical properties depend on approximately 50–60 different spraying parameters (Fauchais, 2004). For this reason, much research has been conducted to clarify the dependencies between operating parameters and coating properties. Among feedstock or power parameters, also process kinematics plays a decisive role in the resulting coating characteristics. Spraying distance, velocity, angle and spray path have to be optimized in order to fulfil coating quality requirements and to take into account the special feature or boundary conditions given by the substrate and its intended functionality in engineering applications. Heat and mass transfer processes during coating can be partially controlled by the process kinematics and need to be considered in the planning process of robot trajectories for thermal spraying.

Offline programming of industrial robots allows the production of high-performance coatings on complex-shaped parts, and it is increasingly being used in thermal spraying. Commercially available offline programming tools are being combined or extended with modules designed for the generation of trajectories for thermal spraying, which allow maintaining constant kinematic parameters during the process. Normally, the trajectory is planned from the geometric model of the substrate and considering the chosen kinematic parameters.

Research has focused not only on robot trajectory generation but also on its optimization. Models of the material deposit have been created and used to adapt spray paths to complex-shaped geometries in order to assure a continuous coating thickness. Similarly, a few authors have also directed their work to the optimization of spray paths in order to control the heat transfer to the substrate or to the already deposited coating and thus tailor some coating properties. The necessity of including heat and mass transfer aspects in the robot trajectory planning process has led to the coupling of offline programming tools with numerical simulation software. The objectives hereby are to transfer the programmed robot trajectory to the process simulations and thus to be able to predict coating properties and optimize the robot trajectory attending to dimensional and functional coating requirements.

The generation of robot trajectories for high-quality coatings needs to be done in close connection with simulation models of the heat and mass transfer and related to resulting phenomena, like the generation of residual stresses. Such models are necessary to optimize the robot trajectory regarding the coating quality and the functionality and reliability of the final coated product. Research advances in the direction of virtual coating processes, in which the robot trajectory is integrated, together with thermal and mass deposit models, and coating optimization will be, to a given extent, done offline.

References

- Ahmaniemi, S., Vuoristo, P., Mäntylä, T., Latokartano, J., 2002. Optimisation of the robot controlled plasma spraying of thermal barrier coating for gas turbine transition duct. In: Lugscheider, E.F., Berndt, C.C. (Eds.), *Proceedings of the International Thermal Spray Conference*. DVS Media GmbH, Düsseldorf, pp. 208–212.
- Bussmann, M., Chandra, S., Mostaghimi, J., 1999. Numerical results of off-angle thermal spray particle impact. In: Lugscheider, E.F., Kammer, P.A. (Eds.), *2nd United Thermal Spray Conference*. DVS Media GmbH, Düsseldorf, pp. 783–786.
- Cai, Z., Deng, S., Liao, H., Coddet, C., Zeng, C., 2011. New method of generating robot trajectory on complex geometric workpiece. In: *Proceedings of the International Thermal Spray Conference*. DVS Media GmbH, Düsseldorf.
- Cai, Z., Deng, S., Liao, H., Zeng, C., Coddet, C., 2012. Robot trajectory generated on free-form work pieces for thermal spraying. In: Lima, R.S., Agarwal, A., Hyland, M.M., Lau, Y.-C., Li, C.-J., McDonald, A., Toma, F.-L. (Eds.), *Proceedings of the International Thermal Spray Conference*. ASM International, Materials Park, pp. 429–435.
- Candel, A., 2009. Entwicklung von thermisch gespritzten Schichtverbundwerkstoffen durch Optimierung robotergestützter Brennerbewegungsabläufe. Shaker Verlag GmbH, Aachen.
- Candel, A., Gadow, R., 2006. Optimized multiaxis robot kinematic for HVOF spray coatings on complex shaped substrates. *Surf. Coat. Technol.* 201, 2065–2071.
- Candel, A., Gadow, R., 2009. Trajectory generation and coupled numerical simulation for thermal spraying applications on complex geometries. *J. Therm. Spray Technol.* 18 (5–6), 981–987.
- Dai, W., 2000. PC-basierte, interaktive Off-line-Programmierung von Schweißrobotern mit verbesserter Nutzerunterstützung. Verlag Mainz GmbH, Aachen.
- Deng, S., Liao, H., Zeng, C., Charles, P., Coddet, C., 2005. Development of robotic trajectories autogeneration in thermal spraying. A new extended program of ABB RobotStudio™. In: *2. Recontres Internationales sur la Projection Thermique*.
- Deng, S., Li, H., Liao, H., Coddet, C., Zeng, C., Charles, P., Urito, P., 2006. New functions of Thermal Spray Toolkit. A software developed for off-line and rapid robot programming. In: Marple, B.R., Moreau, C.C. (Eds.), *Proceedings of the International Thermal Spray Conference*. ASM International, Materials Park, pp. 1437–1442.
- Deng, S., Cai, Z., Fang, D., Liao, H., Montavon, G., 2012a. Application of robot offline programming in thermal spraying. *Surf. Coat. Technol.* 206, 3875–3882.
- Deng, S., Fang, D., Cai, Z., Liao, H., Montavon, G., 2012b. Application of external axis in robot-assisted thermal spraying. *J. Therm. Spray Technol.* 21 (6), 1203–1215.
- Djuric, Z., Grant, P., 2003. An inverse problem in modelling liquid metal spraying. *Appl. Math. Model.* 27, 179–396.
- Duncan, S., Jones, P., Wellstead, P., 2004. Robot path planning for spray coating: a frequent domain approach. In: *Proceedings of the 2004 American Control Conference*, Boston, MA, pp. 4643–4648.
- Escribano, M., Gadow, R., Killinger, A., Wenzelburger, M., 2003. Metallic and dielectric coatings on glass ceramic – characterization and modelling of residual stresses. In: Kriven, W. M., Lin, H.-T. (Eds.), *Ceramic Engineering and Science Proceedings*. The American Ceramic Society, Westerville, pp. 193–200.
- Fang, D., Deng, S., Liao, H., Coddet, C., 2010a. The effect of robot kinematics on the coating thickness uniformity. *J. Therm. Spray Technol.* 19 (4), 796–804.
- Fang, D., Deng, S., Liao, H., Coddet, C., 2010b. The improvements of Thermal Spray Toolkit, extended software for robotic off-line programming. In: *Proceedings of the International Thermal Spray Conference*. DVS Media GmbH, Düsseldorf.

- Fang, D., Deng, S., Liao, H., Coddet, C., 2011. Automatic generation of robot trajectory for free-form surfaces in thermal spraying. In: Proceedings of the International Thermal Spray Conference. DVS Media GmbH, Düsseldorf.
- Fasching, M.M., Prinz, F.B., Weiss, L.E., 1993. Planning robotic trajectories for thermal spray shape deposition. *J. Therm. Spray Technol.* 2 (1), 45–57.
- Fauchais, P., 2004. Understanding plasma spraying. *J. Phys. D. Appl. Phys.* 37, R86–R108.
- Floristán, M., Müller, P., Gebhardt, A., Killinger, A., Gadow, R., Cardella, A., Li, C., Stadler, R., Zangl, G., Hirsch, M., Lacqua, H.P., Kasperek, W., 2011. Development and testing of 140 GHz absorber coatings for the water baffle of W7-X cryopumps. *Fusion Eng. Des.* 86 (9–11), 1847–1850.
- Floristán, M., Montesinos, J.A., García-Marín, J.A., Killinger, A., Gadow, R., 2012. Robot trajectory planning for high quality thermal spray coating processes on complex shaped components. In: Lima, R.S., Agarwal, A., Hyland, M.M., Lau, Y.-C., Li, C.-J., McDonald, A., Toma, F.-L. (Eds.), Proceedings of the International Thermal Spray Conference. ASM International, Materials Park, pp. 448–453.
- Floristán, M., 2013. Off-line generation of robot trajectories for Thermal Spray processes with respect to the heat and mass transfer. Thesis, University of Stuttgart, Faculty for Mechanical Engineering, 2012, Shaker Verlag, Aachen. ISBN 978-3-8440-1881-3.
- Friedrich, C., 2002. Atmosphärisch plasmagespritzte dielektrische oxidkeramische Schichten für Ozongeneratoren. Shaker Verlag GmbH, Aachen.
- Friedrich, C., Gadow, R., Killinger, A., Li, C., 2001. IR thermographic imaging – a powerful tool for on-line process control of thermal spraying. In: Berndt, C.C., Khor, K.A., Lugscheider, E.F. (Eds.), Proceedings of the International Thermal Spray Conference. ASM International, Materials Park, pp. 779–786.
- Friis, M., Persson, C., Wigren, J., 2001. Influence of particle in-flight characteristics on the microstructure of atmospheric plasma sprayed yttria stabilized ZrO₂. *Surf. Coat. Technol.* 141, 115–127.
- Gadow, R., Killinger, A., Li, C., 2002. On-line process control of plasma sprayed ceramic coatings with IR thermographic imaging. In: Lugscheider, E.F., Berndt, C.C. (Eds.), Proceedings of the International Thermal Spray Conference. DVS Media GmbH, Düsseldorf, pp. 573–579.
- Gadow, R., Riegert-Escribano, M.J., Buchmann, M., 2005. Residual stress analysis in thermally sprayed layer composites, using the hole milling and drilling method. *J. Therm. Spray Technol.* 14 (1), 100–108.
- Hamatani, H., Ichiyama, Y., Kobayashi, J., 2002. Mechanical and thermal properties of HVOF sprayed Ni based alloys with carbide. *Sci. Technol. Adv. Mat.* 3, 319–326.
- Hansbo, A., Nylén, P., 2000. Modeling of spray deposition and robot motion optimization for a gas turbine application. In: Berndt, C.C. (Ed.), Proceedings of the 1st International Thermal Spray Conference, pp. 203–209.
- Houdková, S., Kasparová, M., Zahálka, F., 2010. The influence of spraying angle on properties of HVOF sprayed hardmetal coatings. *J. Therm. Spray Technol.* 19 (5), 893–901.
- Ilavsky, J., Allen, A.J., Long, G.G., Krueger, S., Berndt, C.C., Herman, H., 1997. Influence of spray angle on the pore and crack microstructure of plasma-sprayed deposits. *J. Am. Ceram. Soc.* 80 (3), 733–742.
- Jones, P.D.A., Duncan, S.R., Rayment, T., Grant, P.S., 2003. Control of temperature profile for a spray deposition process. *IEEE Trans. Control Syst. Technol.* 11 (5), 656–667.
- Jones, P.D.A., Duncan, S.R., Rayment, T., Grant, P.S., 2007. Optimal robot path for minimizing thermal variations in a spray deposition process. *IEEE Trans. Contr. Syst. Technol.* 15 (1), 1–11.

- Kang, C.W., Ng, H.W., Yu, S.C.M., 2006. Imaging diagnostics study on obliquely impacting plasma-sprayed particles near to the substrate. *J. Therm. Spray Technol.* 15 (1), 118–130.
- Kerama, J.G., 1999. *Robot Technology Fundamentals*. Delmar Publishers Inc., New York.
- Killinger, A., 2010. Funktionskeramische Schichten durch thermokinetische Beschichtungsverfahren. Shaker Verlag GmbH, Aachen.
- Kout, A., Müller, H., 2009. Parameter optimisation for spray coating. *Adv. Eng. Softw.* 40, 1078–1086.
- Krebs, B., 2011. Konturgenau Bauteilbeschichtung für den Verschleißschutz mittels Atmosphärischen Plasmaspritzens und Lichtbogenspritzens. Vulkan Verlag GmbH, Essen.
- Leigh, S.H., Berndt, C.C., 1997. Evaluation of off-angle thermal spray. *Surf. Coat. Technol.* 89, 213–224.
- Li, C., 2003. Herstellung und Optimierung plasmagespritzter Schichten auf Glaskeramik für elektrische Anwendungen. Shaker Verlag GmbH, Aachen.
- Montavon, G., Sampath, S., Berndt, C.C., Herman, H., Coddet, C., 1997. Effects of the spray angle on splat morphology during thermal spraying. *Surf. Coat. Technol.* 91, 107–115.
- Montavon, G., Berndt, C.C., Trifa, F.I., Guessasma, S., 2005. Correlating the spray pattern to the coating architecture: exploring the dominant mechanisms and process parameters. In: Lugschneider, E. (Ed.), *Proceedings of the International Thermal Spray Conference 2005*. DVS Media GmbH, Düsseldorf, pp. 798–809.
- Nylén, P., Edberg, M., 1997. Robot trajectory generation and coating temperature prediction of plasma sprayed coatings. In: Berndt, C.C. et al., (Ed.), *Proceedings of the 1st United Thermal Spray Conference*. ASM International, Materials Park, pp. 583–591.
- Rayment, T., Grant, P.S., 2006. Modelling of the heat flow in spray formed steel shells for tooling applications. *Metall. Mater. Trans. B* 37B, 1037–1047.
- Smith, M.F., Neiser, R.A., Dykhuizen, R.C., 1994. An investigation on the effects of droplet impact angle in thermal spray deposition. In: Berndt, C.C., Sampath, S. (Eds.), *Proceedings of the 7th National Thermal Spray Conference*. ASM International, Materials Park, pp. 603–608.
- Strock, E., Ruggiero, P., Reynolds, D., 2001. The effect of off-angle spraying on the structure and properties of HVOF WC/CoCr coatings. In: Berndt, C.C., Khor, K.A., Lugschneider, E.F. (Eds.), *Proceedings of the 2nd International Thermal Spray Conference*. ASM International, Materials Park, pp. 671–676.
- Tillmann, W., Vogli, E., Krebs, B., 2008. Influence of the spray angle on the characteristics of atmospheric plasma sprayed hard material based coatings. *J. Therm. Spray Technol.* 17 (5–6), 948–955.
- Trifa, F.-I., Montavon, G., Coddet, C., 2005. On the relationships between the geometric processing parameters of APS and the $\text{Al}_2\text{O}_3\text{-TiO}_2$ deposit shapes. *Surf. Coat. Technol.* 195, 54–69.
- Trifa, F.-I., Montavon, G., Coddet, C., 2007. Model-based expert system for design and simulation of APS coatings. *J. Therm. Spray Technol.* 16 (1), 128–139.
- Vijay, M., Selvarajan, V., Yugeswaran, S., Ananthapadmanabhan, P.V., Sreekumar, K.P., 2009. Effect of spraying parameters on deposition efficiency and wear behavior of plasma sprayed alumina–titania composite coatings. *Plasma Sci. Technol.* 11 (6), 666–673.
- Wenzelburger, M., Escribano, M., Gadow, R., 2004. Modeling of thermally sprayed coatings on light metal substrates: layer growth and residual stress formation. *Surf. Coat. Technol.* 180–181, 429–435.
- Wenzelburger, M., López, D., Gadow, R., 2006. Methods and application of residual stress analysis on thermally sprayed coatings and layer composites. *Surf. Coat. Technol.* 201, 1995–2001.

- Xia, W., Zhang, H., Wang, G., Yang, Y., 2009. A novel integrated temperature investigation approach of sprayed coatings during APS process. *J. Mater. Process. Technol.* 209 (6), 2897–2906.
- Yilmaz, S., Kurt, A.O., Demir, A., Tatli, Z., 2007. Effects of TiO₂ on the mechanical properties of the Al₂O₃–TiO₂ plasma sprayed coating. *J. Eur. Ceram. Soc.* 27, 1319–1323.
- Zieris, R., Schmidt, A., 2004. Off-line programming for spraying and laser cladding of three dimensional surfaces. In: *Proceedings of the International Thermal Spray Conference*. ASM International, Materials Park, pp. 453–455.

Index

Note: Page numbers followed by *f* indicate figures and *t* indicate tables.

A

Aerodynamic interactions, 131*f*
Aerospace industry, 10–12
Air plasma spraying (APS), 22–23,
22*f*, 237
Aluminium (Al), 153, 154*f*
ANSYS[®], 274
Antifouling coatings, 216
Antithixotropy, 62
Aqueous suspension, 71
Arc spraying (AS), 1–2, 8–9, 216–217
Atmospheric plasma spraying (APS)
 feedstock suspensions and solutions, 52
 process kinematics, 262, 262*f*
Atomization, 85–86, 151–152
Attractive interaction, 53–55
Automotive industry, 10–12
Axial III torch, 23

B

Bioglasses, 104
Biomass incineration boilers
 advantages, 242
 diffusion coatings drawbacks,
 242–243
Biomedical applications, coatings
 biocompatible coatings, 104
 bioglasses, 104
 HVSFS bioglass, 106–107, 107*f*
 hydroxyapatite, 104
 single-anode torch SPS process, 105
 SPS HA coating, 105, 106*f*

C

Ceramic films
 advantages and usefulness, 125
 chemical process, 124*t*
 definitions, 124–125
 history, 125
Ceramic suspensions rheology, 59–64

Cermets

 cold spray techniques, 157–158, 158*f*
 suspension spraying, 114–115
Chemical phenomena, 131–133
Chemical vapor deposition (CVD), 17–19
Coating buildup
 measurements and testing, 31–32
 models, 36–37
Coating properties, 91–93
Cold spraying, 1–2, 9
 applications, 158–160
 bonding strength, 148–149, 149*f*
 characteristics, 144–145
 Cu coatings deposition, 148–151, 148*f*
 electrical conductivity, 150–151, 150*f*
 environmental barrier coatings, 237–238
 functionalized thermal spray coatings, 216
 gas velocity and temperature distributions,
 144*f*
 high-melting-point metals and alloys,
 155–157
 high-pressure, 146, 147*f*
 low-melting-point metals and alloys,
 152–154
 low-pressure, 145–146, 146*f*
 mechanical properties, 149–150, 150*f*
 particle velocity and temperature, 144*f*
 Plasma Giken's PCS-1000, 146, 147*f*
 properties of, 148–151
 repair and restore, 160, 160*f*
 spray torches, 27–28
 Ta and Nb, 157, 158*f*
 thick coatings deposition, 151, 151*f*
 typical cold spray system, 145, 145*f*, 148,
 149*f*
Colloidal stability, 53–59
Combustion flames, 30
Computational fluid dynamics (CFD)
 modeling, 98–99
Controlled atmosphere. *See* Soft vacuum
 plasma spraying

- Coordinated external rotational axis, 270–271
 Copper (Cu), 154, 155*f*
 Corrosion, 231
 Corrosion protection coatings, 215
 Coupled plasma (ICP) spray, 83–84
- D**
- Debye–Hückel equation, 55–56
 Deposition efficiency (DE), 91
 Derjaguin–Landau–Verwey–Overbeek (DLVO), 56–57
 Detonation gun (D-guns), 2, 8, 24–25
 Detonation thermal spray process, 244
 Diamond Jet system, 97–98
 Dielectric properties, TiO₂ coatings, 135–136
 Diffusion combustion, 34
 Direct current plasma spraying, 21–24
 Drilling method, 272–273
 Droplet formation, 86–87, 88*f*
 DYMET systems, 145–146
 Dynamic light scattering, 68
- E**
- Electrodeposition, 214–215
 Electromagnetic applications, 159, 159*f*
 Electron energy loss spectroscopy (EELS), 182, 183*f*
 Electrostatic interaction, 54–58
 Environmental barrier coatings (EBCs)
 degradation mechanisms, 231, 232*t*
 development and application, 238
 mullite, 232–233
 silicon-based ceramics, 232–233
 Erosion behavior, 197–198
 Evaporation, suspension–gas interaction, 86
- F**
- Feeder, 94–95
 Feedstock, cold spray, 151–152
 First-order process maps, 31
 Flame spraying, 1–2, 5–8
 ductile metals wires, 20
 functionalized thermal spray coatings, 216–217, 217*f*
 gas temperature vs. gas velocity, 19–20, 20*f*
 principle of, 19, 19*f*
- Flow behaviour
 curves analysis, 60, 61*t*
 shear stress vs. shear rate, 60, 60*f*
- F4MB torch, 109–110
 Fracture resistance, 192
 Functional coatings, 207
 Functionalized thermal spray coatings
 capsules technology
 (see Microencapsulation)
 functional and smart coating, 207
 liquid–solid self-lubricated coatings, 214
 low-friction, 218–225
 solid lubricants, 214
 Functionally graded material (FGM) coatings, 235
- G**
- Gas-phase synthesis, 51
 Geothermal piping systems
 binary cycle, 244, 245*f*
 coupon tree insertion, 244, 245*f*
 Gouy–Chapman theory, 56
 Gravitational forces, 70
- H**
- Hard sphere interaction, 53
 Heat and mass transfer, 259–260, 276
 High-energy gases, 34–35
 High-pressure warm spray (HP-WS)
 fuel injector geometry, 198, 199*f*
 numerical simulation profiles, 198, 200*f*
 Ti–6Al–4V coatings, 199–201
 High-velocity air-fuel (HVAF), 25–26
 functionalized thermal spray coatings, 216–217
 gas/particle temperatures, 173*f*, 175
 gas/particle velocity, 173*f*, 174–175
 gas velocity, 174–175
 temperature–velocity trajectories, 175–176, 175*f*
 High-velocity oxy-fuel (HVOF), 8
 biomass incineration boilers, 243
 corrosion barrier coatings, 164–166
 different types of, 25, 26*f*
 environmental barrier coatings, 237
 functionalized thermal spray coatings, 216–217

- for HVFSFS, 97–99
 - marine exposure tests, 167–170
 - particle temperatures vs. particle velocities, 26, 27*f*
 - porosity vs. oxygen content, 166–167, 167*f*
 - solution spray techniques, 127–128
 - surface roughness and Vickers hardness, 195–197, 197*f*
 - XRD patterns, 191–192
- High-velocity suspension flame spraying (HVFSFS)
- cone-shaped defect, 90*f*
 - Cr₂O₃ coating microstructure, 115*f*
 - light microscope image, 113*f*
 - porosity structure, 91
 - semimolten droplets, 89
 - wipe test, 88–89, 89*f*
- Hydroturbines, 248–249
- Hydroxyapatite, 104
- I**
- Idaho National Engineering and Environmental Laboratory (INEEL), 244
- Inductively coupled plasma (ICP), 96
- Injection, solution spray techniques, 130–131
- Inner Helmholtz plane (IHP), 56
- Interfacial polymerization, 210–211
- Iron (Fe), 155, 155*f*
- ITER Vacuum Vessel, 160, 161*f*
- K**
- Kinetic Metallization system, 145–146
- Krieger–Dougherty model, 62–64
- L**
- Laser cladding process, 242–243
- Laser diffraction, 68
- Laser Doppler, 68
- LERMPS, 267
- Liquid feedstock injection, 126–127, 127*f*
- Liquid phase, suspension spray techniques, 82
- Low-friction coatings, 216
- Low-pressure plasma spraying (LPPS), 23
- M**
- Marine exposure tests
- corrosion damage, 167–170, 169*f*
 - Hastelloy coatings cross sections, 167–170, 168*f*
 - iron ions dissolution rate, 167–170, 169*f*
- MATLAB®, 267–269, 274
- MCrAlY alloys, 156–157, 156*f*
- Meander-shaped spray path, 263–264
- Metal matrix coatings
- CoF measurements, 222, 224*t*
 - cross-sectional analysis, 222, 223*f*
 - friction evolution coefficient, 222–223, 225*f*
 - liquid-filled capsules, 221
 - methods, 221–222
- Metals, suspension spraying, 114–115
- Mettech Axial III plasma torch, 108–109
- Microencapsulation
- applications, 210
 - aqueous dispersions, 212*f*
 - benefits, 209
 - definition, 209
 - lubricant-filled microcapsules, 210–213
 - physical and chemical properties, 210
- Microstructure
- comparison, 188–189, 188*f*
 - cross-sectional image, 189, 190*f*
 - nitrogen flow rate, 189, 189*f*
 - SEM observations, 189–191, 190*f*
 - solution spray techniques, 133–134
 - XRD patterns, 191–192, 191*f*
- Miniemulsion, 211, 211*f*
- Mullite, 232–233
- N**
- Nanosized feedstocks, 91
- Nanosuspensions, 71
- Nickel (Ni), 156, 156*f*
- Nozzle, suspension, 86
- Numerical simulation, 170–172, 274–276
- O**
- Offline robots programming, 265–271
- Offshore wind turbine towers
- atmospheric exposure, 247, 247*t*
 - different corrosion zones, 246, 246*f*
 - underwater and splash zone areas, 247, 247*t*

1D models, HVOF/HVAF, 34
 Optical properties, 215
 Optimization, process kinematics
 curved surfaces, 272
 genetic algorithms, 272–273, 273f
 heat transfer, 272
 mirror box-shaped, 272–273
 spray painting and lacquering
 processes, 271
 Optoelectronic properties, 137
 Outer Helmholtz plane (OHP), 56
 Oxidation, 231

P

Particles in-flight, 35–36
 Particle size distribution (PSD)
 energies association, 71t
 mean diameter types, 67t
 measuring systems, 68
 Pelton wheel turbine, 248, 248f
 Photocatalytic hydrogen production,
 249–251
 Photovoltaic power generation, 252–253
 Physical vapor deposition (PVD), 17–19
 Plasma jet, 28–29, 29f
 Plasma plumes, 30
 Plasma spraying, 2, 9
 functionalized thermal spray coatings, 216,
 218
 Plasma torches, 96–97, 97f
 PlazJet torch, 23
 Polyelectrolytes, steric interaction, 58
 Polymer matrix coatings
 average CoF, 220, 221t
 cross section, 219–220, 220f
 liquid–solid self-lubricating, 218
 method, 218–219
 nozzle, 219
 self-lubricating coating surface,
 219, 220f
 tribological tests, 220
 Polymer pyrolysis, 51
 Polyurea microcapsule synthesis,
 211, 211t
 Process kinematics
 definition, 259–260
 optimization, 271–273
 parameters, 260, 261f

R

Rare earth silicates, 234–235
 Renewable energy
 applications, 241–242
 coating techniques, 241
 low-cost method, 241–242
 Residual stresses, 264
 RF induction plasmas, 24
 Rheology
 alumina suspensions, 64, 65f
 characteristic, 59
 definition, 59
 suspensions feedstock, 72
 viscosity vs. volume fraction, 62–64, 63t
 Rheopexy. *See* Antithixotropy
 RobotStudio™, 267, 268f
 Robot systems
 automation systems, 259–260
 complex-shaped components, 260
 coordinated external rotational axis,
 270–271
 definition, 259–260
 offline programming, 265–271
 RotaPlasma torch, 22–23

S

Sawtooth-shaped profile, 260–261
 Sensors, 32
 Single-anode torch SPS process, 105
 Soft vacuum plasma spraying, 23–24
 Sol-gel film deposition process, 124–125
 Solgel technology, 51
 Solid oxide fuel cell (SOFC) development
 HVSFS YSZ electrolyte, 109f
 PEM-FC, 107
 Solution feedstock
 gravitational forces, 70
 PSD (*see* Particle size distribution (PSD))
 surface area, 69
 suspension stability, 66
 types and preparation, 73–74
 Solution precursor flame spray (SPFS), 127
 Solution precursor plasma spraying (SPPS),
 40, 74, 75t, 126–127, 250
 Solution spray techniques
 applications, 138
 ceramic films and coatings (*see* Ceramic
 films)

- chemical composition, 128, 129*t*
 - in-flight, 128, 130*f*
 - microstructure, 133–134
 - properties, 134–137
 - Spray angle
 - Al₂O₃/TiO₂ APS coatings, 262, 262*f*
 - definition, 260–261
 - in-flight particle velocity, 260–261
 - roughness/porosity, 263
 - sawtooth-shaped profile, 260–261
 - Spray distance, 263
 - Spray forming, 160
 - Spray manufacturing and annealing in real time (SMART), 237
 - Spray path, 263–265
 - Spray pattern, 32
 - Spray pyrolysis, 126, 126*f*
 - CZTS films, 137
 - thermal conductivity vs. temperature, 136*f*
 - Spray torches, 19–28
 - Spray velocity, 263
 - SprayView[®], 30–31
 - SprayWatch[®], 30–31
 - Sputtering target, 158–159, 159*f*
 - Stainless steel, 155, 155*f*
 - Static light scattering, 68
 - Steady-state 3-D models, 33
 - Steric interaction, 54, 58–59
 - Submicron suspensions, 71
 - Submicron suspensions-nanosuspensions, 71
 - Substrate geometric model, 266
 - Surface area, 69
 - Surface degradation, 232
 - Surface roughness
 - cross-sectional images, 195, 196*f*
 - map, 197*f*
 - variation, 195, 196*f*
 - Suspension–gas interaction
 - breakup mechanisms, 87, 87*f*
 - droplet formation process, 88, 88*f*
 - evaporation, 86
 - Suspension injection, 84–86
 - Suspension plasma spraying (SPS), 40, 250, 250*f*
 - Suspensions feedstock
 - ceramic suspensions rheology, 59–64
 - granules microstructure, 74*f*
 - rheology, 62–64
 - stability and rheology, 53–64
 - stabilizing agents types, 72*t*
 - types and preparation, 71–73
 - viscosity evolution, 73*f*
 - Suspension spraying
 - Al₂CO₃ coating, 91, 92*f*
 - applications, 99–115
 - APS vs. HVSFS HA coatings, 82–83, 83*f*
 - catalytically active coatings, 110–112
 - coating formation and achieved
 - microstructures, 88–91
 - equipment, 93–99
 - HVOF process, 84
 - liquid phase, 82
 - nanosized feedstocks, 91
 - properties, 82, 116
 - thermal spraying, 82
 - Suspension stability, 66
- ## T
- Tensile strength, 186–187, 186*f*
 - Thermal barrier coatings (TBCs)
 - different coating technologies, 101*f*
 - fabrication, 102–103
 - zirconia-based TBCs, 100
 - Thermal-resistant coatings, 215
 - Thermal spray coatings
 - aerospace industry, 10–12
 - applicability, 5, 6*t*
 - applications, 10, 11*t*
 - automotive industry, 10–12
 - coating build-up process, 4
 - current markets, 10
 - different coating processes comparison, 3, 3*f*
 - family tree, 1–2, 2*f*
 - feedstock production, 13
 - growth of, 12
 - metallizing, 1–2
 - Thermal spraying
 - characteristics, 5, 7*t*
 - coating applications and developments, 38–39
 - fabrication techniques, 236–238
 - high-energy gas temperatures and velocities, 28–30
 - in-flight particle temperatures, velocities, and diameters, 30–31
 - measurements and testing, 28–32

- Thermal spraying (*Continued*)
 PS with physical vapor deposition, 39–40
 revenue generation, coating services,
 38–39, 39f
 SPS and SPPS, 40
 suspension spray techniques, 82
- Thermoelectric power generation, 251–252
- Thermophotovoltaic (TPV) power generation,
 253–254
- Thermophysical phenomena, 131
- Thermophysical properties, 134–135
- Thixotropic, 62
- 3D compressible models, 35
- Three-dimensional printer, 160
- Tin (Sn), 153, 153f
- Titanium (Ti), 157, 157f
- Titanium oxide coatings, 110, 111f
- Titanium splats, WS
 bonding, 180–182
 cross section TEM images, 180, 181f
 grain refinement, 180, 181f
 SEM top view and TEM cross-sectional
 observation, 182–184, 184f
 STEM images and EELS analysis, 182, 183f
 TEM and EFTEM images, 180–182, 182f
 TEM cross-sectional observation, 182, 183f
 top view and cross section, 180, 180f
- Tokyo Bay Aqua-Line Highway Bridge,
 164–166, 165f
- TopGun system, 97–98
- Trajectory generation, 266–269
- Transition temperature, 31–32
- Triplex Torch, 23
- Tubular coating tensile (TCT) tests
 fracture surface, 184–186, 185f
 stress–strain curves, 184–186, 185f
 tensile strength, 186–187, 186f
 tensile strength vs. elongation to failure,
 187–188, 187f
- 2D compressible models, 35
- U**
- Ultra-Steel Project, 164–166
- V**
- Vacuum plasma spraying (VPS).
See Low-pressure plasma spraying (LPPS)
- Vickers hardness, 192
- Virtual models, robot trajectory
 implementation, 269
- W**
- Warm spraying (WS)
 critical velocity, 178f
 cross sections, 176–177, 177f
 gas/particle temperature, 173f, 175
 gas/particle velocity, 173f, 174
 gas velocity, 174
 HVOF (*see* High-velocity oxy-fuel
 (HVOF))
 microstructure and mechanical
 properties, 176
 numerical simulation, 170–171
 operating conditions, 171–172, 171f
 oxygen contents, 178–179, 179f
 process map, 163
 surface roughness and Vickers hardness,
 195–197, 197f
 temperature–velocity trajectories,
 175–176, 175f
 titanium deposition analysis,
 179–180, 179f
 titanium particles temperature and velocity,
 176–177, 177f
 XRD patterns, 191–192
- Water-stabilized plasma torch, 23
- WC–Co cermet coatings
 cross-sectional images, 192–194, 195f
 indentation fracture toughness test,
 192, 194f
 microstructure (*see* Microstructure)
 SEM observation, cross section,
 192, 193f
- Wear-resistant coatings, 112–114
- Wire-arc spraying, 21, 21f
- Y**
- Yield stress, 62
- Yttria-stabilized zirconia (YSZ), 108,
 233–234
- Z**
- Zeta potential, 56
- Zinc (Zn), 153, 154f
- Zircon (ZrSiO₄), 238–239, 238f
- Zirconia, 100